PROCEEDINGS OF THE

SECOND JOINT MEETING OF THE U.S.-JAPAN CONFERENCE

ON NATURAL RESOURCES

(UJNR) PANEL ON EARTHQUAKE PREDICTION TECHNOLOGY

JULY 13-17, 1981

Panel Chairmen:

David P. Hill
U.S. Geological Survey
Menlo Park, California 94025
U.S.A.

Keiji Nishimura
Geographical Survey Institute
Ibaraki-Ken 305
Japan

tw anal

U.S. Geological Survey

Open-File Report 82-180

TABLE OF CONTENTS

INTRODUCTION

The Second Joint Meeting of the UJNR Panel on Earthquake Prediction Technology was held at the U.S. Geological Survey facilities in Menlo Park, California, during the week of July 13, 1981. This panel, which was established in 1978, is the newest of 17 panels under the United States/Japan Cooperative Program in National Resources (UJNR). The UJNR program is based on a 1964 cabinet-level agreement to foster the exchange of scientists, information, equipment, and knowledge between government agencies in Japan and the United States concerned with problems involving natural resources.

Mr. Keiji Nishimura headed the Japanese delegation of four panel members and two observers. From the United States side, seven panel members and eight observers participated in the meeting, and an audience of up to 40 people attended the technical sessions on July 16 and 17.

In addition to the technical sessions, the meeting included a field trip along the San Andreas fault led by Bob Nason and a tour of USGS laboratory facilities in Menlo Park. Following the meeting, members of the Japanese delegation visited the National Bureau of Standards in Boulder, Colorado; and the National Geodetic Survey, the National Defense Mapping Agency, Goddard Space Flight Center, and the U.S. Geological Survey in Washington, D. C.

The twenty scientific papers presented during the technical session are summarized in these proceedings. These papers represent an important part of the mutual exchange of information fostered by this panel on progress and problems in research on earthquake prediction in Japan and the United States.

I wish to express my gratitude to the many people who helped contribute to the successful conclusion of this meeting. I am particularly grateful to Tom Burdette and Elsie Hirscher for their most able assistance in arranging the many details that resulted in the smooth progress of the meeting.

David P. Hill
Chairman: U.S. Panel

U. S. MEMBERS OF THE U. J. N. R. PANEL

Dr. David P. Hill, Chairman*
Chief, Seismology Branch
U.S. Geological Survey
345 Middlefield Road - MS-77
Menlo Park, CA 94025

Dr. Peter L. Bender*
Senior Scientist, NBSIBS
Jila, University of Colorado
Boulder, Colo. 80209

Capt. John Bossler
Director, National Geodetic Survey
6001 Executive Blvd. C1X1
Rockville, Md. 20852

Dr. John Filson
Chief, Office of Earthquake Studies
U.S. Geological Survey
National Center - MS-905
Reston, Va 22092

Dr. Edward Flinn
Chief Scientist, Geodynamics
Resource Observation Division
NASA Hdqtrs., Code ERG-2
Washington, D.C. 20546

*Mr. Leon L. Beratan, Chief
Earth Sciences Branch
Div. Health Siting & Waste Mgmt.
U.S. Nuclear Regulatory Commission
Washington, D.C. 20555

*Dr. Leonard Johnson
Program Director, Geophysics
Division of Earth Science, NSF
1800 G Street, N. W.
Washington, D.C. 20550

*Dr. C. Barry Raleigh
Coordinator, Earthq. Pred. Program
U.S. Geological Survey
345 Middlefield Road - MS-77
Menlo Park, Calif. 94025

*Dr. Wayne Thatcher
Research Geophysicist
U.S. Geological Survey
345 Middlefield Road, MS-77
Menlo Park, Calif. 94025

*Dr. Robert L. Wesson
Assistant Director for Research
U.S. Geological Survey
National Center, MS-104
Reston, Va. 22092

---

*Members in attendance at the meeting.

JAPAN MEMBERS OF THE U.J.N.R. PANEL

*Mr. Keiji Nishimura, Chairman
Director General
Geographical Survey Institute
Kitazato-1, Yatabe-Machi, Tsukuba-Gun
Ibaraki-Ken 305
Japan

*Dr. Naomi Fujita, Secretary
Director
Crustal Dynamics Department
Geographical Survey Institute
Kitazato-1, Yatabe-Machi, Tsukuba-Gun
Ibaraki-Ken 305
Japan

*Dr. Kazuo Hamada
Senior Researcher
Second Research Division
National Research Center for Disaster Prevention
3-1, Tennodai, Sakura-Mura, Niihari-Gun
Ibaraki-Ken 305
Japan

Dr. Nobuhiro Kawajiri
Chief
Space Research Section, Kashima Branch
Radio Research Laboratories
893-1, Hirai, Kashima-Machi, Kashima-Gun
Ibaraki-Ken 314
Japan

Mr. Eiichi Kuribayashi
Director
Earthquake Disaster Prevention Department
Public Works Research Institute
Asahi-1, Toyosato-Machi, Tsukuba-Gun
Ibaraki-Ken 305
Japan

---

*Members in attendance at the meeting.

Dr. Akio Mogi
Director
Surveying Division, Hydrographic Department
Maritime Safety Agency
5-3-1, Tsukiji, Chuo-Ku
Tokyo 104
Japan

*Mr. Koji Ono
Chief
Tectonophysics Research Section
Environmental Geology Department
Geological Survey of Japan
1-1-3, Higashi, Yatabe-Machi, Tsukuba-Gun
Ibaraki-Ken 305
Japan

Dr. Michio Otsuka
Director
International Institute of Seismology and
Earthquake Engineering
Building Research Institute
Tatehara-1, Oho-Machi, Tsukuba-Gun
Ibaraki-Ken 305
Japan

Mr. Shoichi Seino
Chief
Applied Optics Section, First Division
National Research Laboratory of Metrology
1-1-4, Umezono, Sakura-Mura, Niihari-Gun
Ibaraki-Ken 305
Japan

Dr. Shigeji Suyehiro
Director
Department of Observation
Japan Meteorological Agency
1-3-4, Ote-Machi, Chiyoda-Ku
Tokyo 100
Japan

---

*Members in attendance at meeting.

Opening Remarks of

DAVID P. HILL

U.S. Chairman
Panel on Earthquake Prediction Technology

It is with great pleasure that on behalf of the U.S. panel members I welcome the Japanese panel members to this Second Joint Meeting of the UJNR Panel on Earthquake Prediction Technology.

I am particularly pleased for this opportunity to meet and get acquainted with the new Chairman of the Japanese side, Mr. Keiji Nishimura, Director General of the Geographical Survey Institute and, of course, to see once again old friends and acquaintences from the first joint meeting.

I would also like to bring you special greetings from Ted Flynn who was unable to be here because of previous commitments; and also from John Bossler and John Filson, both of whom you will see in Washington when you go there.

The first joint Meeting of this panel was held in Tokyo on December 17 and 18 in 1979. Much of the time in that meeting was spent acquainting each other with programs of our respective agencies. But we also had time for some technical discussions focused on two interesting earthquakes--the Izu-Oshima earthquake of January 1978 and the Imperial Valley earthquake of October 1979. Both of these earthquakes were about magnitude 6 1/2. Since that time in California we have had six earthquakes greater than magnitude 6 and there are at least three that I know of and perhaps more in Japan. We will hear some more details about these earthquakes during this technical session to come, and I think we will see that we have learned a great deal from our studies of these earthquakes, although we still have much to learn before we can reliably do earthquake prediction on a useful basis. I trust that this panel will contribute significantly to our mutual progress in both countries on this important problem.

Thank you.

Opening Remarks of

KEIJI NISHIMURA

Japanese Chairman
Panel on Earthquake Prediction Technology

Ladies and gentlemen:

Thank you very much on behalf of the Japanese delegation for the very kind and gracious remarks by the Chairman of the U.S. panel, Dr. Hill. I also would like to take this opportunity to thank the members of the U.S. panel for inviting all of us from the Japanese side to the 2nd Joint Meeting of the U.S.-Japan Conference on Natural Resources, Panel on Earthquake Prediction Technology. Mr. Sasaki, former Chairman of the Japanese side retired from G.S.I. last year and I succeeded him, as mentioned by Dr. Hill.

On behalf of the Japanese side of the panel, I would like to express our sincere appreciation to Dr. Hill and to all members of the U.S. panel for the kind invitation to all of us to the second joint meeting. I also want to personally deliver, right now, to all of you special greetings from Mr. Sasaki and other members of the Japanese panel who could not attend this meeting.

It was our special pleasure, thanks to the cooperation and kind guidance of the U.S. panel members, that we were able to successfully bring to a fruitful conclusion the first joint meeting held in Tokyo in December 1979. Since then just about a year and a half's time has elapsed. During this time frame, exchange of many kinds of papers and data has been promoted between our two countries. Exchange of researchers, although the dispatch from Japan to the United States is much more in number than that in the opposite direction, has also increased, and some of the Japanese researchers who are temporary residents in your country are also taking part in this meeting either as a deputy or as an observer. We also would like to thank the U.S. side for making such arrangements possible for the Japanese researchers now visiting and staying in the United States.

During this particular period some destructive and devastating earthquakes have occurred in the world--in Mexico, for example, as well as in Algeria, in the El Assnam earthquake, in southern Italy, etc. These have done considerable damage to each country involved. In Japan there were a few earthquakes even though the damage from them has been slight. Research for earthquake prediction will play an increasingly important role in protecting life and property of local citizens from earthquakes.

In this context I am convinced that this joint meeting will contribute to the enhancement of technology for earthquake prediction

and for the promotion of counterdisaster measures not only for both our countries but also for earthquake-prone countries of the world. I do expect this joint meeting to produce fruitful results through an active exchange of views between the members of our two panels.

Finally, I would like to express our hearty gratitude to Dr. Hill and the members concerned of the U.S. panel for their efforts in making all necessary preparations for this meeting.

Thank you very much, all of you.

RESOLUTIONS OF THE

U.S.-JAPAN PANEL ON EARTHQUAKE PREDICTION TECHNOLOGY

U.J.N.R.

July 17, 1981

The UJNR Panel on Earthquake Prediction Technology recognizes the critical importance of promoting prediction research in both countries. The Second Joint Meeting was extremely beneficial in furthering friendship and deepening understanding of the common research problems of both Japan and the U.S.

The Panel members from Japan particularly appreciated the opportunity to participate in a field trip to the central San Andreas fault zone. Technical sessions comprised presentation of 20 papers, including extensive discussion of areas of intensified observation in Hanto-Tokai District, Japan, and in Southern California.

Discussion was extremely fruitful, and the Panel unanimously adopted the following resolutions:

1. One of the most important means of achieving joint progress is by the long-term exchange of researchers between our two countries. Since the First Joint Meeting, such exchanges have been initiated and are already achieving extremely valuable results. Efforts should be made to cooperate on instrumental development and observations as, for example, in the use of multiwavelength laser ranging techniques.

2. We agree that data exchange is mutually beneficial and strongly encourage it. In particular, the Panel emphasized the importance of exchanging mutual experience in the area of automatic processing of seismic data and in the investigation of possible error sources of leveling measurements.

3. Cooperation in the application of space techniques to prediction research is already in progress. Further development is needed in instrumentation such as VLBI.

4. The next joint meeting will be held in Japan in 1982.

Closing Remarks of Dr. Hill:

On behalf of the U.S. panel members, I want to thank the Japanese members, Mr. Nishimura, Dr. Fujita, Dr. Hamada, and Mr. Ono, for the time they have taken to travel to the U.S. and participate in the Second Joint Meeting of the Panel on Earthquake Prediction Technology. The opportunities for personal contact and exchange of ideas provided by these meetings represents, in my mind, one of the most effective functions of our panel.

Speaking for the American side--both the panel members and observers--the presentation of papers by the Japanese members and participants, Mr. Seno and Mr. Komaki, were very effective in bringing us up to date on a number of interesting developments in Japan both on the descriptions and the understanding of recent earthquakes and tectonic processes as well as on new developments of instrumental and observational techniques. I am certainly encouraged that many of the results presented in the papers by both sides point favorably toward the likelihood of reliable earthquake prediction, although we still clearly have a lot of work to do.

We look forward to working with Mr. Komaki and Mr. Matsumura over the next year and anticipate that a substantial useful benefit will result from their visit to this country.

We wish you a pleasant visit for the remainder of your stay in this country and a safe return to Japan. And finally, we thank you for your invitation to hold the Third Joint Meeting in Japan and we look forward to seeing you next year.

Thank you.

Closing Remarks of Mr. Nishimura:

At this point I have the pleasure of making my closing remarks on behalf of the Japanese delegation.

First of all, I would like to take this opportunity to thank Dr. Hill for his very kind and gracious words.

Five days have elapsed since our arrival in this area. Every day of this period has been very useful. We have been able to exchange ideas and opinions with many of you and also we have been blessed with opportunities to tour through and observe many of your fine facilities and sites.

During these past two days many presentations were given outlining the results of research activities in the past; and today, at the end of this business session, the resolution was passed unanimously. We feel that these two days have been full of results and have been very effective.

During the past five days we have been impressed with some differences between the U.S. and Japan as to the nature and the natural settings, the organizational structure of research facilities, etc. However as we look at these differences between our two countries, we have been able to perceive all and recognize the abundant and rich variety of individuality in these environmental conditions and organizational structures and facilities of our two countries. These distinct individualities and individual characteristics that exist between our two countries despite the differences should be nurtured with utmost care and with a great deal of encouragement because by so-doing we feel that we can both mutually absorb the fine features of our respective systems.

Recently it has been decided that the Third UJNR Meeting of the Panel on Earthquake Prediction Technology will be held in Japan in 1982. It will be held in Tokyo. We accept our responsibility to be your host and to represent our country in hosting the participants on the U.S. side at the forthcoming third meeting in Japan. When you come to the Third UJNR Panel on Earthquake Prediction Technique Meeting to be held next year, we pledge to do our utmost efforts to enhance past achievements by this panel on the basis of what has already been achieved during the Second Panel one.

We certainly hope to have as many of you participating during the forthcoming Third UJNR Meeting in Tokyo next year. The old members of the Japanese panel as well as all those who will be involved in implementing the third meeting in Japan will be sincerely looking forward to

S C I E N T I F I C

P A P E R S

P R E S E N T E D

A T

C O N F E R E N C E

EARTHQUAKE PREDICTION STUDIES IN SOUTHERN CALIFORNIA

C. B. Raleigh
U.S. Geological Survey
Menlo Park, California, U.S.A.

The San Andreas fault in southern California constitutes the most significant seismic gap in the United States. For this reason, efforts to detect precursory phenomena and to determine the detailed seismicity and secular strain accumulation have been increasingly concentrated in that region.

In mid-1979, reports of increased emanation of radon from wells in the Transverse Ranges gave rise to some concern that a moderate-to-large earthquake might be imminent. An ad hoc review panel examined the data along with other observations and concluded that no other sufficiently anomalous observations existed that would warrant issuing a public warning. Geodetic observations had indicated a change from north-south compressional strain accumulation to northeast-southwest extension in the Salton Sea area and also farther to the north in the Los Padres network near Gorman. However, the changes were not so large as to cause alarm.

Upon remeasurement of the Palmdale network in October of 1979, Savage and Prescott found a remarkable change from north-south compression at 2×10^{-7} p.a. to an east-northeast extension of 1.5×10^{-6} in six months. This surprisingly rapid change had the effect of reducing the normal stress on the San Andreas and thus represented an ominous event. No large earthquakes have yet occurred in the Palmdale area but the strain event led to a significant intensification of the prediction effort in the region of the gap.

Data from water wells, instrumental and geodetic strain observations, seismicity, radon, and other geophysical precursors have been closely monitored. Periodic review meetings are conducted in southern California to examine the data in hopes of detecting clear precursory changes prior to some future earthquake on the San Andreas fault.

CRUSTAL MOVEMENTS IN THE NORTHEASTERN PART OF IZU PENINSULA

Naomi Fujita and Takashi Tada
Geographical Survey Institute

The crustal activities in the Izu Peninsula have been comparatively steady since the Kita-Izu earthquake (M 7.0) of 1930. Since the 1974 Off Izu Peninsula earthquake (M 6.9), the crustal movements in the Izu Peninsula have been activated. The destructive earthquakes which have occurred are the 1976 Kawazu earthquake (M 5.4), the 1978 Izu-Oshima-Kinkai earthquake (M 7.0) and the 1980 Off Eastern Izu Peninsula earthquake (M 6.7). The earthquake hypocenters have clearly moved northward (Fig. 1).

The central region of the anomalous crustal uplift which began at the first half of 1975 in the eastern part of Izu Peninsula was in the west of Ito (Hiekawa) at early stage. Figure 2 shows the vertical crustal movement during the period of 1967 to 1977. The crustal uplift in this region has been weakened since 1978 and the recent vertical movement in the region is in tendency of subsidence. Figure 3 shows the vertical changes of bench marks around Hiekawa.

The uplift velocity around the Ito tidal station (Ito TS), which is located in the south of Ito, increased again in the latter half of 1978. The central region of the uplift moved away from the west (Hiekawa) to the south (Ito TS) of Ito. Figure 4 shows the vertical changes of bench marks around the Ito tidal station, and Figure 5 shows the monthly mean sea level change at the Ito tidal station. The occurrence of the earthquake swarm off the Kawanazaki was preceded a few months by the crustal uplift.

The vertical crustal movement in the Izu Peninsula during the period from 1967 to 1979 (Fig. 6) shows that the uplift zones are divided into two regions. The subsidence in the southern part was accompanied with the 1978 Izu-Oshima-Kinkai earthquake (M 7.0).

The horizontal crustal strain fields changed, accompanying the change of the uplift pattern. The horizontal strain fields in the eastern part of the Izu Peninsula (Fig. 7) shows that the direction of the extension axes rotated from NW-SE to NE-SW accompanying the migration of the crustal uplift region as mentioned above.

Off the Kawanazaki, the earthquake swarms occurred intermittently in November 1978, and March and May 1979. Afterwards the uplift velocity around the Ito tidal station became slow and also the earthquake swarm activity went down. On June 22, 1980, however, earthquake swarms became active again and the 1980 Off Eastern Izu Peninsula earthquake (M 6.7) occurred on June 29, 1980. Figure 8 shows the crustal deformations

associated with this earthquake. By analyzing the crustal deformation, the earthquake mechanism, and the distribution of aftershocks, the earthquake fault is the left-lateral strike-slip one whose parameters are as follows:

length:	18 km,	strike:	N-S
width:	8 km,	dip:	90°
depth:	0 km,	dislocation:	1.3 m.

The strike of the 1978 Izu-Oshima-Kinkai earthquake is in E-W and perpendicular to that of this earthquake.

The earthquakes in and around the Izu Peninsula have migrated northward since the 1974 Off Izu Peninsula earthquake (M6.9). In June 1980 the earthquake front arrived off the Kawanazaki. Furthermore, it is noted that in the northeastern part of the Izu Peninsula there are anomalous upheavals more than 20 cm for the recent ten years and anomalous shear strains more than 4×10^{-5} since 1931.

The unreleased area of strain energy since 1923 has the diameter of 20 km in and around the northestern Izu Peninsula (Fig. 9). The possibility is pointed out that the coming earthquake may have the magnitude of 6.5 or so within the area.

Finally the pattern of crustal movement around Ito is discussed (Fig. 10). The intermittent upheavals are conspicuous during the period from 1924 to 1933 and from 1975 to 1981. It seems that the energy release due to upheaval may be larger than the seismic energy released in and around the northeastern Izu Peninsula. The upheaval may be caused by the aseismic dip slip in the deep crust, the intrusion of magma to the shallow crust, etc. Anyway, the aseismic energy release due to upheaval in and around the northeastern Izu Peninsula should be considered in the process of energy release in the northern end of Philippine Sea Plate, as well as the seismic energy release.

References

Fujii, Y., 1977, Creep dislocation model of crustal upheaval in Izu Peninsula (in Japanese), Rep. Coord. Comm. Earthq. Pred., 17, 68-71.

Fujita, N. and T. Tada, 1979, Recent crustal activities in Izu and Tokai district, Proceedings of 1st Joint Meeting, UJNR Panel on Earthquake Prediction Technology, 215-229.

Geographical Survey Institute, 1979, Crustal deformation in the central part of Izu Peninsula (5) (in Japanese), Rep. Coord. Comm. Earthq. Pred., 22, 100-103.

Geographical Survey Institute, 1980, Crustal deformation in the eastern Izu district (in Japanese), Rep. Coord. Comm. Earthq. Pred., 23, 48-52.

Geographical Survey Institute, 1981, Crustal deformation in Izu Peninsula (in Japanese), Rep. Coord. Comm. Earthq. Pred., 26, in press.

Hagiwara, Y., 1977, The Mogi model as a possible cause of the crustal uplift in the eastern part of Izu Peninsula and the related gravity change (in Japanese with English abstract), Bull. Earthq. Res. Inst., 52, 301-310.

Ishibashi, K., 1977, Creep dislocation model of the Izu Peninsula uplift --Significance of the East-Off-Izu Tectonic line -- (in Japanese), Rep. Coord. Comm. Earthq. Pred., 17, 65-67.

Kaidzu, M. and T. Tada, 1980, Recent crustal uplift in the northeastern part of Izu Peninsula (in Japanese), The Earth Monthly, 14, 132-136.

Karakama, I., I. Ogino, K. Tsumura, K. Kanjo, M. Takahashi and R. Segawa, 1980, The earthquake swarm east off the Izu Peninsula of 1980 (in Japanese with English abstract), Bull. Earthq. Res. Inst., 55, 913-947.

Nakamura, K., 1980, Tectonics in the Izu Peninsula and bending hypothesis of plate (in Japanese), The Earth Monthly, 14, 94-102.

Tada, T., 1981, On the anomalous crustal activities in Izu Peninsula (1), read at spring meeting of Seismological Society of Japan.

Tsumura, K., 1980, Recent seismic activities in the Izu Peninsula and earthquake prediction (in Japanese with English abstract), Proceedings of Earthquake Prediction Research Symposium (1980), 47-51.

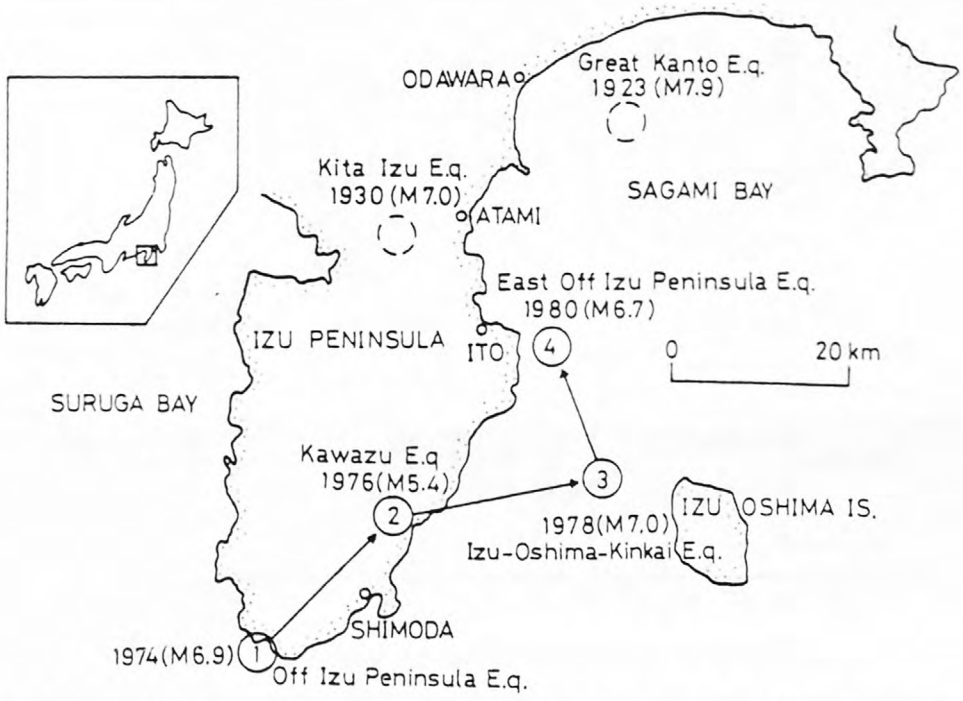

Fig. 1 Distribution of the recent destructive earthquakes in and around the Izu Peninsula. Solid circles indicate the recent destructive earthquakes and arrows indicate the northward migration of hypocenters.

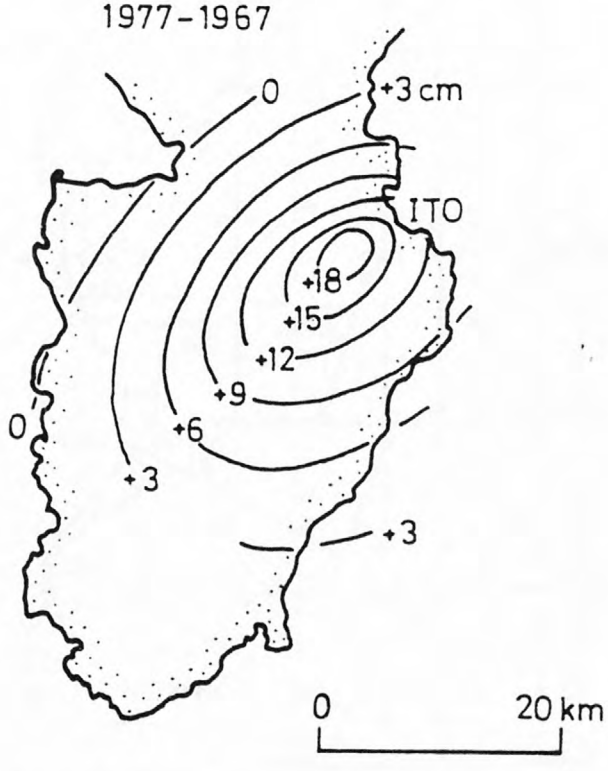

Fig. 2 Vertical crustal movement in the northeastern part of Izu Peninsula during the period from 1967 to 1977.

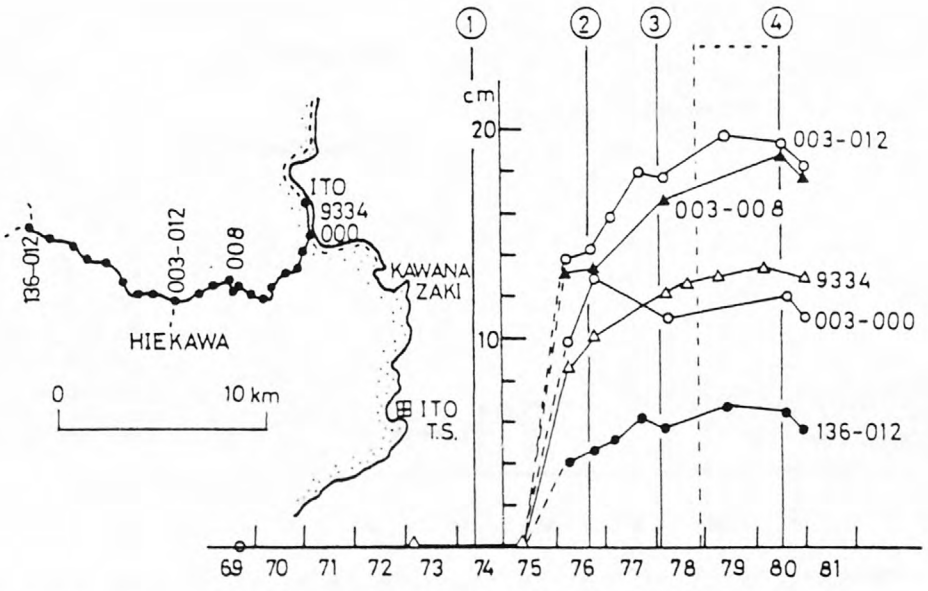

Fig. 3 Vertical changes of bench marks around Hiekawa.

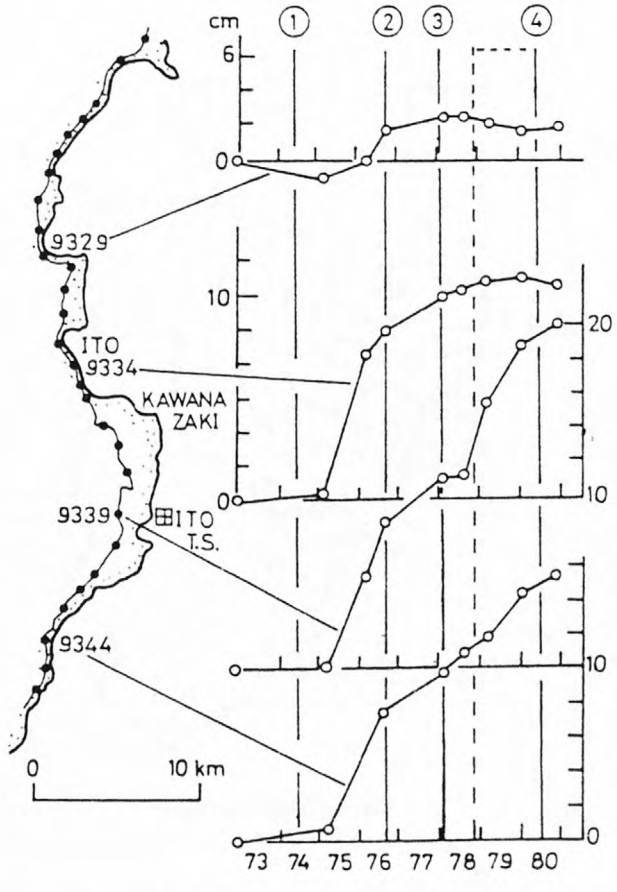

Fig. 4 Vertical changes of bench marks around the Kawanazaki.

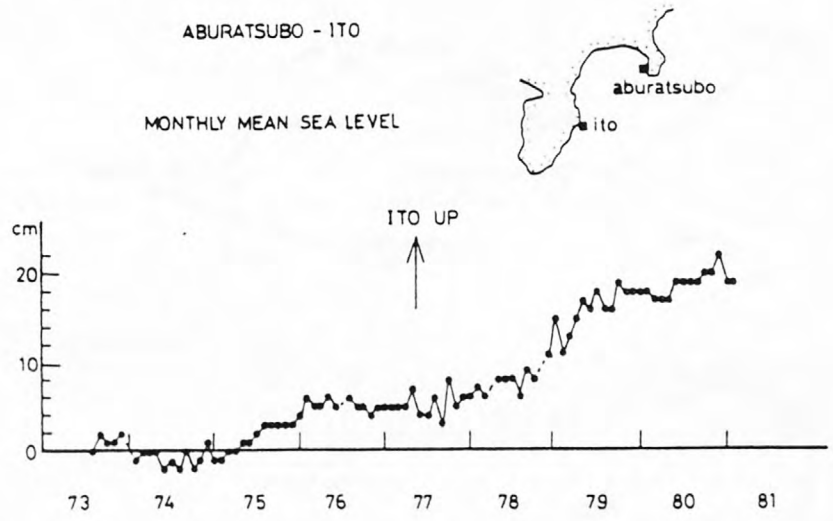

Fig. 5 Vertical crustal movement at the Ito tidal station deduced from the monthly mean sea level, referring to the Aburatsubo tidal station.

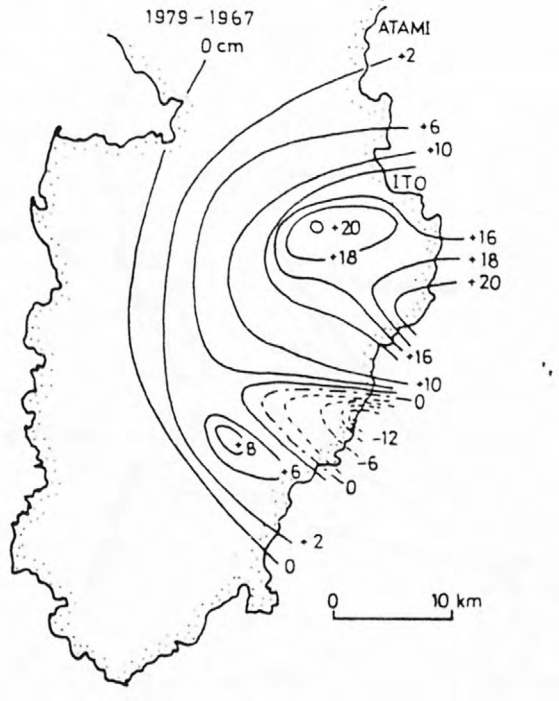

Fig. 6 Vertical crustal movement in the Izu Peninsula during the period from 1967 to 1979.

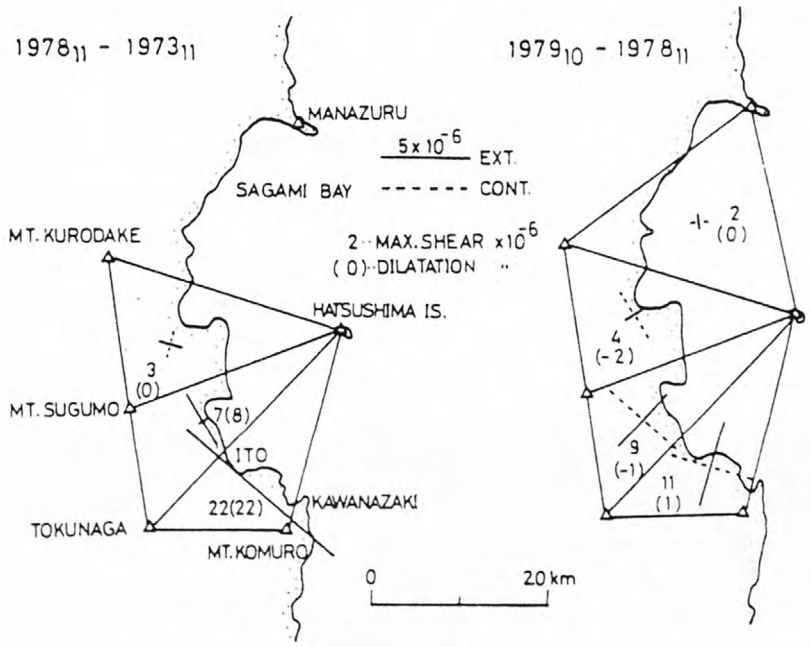

Fig. 7 Horizontal crustal strain in the northeastern part of Izu Peninsula during the period from 1973 to 1978 and from 1978 to 1979.

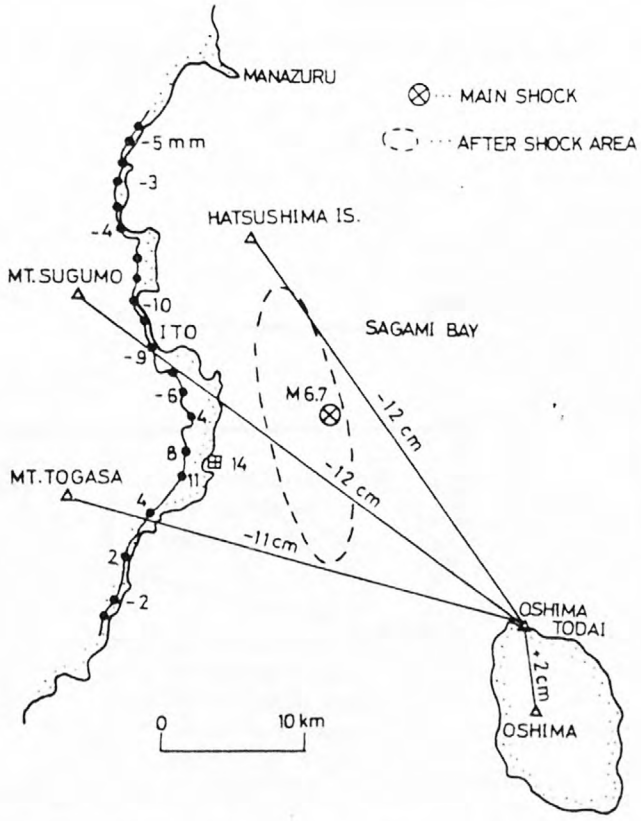

Fig. 8 Crustal deformations associated with the 1980 Off Eastern Izu Peninsula Earthquake. These crustal deformations are interpreted by the left lateral strike (N-S) slip faulting.

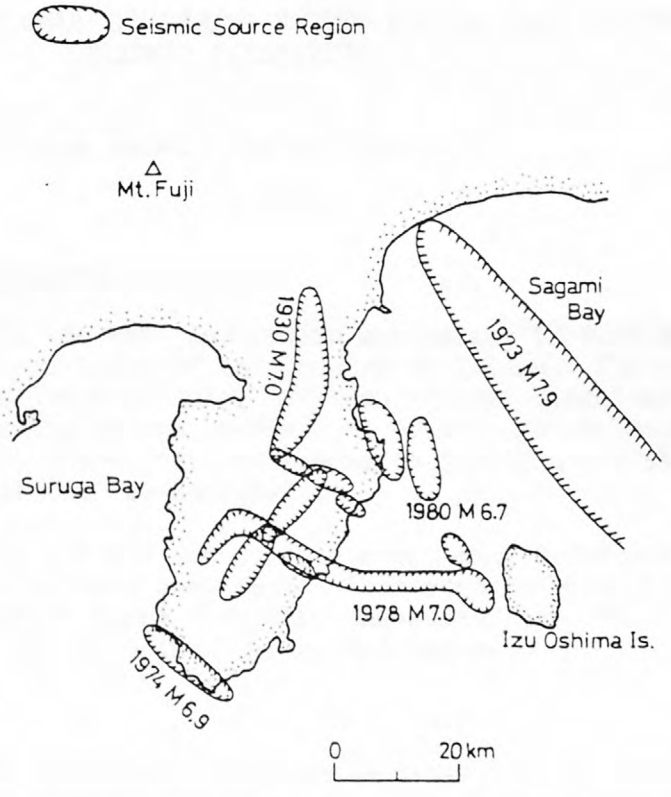

Fig. 9 Recent seismic source regions in and around Izu Peninsula.

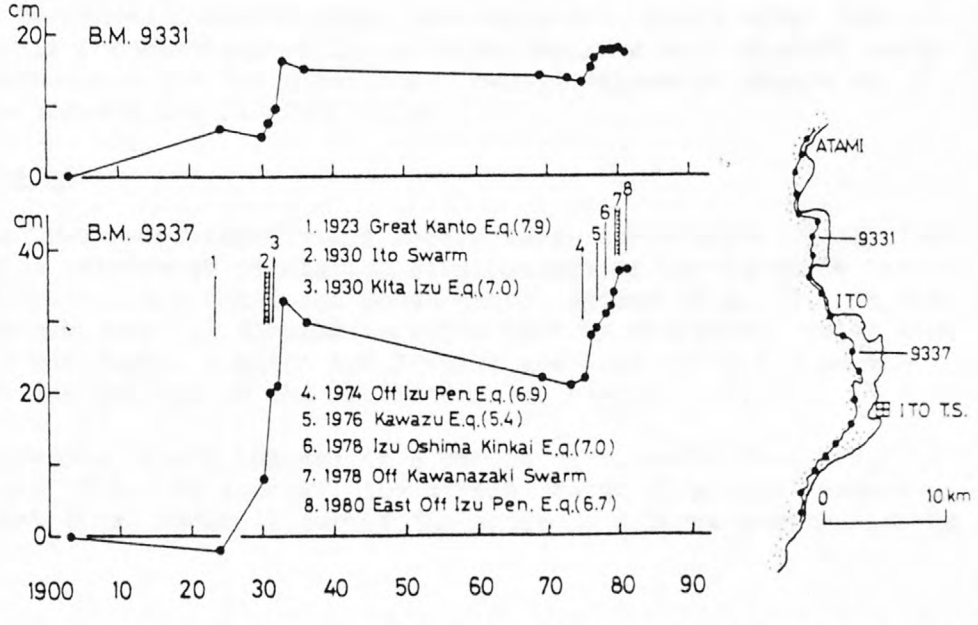

Fig. 10 Vertical changes of B.M. No. 9331 and B.M. No. 9337 around Ito.

PRECURSORS OF THE NEAR IZU-OSHIMA EARTHQUAKE AND THE FOLLOWING SEISMIC ACTIVITIES

Japan Meteorological Agency

1. Near Izu-Oshima Earthquake

On January 14, 1978, the Near Izu-Oshima earthquake (M 7.0) occurred about 10 km off the western coast of the Izu-Oshima Island. The rupture extended westward to the Izu Peninsula, and then changed direction to the northwest, eventually ending in the middle part of the Izu Peninsula. The epicentral region is, therefore, considered to lie from the sea east to the the middle part of the Izu Peninsula.

In the Izu Peninsula and its surrounding area, many different kinds of geophysical observations have been made. Some precursors of the earthquake were recognized. Among them, the changes of seismic activity and dilatational strain are described in the following.

2. Foreshocks

On January 13, 1978, a swarm of earthquakes started near Izu-Oshima. The activity became much higher with more perceptible shocks following an event shock at 0812 hours, January 14, which was felt in Izu-Oshima with an intensity III of JMA Scale (Fig. 1).

Under such circumstances, taking into consideration anomalous changes which had been recorded by strainmeters, the Japan Meteorological Agency issued an earthquake information to the public at 1050 hours, which was "In the near future, an earthquake large enough to cause some damage may occur". The mainshock occurred about one-and-a-half hours after the issuance of this information, which could be regarded as a kind of warning. This earthquake and its aftershocks caused extensive damage on Izu-Oshima Island and the Izu Peninsula.

3. Strain Change

To catch precursors immediately before large earthquakes, a continuous observation network of dilatation strainmeters of the borehole type has been deployed in the Tokai and South Kanto regions (Fig. 2). At the time of the earthquake, 12 strainmeters had been in operation, which are underlined in the figure. Ajiro and Irozaki are located in the northeastern coast and the tip of the Izu Peninsula, respectively.

Figure 3 shows strain changes in a period of 3 months from November 1977 to January 1978. At Irozaki, the strain change of gradual expansion until that time, suddenly turned its sense to a large compression on

December 4. On January 11, it again changed to expansion. The earthquake occurred 3 days after the second turn in the strain change. Also at Ajiro, from December 19, the sense of strain change showed a sudden turn to compression. These changes occurred for the first time since the start of observations in April 1976 and are considered to be precursors, though the two changes did not take place concurrently.

The strainmeter at Ajiro showed very complicated changes for about two-and-a-half years after the earthquake. Near the Izu Peninsula, the seismic activity became active after the Off Izu Peninsula earthquake (M 6.9) of May 9, 1974, which broke a quiet period of about 40 years since the North Izu earthquake of 1930. Also after the Near Izu-Oshima earthquake of 1978, swarm activity continued from November 1978 to January 1979 in the region north of the epicentral region of the earthquake of 1978. More swarms occurred in March and May of 1979. Furthermore, a swarm occurred in June 1980 for about three months off the eastern coast of the Izu Peninsula. Figure 4 shows the location of those swarms and aftershocks. From the series of those earthquakes, which started in 1974 off the tip of the Izu Peninsula, it seems that the seismic activity was moving to the north. However, no definite interpretation can be made as to whether this is significant for the future activity in this region.

Figure 5 shows a comparison between the record of the strainmeter in Ajiro and the change of the number of earthquakes recorded in Kamata about 11 km to the south of Ajiro. As mentioned previously, since the sudden change of the strain in Ajiro to compression on December 19, 1977, which is considered to be a precursor, the general strain change continued largely as compression with repetitions of complicated short-period changes. However, the trend changed to dilatation in January 1979, when the swarm activity came to an end. After the swarm activity from June to September 1980, the anomalous strain change almost disappeared, and its secular change became smaller. These changes recorded by the strainmeter seem to be associated with the seismic activity around the Izu Peninsula.

4. Conclusion

In and near the Izu Peninsula, the seismicity has been very high in these years, and many different networks of high density of geophysical observations have been in operation. It is highly hoped that more can be learned about the mechanism immediately before earthquakes, before an earthquake of M 8 actually takes place in the Tokai region.

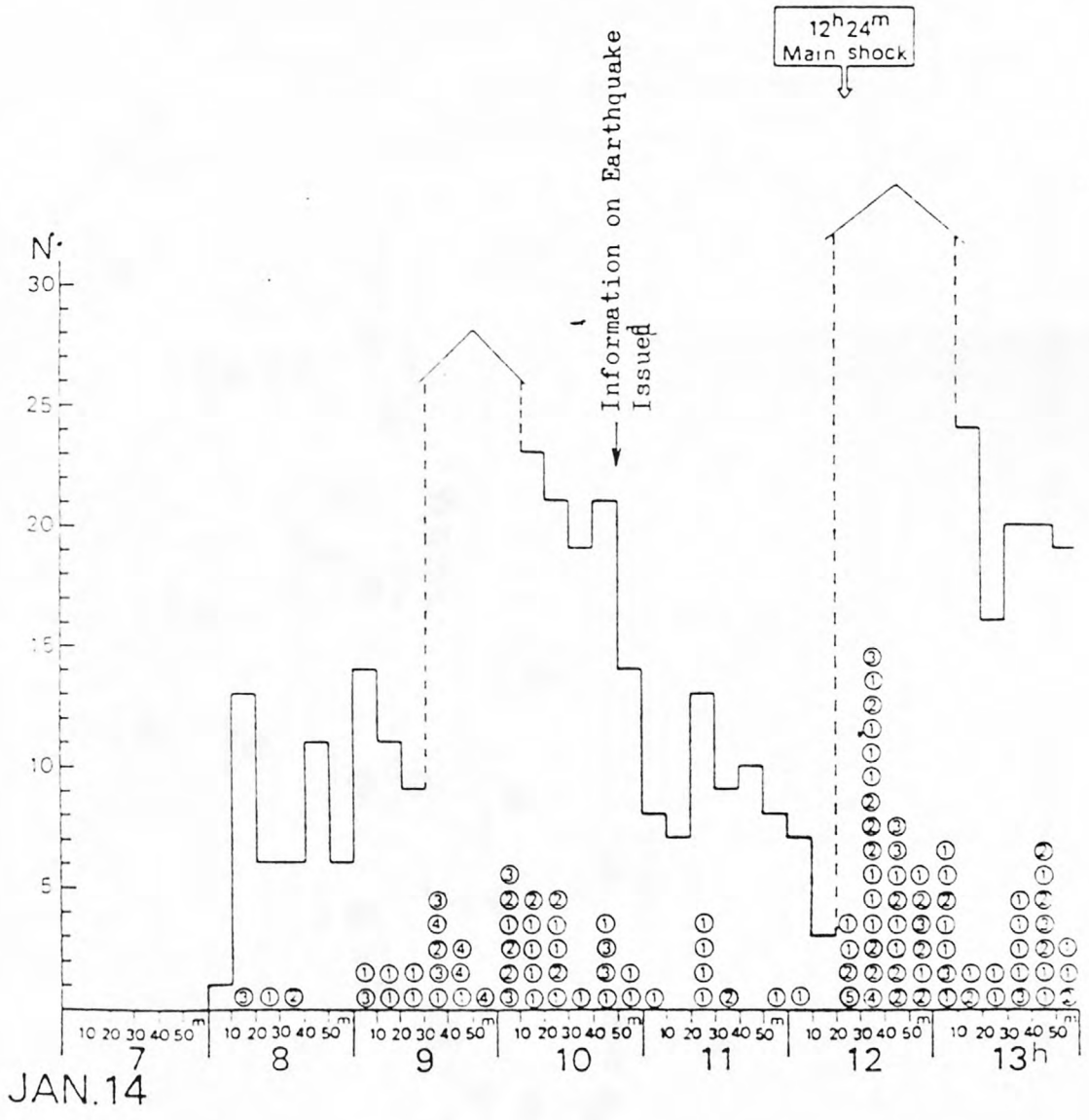

Fig. 1. Foreshock activity prior to the Near Izu-Oshima Earthquake of 1978 (M:7.0). The number shows the frequency of occurrence in every ten minutes at the Oshima Weather Station. Numbers in circles show the intensity of perceptible earthquakes.

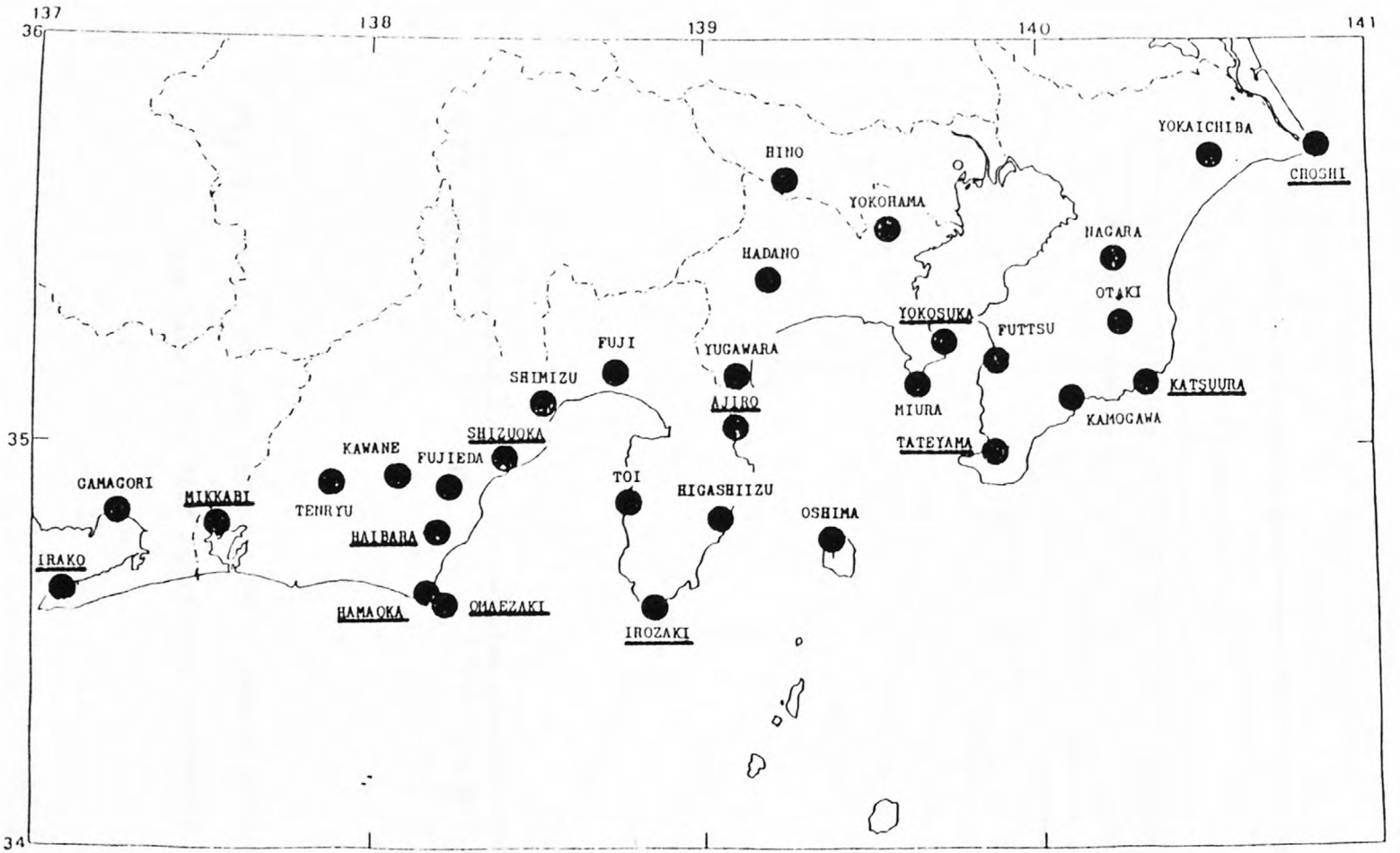

Fig. 2. Network of dilatation strainmeters of borehole type in Tokai and South Kanto regions as of April, 1981.

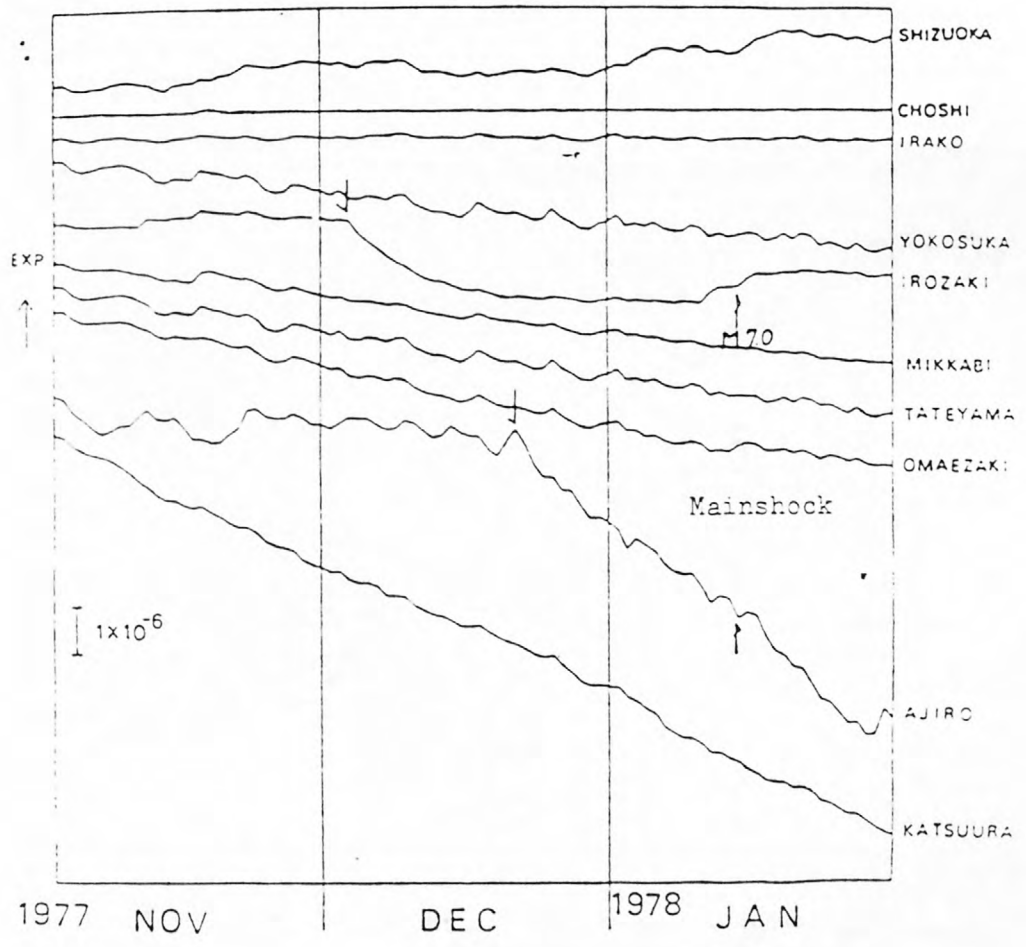

Fig. 3. Strain changes recorded by dilatation strainmeter of borehole type before the Near Izu-Oshima Earthquake.

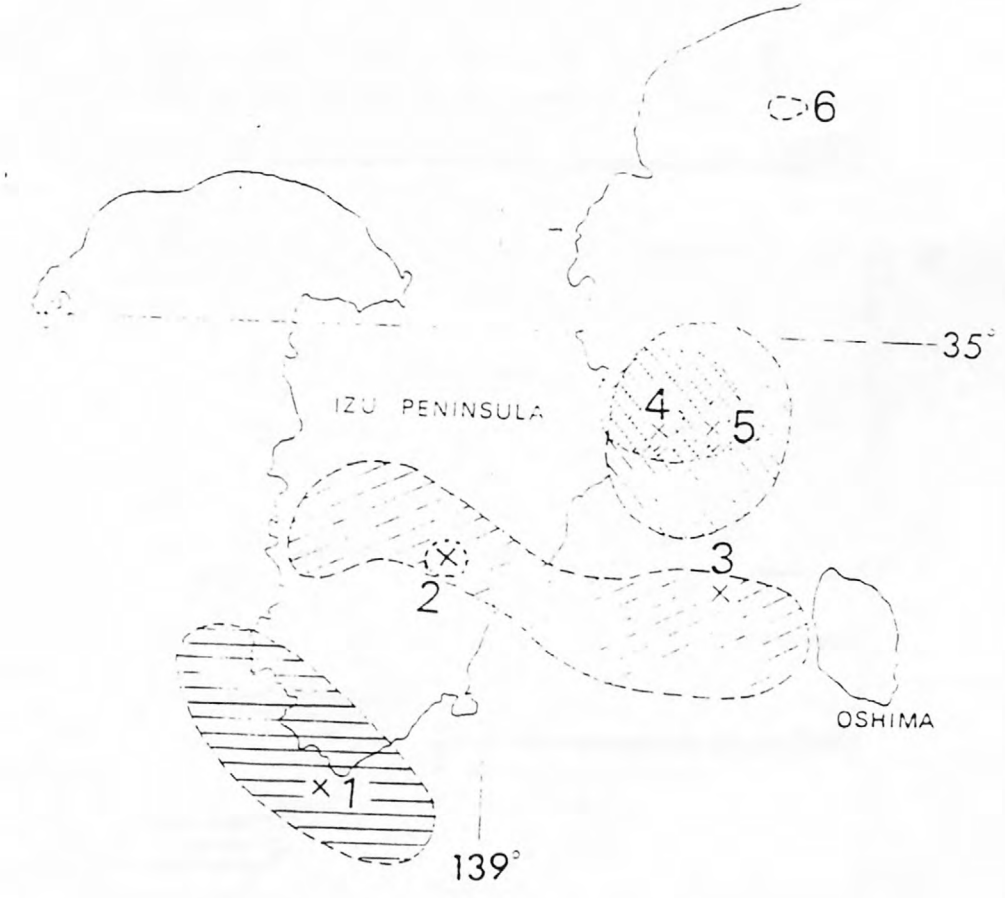

Fig. 4. Epicenters, aftershock regions, and swarm regions after the Off Izu Peninsula Earthquake of 1974.

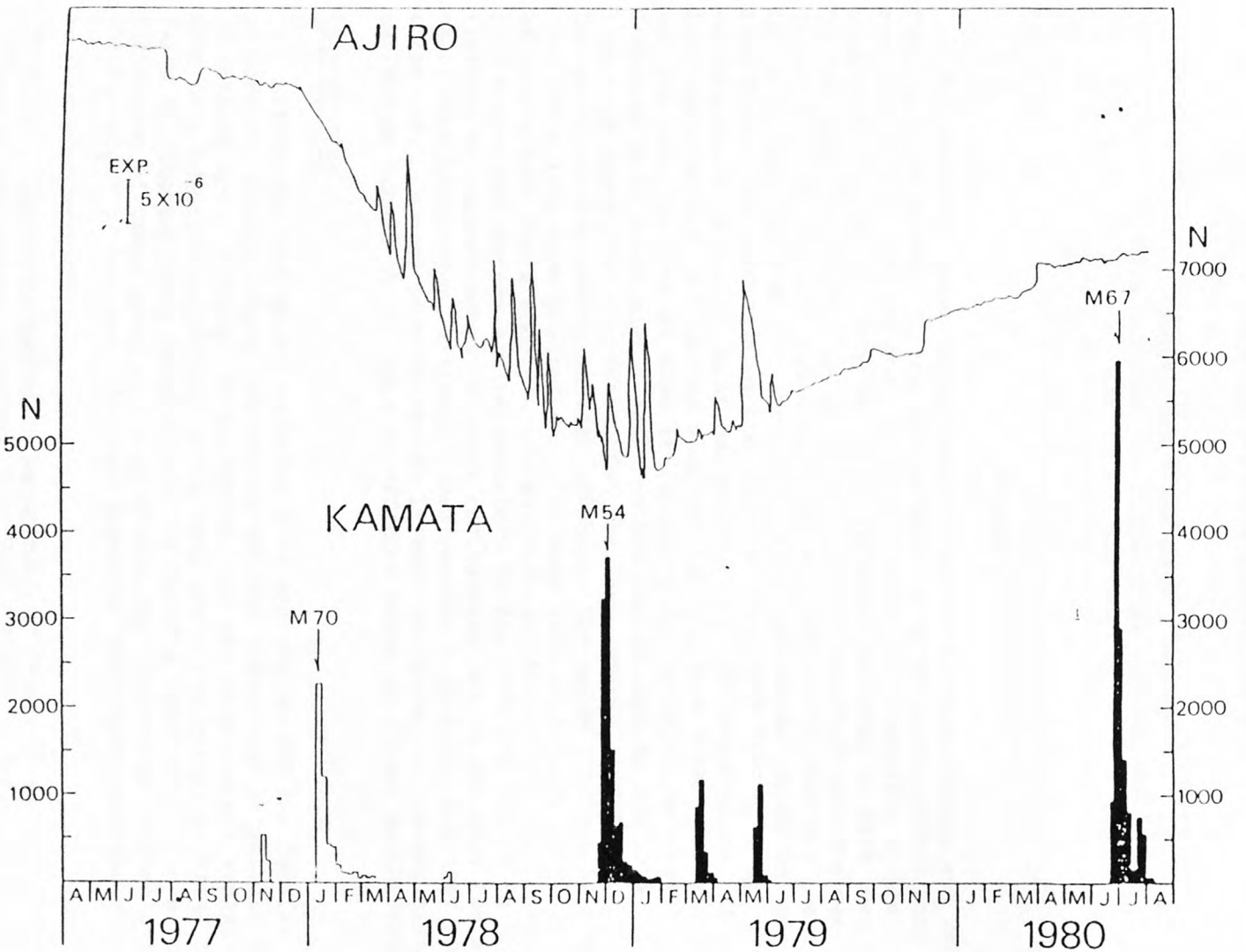

Fig. 5. The strain change (daily mean) at Ajiro and frequency of earthquakes recorded at Kamata related to the Near Izu-Oshima Earthquake and the following aftershocks and swarm activity.

SEISMICITY, TECTONICS AND EARTHQUAKE PREDICTION AT THE SUBDUCTION ZONE OFF NORTHERN HONSHU, JAPAN

Tetsuzo Seno* and Michio Otsuka**
International Institute of Seismology and
Earthquake Engineering

Abstract

Frequency of great earthquakes along the northern Honshu arc decrease from north to south. At the northernmost section, great events have recurred with a time interval of 80-100 years; in contrast, at the southernmost section, only one historic event is known to have occurred for the past 400 years. Large earthquakes of Ms=7-7.5 have frequently occurred along the arc; the most prominent feature is that there are two specific rupture zones for large events at the deeper (40-60 km) plate interface. Many earthquakes that preceded the 1978 Ms=7.5 Miyagi-Oki earthquake, which is the most recent event at the deeper plate interface, involved fractures within the slab near its rupture zone. The stress buildup near the rupture zone is likely to be the cause for these fractures within the slab. This feature can be used as one tool for a long-term earthquake prediction for the large events near the coast. For the great shallow events further offshore, the seismicity gap is a major tool for a long-term prediction. For both type of events, there is no effective tool for a short-term prediction at the present time. Installation of strainmeters and seismometers in the offshore region in the vicinity of rupture zones of these earthquakes may be one tool for a short-term prediction, although there remains a question how they are effective. Tsunami warning system is most warranted to prevent disasterous damage caused by tsunamis of offshore great or silent earthquakes.

Introduction

Historical and recent seismicity in the region off the Pacific coast of northern Honshu, Japan represents typical subduction seismicity along the island arc. Although it is typical, we can find a great variety of mode of subduction seismicity along this arc. Historically, great or large earthquakes have recurred off the Pacific coast of northern Honshu. Occurrence of these great or large events has never been uniform over the entire length of the arc. At some segments, they have recurred quite

---

*Present (temporary) address: Department of Geophysics, Stanford University, Stanford, California 94305, U.S.A.

**Present address: Department of Physics, Kyusyu University, Fukuoak, Japan.

regularly and at others not. Recent seismicity including smaller earthquakes also shows a spatio-temporal variation in activity; it seems closely related to the occurrence of great or large earthquakes.

In this short paper, we summarize historical seismicity for great and large earthquakes and recent seismicity during a past few decades along the northern Honshu arc. Focal mechanisms for earthquakes before and after recent great and large earthquakes are also discussed in connection with earthquake prediction. Possible tools for earthquake prediction for this offshore region are discussed.

Pattern of Occurrence of Great Earthquakes

It is convenient to divide the subduction zone along the northern Honshu arc into five sections, A, B, C, D, and E, in order to discuss the pattern of occurrence of great earthquakes (Fig. 1). In Figure 1, specific rupture zones and the events which are very likely to have ruptured the zones are shown. Shaded are the deep thrust zones which will be stated later.

In the northernmost zone A, great earthquakes have recurred regularly in a 80-100 year time interval since the year 1677. The most recent event is the 1968 Ms=8.1 Tokachi-Oki earthquake, which showed a thrust-type mechanism (Kanamori, 1971a). In zone B, no typical thrust-type great earthquake is known to have unequivocally ruptured the segment of the boundary. The 1933 Sanriku earthquake occurred at the trench axis east of this zone; this event involved normal faulting (Kanamori, 1971b). The 1896 M=7.1 earthquake caused a great disaster by its tsunami. This event was a silent tsunami earthquake which has a seismic moment comparable to great earthquakes (Kanamori, 1972). There are two events in 869 and 1611 which are located in zone B by Usami (1975). Both events caused a disasterous tsunami; Hatori (1976) noted that the pattern of inundation height of the 1611 event is like that of the 1933 event. However, their location, type of faulting, and source spectrum are unclear. In zone C, at least two great earthquakes are known to have occurred in 1793 and 1897, both of which caused a similar distribution of tsunami inundation height (Hatori, 1975). In zone D, a series of great or large earthquakes occurred in 1938; their Ms ranges from 7.1 to 7.8 (Abe and Tsuji, 1976). Two of these events involved normal faulting (Abe, 1977). The only other large event known in zone D is the Ms=7.8 1905 earthquake at northwest of the rupture zone of the 1938 events. However, JMA magnitude of this event was determined as 7.0 by Utsu (1979) and no tsunami was reported along the coast (Utsu, 1979). Thus it is possible that this event is not a great earthquake. In zone E, the only known event is the 1677 earthquake which caused a disastrous tsunami from the southern Sanriku coast to Boso Peninsula (Hatori, 1976).

The historical seismicity data for great earthquakes along the northern Honshu arc shows that the number of known events decreases from north to south; zone B with no known typical thrust type earthquake is an

exception. The reader might think that this is due to the incompleteness of historical seismicity data for the region. However, it is difficult to imagine that the southern coast of northern Honshu, which had enough population at the year 1600, had failed to document great earthquakes and in contrast the northern coast had not. Thus we believe that the apparent decrease of frequency of great earthquakes from north to south is a real feature which represents a longer-term pattern of seismicity along the arc.

Pattern of Occurrence of Large Earthquakes

Large earthquakes are defined here as those having Ms=7-7.7. Some of the large earthquakes which have occurred along the northern Honshu arc are located within the rupture zones of great earthquakes (Utsu, 1974); however, many are located at the margins of the rupture zones of great earthquakes (Nagamune, 1977). One of the most prominent features of occurrence of large earthquakes is the existence of rupture zones at the deeper (40-60 km) part of the plate interface than the rupture zones of great shallow events. The areas off Miyagi prefecture and off Aomori prefecture, are the two locations for these deeper rupture zones (Fig. 1, hatched area). The zone off Miyagi prefecture has more complete documents for large events than the zone off Aomori prefecture; there have recurred large Ms=7.4 earthquakes with a 30-40 year time interval. The most recent earthquake is the 1978 Ms=7.5 Miyagi-Oki earthquake, which showed a thrust type mechanism (Seno et al., 1980).

The area near the coast between Miyagi and Aomori prefectures has historic records for only two large earthquakes in 1717 and 1772 (Usami, 1975); however, the locations of these events does not seem very reliable.

The rupture zone of the 1938 earthquakes in zone D is located more landward than those of shallow great events in other zones. There is a possibility that the three thrust-type events of the 1938 earthquakes have ruptured the deeper part of the plate interface; the focal depths of these events were determined as 30, 40, and 45 km (Abe and Tsuji, 1976).

Recent Seismicity

In this section, we discuss the recent seismicity for the past few decades including smaller-magnitude activity. The recent (1964-1974) seismicity map based on the ISC data (Fig. 2, Utsu, 1979; Seno, 1979a) shows a gap in activity for the two areas; one is zone C and the other is the landward of zone B. Another seismcity map (1969-1978 June) based on the JMA data (Fig. 3, Utsu, 1979) also presents clear gaps in these areas.

It is noted that the gap in zone C is also a gap in activity for great earthquakes, because about 80 years has passed since the last 1897 event ruptured the zone (Seno, 1979a, b). For the gap at the landward of zone B, only two historic large events are reported in 1717 and 1772 as stated previously. Activity for large earthquakes is much less than the

two areas off Aomori and Miyagi prefectures. We believe that the aseismic character at landward of zone B shown in Figures 2 and 3 is a long-term characteristic.

Kanamori (1981) reported that the focal area of the 1968 Tokachi-Oki earthquake had presented quiescence during a three-year period before the mainshock using earthquakes with M (JMA) greater than 5. Katsumata and Yoshida (1980) showed than an area near the mainshock location with a dimension of about one-fourth of the aftershock area of the 1968 event have presented quiescence during the periods 1948-1963 and 1968 May-1978. They called this area as a core of focal region.

There appeared no clear quiescence before the 1978 Miyagi-Oki earthquake within or near its rupture zone; however, activity for moderate size (M=5-6) earthquakes was high in the surrounding area around the rupture zone during a two year period before the mainshock (Seno, 1981; Seno et al., 1980).

Recently, a sequence of moderate and large earthquakes occurred in the northern half of the gap in zone C on January 18, 1981. The Ms of the mainshock is 6.9 and other six fore- and aftershocks have Ms around 6 (Seno and Eguchi, 1981). The aftershock zone of this earthquake almost took up the northern half of the gap. The total seismic moment of this series of earthquakes is less than 5×10^{25} dyn-cm, about by two factors less than that expected for a future great shock in zone C (Seno, 1979a). Ms=7 class earthquakes had preceded the 1968 Tokachi-Oki earthquake within and at the margin of its rupture zone in 1931, 1943, 1952 and 1960 (e.g., Utsu, 1974). Thus the occurrence of the 1981 earthquakes does not seem to reduce the possibility of occurrence of a future great shock in zone C.

Focal Mechanisms of Earthquakes before and after Great or Large Earthquakes

Focal mechanisms of earthquakes that preceded the 1968 Tokachi-Oki earthquake and those of its aftershocks were studied by Nakajima (1974). During the whole period 1926-1969, focal mechanisms of the earthquakes that occurred in the rupture zone of the 1968 event are similar to that of the mainshock, ie., of thrust type. In contrast, earthquakes which occurred north and south of the rupture zone showed a variety of mechanism types including strike-slip faulting and normal faulting, except for a one-and-a-half-year period just before the mainshock. He suggested that during the period just before the mainshock, the stress field in the vicinity of the rupture zone was uniform and occurrence of the mainshock and large aftershocks produced a complex stress field near the rupture zone.

Seno (1981a) and Seno and Pongsawat (1981) studied the focal mechanisms of earthquakes that preceded the 1978 Miyagi-Oki earthquake in the vicinity of its rupture zone. Many events had mechanism types different from that of the mainshock. Many down-dip compression and

down-dip tension-type events were found below the plate interface near the rupture zone (Fig. 4a, b). These events within the slab form a double seismic zone, which is continuous to the double seismic zone in the deeper part (Fig. 4b). They suggested that these events had been caused by the stress buildup within the slab near the rupture zone due to the mechanical coupling through the plate interface.

Seno (1981b) recently studied the focal mechanisms of earthquakes landward of zones A and B, which are located near the deeper (40-60 km) thrust zone. In the area landward of zone B, no event which is likely to have occurred within the slab below the deeper thrust zone was found. The activity along the plate interface in the depth range of 40-60 km was also much less than that found in the rupture zone of the Miyagi-Oki earthquake. In the area landward of zone A, that is, in the vicinity of the hatched area in Figure 1, several events which are likely to have occurred within the slab were found. However, the activity within the slab in that depth range was much less than that found near the rupture zone of the Miyagi-Oki event. These features can be explained by the hypothesis that the plate interface landward of zone B is largely decoupled mechanically and this produces too small stress to produce the fractures within the slab, and in contrast, the area landward of zone A, coupling and decoupling occur repeatedly along with the occurrence of large earthquakes in the hatched area, and now, the stress buildup is not so large as in the vicinity of the rupture zone of the Miyagi-Oki event (Seno, 1981b). This is concordant with the aseismic character in the area landward of zone B stated previously.

Earthquake Prediction

Large earthquakes which occur at the deeper (40-60 km) thrust zone sometimes cause severe damage in the local area on the coast, e.g., the 1978 Miyagi-Oki earthquake caused damage in Sendai area in Miyagi prefecture. In contrast, great shallow events located further offshore, whose ground motion is less severe than that of the near-coast events, sometimes cause destructive damage by tsunamis. Earthquake prediction for both type of events is of course desired to reduce the damage caused by these events.

For the events near the coast, one possible indicator for the occurrence of the events in the near future is the seismic activity within the slab near the future location of the event, which was stated previously. Two relatively large events of down-dip compression type preceded the 1978 Miyagi-Oki earthquake during a one-year period just before the earthquake; the June 8, 1977 M=5.8 and the Feb. 20, 1978 M=6.7 earthquakes. The latter is one of the largest events of down-dip compression type beneath northern Honshu for the past few decades. It is noted that this event preceded the Miyagi-Oki earthquake only by a half year at the northwest of the rupture zone of the Miyagi-Oki event.

Takagi (1980) reported that the seismic activity within the wedge portion between the trench and frontal arc decreased significantly after

the occurrence of the June 8, 1977 earthquake until the occurrence of the Miyagi-Oki event. If this is a common feature to all the large earthquakes near the coast, this could also be used as one indicator for a near future occurrence of the events. However, both of the activities within the slab and wedge portion cannot be used as a short-term earthquake prediction.

For the great earthquakes in the offshore region, the likely location for future shocks can be forecast by seismicity gaps; both kinds of gaps, i.e., the 1st and 2nd kind by Mogi (1979), can be used for this long-term prediction. However, at the present time, there is no effective method for a short-term prediction for these great events. It is difficult to conclude in advance if foreshock activity is <u>really</u> foreshock activity. Imagine if we could say whether or not the earthquakes in January 1981 in the gap in zone C are foreshock activity of the expected great shock. Future operation of strainmeters and seismometers in the deep sea terrace near the rupture zone of great earthquakes, which are monitored by land stations, may be a possible tool for a short-term prediction, although there remains a question of how they could be effective in real earthquake prediction. Installation of seismometers in the offshore region would, rather, contribute to elucidating a detailed process of subduction beneath the northern Honshu arc, which in turn will provide useful basic data for earthquake prediction.

For the offshore great earthquakes, early establishment of an effective tsunami warning system is important. When these events cause severe ground motion, it is easy to forecast the threat of tsunamis along the coast. However, silent tsunami earthquakes sometimes have caused severe damage. Thus rapid determination of seismic moments of the offshore events is needed. Along this line, Kanamori and Given (1981) and Koyama <u>et al</u>. (1980) proposed a rapid determination of seismic moments using the IDA data and JMA data, respectively.

More detailed studies on the seismicity pattern and subduction process along the northern Honshu arc are needed for both long- and short-term predictions in this offshore region.

References

Abe, K., Tectonic implications of the large Shioya-Oki earthquakes of 1938, Tectonophysics, 41, 269-289, 1977.

Abe, K., and H. Tsuji, Magnitudes of the Shioya-Oki earthquakes, Ann. Meeting Seism. Soc. Japan, Abs., no. 1, 24, 1976 (in Japanese).

Hatori, T., Tsunami magnitude and wave source regions of historical Sanriku tsunamis in northeast Japan, Bull. Earthq. Res. Inst., 50, 397-414, 1975 (in Japanese).

Hatori, T., Propagation of tsunamis from sources off the Pacific coast of northeast Japan, Bull. Earthq. Res. Inst., 51, 197-207, 1976 (in Japanese).

Kanamori, H., Focal mechanism of the Tokachi-Oki earthquake of May 16, 1968: Contortion of the lithosphere at the junction of two trenches, Tectonophysics, 12, 1-13, 1971a.

Kanamori, H., Seismological evidence for a lithospheric normal faulting - the Sanriku earthquake of 1933, Phys. Earth Planet. Inter., 4, 289-300, 1971b.

Kanamori, H., Mechanism of tsunami earthquakes, Phys. Earth Planet. Inter., 6 346-359, 1972.

Kanamori, H., and J. W. Given, Use of long-period surface waves for fast determination of earthquake source parameters, preprint, 1981.

Koyama, J., M. Takemura and J. Suzuki, Seismic moment determination qualified for routine processing of seismic data, Zisin, 33, 187-198, 1980 (in Japanese).

Mogi, K., Two kinds of seismic gaps., Pageoph, 117, 1-15, 1979.

Nagamune, T., Class M 7 earthquakes and tectonic structures, Ann. Meeting Seism. Soc. Japan, Abs., no. 2, 119, 1977 (in Japanese).

Seno, T., Intraplate seismicity in Tohoku and Hokkaido and large interplate earthquakes: A possibility of a large interplate earthquake off the southern Sanriku coast, northern Japan, J. Phys. Earth, 27, 21-51, 1979a.

Seno, T., On the earthquake expected off Miaygi prefecture, Rep. Coord. Comm. Earthq. Predict., 21, 38-43, 1979b (in Japanese).

Seno, T., Seismicity and earthquake mechanisms prior to the Miyagi-Oki earthquake of June 12, 1978, in preparation, 1981.

Seno, T., Seismicity and tectonics off the Pacific coast of northern Honshu, Japan: Deeper (40-60 km) thrust zones and seismicity within the slab., EOS, 62, 325, 1981.

Seno, T., and T. Eguchi, The Miaygi-Oki (Ms=6.9) earthquake of January 18, 1981 and its implications to subduction tectonics off the Pacific coast of northern Honshu, Japan, 21st, Assem. IASPEI, Abs., 1981a.

Seno, T., and B. Pongsawat, A triple-planed structure of seismicity and earthquake mechanisms off Miyagi prefecture, northeastern Honshu, Japan, Earth Planet. Sci. Lett., in press, 1981b.

Seno, T., K. Shimazaki, P. Somerville, K. Sudo, and T. Eguchi, Rupture process of the Miyagi-Oki, Japan, earthquake of June 12, 1978, Phys. Earth. Planet. Inter., 23, 39-61, 1980.

Takagi, A., Closing remarks and precursory seismic activity of the 1978 Miyagi-Oki earthquake, Proc. Earthq. Predict. Res. Symp., (1980), 231-241, 1980 (in Japanese).

Usami, T., Descriptive catalogue of disaster earthquakes in Japan, Univ. of Tokyo Press, Tokyo, 327p, 1975 (in Japanese).

Utsu, T., Space-time pattern of large earthquakes occurring off the Pacific coast of the Japanese Islands, J. Phys. Earth, 22, 325-342, 1974.

Utsu, T., Some remarks on a seismicity gap off Miyagi prefecture, Rep. Coord. Comm. Earthq. Predict., 21, 44-46, 1979 (in Japanese).

Figure Captions

Fig. 1: Seismicity pattern for great earthquakes along the northern Honshu arc. Shaded areas show the specific rupture zones for large earthquakes at the deeper (40-60 km) thrust zone.

Fig. 2: Distribution of earthquakes during 1964-1974 (data from ISC). Earthquakes with M_5 are plotted for focal depths 0-100 km (after Utsu, 1979).

Fig. 3: Distribution of shallow earthquakes with M_5 from 1969 to the time of Miyagi-Oki earthquake of 1978 (data from JMA, after Utsu, 1979).

Fig. 4a: Epicentral distribution of the types of focal mechanisms of earthquakes that preceded the Miyagi-Oki earthquake. Capital C, T and D denotes the events of down-dip compression, down-dip tension, and thrust types, respectively (after Seno, 1981a).

Fig. 4b: A cross-section of types of focal mechanisms. pP-P depths and well constrained depths are used in this cross-section. A. F. denotes the aseismic front (after Seno, 1981a).

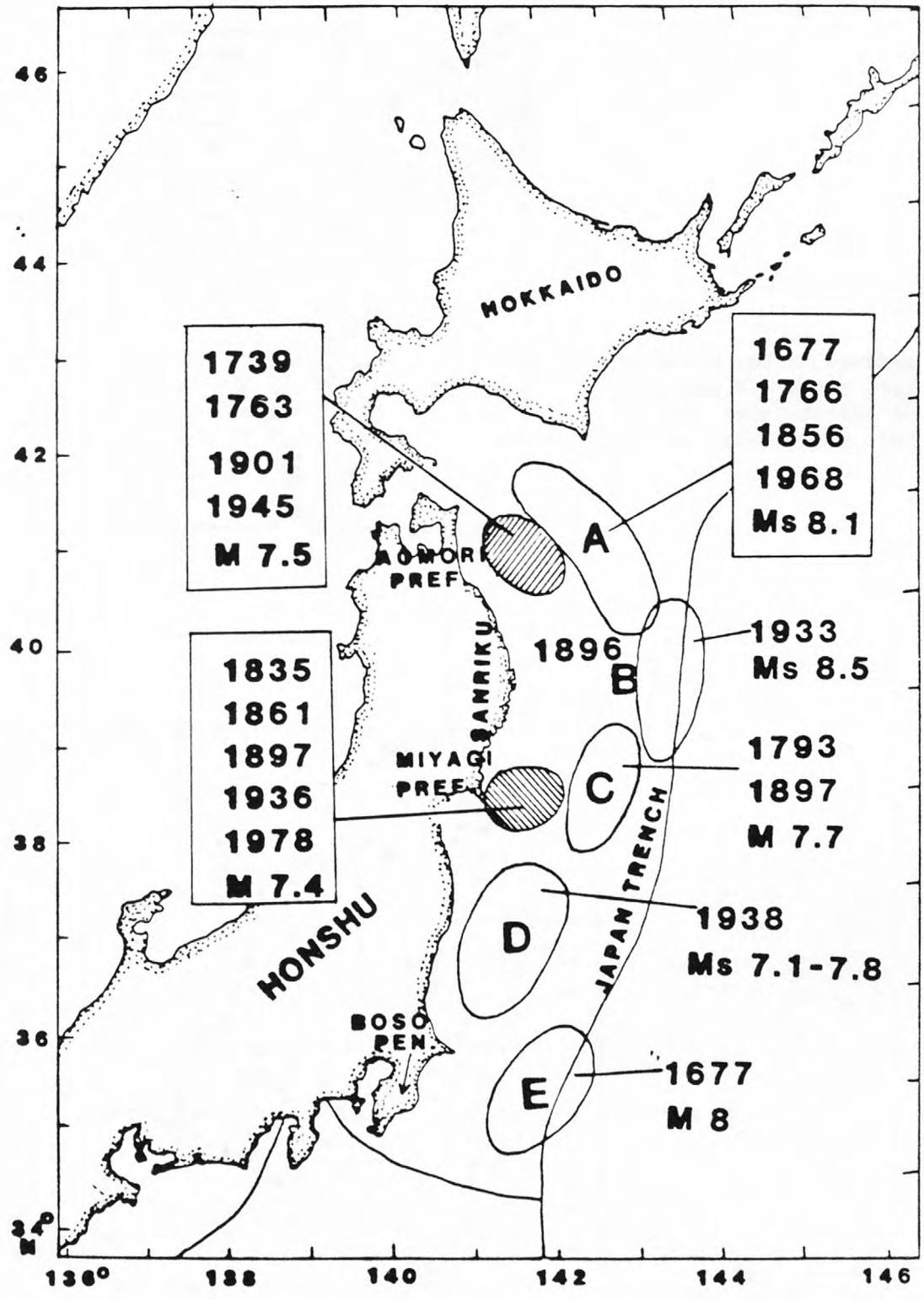

Fig. 1. Seismicity pattern for great earthquakes along the northern Honshu arc. Shaded areas show the specific rupture zones for large earthquakes at the deeper (40-60 km) thrust zone.

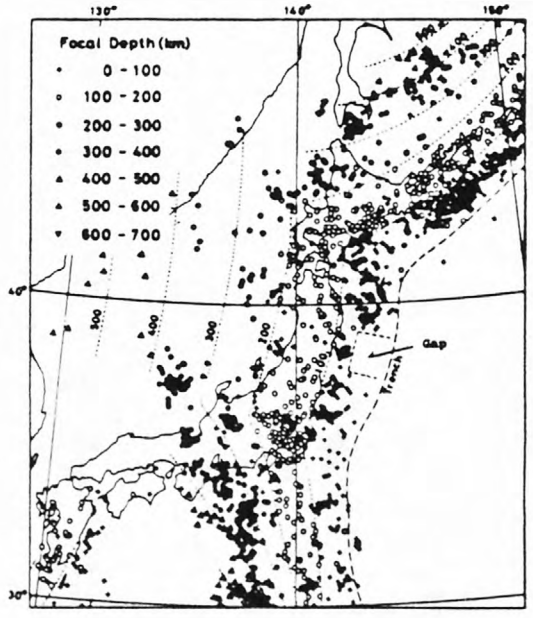

Fig. 2. Distribution of earthquakes during 1964-1974 (data from ISC). Earthquakes with M $\geq$ 5 are plotted for focal depths 0-100 km (after Utsu, 1979).

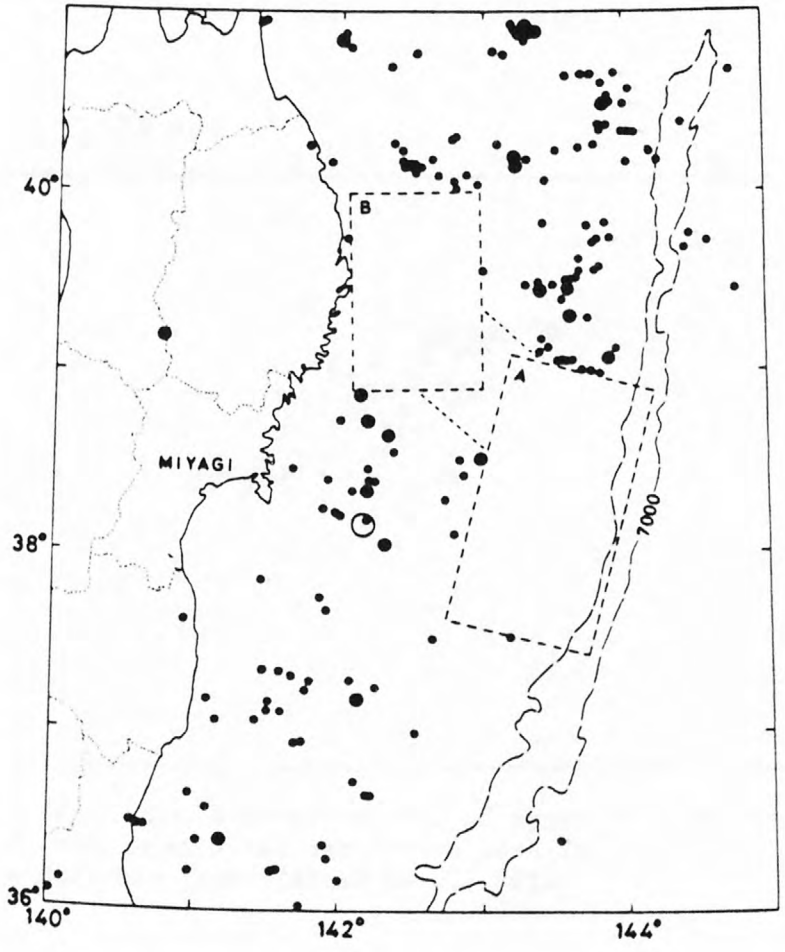

Fig. 3. Distribution of shallow earthquakes with M $\geq$ 5 from 1969 to the time of the Miyagi-Oki earthquake of 1978 (data from JMA, after Utsu, 1979).

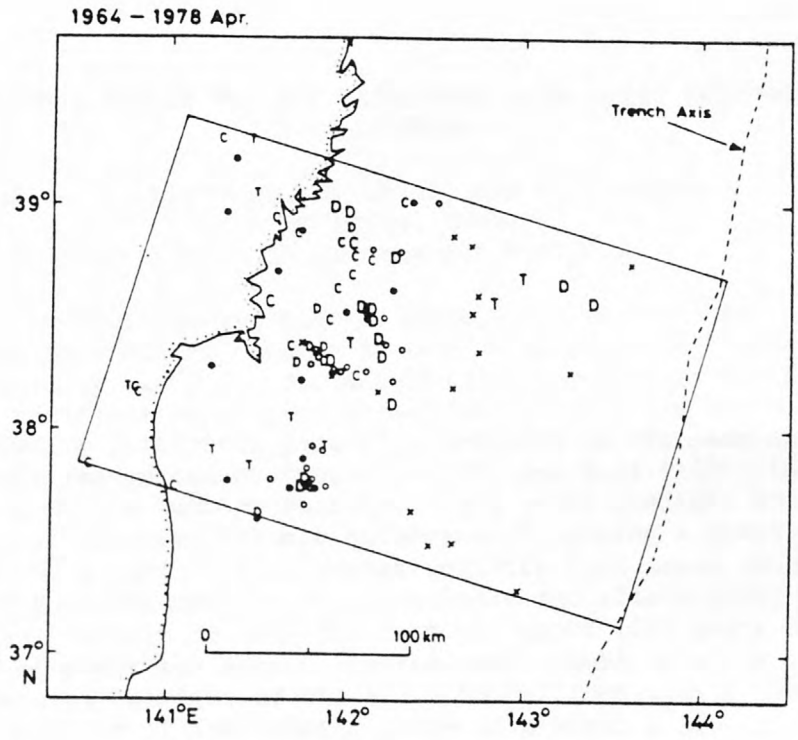

Fig. 4a. Epicentral distribution of the types of focal mechanisms of earthquakes that preceded the Miyagi-Oki earthquake. Capitals C, T, and D denote the events of down-dip compression, down-dip tension, and thrust types, respectively (after Seno, 1981a).

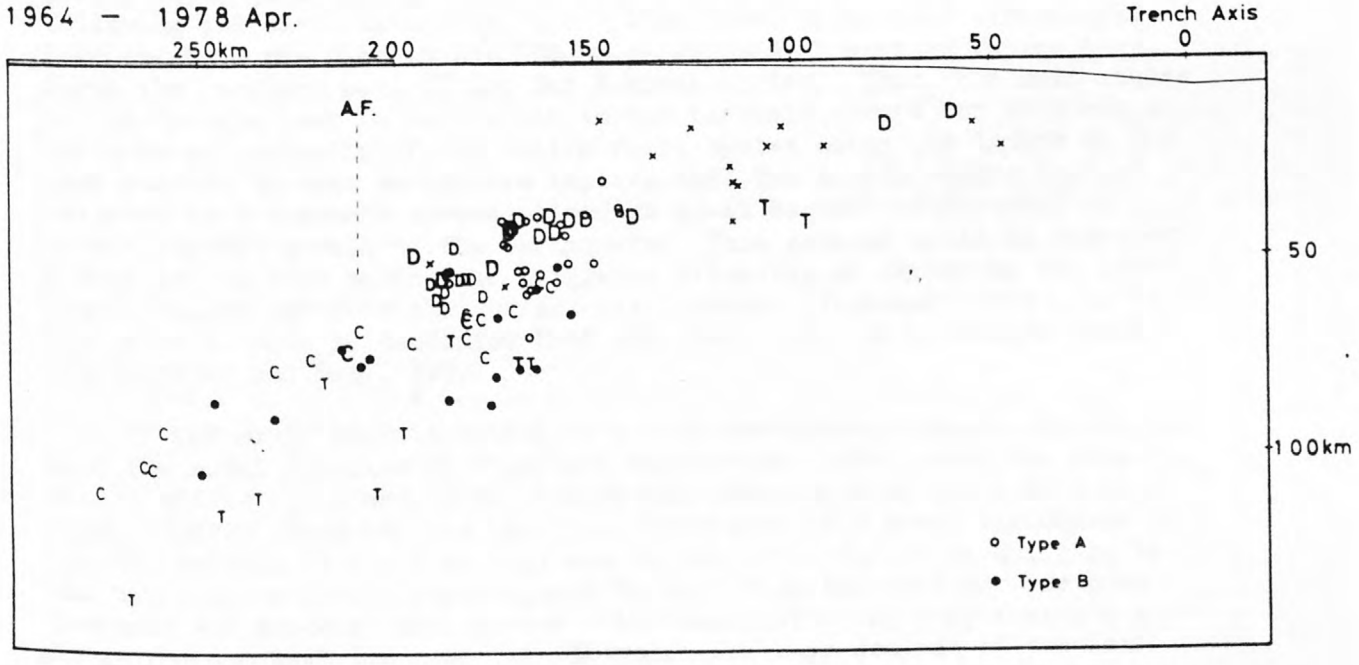

Fig. 4b. A cross-section of types of focal mechanisms. pP-P depths and well constrained depths are used in this cross-section. A.F. denotes the aseismic front (after Seno, 1981a).

EVIDENCE FOR A CYCLIC PATTERN ASSOCIATED WITH GREAT EARTHQUAKES IN CALIFORNIA

W. L. Ellsworth, A. G. Lindh, and B. L. Moths,
U.S. Geological Survey
Menlo Park, California 94025, U.S.A.

The cyclic accumulation of elastic strain in the crust and its release in great earthquakes appears to have modulated the historic pattern of seismicity along the San Andreas fault system in California. The space-time distribution of moderate-to-large magnitude earthquakes ($M > 5.5$) observed in California generally conforms to the same stages of the seismic cycle recognized by Fedotov (1968) and Mogi (1981) in the subduction zones of the western Pacific. This cycle consists of an extended period of relative seismic quiescence following a great earthquake, followed by a period of increased activity that leads to the cycle-controlling earthquake and its foreshocks and aftershocks. The historic record available in California is too short (200 years or less) and the sample of great earthquakes is too small (two) to allow us to demonstrate the applicability of the cycle to California with certainty. However, consideration of the seismic cycle as a working hypothesis leads to some interesting conclusions about the potential for future great earthquakes and the mechanical behavior of the San Andreas fault system.

The example of the 430-km-long northern segment of the San Andreas fault that ruptured in the 1906 earthquake provides the clearest support for the seismic cycle (Ellsworth, et al., 1981). The production rate of $M \geq 5$ earthquakes was significantly higher during at least the 50-year period before the 1906 earthquake than it was in the 50-year period following the earthquake (Fig. 1). Since about 1955, $M > 5$ earthquakes have begun to reappear in the 100-km-broad coastal belt of faults that forms the northern part of the San Andreas system. Thus, the main stages of the cycle appear to be present in the historic record for this region. The apparent quieting of the entire fault system along the length of the 1906 rupture by that earthquake implies that the strain redistribution extended to a distance several times as great as that predicted from simple elastic models of the earthquake. This paradox could be resolved either if the 1906 earthquake triggered afterslip at depth, as the lower crust "caught up" with the surface displacement (Thatcher, 1975), or if the brittle crust is decoupled from the lower crust at a shallow depth (Lachenbruch and Sass, 1980).

If the cycle repeats itself in a time-predictable manner, in accord with the model proposed by Shimazaki and Nakata (1980), then the length of the active stage should be of constant duration from cycle to cycle (Mogi, 1981). This implies that the occurrence of a great earthquake on the San Andreas fault in central and northern California is unlikely in the next few decades. Recurrence interval estimates derived from both geologic and geodetic data support this conclusion, as they indicate a long-term average recurrence of 150 years for this section of the San Andreas fault (Ellsworth, et al, 1981).

The other great earthquake that has occurred on the San Andreas fault in historic time ruptured about 350 km of the south-central segment of the fault in 1857. Unfortunately an inadequate historical record for this region prevents us from examining the regional level of earthquake activity preceding the time of the earthquake. Since 1857, there is an apparent, long-term increase in activity within the San Andreas system along the length of the 1857 rupture (Fig. 1), although the fault itself has remained quiet. No $M \geq 6$ events are known, for example, prior to 1920, and since that time there have been at least six, if events near Parkfield are excluded from the tally.

According to the seismic cycle hypothesis, the 60-year-long active period that began around 1920 would suggest that a major earthquake is more probable on this segment of the San Andreas fault than it is along the 1906 fault break. This conclusion can be reached more directly by noting that a greater length of time has elapsed since the 1857 earthquake than has since the 1906 earthquake (124 years versus 75 years). In fact, the mean interevent time for earthquakes large enough to produce ground rupture at Pallet Creek, on the San Andreas fault northeast of Los Angeles, is about 160 years (Sieh, 1978). Since individual recurrence intervals at this site vary by up to several decades, the probability of a major event involving at least part of the 1857 rupture is considered to be high.

The long-term behavior of moderate-to-large magnitude seismicity within the northern and south-central portions of the San Andreas system contrasts sharply with the behavior of the central and southern segments of the system. While the former regions display long-term rate variations that agree with the hypothesized stages of the cycle, the latter regions are characterized by a nearly constant earthquake production rate, at least during the period of reliable historic data (Fig. 1). Are these segments of the San Andreas fault incapable of rupturing entirely in a single earthquake, or do they represent seismic gaps that may fail at any time? The seismic cycle hypothesis would, by itself, favor the latter hypothesis, especially for the southernmost San Andreas fault.

The region along this 200-km-long segment of the fault has been one of the most seismically active areas in California since at least the 1890's, when the reliable earthquake record begins in this region. This long period of activity agrees well in form with the seismic history of the San Francisco Bay region from before the 1906 earthquake, where an active stage of about a century's duration can be inferred. The San Andreas fault is also locked along this southernmost segment and produces very few microearthquakes. This is also the character of the segments of the fault that produced the 1857 and 1906 events. There is also some new evidence for shear strain accumulation across this segment of the fault along the Salton Sea (Savage, et al.,1981). We conclude that the weight of the evidence strongly supports the possibility that this segment of the fault can fail in a single large earthquake and that the rupture

could extend to the north to include part of the 1857 break. Since we do not as yet have a reliable chronology for prehistoric events on this segment of the fault, we must conclude from the stability of the long-term level of seismicity seen in Figure 1 that the likelihood of such an event is as least as great here as it is for a repeat of the 1857 earthquake.

In contrast, the 150-km-long central segment of the San Andreas may not be capable of failing in a single, large-magnitude event. This segment is presently moving aseismically in rigid block motion, and is characterized by numerous small-magnitude earthquakes ($M < 5$) (Wesson, et al., 1973). Furthermore, no detectable strain has accumulated in the crust to the southwest of the fault since at least the mid-1880's (Thatcher, 1979). We would also note that this segment of the fault was immune to either strain or seismicity rate variations at its northern end, where it joins the 1906 rupture, as a consequence of that earthquake (Thatcher, 1979; Ellsworth, et al., 1981). Either this segment of the fault has maintained itself in a critical equlibrium, on the verge of rupturing in a large earthquake, for over a century; or aseismic slip, and small earthquakes to a much lesser extent, effectively accomodate the plate motion. We believe that the latter view more properly reflects the actual situation.

In summary, the evidence for a seismic cycle in California is supportive rather than decisive. The stages of the cycle, as described by Mogi (1981) for Japan, are clearly present for both the portions of the San Andreas system that ruptured in the 1857 and 1906 earthquakes. However, the historic records of earthquakes is too short to eliminate other interpretations. Application of the seismic cycle hypothesis in a predictive mode suggests that the portion of the San Andreas system along the 1906 rupture is entering a period when moderate-to-large earthquakes will be more frequent than they have been in the three-quarters-century following that event. However, the repeat of a M 8 earthquake on this segment of the San Andreas is not considered likely for at least several decades. The likelihood of a M 8 earthquake is considered to be much higher along the south-central and southern segments of the San Andreas fault, where an active stage of the cycle has tentatively been identified. In contrast, the available evidence suggests that the central, creeping segment of the San Andreas fault will not produce a major earthquake in the near future, if ever.

References

Ellsworth, W. L., Lindh, A. G., Prescott, W. H., and Herd D. G., 1981, The 1906 San Francisco earthquake and the seismic cycle, in Simpson, D. W., and Richards, P. G., eds., Earthquake prediction: an international review: American Geophysical Union Maurice Ewing Series 4, p. 126-140.

Fedotov, S. A., 1968, The seismic cycle, quantitative seismic zoning, and long-term seismic forecasting, in Medvedev, S., ed., Seismic zoning of the USSR: Moscow, Izdatel'stvo "Nauka", p. 133-166.

Mogi, K., 1981, Seismicity in western Japan and long term earthquake forecasting, in Simpson, D. W., and Richards, P. G., eds., Earthquake prediction: an international review: American Geophysical Union Maurice Ewing Series 4, p. 43-52.

Savage, J. C., Prescott, W. H., and Lisowski, M., 1981, Deformation across the Salton Trough, California, 1973-1980 (abs.): Earthquake Notes, v. 52, p. 24.

Sieh, K. E., 1978, Pre-historic large earthquakes produced by slip on the San Andreas fault at Pallett Creek, California: Journal of Geophysical Research, v. 83, p. 3907-3939.

Thatcher, W., 1975, Strain accumulation on the northern San Andreas fault zone since 1906: Journal of Geophysical Research, v. 80, p. 4873-4880.

Thatcher, W., 1979, Systematic inversion of geodetic data in central California: Journal of Geophysical Research, v. 84, p. 2283-2295.

Wesson, R. L., Burford, R. O., and Ellsworth, W. L., 1973, Relationship between seismicity, fault creep, and crustal loading along the central San Andreas fault, in Kovach, R. L., and Nur, A., eds, Conference on tectonic problems of the San Andreas fault, Proceedings, Stanford University Publications Geological Science, v. 13, p. 303-321.

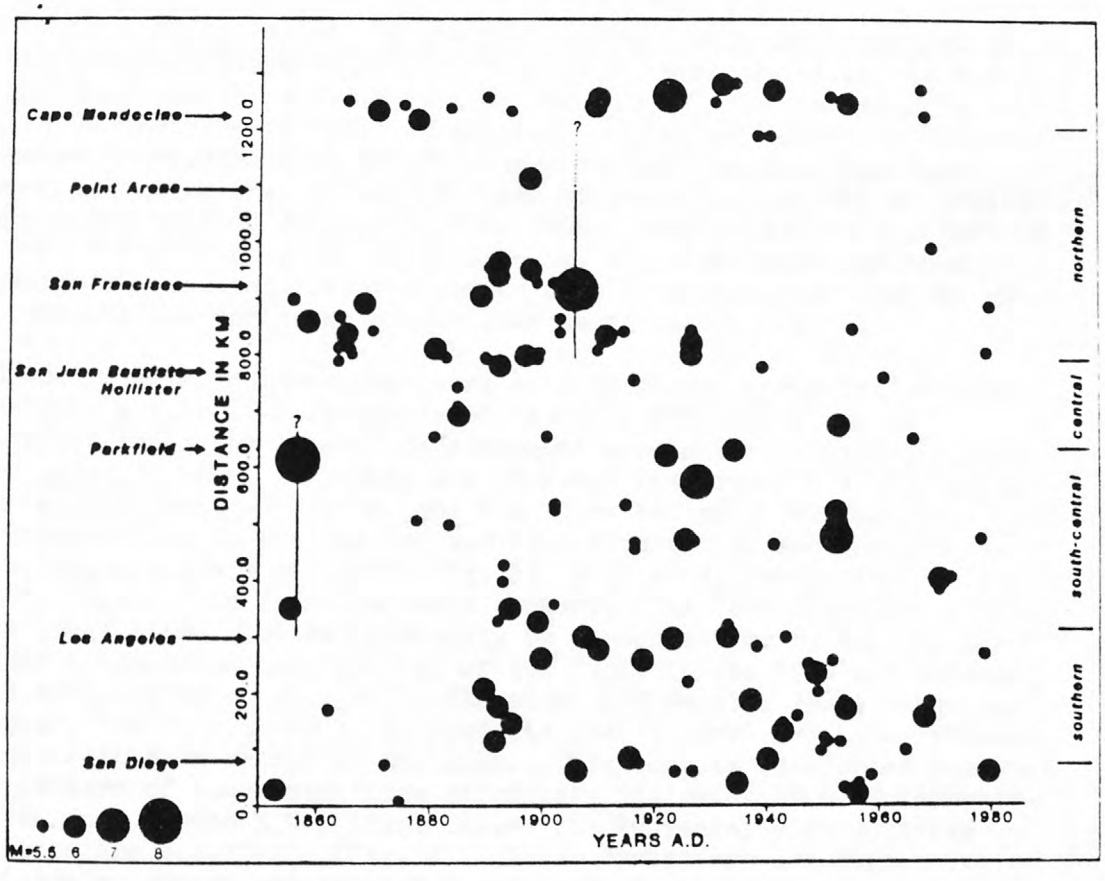

Fig. 1. Space-time plot of seismicity along the San Andreas and associated fault systems. Symbol size is proportional to magnitude. Surface faulting in great earthquakes of 1857 and 1906 shown by solid vertical lines. Surface faulting dotted offshore and dashed where uncertain.

HISTORIC SEISMICITY OF THE SAN JUAN BAUTISTA, CALIFORNIA REGION

A. G. Lindh, B. L. Moths, W. L. Ellsworth, and J. Olson
U.S. Geological Survey
Menlo Park, California 94025, U.S.A.

The 430-km-long segment of the San Andreas fault that ruptured in the great 1906 earthquake (M 8) has been seismically quiet at the M 6 level for the last 75 years (Ellsworth et al., 1981). The historic record of earthquakes in the 19th century for the southernmost 100 km of the rupture, extending from San Francisco to just north of San Juan Bautista, indicates that it was the site of three or four M 6 or greater earthquakes in the 110 years preceding 1906: 1800?; 1838, M 7?; 1865, M 6.5; 1890, M 5.9 (Toppozada, 1980). We believe that these earthquakes are plausibly accounted for by repeated slip on the southernmost 50 km of fault, just to the northwest of San Juan Bautista (Fig. 1).

Geodetic data indicate that strain is currently accumulating across this zone at a rate (0.6 μstrain/a; Prescott, 1980) which can be explained if the right lateral displacement across the fault is 2 cm/a, and the upper 10 km of the fault are locked. This rate of strain accumulation is consistant with short and long term geologic determinations of displacement rates in the region, and is sufficient to account for a M 6.5 earthquake every 30 years (Fig. 2), a close approximation to this segment's behavior in the nineteenth century. The long interval without a large event since 1906 can plausibly be accounted for by the 1.5 m of slip that occurred on this portion of the fault in the 1906 earthquake. If this model (Bufe et al., 1977; Shimazaki and Nakata, 1980; Sykes and Quittmeyer, 1981) is correct, it suggests that a large (>M 6) earthquake could occur in this region at any time. This idea is reinforced somewhat by the pattern of lower magnitude seismicity following 1906. Quiescence extending down to the M 4.5 level lasted for 40 years, with activity resuming in the mid-1940's (Fig. 2). These variations are suggestive of a small scale, stress modulated "seismic cycle".

Since 1979, a sequence of M 4 earthquakes have occurred on the San Andreas in the region northwest of San Juan Bautista. Micro-earthquake hypocenters associated with each of these larger events map out nonoverlapping areas on the fault plane and highlight two portions of the fault where future large events might reasonably be expected (top, Fig. 3). One is a 10-15-km-long zone between San Juan Bautista and Pajaro (0-15 km on the horizontal scale at the top of Figure 3) that has not ruptured in the past twelve years. The other is a 40 km zone northwest of Pajaro (15-55 km, top Fig. 3), which not only has been anomalously quiet in the last twelve years, as compared to the preceding eighteen (Fig. 2), but also was the probable location of at least some of the large earthquakes of the nineteenth century.

In cross section, the pattern of microseismicity on the fault plane at San Juan Bautista strongly resembles that at Parkfield, some 150 km to the southeast (bottom, Fig. 3). Lindh and Boore (1980) have determined that fault slip during the M 5.5-6 1966 Parkfield earthquake, (dashed line, bottom, Fig. 3), started near a dense cluster of activity at the leading edge of the seismically active zone (left side, bottom, Fig. 3), and propagated 20-25 km southeast to a single deep cluster (right side, bottom, Fig. 3). By analogy, we speculate that the 1865 earthquake near San Juan Bautista occurred within the dashed line shown in the top of Figure 3. Furthermore, several of the recent M 4 earthquakes have occurred at the ends of the 40-km-long zone on which we believe a >M 6 event is possible today.

Further similarities exist between the San Juan Bautista and Parkfield regions. Each region contains the terminus of a historic rupture zone for a great earthquake on the San Andreas fault, 1906 to the north and 1857 to the south. In both cases the transition from locked to creeping behavior is accompanied on the east side of the San Andreas by a change from a high-density, high-velocity basement (gabbroic and/or greenstones) to a low-velocity, low-density crustal section of predominantly graywacke character. The transition from locked to creeping behavior is also accompanied by the appearance of a high level of microseismicity on the fault plane that persists along the length of the creeping zone, by geometrical complexities in the fault zone, and by the occurence of moderate (M 5-6) earthquakes. We believe that the distribution of rock types along the fault plays a major role in determining whether or not a given section of fault slips seismically or aseismically, in determining the character of the microseismicity, and in determining where large earthquakes will occur. Thus we believe an integrated study of the geology, tectonics, seismic velocities, densities, and seismicity of a region forms a rational basis on which to build an earthquake prediction program.

References

Bufe, C. G., Harsh, P. W., and Burford, R. O., 1977, Steady-state seismic slip--a precise recurrence model: Geophysical Research Letters, v. 4, p. 91-94.

Ellsworth, W. L., Lindh, A. G., Prescott, W. H., and Herd, D. G., 1981, The 1906 San Francisco earthquake and the seismic cycle, in Simpson, D. W., and Richards, P. G., eds, Earthquake prediction: an international review: American Geophysical Union Maurice Ewing Series 4, p. 127-140.

Lindh, A. G., and Boore, D. M., 1981, Control of rupture by fault geometry during the 1966 Parkfield earthquake: Seismological Society of America Bulletin, v. 71, no. 1, p. 95-116.

Prescott, W. H., 1980, The accommodation of relative motion along the San Andreas fault system in California: Ph.D. Thesis, Stanford University, 195 p.

Shimazaki, K., and Nakata, T., 1980, Time-predictable recurrence model for large earthquakes: Geophysical Research Letters, v. 7, no. 4, p. 279-282.

Sykes, L. R., and Quittmeyer, R. C., 1981, Repeat times of great earthquakes along simple plate boundaries, in Simpson, D. W., and Richards, P. G., eds., Earthquake prediction: an international review: American Geophysical Union Maurice Ewing Series 4, p. 217-247.

Toppozada, T. R., Real, C. R., Bezore, S. P., and Parke, D. L., 1980, Preparation of isoseismal maps and summaries of reported effects for pre-1900 California earthquakes: California Division of Mines and Geology Open-File Release 80-15, 78 p.

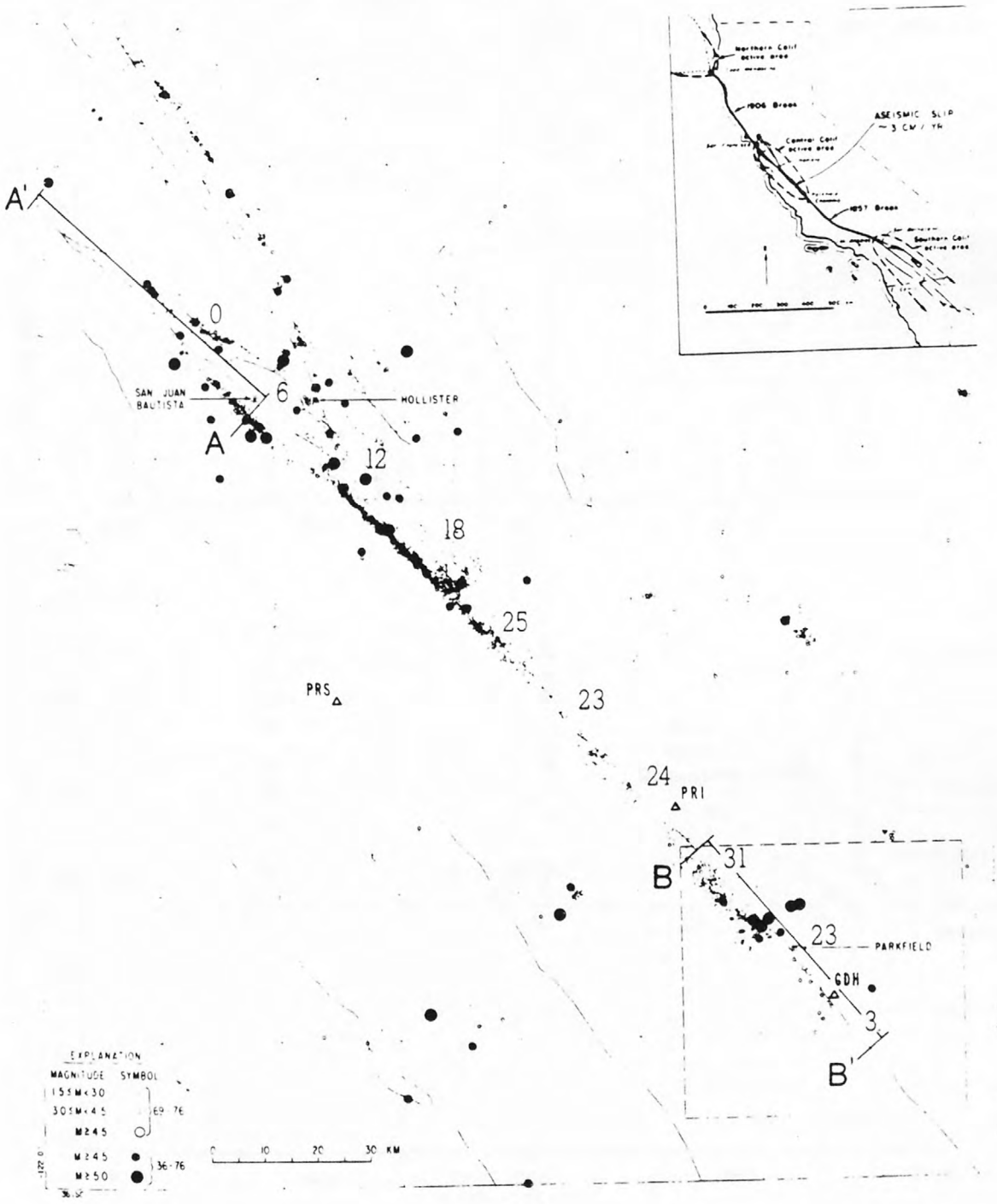

Fig. 1. Map showing the recent microseismicity (small dots) and the moderate earthquakes since 1936 (solid dots). The aseismic slip rate along the central portion of the San Andreas is shown by large numerals (mm/A).

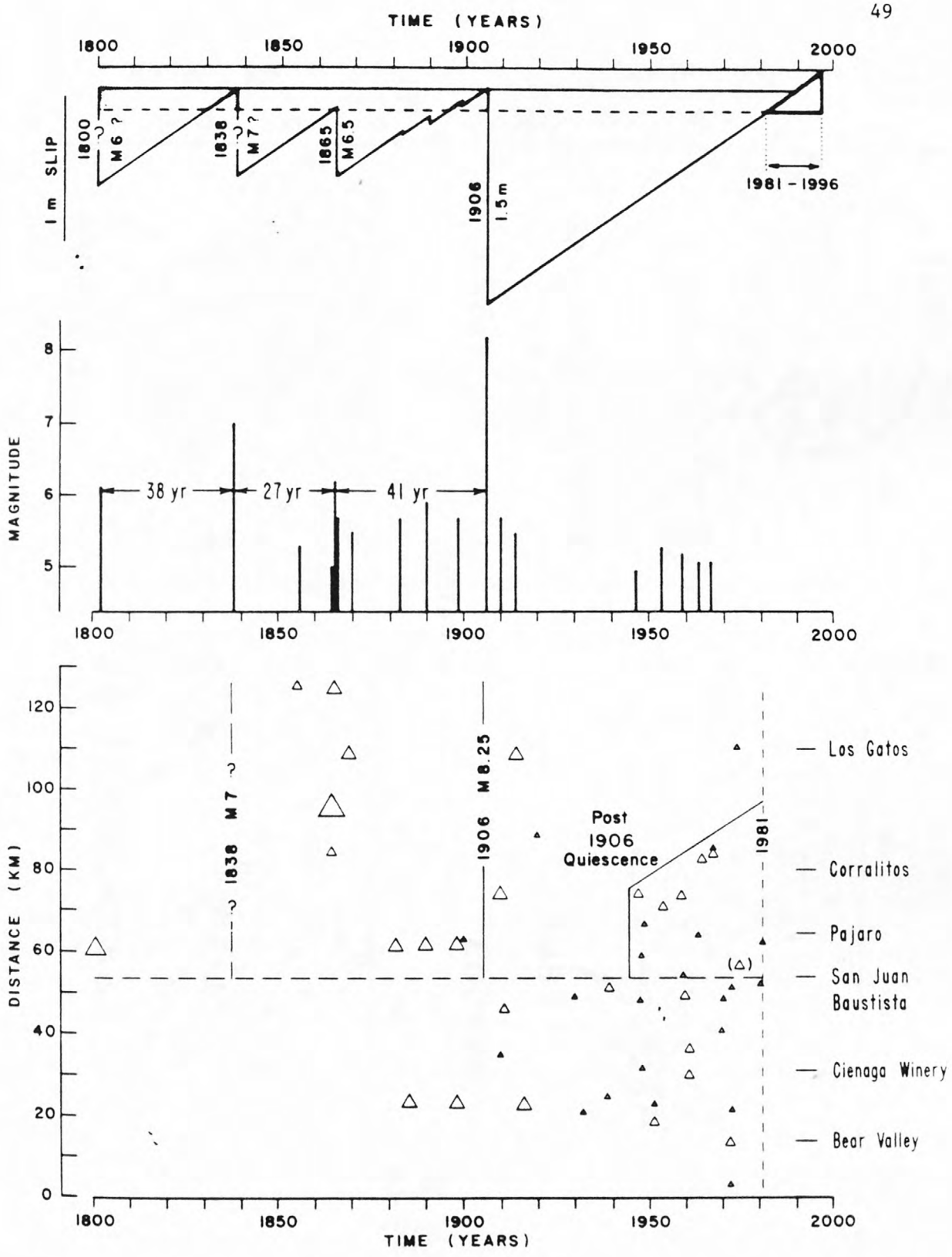

Fig. 2. (top) Equivalent slip plot of the events of M 5.5 from the middle figure. Magnitudes converted to moment by the usual relation log M_O = 16 + 1.5 M_L, equivalent slip (u) based on a fault plane of area 10 x 40 km (A) and M_O = Au.
(middle) Stick figure of the events above the dashed line in the space time plot. This represents activity at the southern end of the 1906 break.
(bottom) Space time plot of the seismicity along the San Andreas from Bear Valley to Los Gatos. M 5 prior to 1900, M 4.5 since that time.

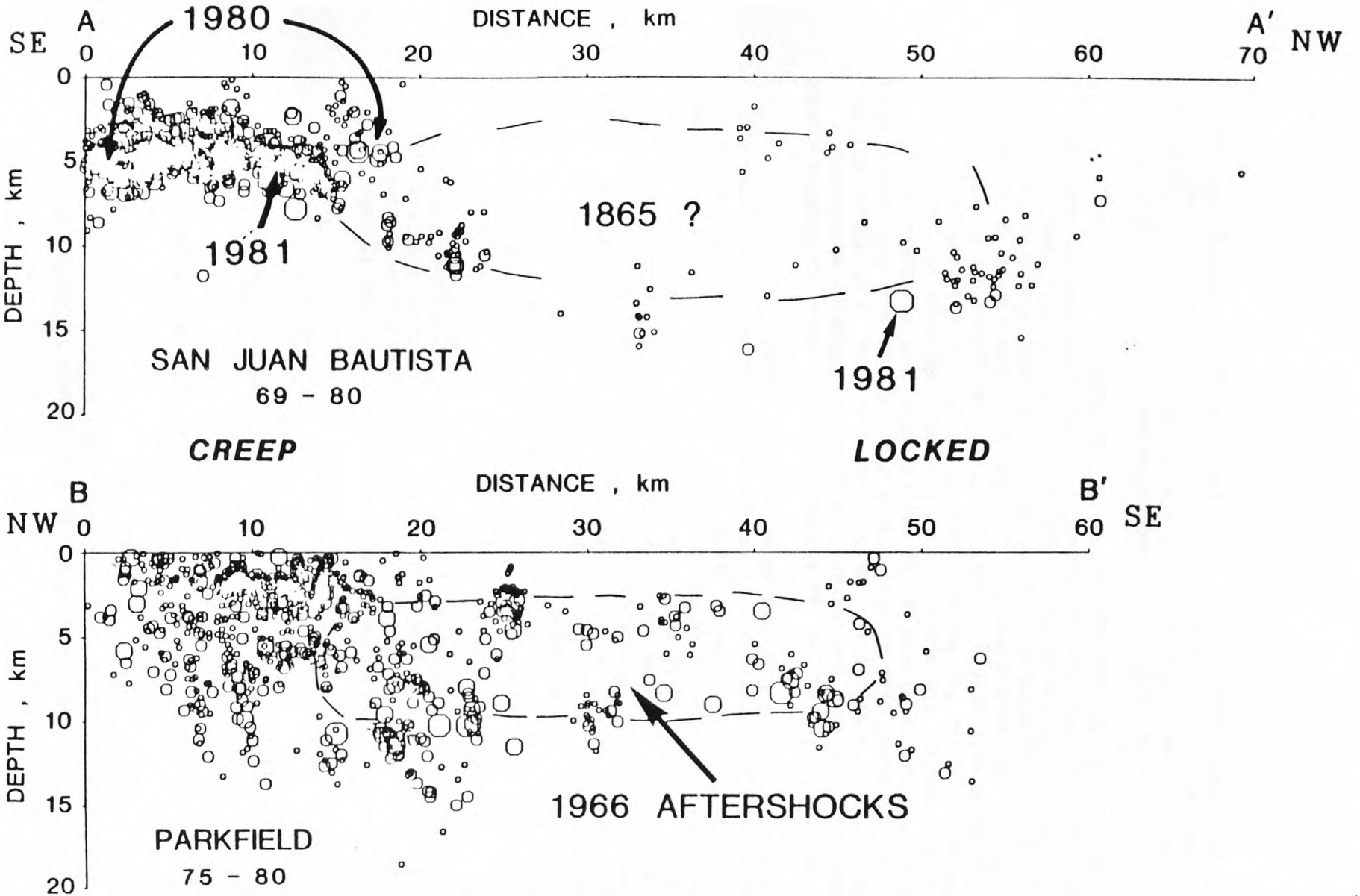

Fig. 3. (bottom) Cross section in the plane of the San Andreas, of the seismicity in the Parkfield area since 1975. (top) Similar plot of the activity in the San Juan Bautista region since 1969. Arrows identify hypocenters of M 4 earthquakes from 1980-81. Note that NW is to the right in the top figure, but to the left at the bottom; thus both cross sections are oriented such that the creeping portions of the fault are to the left in each case, and the locked portions to the right. The locations of the two cross sections are shown in Figure 1.

TIME-PREDICTABLE RECURRENCE OF DAMAGING EARTHQUAKES NEAR PARKFIELD, CALIFORNIA

W. H. Bakun
U.S. Geological Survey, Menlo Park, California
and
T. V. McEvilly
University of California, Berkeley, California

Abstract

Occurrence of moderate-sized earthquakes on the San Andreas fault near Parkfield in central California can be explained by the "time-predictable recurrence model". The model predicts that the next moderate-sized Parkfield earthquake will occur between 1994 and 2003.

The ratio of seismic moment for the main shock of Parkfield, California sequences in 1922 and 1934 (1:3) is nearly equal to the ratio of time intervals to the subsequent Parkfield earthquake sequence (12 yrs: 32 years), consistent with the time-predictable earthquake recurrence model (1,2). If this seismic moment-time interval proportionality holds, the relative seismic moment of the main shock of the Parkfield sequence in 1966 implies that the next Parkfield sequence will occur between 1994 and 2003. Although this model does not predict earthquake size, the predicted shock is expected to be comparable to the four Richter magnitude M_L 5 1/2 to 6 Parkfield earthquakes this century, which were locally damaging in the sparsely populated epicentral region and felt from the San Francisco to the Los Angeles metropolitan areas.

Parkfield lies on the San Andreas fault in central California midway between San Francisco and Los Angeles (Fig. 1). Similar earthquake sequences near Parkfield with main shocks occurring on 03 March 1901 at 0745 GMT, 10 March 1922 at 1121 GMT, 8 June 1934 at 0447 GMT, and 28 June 1966 at 0426 GMT provide a unique data set for testing models of earthquake recurrence. The similarity of intensity patterns (3) and surface fractures along the San Andreas fault trace (4) for all four sequences and the comparable spatial extent of aftershock epicenters in 1934 (5) and 1966 (6) are consistent with all four sequences rupturing the same 20- to 30-km-long section. Epicenters for the main shocks in 1922, 1934, and in 1966 are at the northwest end of the section (7); lack of instrumental data preclude the determination of the epicenters for the 1901 sequence and aftershocks during the 1922 sequence.

The time-predictable recurrence model was developed to explain the recurrence of small earthquakes on a 9-km-long section of the Calaveras fault zone east of San Jose, California and used to correctly predict a small earthquake there in 1976 (1). Also, the model rationalizes the

recurrence of large earthquakes at three sites of plate convergence in Japan (2). Assumed is a constant fracture stress, which might be thought of as the failure stress of the strongest point on the rupture zone, and a constant long-term loading rate, perhaps corresponding to a steady rate of relative plate motion. Failure occurs when the constant loading rate increases the stress on the fault to the fracture stress.

The model applied to the Parkfield section of the San Andreas fault is shown in Figure 2. Smaller shocks ($M_L \leq 5$) are ignored: their contribution to cumulative seismic moment is small, catalogs of earthquakes for central California are incomplete at the M_L 5 level before 1925, and M_L 5 foreshocks and isolated earthquakes near Parkfield tend to occur northwest of the sequence rupture zone (8). To quantify relative seismic moments, we calculated the mean of the ratio of the Love-wave spectral amplitudes (9) from 33 sec to 10 sec recorded at Berkeley (BRK in Fig. 1) for 1922 and 1966 relative to 1934. There is little uncertainty in the relative moments (1:3) of 1922 and 1934 since their spectral shapes are similar. (Absolute seismic moments calculated from the Love-wave spectra at BRK are 5×10^{24} and 1.5×10^{25} dyne-cm for the 1922 and 1934 main shocks respectively [11].) The relative moment of 1966 is less certain since its spectral shape differs considerably. Error bars in Figure 2 represent the standard deviation of the seismic moments of 1922 and 1966 relative to 1934 taken as unity. Given that the earthquakes ruptured the same area of fault, the relative seismic moments are relative coseismic displacements and hence relative stress drops. The 1934 to 1966 time interval was used to calibrate the long-term loading rate; loading for other times are represented in Figure 2 by slanted lines, drawn parallel to the rate from 1934 to 1966. Seismic slip on the rupture zone during the main shocks imply an effective loading rate about half (13) the 3-4 cm/yr of right-lateral plate motion across the San Andreas fault in central California (16). The model suggests that the long-term loading rate should have recovered the stress drop of the 1922 shock by 1932 to 1934. Going forward in time, the model suggests that the long-term loading rate should recover the stress drop of the 1966 event sometime between 1994 and 2003.

Going back in time from 1922, we can only say the the model is consistent with what we know about Parkfield earthquakes in 1901 and 1857. The seismic moment implied for 1901 by the intersection of the vertical line with the long term loading rate (Fig. 2) is consistent with the comparable intensities reported for the 1901, 1922, 1934, and 1966 shocks (3). Going further back in time is more uncertain. We know of no damaging Parkfield earthquakes between 1857 and 1901. The model suggests that the slip on the Parkfield section during the Great 1857 earthquake sequence was comparable to two 1966 events (Fig. 2). Clearly, data are insufficient to identify the specific events in the 1857 sequence responsible for the slip implied in Figure 2. On the basis of intensity patterns, Sieh has identified the two felt foreshocks to the Great 1857 quakes as two magnitude 5 to 6 Parkfield earthquakes and suggested that these foreshocks near Parkfield may have triggered the Great 1857

earthquakes, which then ruptured southeast from the Parkfield section (3). One admittedly speculative interpretation, is that one, or both, of the 1857 foreshocks contributed a significant portion of the 1857 slip on the Parkfield section, shown in Figure 2.

Although this model does not predict the size of future events, there is little reason to expect a shock significantly different from the M_L 5.5-6 shocks which occurred at Parkfield in 1901, 1922, 1934, and 1966. A repeat of the Great 1857 earthquake sequence is not anticipated (17) because of the very large slip (18) during that event on the northern part of its rupture zone. However, it is not possible to reject completely this possibility. Based on historical evidence, a magnitude M_L 5.5-6 future Parkfield earthquake will be locally damaging in the sparsely populated epicentral region and perceptible both in the San Francisco and Los Angeles metropolitan areas.

References and Notes

(1) Bufe, C. G., P. W. Harsh, and R. O. Burford, Geophys. Res. Lett., 4, 91 (1977).

(2) Shimizaki, K. and T. Nakata, Geophys. Res. Lett., 7, 279 (1980).

(3) Sieh, K. E., Bull. Seismol. Soc. Am., 68, 1731 (1978).

(4) Brown, R. and J. Vedder, U.S. Geol. Surv. Prof. Pap. 579, (1967), p. 9-10.

(5) Wilson, J. T., Bull. Seismol. Soc. Am., 26, 189 (1936).

(6) McEvilly, T. V., W. H. Bakun, and K. B. Casaday, Bull. Seismol. Soc. Am., 57, 1221 (1967).

(7) Bakun, W. H. and T. V. McEvilly, Science, 205, 1375 (1979).
Love-P_n arrival times at BRK are 66.7, 68.3, and 68.2 sec for the main shocks in 1922, 1934, and 1966, respectively. Assuming time-invariant P_n and Love velocities and constraining the epicenters to the fault trace, a decrease of 1 sec in the Love-P_n time at BRK requires a 3.9 km shift to the northwest in epicenter location. If the Love-P_n times are accurate to $\pm$ 1 sec, then the 1922 epicenter is constrained to the 11-km-long section northwest of the common epicenter of the 1934 and 1966 main shocks.

(8) Bakun, W. H. and T. V. McEvilly, Bull. Seismol. Soc. Am., 71, 423, (1981).

(9) Enlargements of the north-south (NS) and east-west (EW) Bosch-Omori seismograms from the 1922 and 1934 events were digitized manually. We removed minute marks, differences in recorder drum rates, trace skew, etc., and corrected for instrument response.
The NS and EW components were rotated to N 45°E for consistency with the alignment of the Press-Ewing seismograph that recorded the 1966 main shock. BRK lies near a maximum in the SH radiation and N 45°E is nearly transverse to the great circle azimuths from the epicenters to BRK (10). The Love-wave displacement spectrum is the Fourier amplitude of the two-minute window centered on the Love wave arrival.

(10) Filson, J. and T. V. McEvilly, Bull. Seismol. Soc.. Am., 57, 1245 (1967).

(11) Seismic moment = $\frac{u^{dc}_{\theta}}{A_L \cos 2\theta} \cdot [2\pi\Delta c\omega]^{\frac{1}{2}} \cdot \left|\frac{\chi}{\sin\chi}\right|$, where u^{dc}_{θ} = component of displacement in the θ direction due to a double-couple source, A_L is the Love-wave amplitude factor, Δ = epicentral distance, c = phase velocity, ω = circular frequency, and χ = directivity function (12).
Using u^{dc}_{θ} = 1/3 cm-sec and 1 cm-sec at 20 sec period, $A_L = 9.1 \times 10^{-19}$ cm/dyne, $\theta = 0$, Δ = 240 km, c = 3.7 km/sec, and $|\chi/\sin\chi| = 1$, the seismic moments for the 1922 and 1934 main shocks are 5×10^{24} and 1.5×10^{25} dyne-cm, respectively. Such single-station absolute moment determinations are accurate only to a factor of about 2.

(12) Ben-Menahem, A. and D. G. Harkrider, J. Geophys. Res. 69, 2605 (1964); M. D. Trifunac and J. N. Brune, Bull. Seismol. Soc. Am. 60, 137 (1970).
(13) Seismic slip u = seismic moment/μA, where μ is the modulus of rigidity and A is the rupture area. Using 1.4×10^{25} dyne-cm for the seismic moment of the 1966 main shock (14), $\mu = 2 \times 10^{11}$ dyne/cm^2, and A = 5 km x 25 km (15), $\bar{u}_{1966} = 56$ cm, corresponding to a seismic slip rate on the rupture zone of 1.7 cm/yr.
(14) Tsai, Y.-B. and K. Aki, J. Geophys. Res. 75, 5729 (1970).
(15) Lindh, A. G. and D. M. Boore, Bull. Seismol. Soc. Am. 71, 95 (1981).
(16) Savage, J. C. and R. O. Burford, J. Geophys. Res. 78, 832 (1973); W. Thatcher, J. Geophys. Res. 84, 2283 (1979).
(17) Sykes, L. R. and R. C. Quittmeyer, Earthquake Prediction, Maurice Ewing Series 4, AGU, in press.
(18) Sieh, K. E., Bull. Seismol. Soc. Am. 68, 1421, (1978).

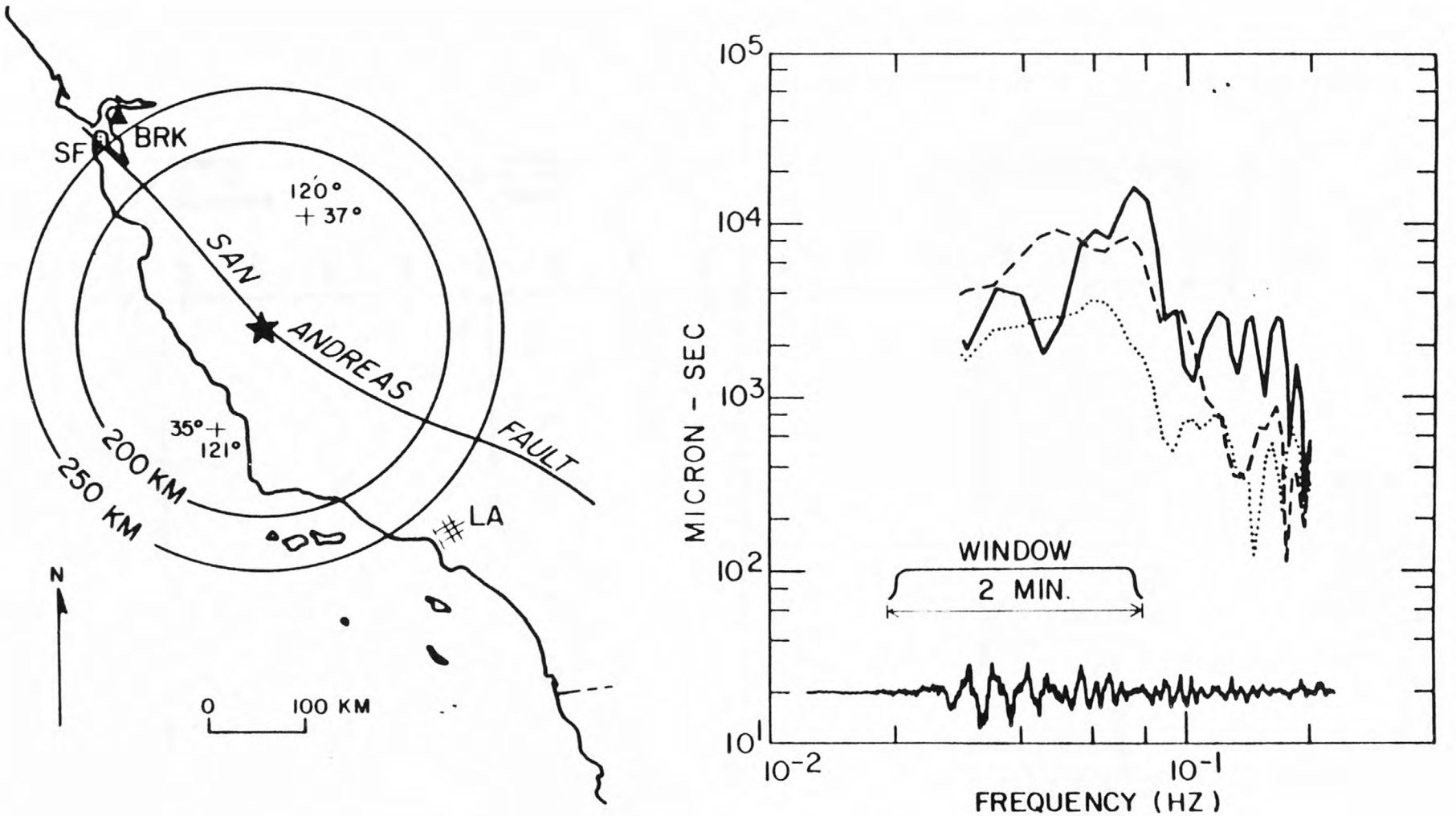

Fig. 1. (Left) Location of the Parkfield epicentral region and trace of the San Andreas fault relative to Berkeley (BRK). (Right) Love-wave displacement spectra at BRK for the main shocks of the Parkfield sequences in 1922 (dotted), 1934 (dashed) and in 1966 (solid). Also shown is the window (5 percent cosine taper of 2-minute diration, centered on the Love-wave arrival) applied to the Press-Ewing (To = 30 sec) N 45°E seismogram for the 1966 main shock.

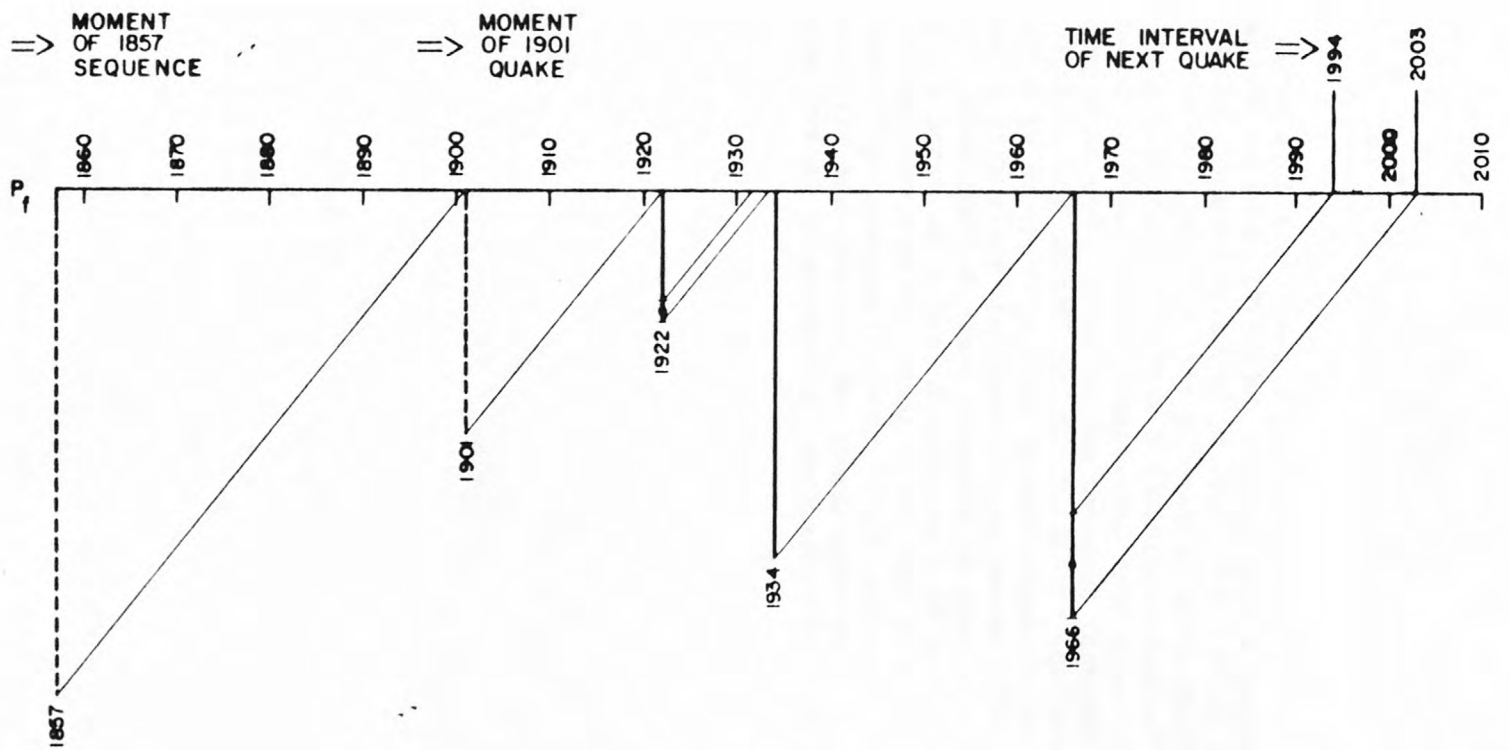

Fig. 2. Time-predictable earthquake recurrence model applied to the Parkfield section of the San Andreas fault. Relative seismic moments of known damaging Parkfield earthquakes are represented by vertical lines. Earthquakes occur when the loading rate (slant lines) recovers the stress drop of the preceding earthquake and stress on the section equals the failure stress P_f of the section.

STRAIN ACCUMULATION IN SOUTHERN CALIFORNIA

J. C. Savage
U.S. Geological Survey
Menlo Park, California 94025, U.S.A.

Frequent surveys of seven trilateration networks in southern California over the interval 1973-1980 suggest that a regional change in strain accumulation may have occurred in 1978-1979. Prior to 1978 the strain accumulation was predominantly a uniaxial north-south compression whereas since that time there has been a diminished rate of north-south compression and an increased rate of east-west extension. The onset of this change appears to occur first in the networks farthest south. The changes occur without any unusual seismicity within the networks, but the overall seismicity in southern California was unusually low prior to and has been unusually high since the onset of the change. The average principal strain rates for the seven networks in the 1973-1980 interval are 0.17 μstrain/a north-south contraction and 0.08 μstrain/a east-west extension. Although the observed change in strain accumulation could be related to unidentified systematic error in the measuring system, a careful review of the measurements and comparisons with three other measuring systems reveal no appreciable cumulative systematic error.

MEASUREMENT OF STRAIN ON 10-KM LINES NEAR PARKFIELD, CALIFORNIA

J. E. Estrem, A. G. Lindh, J. F. Evernden, and D. Reneau
U.S. Geological Survey
Menlo Park, California 94025, U.S.A.

In hopes of better understanding the details of strain accumulation along the San Andreas fault near Parkfield, California, we have installed a 50-monument geodetic network centered on the rupture zone of the 1966 Parkfield earthquake. The line lengths, which range from 1 to 10 km, are surveyed twice yearly with a Hewlett-Packard 3808A laser distance-measuring instrument.

We have conducted a series of tests to determine the precision that can be obtained with the HP instrument. The oscillator frequency is stable to less than 0.1 ppm, if correction is made for long-term drift and thermal effects (Fig. 1). The chief limitation in measuring distances to high precision is the difficulty in estimating an average refractive index because of varying atmospheric conditions along the sight path. To assess this factor, we ran two experiments in which distances of 5 and 10 km were measured every hour for 25 and 55 hours, respectively (Figs. 2 and 3). Temperature, pressure, and humidity were measured at the end points of the lines, and first-order corrections were made to the apparent line lengths on the assumption that these quantities varied linearly along the sight path. Because the actual line lengths presumably did not change, the variations in corrected line lengths give an estimate of the error in the average refractive index that results from using only end-point measurements. Figure 4 shows the 55 hourly measurements of the uncorrected distance, average refractive index, and distance corrected for refractive index. The standard deviation about the mean of these corrected distances is approximately 1 ppm.

We found that, by using various averaging and data-selection strategies, the standard deviations of the corrected distances can be significantly reduced. Figures 5A-5E illustrate the effect of applying these strategies, such as lagging the atmospheric data relative to the time of distance measurement (5B), weighting the atmospheric conditions at one station over another (5C), or, most importantly, using only data taken during the six-hour intervals from midnight to 6 a.m. (5E).

We have remeasured the same 5 and 10 km lines nine times from midnight to 6:00 a.m., and the total spread of nightly six-hour averages remain approximately 1 ppm (Fig. 6).

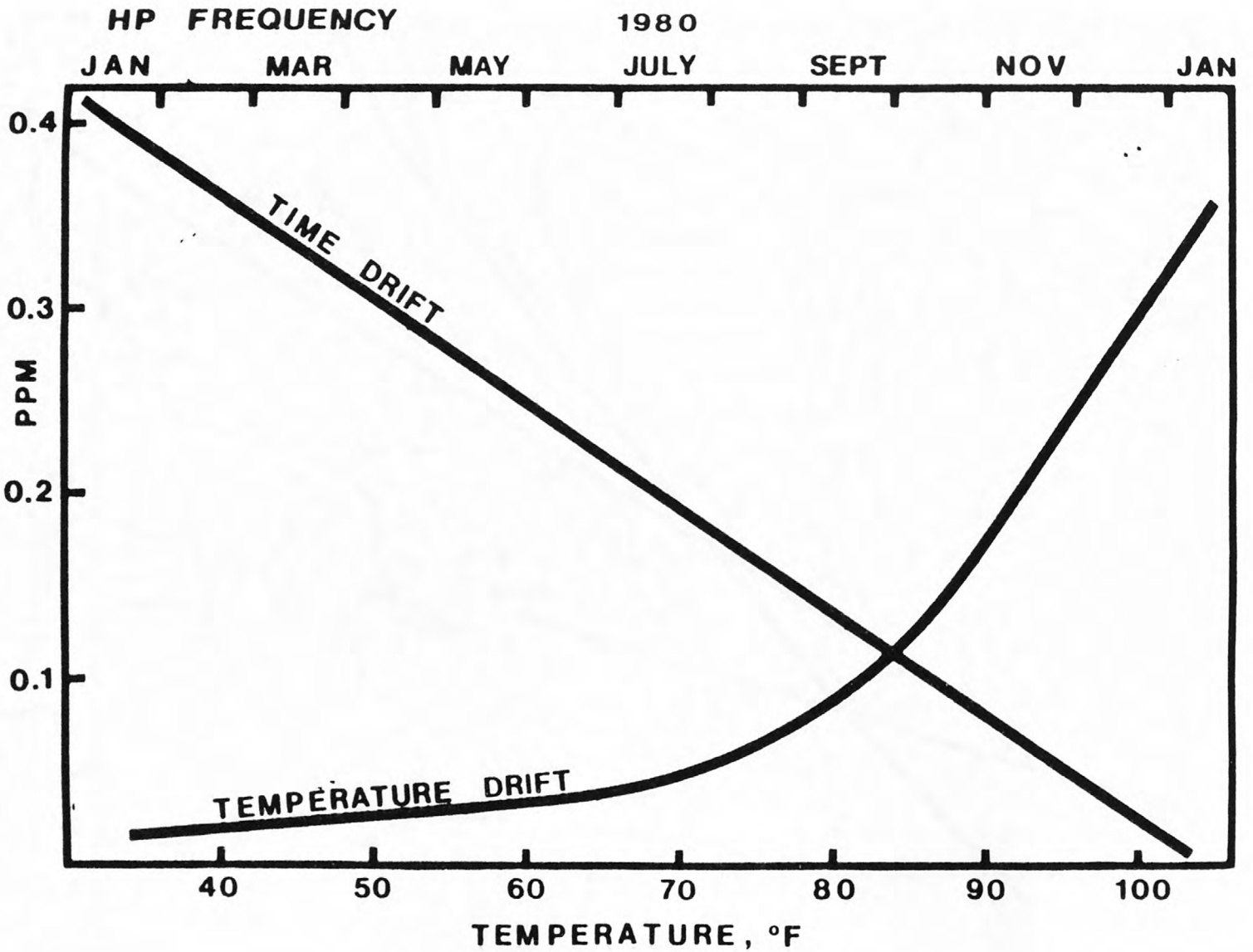

Fig. 1. Crystal oscillator stability versus time and temperature for an HP3808A distance meter. By monitoring the oscillator frequency monthly against an exact frequency standard, and by operating in the field at temperatures below 80° F, it is possible to correct for these effects to better than 0.1 ppm.

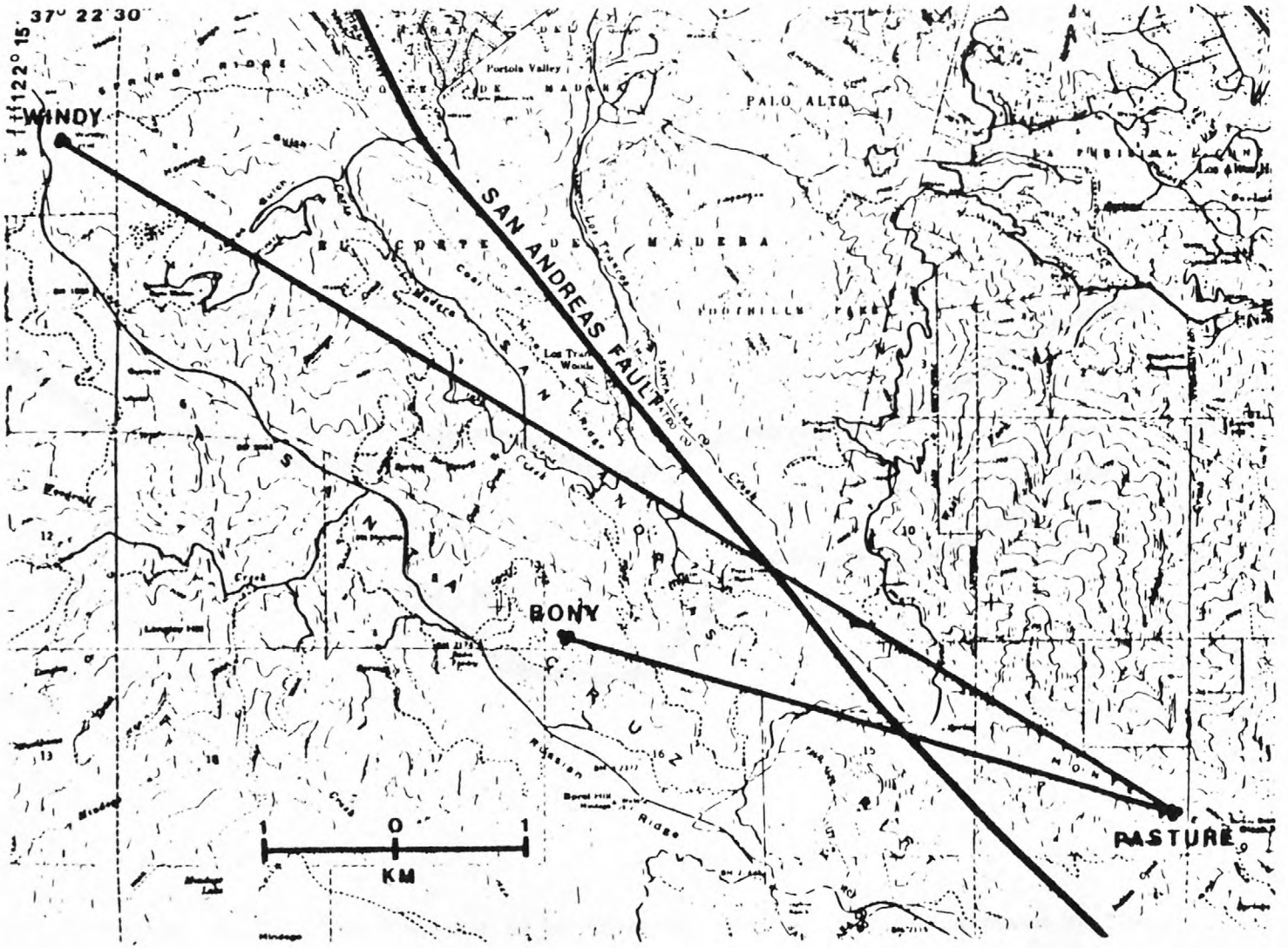

Fig. 2. Location of 5 km and 10 km lines being remeasured at night in the Santa Cruz Mountains near Palo Alto, California.

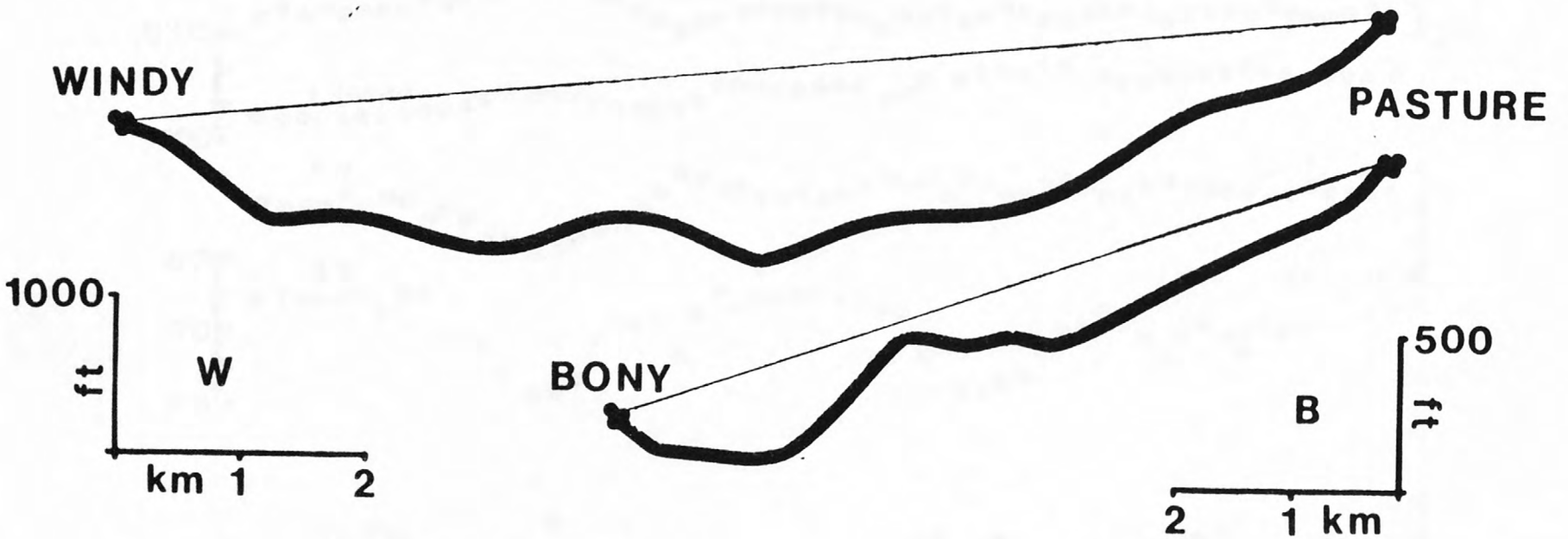

Fig. 3. Profiles of 5 km and 10 km lines showing topographies crossed by laser.

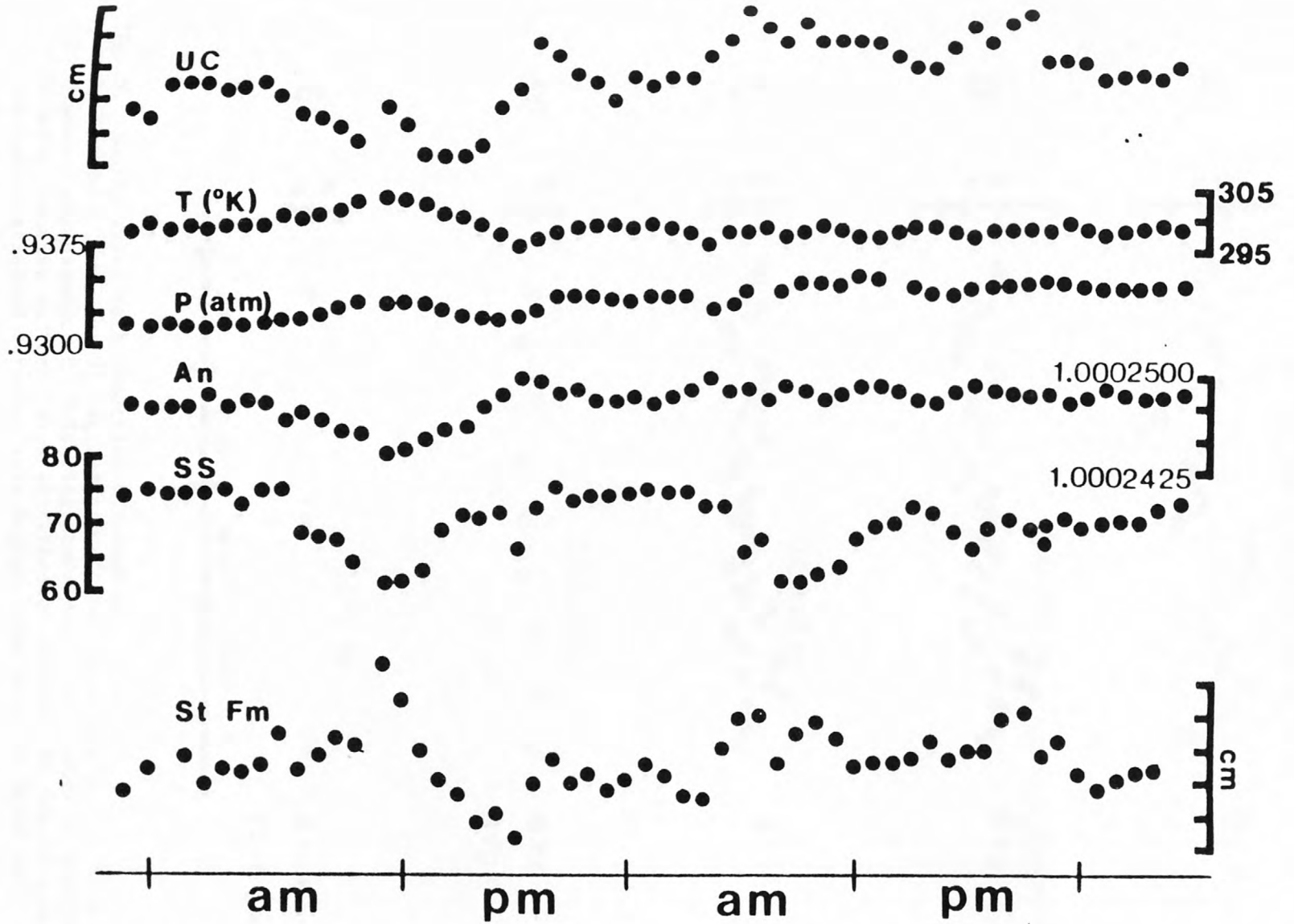

Fig. 4. Hourly data for the 10 km Windy line. UC = uncorrected distances; T = average temperature; P = average pressure; An = average refractive index; SS = strength of reflected laser signal (Max = 80); St Fm = distance corrected by standard formulas (i.e., average refractive index).

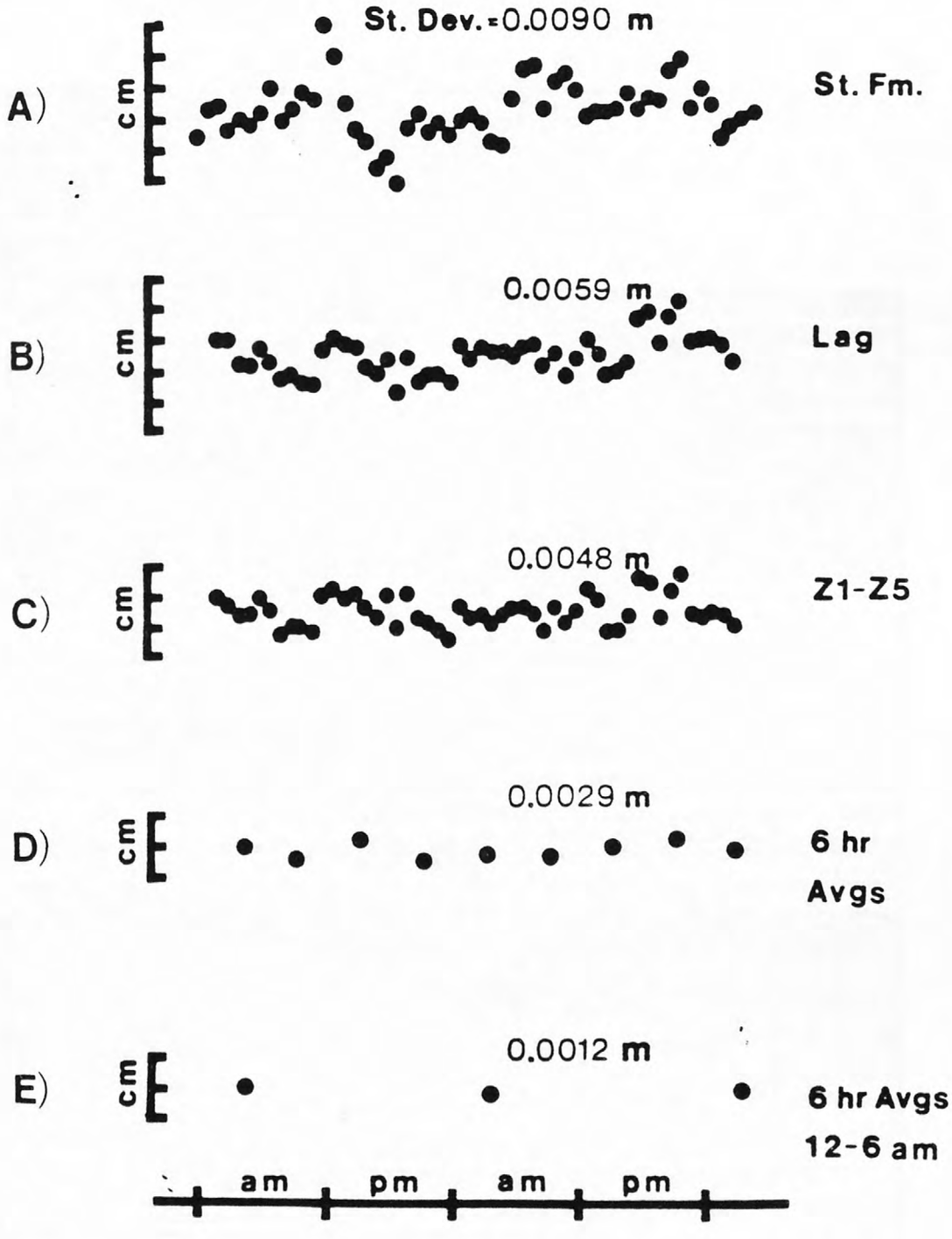

Fig. 5. Hourly Windy data reduction strategies:
A) Standard formulas; B) Lagging atmospheric data relative to time of distance measurement; C) Weighting atmospheric data taken at instrument station relative to that taken at reflector station; D) Grouping data reduced by standard formulas into 6-hour intervals; E) Using only midnight to 6 a.m. data.

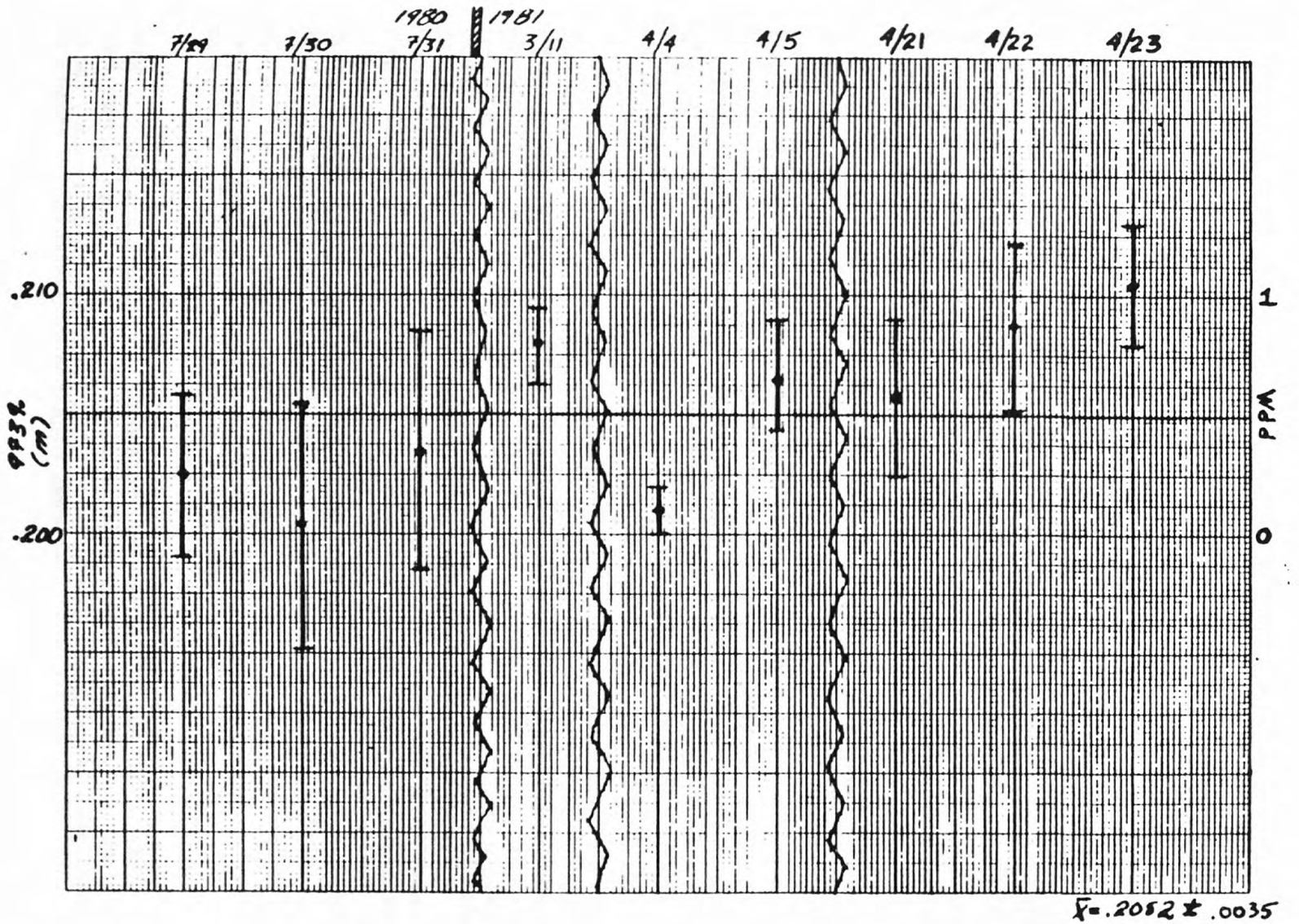

Fig. 6. Six-hour averages of all nighttime Windy measurements. Error bars represent standard deviations of six-hour averages.

LIMITATIONS IN OBSERVATORY STRAINS AND TILT MEASUREMENTS

Frank Wyatt
Institute of Geophysics and Planetary Physics
University of California
San Diego, California, U.S.A.

Strain, tilt, and gravity have been measured at Piñon Flat Geophysical Observatory (PFO) since 1971. We began this effort with the goal of accurately monitoring the deformation occurring in the area of the observatory--a goal we are still pursuing. Over the years, a variety of experiments have been conducted that have served to identify the various sources of noise (deformations unrelated to the regional strain), and new instruments have been designed to reduce the errors in the measurements. Because the signals of interest occur at extremely low frequencies (e.g., one cycle per year), much of our research has involved the intercomparison of instruments. In fact, there are currently 11 institutions participating in experiments at the site utilizing techniques ranging from NASA's project ARIES to the deep borehole sensors of the Carnegie Institute of Washington. Five of these research groups are testing parallel tiltmeters ($\sim$500 m in length). Measuring the coherence among these instruments will help us to determine the level of the common signals and hence the accuracy of the techniques.

The need for additional improvement in both observatory and geodetic instrumentation may be understood by considering the deformation expected from a simple dislocation in the earth's crust. The theoretical strain amplitude for moderate-to-great earthquakes is generally not greater than a microstrain outside of the source region. Since we do not know precisely when or where such an event is going to occur, we should be able to continuously monitor strains much less than this ($\sim$ nanostrain). Indeed, precursory phenomena are probably smaller than the anticipated coseismic deformation, unless inhomogeneities focus the stress. Unfortunately, geodetic surveys, conducted in the uncontrolled atmosphere, are limited presently to the accuracy of roughly 0.1 microstrain and generally require many days to complete. On the other hand, observatory instruments seldom perform as well as their geodetic counterparts over periods of years. Consequently, unless precursory crustal deformations have either extremely large amplitudes or occur in a short period of time, they may not be detected by either method.

There is a surprising conformity to the best long-period records of strainmeters and tiltmeters throughout the world. Since co-located instruments usually do not produce similar signals, we believe that this is an indication of the difficulty in attaching the limited baselength equipment to the earth in a stable manner.

We have conducted a variety of experiments at PFO in an attempt to establish the magnitude and nature of monument displacements. A device called an optical anchor has been developed to measure the horizontal motion of a surface monument relative to the material at depth, in this case 26 m. Nearly two years of records show that a near-surface monument may displace gradually as much as 0.1 mm, and move abruptly 0.05 mm in response to seismic accelerations. A similar study of the vertical stability of adjacent benchmarks has recently been completed. A short baselength equipotential fluid tiltmeter was operated for more than a year. Such a short instrument is particularly sensitive to instabilities of the reference points. The relative vertical displacement was found to be roughly 0.1 mm. While this value compares favorably with the estimated instability of normal geodetic benchmarks ($\sim$ 0.25 mm), we had hoped that the monument at PFO would be much better. The monuments are unusually large granite blocks ($\sim$ 3 m^3) cemented into decomposed granite; this material is not easily excavated by conventional construction equipment.

Apparently the surface layers at PFO are subject to unpredictable displacements of roughly 0.2 mm/year--perhaps due to the weathering process. Since the strainmeter observations from PFO are unsurpassed by measurements elsewhere, we assume that this surface behavior is common. In order to reduce the error of the observed surface strain measurements to a level of 10 nanostrains/year, either an instrument baselength of 10 km is necessary or sophisticated monuments must be constructed. Obviously, more research is needed to achieve our goal of monitoring the true crustal deformation.

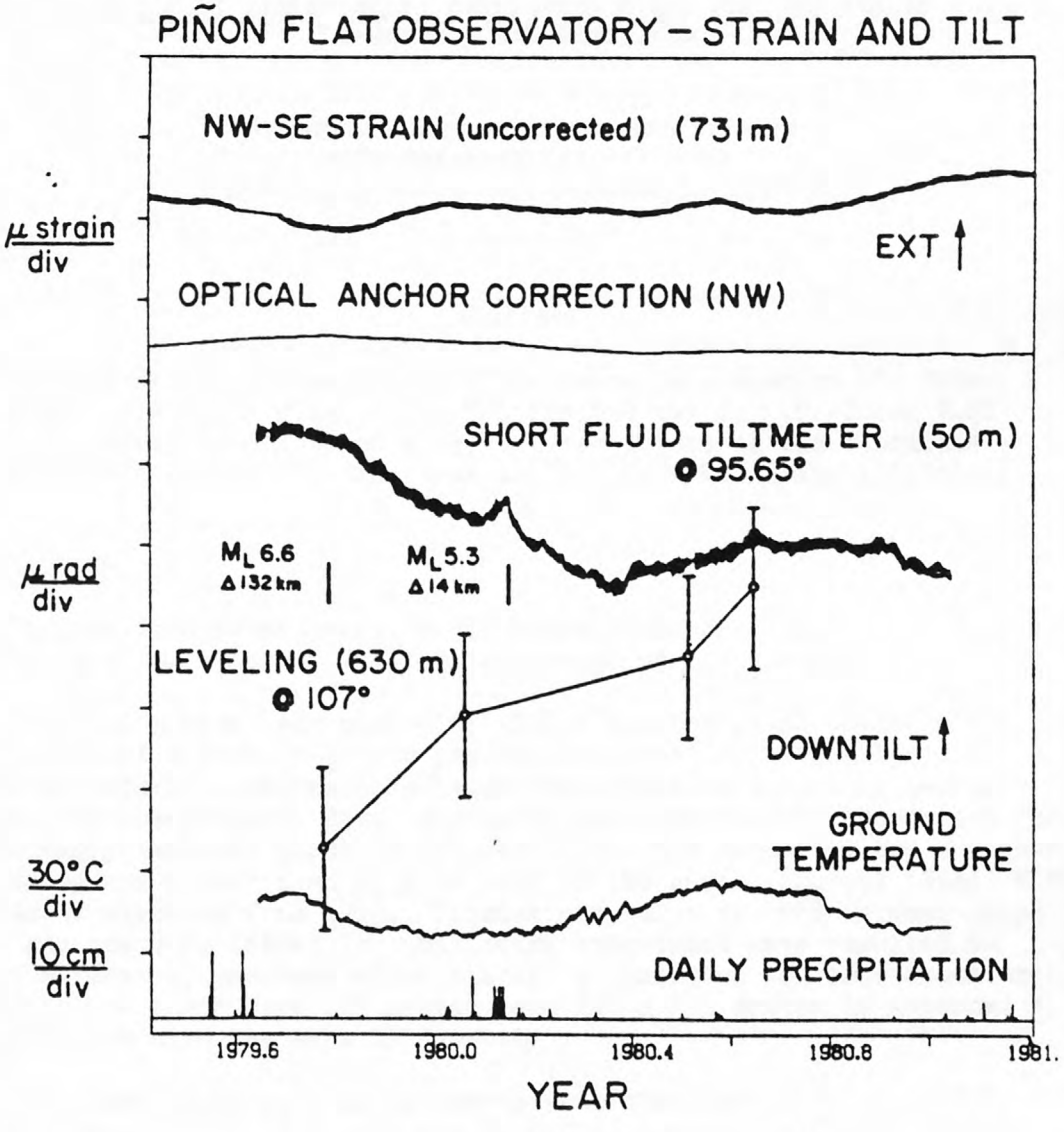

Fig. 1. More than one year of observations from four different types of instruments at Piñon Flat Observatory. The NW-SE strain record is from one of the three 732 m laser strainmeters at the site. The optical anchor record is a measure of the NW-SE displacement of a surface monument, here divided by the associated strainmeter length to form half of the NW-SE strain correction. The short fluid tiltmeter record is from a 50 m long tiltmeter. The leveling record was calculated from leveling data by Arthur Sylvester of the University of California, Santa Barbara. Also shown are the ground temperature at 0.5 m depth and the daily precipitation.

K-3 VLBI SYSTEM BEING DEVELOPED IN RRL FOR THE USE IN US-JAPAN JOINT EXPERIMENT

Yoshikazu Saburi and Nobuhiro Kawajiri
Radio Research Laboratories
Ministry of Posts and Telecommunications

Abstract

Outline of K-3 system which is now being developed on the five-year (1979-1983) plan in the RRL for the use in U.S.-Japan VLBI experiment, is described from the view points of its functions/-characteristics, some features and K-3-Mark III compatibilities.

Introduction

For the last seven years, Radio Research Laboratories (RRL) has been developing a few kinds of VLBI systems, such as K-1 and K-2.[1]

In 1979, a five-year plan (1979-1983) for the development of a high-precision VLBI system (K-3) for geodesy was started. Overall system design is underway, emphasizing bandwidth synthesis and using hydrogen masers, high-performance data recorders, and water vapor radiometers for functionally improved geodetic accuracy. All the apparatus and equipment yielded by the 5-year plan will be used in the Japan (RRL)-US (NASA) VLBI experiment starting from 1983. Discussions begun in 1978 between Japan (RRL) and the U.S. (NASA) for this joint experiment have resulted in mutual agreement, and both sides started preparation for that experiment. NASA will use their Mark III system, and RRL's K-3 system is intended to be compatible with the Mark III system.

The joint experiment is to demonstrate the capability to perform geodetic measurement of global scale, and to investigate polar motion, earth rotation, and so forth.

In building up the K-3 system, consideration is also being given to develop future compact, portable, yet highly accurate VLBI systems, which will be achieved by incorporating future technical development in Japan. In addition to the hardware, this system also includes software for deriving physical quantities such as baseline vectors, polar motion, and the earth's rotation from the measured delay times and fringe rate. Table 1 shows the long-term plan for development of the K-3 system between 1979-1983. Using this system, measurements will attain an accuracy of 0.1 ns (which means several cm in determining the baseline vector) for the time differences of incoming radio waves to the respective antennas.

K-3 System Features

We are now developing K-3 system of the Mark III-compatible and of the same order of accuracy. Table 2 shows the main functions and characteristics of our K-3 system.

Principal features of hardware and software in K-3 system during the current 5-year plan are described briefly below.

Hardware

Usage of IEEE 488 buses to connect each VLBI module with the computer will make troubleshooting easy for optimum apparatus maintenance and serviceability.

Besides the feature mentioned above, the following five items will be considered during system design and construction:

1) For the overall system, simplicity, compactness, and identical equipment for each station.

2) For parts of the system which do not affect system performance, methods used in Mark III will be used as far as possible consistent with making our system easily compatible with the Mark III.

3) The precision of delay time measurement will be 1.0 ns for the S band, and 0.1 ns for the X band. In the near future, we aim to establish measurement accurate within one cm.

4) Maximum design standardization for all the system apparatus and equipment.

Software

At the time of developing our K-3 software, the following points have been emphasized.

1) Architectonic works for data base, including observation schedule and log, processed data, and parameter-estimation data.

2) As to the data acquisition software, including scheduling and logging, which are written in SNAP (Standard Notation for Astronomy Procedure) language in Mark III, some parts of the software in K-3 must be coincident with those in Mark III.

Compatibility with the Mark III System

For the compatibility the data recording format used in Japan (Kashima) and the U.S. must be compatible firstly, because the magnetic tapes with data recorded on them will be exchanged and processed

separately. Moreover, items which must be compatible include the receiving frequencies, polarizations, bandwidths, channels, and recording densities. For all of these items, the devices used for data reproduction and reduction and the way they are used must also be compatible. Therefore, compatibility with the Mark III must extend throughout the system, from antennas/feeding systems to correlation processors. Not only these but the fundamental constants used in the data analysis must also be mutually coincident to avoid discrepancies in the results.

Table 3 shows the items in the K-3 system, which must be considered for compatibility with the Mark III one.

Concluding Remarks

Considering the international observation projects relevant to VLBI technique, such as MERIT (Monitoring of the Earth Rotation and Intercomparison of the Techniques) in 1983/84 and DELP (Dynamics and Evolution of the Lithosphere Plan) from 1980 through 1989, we would like to start the U.S.-Japan joint VLBI experiment in 1983 and continue it for a considerably long term.

Fortunately, at the time of the first SSLG (Standing Senior Liaison Group) meeting held in Tokyo on November 20, 1980, both NASA and RRL desired the continuation of the joint VLBI experiment; for example, for five years beginning in late 1984. We will start the U.S.-Japan VLBI experiment in 1983 and develop our K-3 Mark III-compatible system even further.

For the domestic VLBI observations, RRL has made two kinds of observations by the use of K-1 and K-2 systems.[1] However, these systems were not for the purpose of geodetic application. In the near future, RRL will make a domestic observation as well as an intercontinental one with the use of K-3 system, which will be able to determine the three-dimensional baseline vector geodetically.

RRL is technically supporting the Geographical Survey Institute in Japan to build their VLBI system with an antenna equivalent to the K-3 one, and that system will play an important role as a counterpart of the 26 m antenna at Kashima for geodetic measurement for the next several years.

The authors would like to express their sincere thanks to the staff members of the VLBI system developing group at RRL.

Reference

[1]N. Kawajiri, "Introduction of the VLBI systems developed in the Radio Research Laboratories", IEEE Denshi Tokyo No. 19, pp. 15-19, 1980.

Table 1 Long-term plan for the development of K-3 system between 1979-1983

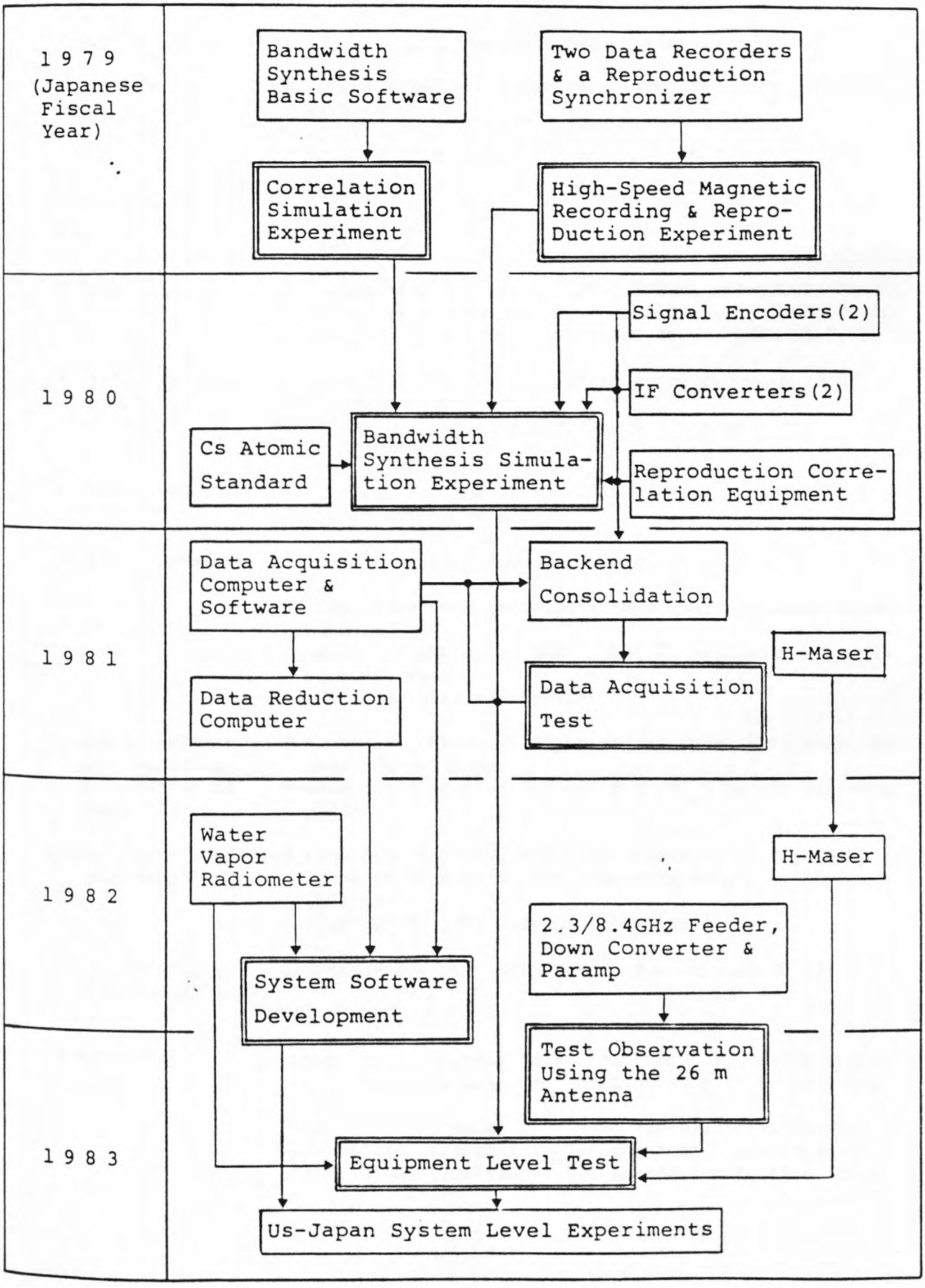

Table 2 Functions and Characteristics of K-3 system

subsystem	function/characteristics
* Antenna	@ 26m in diameter, Cassegrain type with horn reflector; altazimuth @ gain:52.8dB(2.26GHz), 63.2dB(8.3GHz) @ antenna noise temperature: 70K(2.2GHz), 60K(8.3GHz)
* Feeding system	@ frequency:2.22-2.32GHz, 8.18-8.60GHz,band splitting filter @ VSWR: 1.25
* Preamplifier	@ S wide band:frequency 2.20-2.32GHz; gain 30dB; Tr 40K @ X wide band:frequency 8.18-8.60GHz; gain 30dB; Tr 80K @ X narrow band:frequency 8.18-8.28GHz; gain 50dB; Tr 200K
* Frequency down-converter	@ S band LO:frequency 2020MHz, using PLO with 10MHz standard signal @ X band LO:frequency 8080MHz, 4 times as large as S band LO frequency
* IF distributor	@ IF frequency:low IF 100-224MHz, high IF 216-500MHz @ number of channels:28
* Video convertor	@ video frequency down-convertor: IRM(=Image Rejection Mixer) @ video frequency bandwidth: 4MHz,2MHz,1MHz,500kHz,250kHz 125kHz @ number of channels: USB 7, LSB 7, available up to 14 channels each @ LO: 10kHz step synthesizer
* Signal encoder for recording (=Formatter in Mark III)	@ number of channels: 28; sampling speed 8MHz,4MHz,2MHz 1MHz,500kHz,250kHz @ data output nominal rate:4.5 Mbps(1 parity bit/byte added)
* Wide band magnetic recording	@ recording in NRZM; total 28 tracks, simultaneously 7 track recording(two both-way recording), 4.5Mbps/track (135ips) @ reproducing: the same as recording
* Synchronously-reproducing apparatus	@ synchronous precision: about 5μs within 30 sec
* Correlator	@ number of channels: sine component 28, cosine component 28, in a unit, and available up to 6 unit channels @ correlator module: byte unit correlation with dual structure, fringe rotation and fringe accelerator in time domain;fractional bit correction in time domain

Table 2 continued

subsystem	function/characteristics
* Decoder	@ 1 Mbits buffer memory for real time monitor of data quality
* Computer for data acquisition/device control	@ HP 1000 10L; communication/control between this computer and each subsystem with use of IEEE 488 buses @ peripherals: display, floppy disc(x2)
* Computer for data reduction/analysis	@ HP 1000 45F @ 1024 kB memory, real time multi-task, graphic plotting, printer plotter, data base utility routine, high speed calculation @ peripherals: card reader, FDD(x2), 120 Mbytes disc(x2), card puncher, plotter(x2), terminal display(x4)
* Hydrogen masers	@ frequency stability: less than 2.8×10^{-14} (T=18000sec), less than 1×10^{-14} (T= 600 sec)
* Phase-delay calibrator	@ pulse signal: 1 pulse/μs, pulse width less than 50 ps @ cable delay measurement: $\pm$0.5 ps(one way), short term stability $\pm$5 ps, long term stability $\pm$10 ps/hour
* Water Vapor Radiometer	@ two observation frequencies: 20.3GHz, 31.4GHz @ precision: less than 2 cm in excess path at above 10 degrees in elevation
* Total phase stability	@ $\pm$several degrees/several min.(for all channels)
* Total delay time error	@ $\pm$0.1 ns(for 5 hours)

Table 3 The items in the K-3 which must be considered for the compatibility with the Mark III

subsystem	items
* Feeding system & Front end	1) Coincidence of receiving frequency 2) Coincidence of polarization 3) Phase noise less than several degrees 4) Frequency band-width more than 400 MHz 5) Automatic remote control and communication by the computer for data acquisition/device control
* IF distributor & Video converter	1) Use of IRM(=Image Rejection Mixer) 2) Use of 10 KHz step synthesizer 3) Phase noise less than several degrees 4) Coincidence of receiving channels 5) Automatic remote control and communication by the computer for data acquisition/device control
* Signal encoder for recording (=Formatter in Mark III)	1) Coincidence of output data format 2) Coincidence of scheduling/logging format 3) Coincidence of sampling speed 4) Automatic remote control and communication by the computer for data acquisition/device control
* Wideband magnetic recording & synchronized-reproducing apparatus	1) Coincidence of magnetic recording density, speed and format 2) Coincidence of CRC test pattern 3) Coincidence of Number of simultaneously recording channels 4) Automatic remote control by the computers
* Reproducing and correlating apparatus	1) Detection of the signal of phase-delay calibrator 2) Coincidence of No. of reduced-data-channels 3) Reduction of schedules and logs
* Hydrogen maser	No items
* Water vapor radiometer	1) Coincidence of output data format 2) Availability of program tracking 3) Automatic remote control and communication by the computer for data acquisition/device control
* Phase-delay calibrator	1) Coincidence of calibration-method with the use of pulsed signal 2) Coincidence of output data format 3) Automatic remote control and communication by the computer for data acquisition/device control
* Computer for data acquisition/device control	1) Data communication and control between this computer and each subsystem 2) Coincidence of scheduling and logging format
* Computer for data reduction/analysis	1) Number of reduced data channels

Table 3 continued

subsystem	items
* Softwares for data acquisition/device control	1) Coincidence of scheduling and logging format 2) Coincidence of data acquisition and system control
* Softwares for data reduction/analysis	1) Coincidence of fundamental constants

QUASARS AND SATELLITES FOR INVESTIGATING CRUSTAL DEFORMATION

Peter F. MacDoran
Jet Propulsion Laboratory
California Institute of Technology
Pasadena, Calif. 91109, U.S.A.

Quasar Referenced Measurement

Project AIRES (Astronomical Radio Interferometic Earth Surveying) is demonstrating the feasibility of three-dimensional Earth position determination with subdecimeter accuracy over baselines of 100 to 1,000 km. The technique employed - very long baseline interferometry (VLBI) - relies on quasars as a virtually time-invariant frame of reference. Fixed stations used as bases are Caltech's Owens Valley Radio Observatory and the Deep Space Network at Goldstone. The unique elements supplied by ARIES are transportable 4 m and 9 m diameter antennas (Fig. 1).

The sites making up the current ARIES network are mostly located in southern California. The JPL (Pasadena)-Goldstone-Owens Valley baselines form a large triangle that overlies parts of the San Andreas, Garlock, Sierra Nevada, and San Gabriel fault systems. These baselines have been measured over a longer time-period than any other location.

Measurement of the 171 km JPL-Goldstone baseline was begun in 1974. Prior to mid-1979, the measurement record was essentially stable, indicating no significant motion. The next longest measurement record involves the 336 km JPL-Owens Valley baseline, which crosses both the San Andreas and Garlock faults, and passes through the eastern edges of the Tehachapi and Palmdale networks of the U.S. Geological Survey (USGS) (see Fig. 2). Starting in 1976, and up through January 1979, the history of this baseline was also essentially stable. The USGS measurements in the north-south direction indicated that a gradual compression was taking place.

In August 1979, a meeting was held at the Caltech Seismological Laboratory to discuss the radon gas anomaly that was occurring about 5 km from JPL in the San Rafael hills. For the previous two years, the gas output has been normal; but in the summer of 1979, the output rate had suddenly tripled. The most recent ARIES data, a January 1979 measurement of the Owens Valley baseline, showed no significant change from the preceding measurements.

On August 29, 1979, one week after the meeting, ARIES began a series of measurements that eventually spanned the next eleven months. The addition of the August measurement to previous data showed the JPL-Owens Valley baseline undergoing a marginally significant contraction similar in magnitude to the measurements of the U.S. Geological Survey in the same north-south direction: about two-tenths part per million, or about 7 cm per year. Eleven weeks later, however, ARIES recorded a change to extension of 25 cm which was subsequently followed by a complete recovery over the next seven months.

While ARIES team members continued to analyze and recheck the data, these first results were conveyed to the U.S. Geological Survey. The USGS proceeded with resurveys of its Palmdale and Tehachapi networks. USGS reported the occurrence of the largest strain episode ever recorded in the ten-year history of these networks.

Regardless of the USGS results, the ARIES team continued to review these data because of the possibility of an anomaly within the ARIES system. The analysts cautioned that since the quasar radio signals had been recorded at night as well as during the day, the 25 cm extension might have been caused by large variations between daytime ionospheres. To eliminate the effects of the highly variable daytime ionospheres, the nighttime data were processed separately. The results were slightly different in character but continued to exhibit an obviously large-magnitude extension and subsequent compression of the baseline. Measurements have continued at approximately three-month intervals since mid-1980; however, baseline data reduction and analysis are not yet complete.

An operational version of ARIES, called ORION, has been developed which is being procured through commercial industrial sources with the first unit due in January 1983.

Satellite Referenced Measurement

Another approach to the challenge of frequent high-accuracy geodesy at low cost on smaller spatial scales of 2 to 200 km is to use satellites as radio signal sources instead of quasars because satellites can have signal strengths 10^6 stronger than quasars. The satellites of the Global Positioning System (GPS) offer an important new geodetic resource making possible a highly accurate portable radio geodetic system. A concept called SERIES (Satellite Emission Range Inferred Earth Surveying) makes use of GPS radio transmissions without any satellite modifications. By employing the conceptual method of very long baseline interferometry (VLBI) and its calibration techniques, 0.5 to 3 cm three-dimensional baseline accuracy can be achieved over distances of 2 to 200 km, respectively, with only a few minutes of onsite data acquisition. The use of quasar referenced ARIES Mobile VLBI (Ref. 1 and 2) to establish a sparse fundamental control grid will provide a basis for making SERIES GPS measurements traceable to the time-invariant quasar directions.

In the original SERIES implementation (Ref. 3), the GPS was to serve as an incoherent noiselike illuminator of an earth-based interferometer. As is the case with all radio tracking systems, the ionosphere represented an error source which required specific calibration, either by modelling or by direct measurement. SERIES was originally designed to acquire identical data at the two transmitted bands L_1 and L_2, detect signals by cross-correlating noiselike illumination from two stations at each band, forming delays from each band, and then differencing the L_1 and L_2 delays to extract the differential ionospheric delay in each interferometer path. A challenge noted in that design concerned the ability to simultaneously estimate ionospheric effects and baseline

errors using the largest spanned bandwith possible (348 MHz) in order to achieve the required delay precision ($<10^{-10}$ sec) although ambiguous at 86 cm intervals.

In order to address this parameter separability challenge, a property of the GPS signal structure was recognized which allowed a direct measurement of the ionosphere without recourse to interferometric signal detection. That GPS structure was that the identical wideband modulation (P-code) is coherently transmitted on the L_1 and L_2 channels but because of the ionospheric delay dispersion, the L_1 signal arrives first. By cross-correlating the L_1 signal, variability delayed, with the L_2 signal, a maximum results when the delay of the L_2 signal has been matched by the intentional delay on the L_1 signal path. Additionally, a Doppler data type results because of the fact that a delayed L_1 is not an exact replica of the L_2 signal because L_1 comes in and out of phase every 86 cm of path change between the satellite and ground receiver. That effective 86 cm wavelength is the consequence of L_1 being 347.82 MHz higher in frequency than the L_2 channel. This ionospheric measurement technique is called Satellite L-band Ionospheric Calibration (SLIC). SLIC ionospheric delays and Doppler observations were performed in early December 1980.

Techniques have now been developed to synthesize epoch timing marks from the satellite signals with 10^{-10} sec precision using standard components and devices. This evolution in SERIES development has motivated the acronym modification away from the RI portion meaning of radio interferometric to its present meaning of range inferred. (See Fig. 3.)

Recently, the SERIES activities have been directed toward the detailed design and fabrication of a pair of proof-of-concept stations. The SERIES stations are equipped with lightweight, 1.5 m diameter dish antennas mounted on trailers. These antennas were especially designed with dual L-band (1.2 and 1.6 GHz) reception capability which is required for ionospheric calibrations. The electronics and control functions are being housed in modified camper shells suitable for pickup truck transport which will also tow the antenna trailer. (See Fig. 3.) Gasoline electrical power generation is available for each station to enhance system mobility. A microcomputer is used in each SERIES station to convert GPS satellite ephemerides, to azimuth and elevation antenna pointing commands, accurate within one degree. The microcomputer also receives and records on computer tape or floppy disc digital data from the code sequence independent one-way ranging SERIES receiver.

Each station is being equipped with a moderate cost, commercially available rubidium frequency system. Two-station geodetic demonstrations on a 150 m baseline will begin in summer 1981. In the fall of 1981, baseline vector measurements will be demonstrated over a known 22 km baseline test area at the Goldstone Deep Space Communications Complex. In 1982, SERIES demonstrations will be conducted over a 258 km baseline between Goldstone and the Owens Valley Radio Observatory to compare with satellite laser ranging and VLBI baseline measurements using quasar sources.

Acknowledgements

The author acknowledges his many JPL colleagues involved for many years in the demonstration of the ARIES feasibility with special thanks to A. E. Niell, G. M. Resch, J. M. Davidson, T. E. Erickson, K. M. Ong, A. Y. Lam, T. G. Lockhart, D. D. Morabito, J. L. Vavrus, K. S. Wallace, H. F. Fliegel, D. J. Spitzmesser, L. J. Skjerve, R. B. Miller, L. Tanida, S. R. Paine, C. J. Steinberg, N. I. Yamane, M. G. Newsted, E. S. Claflin, B. B. Johnson, and D. W. Fite.

The author wishes to acknowledge the assistance of his JPL colleagues in the SERIES development, D. J. Spitzmesser for innovative R.F. designs, M. G. Newsted for electromechanical subsystems, and L. A. Buennagel for the microprocessor subsystem implementation. Special thanks is also due G. M. Resch and D. W. Curkendall for discussions on overall system design possibilities.

This paper has presented the results of one phase of research carried out at JPL, California Institute of Technology, under contract NAS 7-100, sponsored by the National Aeronautics and Space Administration, Office of Space and Terrestrial Applications.

References

1. MacDoran, P. F., 1974, Radio interferometry for international study of the earthquake mechanism: Acta Astronomica, no. 1, p. 1427-1444.

2. Niell, A. E., Ong, K. M., MacDoran, P. F., Resch, G. M., Fite, D. W., Skjerve, L. J., Spitzmesser, D. J., Morabito, D. D., Tanida, L., Claflin, E. S., Johnson, B. B., Newsted, M. G., Banisch, A., and Dracup, J. F., 1979, Comparison of a radio interferometric differential baseline measurement with conventional geodesy: Tectonophysics, v. 52, p. 49-58.

3. MacDoran, P. F., 1979, Satellite Emission Radio Interferometric Earth Surveying, SERIES-GPS Geodetic System: Bulletin Geodesique, v. 53, p. 117-138.

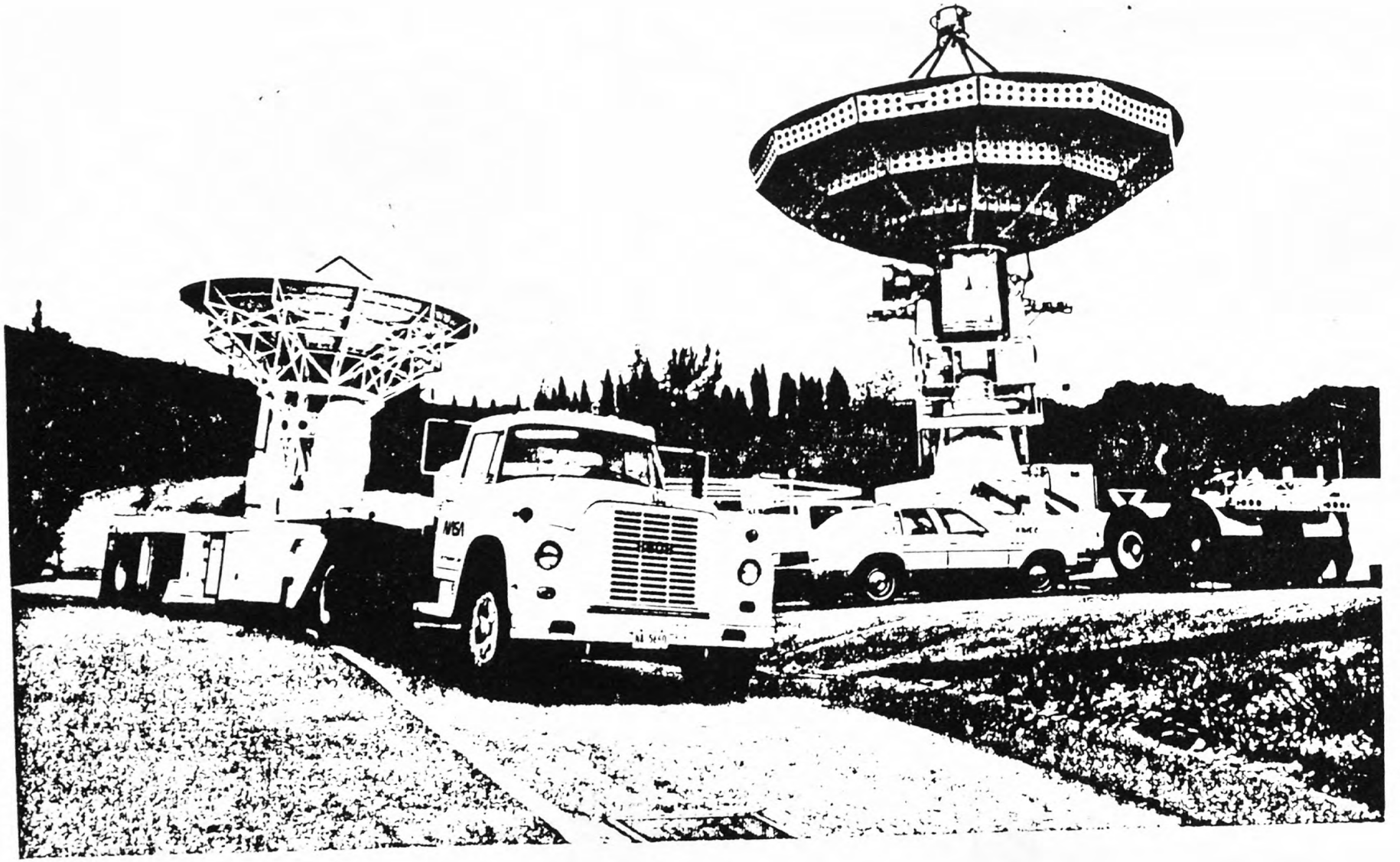

Figure 1

ARIES NETWORK
SOUTHERN CALIFORNIA

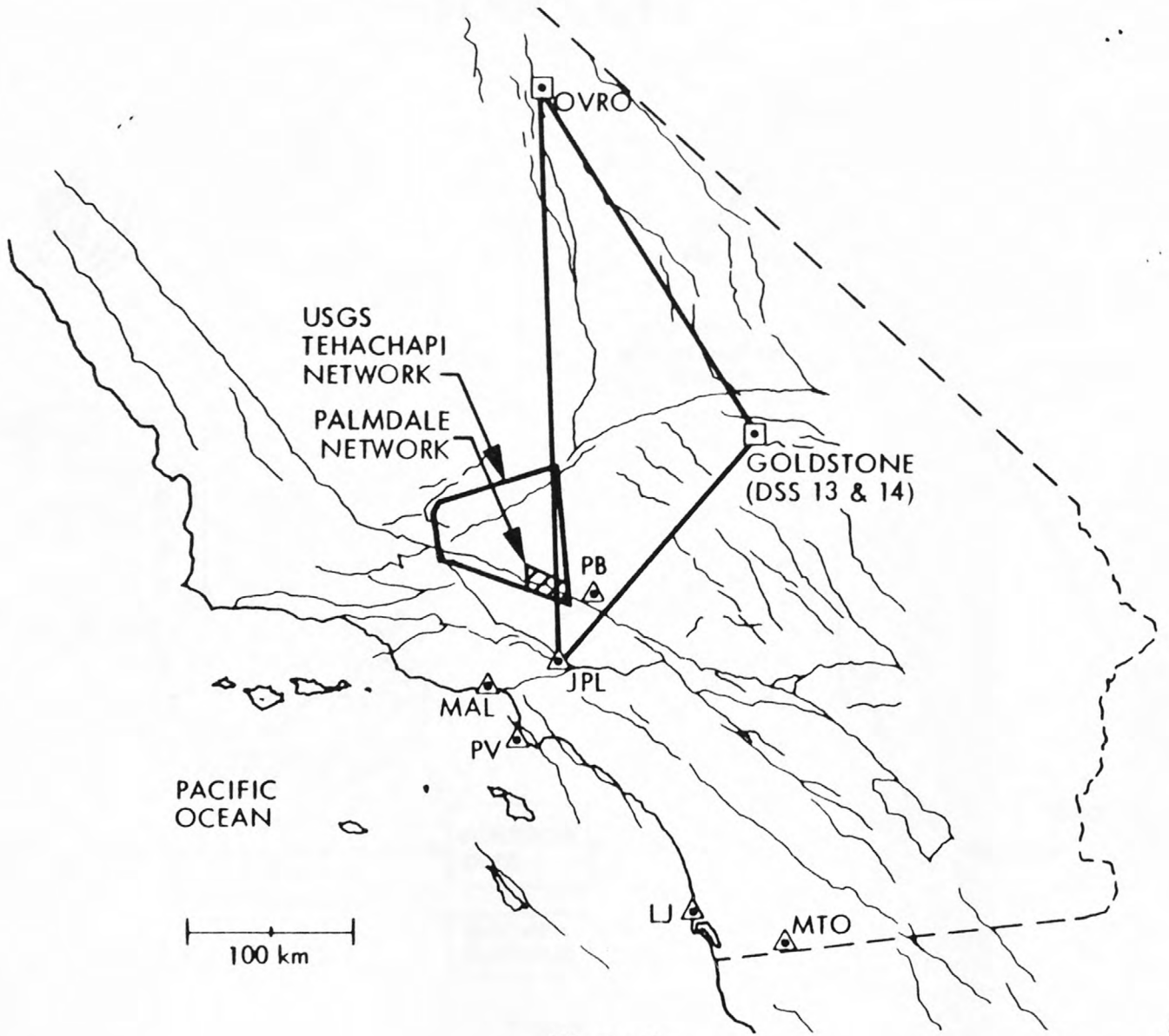

APRIL 1980

Figure 2

Satellite Emission Range Inferred Earth Surveying
SERIES-GPS

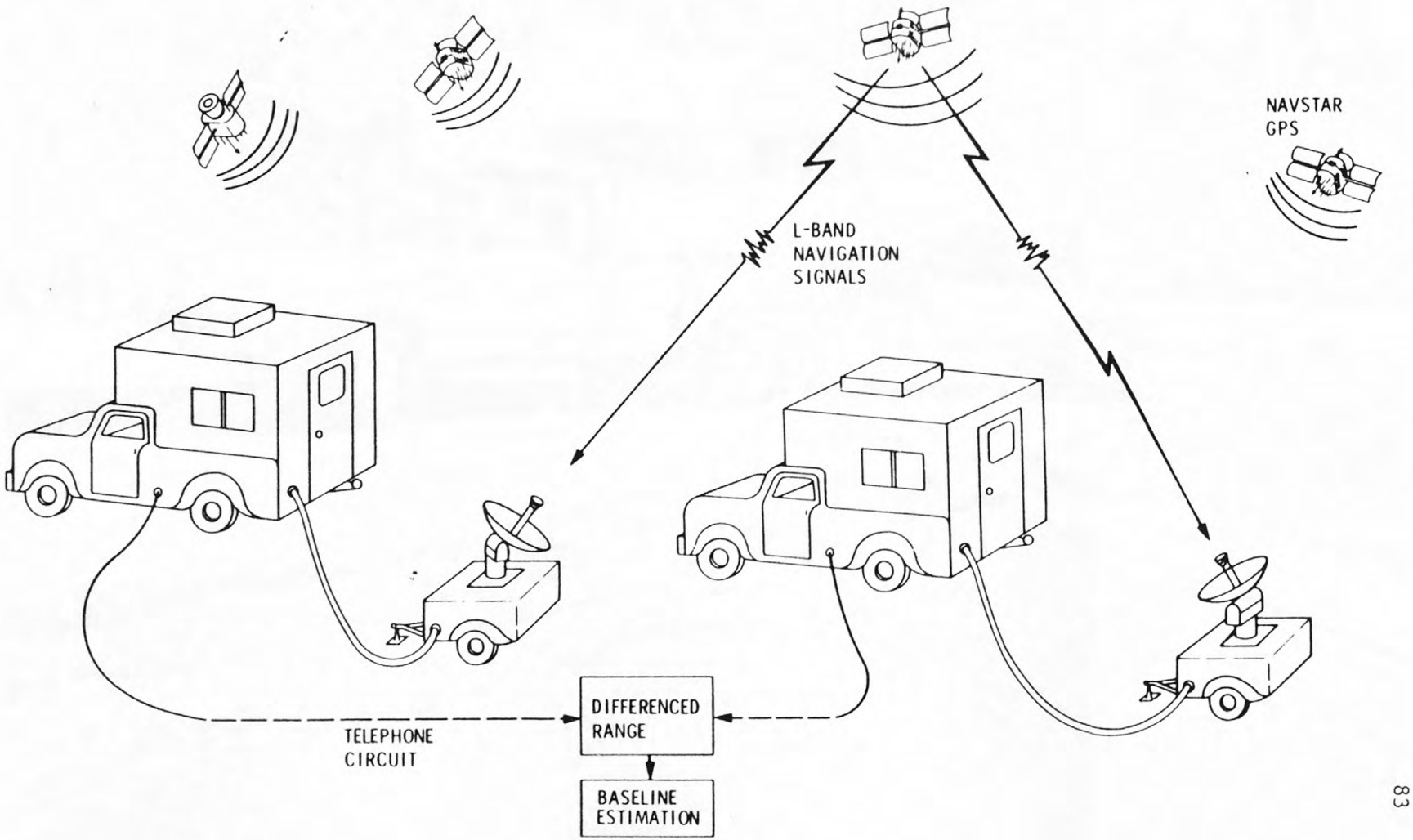

Figure 3

Figure 4

A PLATE MODEL CONSISTENT WITH THE TECTONICS OF THE KANTO-TOKAI AREA, JAPAN

K. Kasahara and K. Hamada
National Research Center for Disaster Prevention

Abstract

According to the earthquake prediction program, seismic observations in the capital area around Tokyo have been gradually and consistently intensified, including deep borehole observations. Such advanced observation provides a lot of useful information like accurate hypocentral locations and fault plane solutions for even small earthquakes. With the cooperation of research by previous investigators, these high quality seismic data enabled us to create a plate model for an area of triple junction of the Asian plate, the Philippine sea plate, and the Pacific plate, which is consistent with three-dimensional hypocentral distribution, the focal mechanism of earthquakes, and regional anomaly of seismic intensities.

The plate model is outlined as follows: The Philippine sea plate, which is moving northwestwards against the Asian plate, is divided into three parts around the Izu peninsula; that is, an east wing (I), a central part (II), and a west wing (III) (see Figure 9). The left-lateral, N-S strike- slip fault system (SL) represented by the Tan-na fault is dominant in the boundary zone between (I) and (II). The right-lateral, NWN-ESE strike- slip fault system (SR), represented by the Irozaki fault, is dominant in the boundary zone between (II) and (III). SL and SR are well developed in the Izu peninsula, which could be called a shear zone as a whole. The east wing (I) penetrates at the Sagami trough beneath the south Kanto, and the north end (A-B) reaches to northern Saitama prefecture and central Ibaraki prefecture. The east end (C-D) of the east wing (I) penetrates down to 50 to 80 km depth, makes contact with the Pacific plate, and is guided by it. The central part of the Philippine sea plate collides with the Asian plate beneath eastern Yamanashi prefecture. The west wing (III) of the Philippine sea plate penetrates at the Suruga trough and goes down northwestwards.

Seismic activity is particularly high in an area south of the north end of the Philippine sea plate (A-B) and west of the east end of it (C-D). The hypocenter in this area depicts the Philippine sea plate, which declines eastwards and northwards. Seismically active zones 60 to 90 km deep beneath southwestern Ibaraki prefecture and central Chiba prefecture, correspond to the east end (C-D) of the Philippine sea plate. Seismically active zones in eastern Yamanashi prefecture correspond to the north end of the central part (II) of the Philippine sea plate. There is a seismic plane which declines northwestwards at the Suruga trough, corresponding to the descending Philippine sea plate.

Local varieties of the focal mechanism solution in the area of triple junction of the plates under consideration are consistent in general with the present model.

It is known that abnormally strong intensities are observed in the Izu peninsula and Ohshima Island for earthquakes with 60 to 90 km depth beneath central Chiba prefecture. This phenomenon is well understood, considering the existence of the high-Q Philippine sea plate.

Based on the present model, earthquakes in the south Kanto, the capital area, are classified into four:

(1) Earthquakes 60 to 90 km deep, in central Chiba prefecture and the southwestern Ibaraki prefecture, occurring on the plate boundary between the Philippine sea plate and the Pacific plate.

(2) Earthquakes on the upper boundary between the Philippine sea plate and the Asian plate. The 1923 Kanto earthquake (M=7.9) was one of these, and the 1855 Ansei-Edo earthquake could also be newly interpreted as one of them.

(3) Earthquakes 60 to 80 km deep near the lower boundary between the Philippine sea plate and the Asian plate.

(4) Shallow earthquakes within the Asian plate associated with active faults such as the 1931 Nishi-Saitama earthquake.

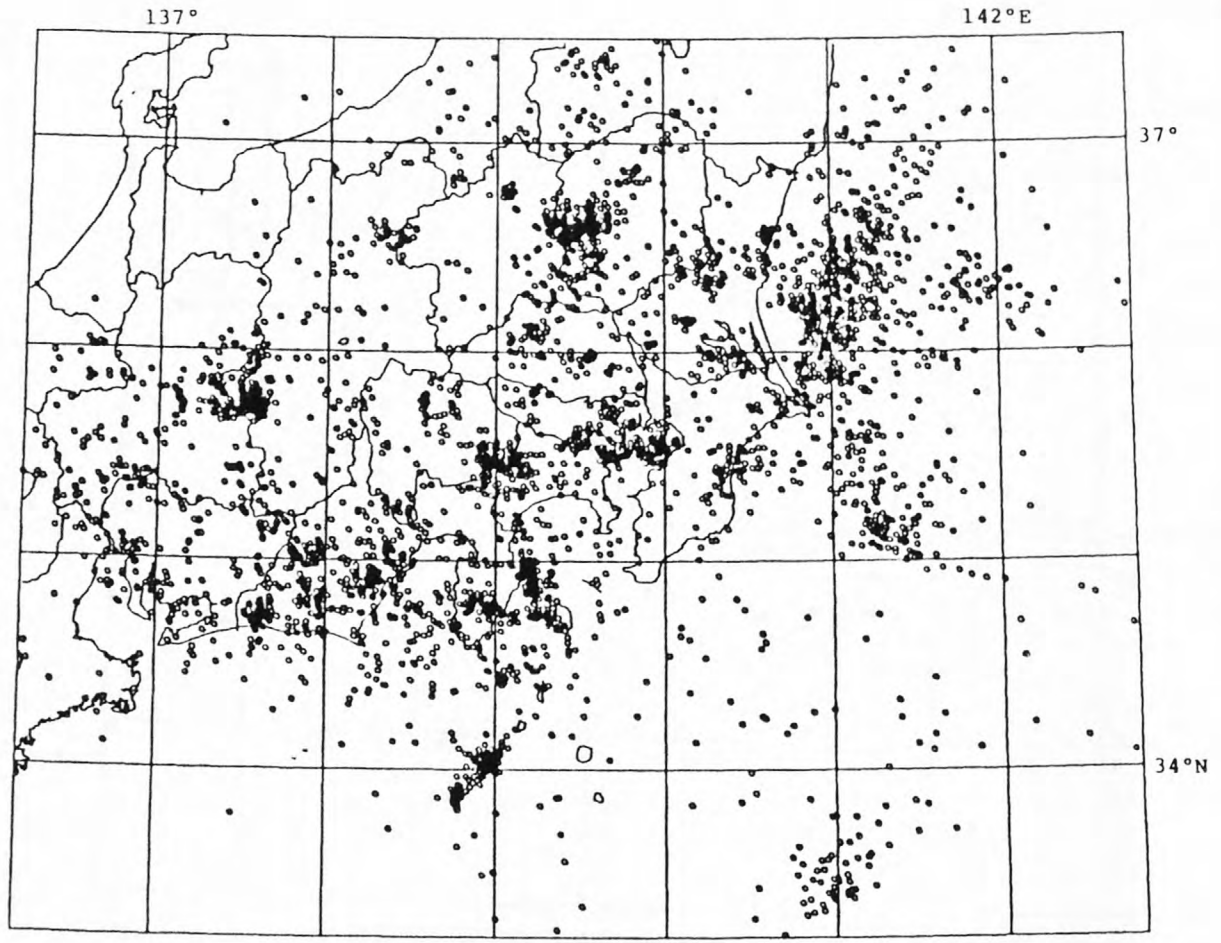

Fig. 1. Hypocentral distribution of microearthquakes in the period from May, 1978 to February, 1981. Depth range: 0-30 km.

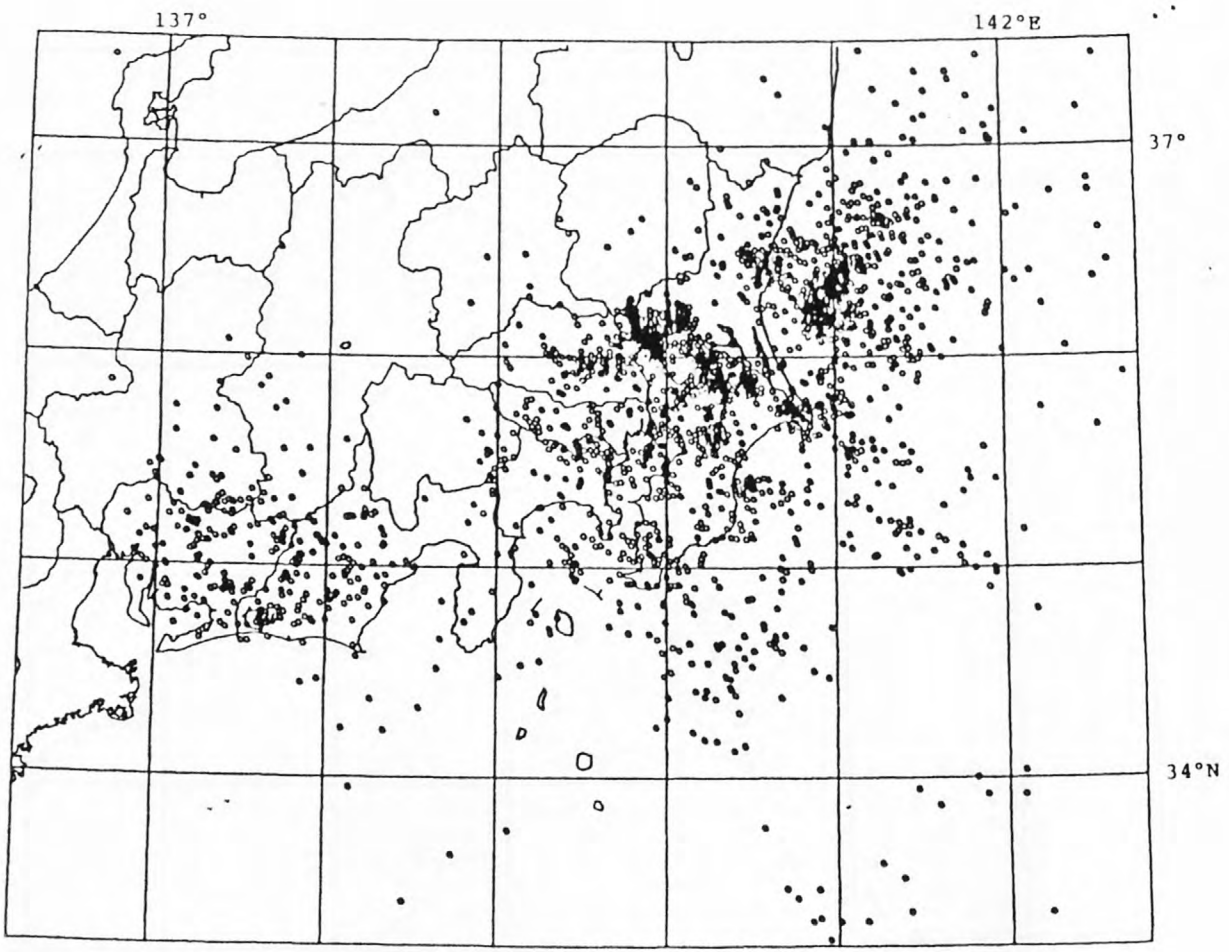

Fig. 2. Hypocentral distribution of microearthquakes in the same period as shown in Fig. 1. Depth range: 30-60 km.

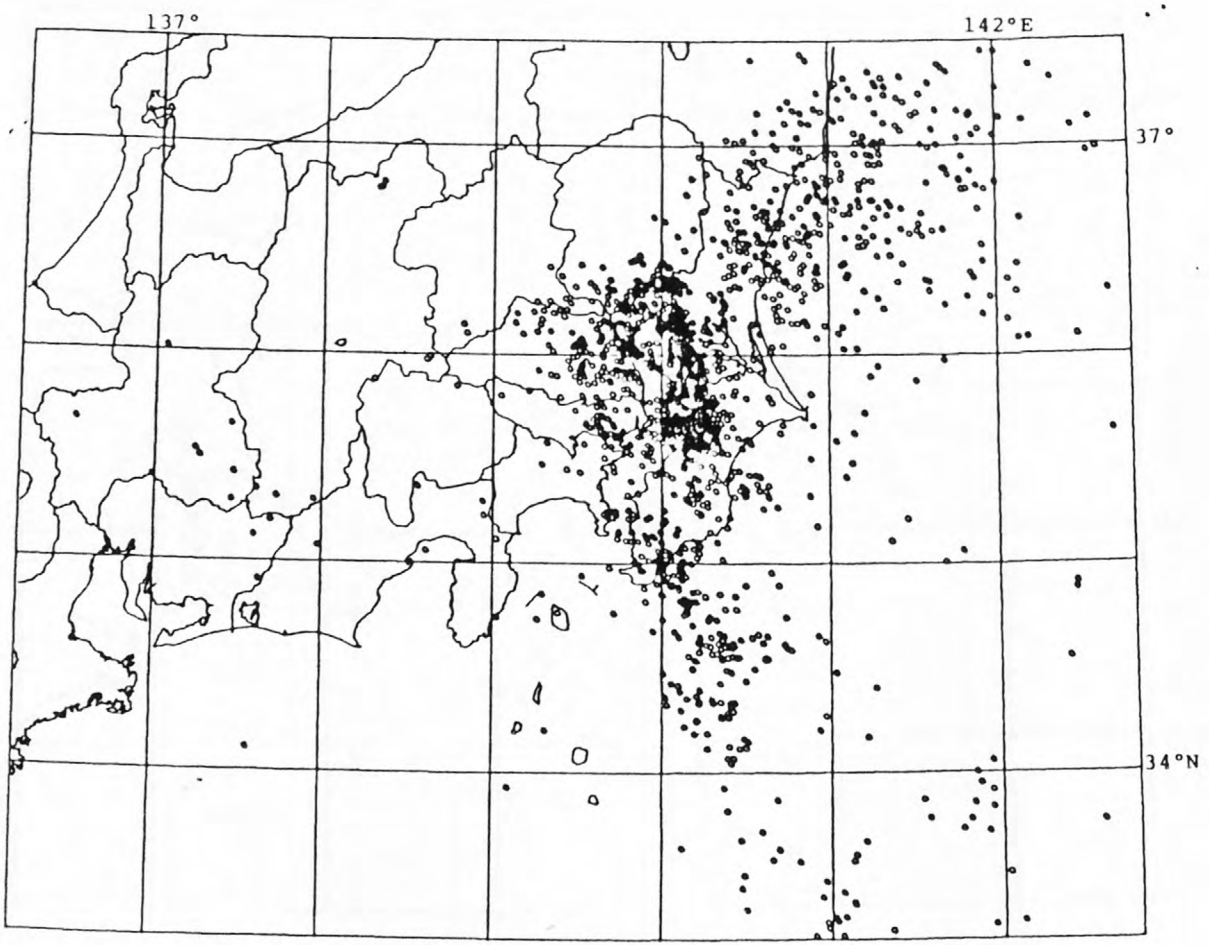

Fig. 3. Hypocentral distribution of microearthquakes in the same period as shown in Fig. 1. Depth range: 60-90 km.

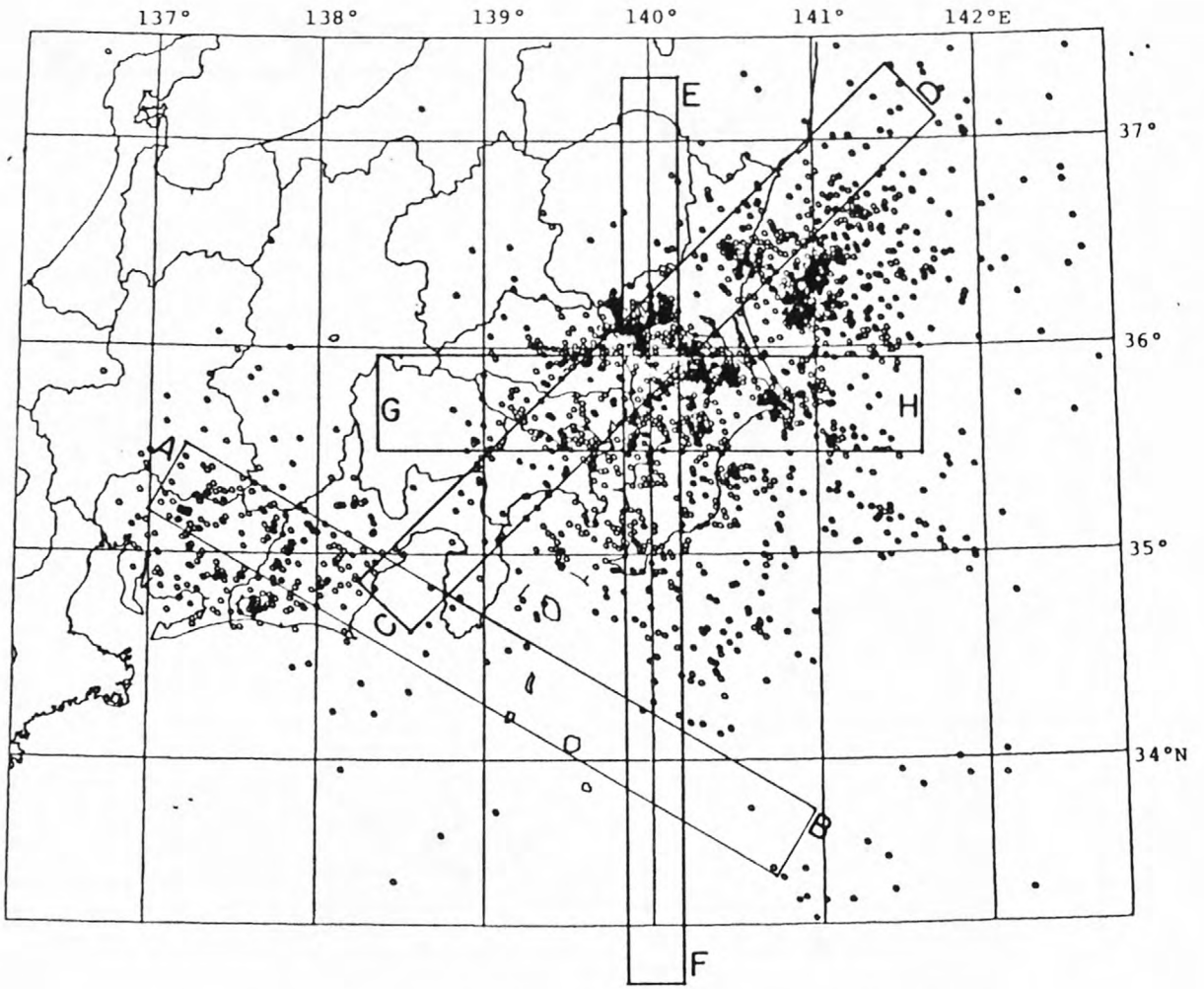

Fig. 4. The four rectangular regions for which vertical distributions of microearthquakes are illustrated in Figs. 5-8. The hypocenters shown in the figure are the same as in Fig. 2.

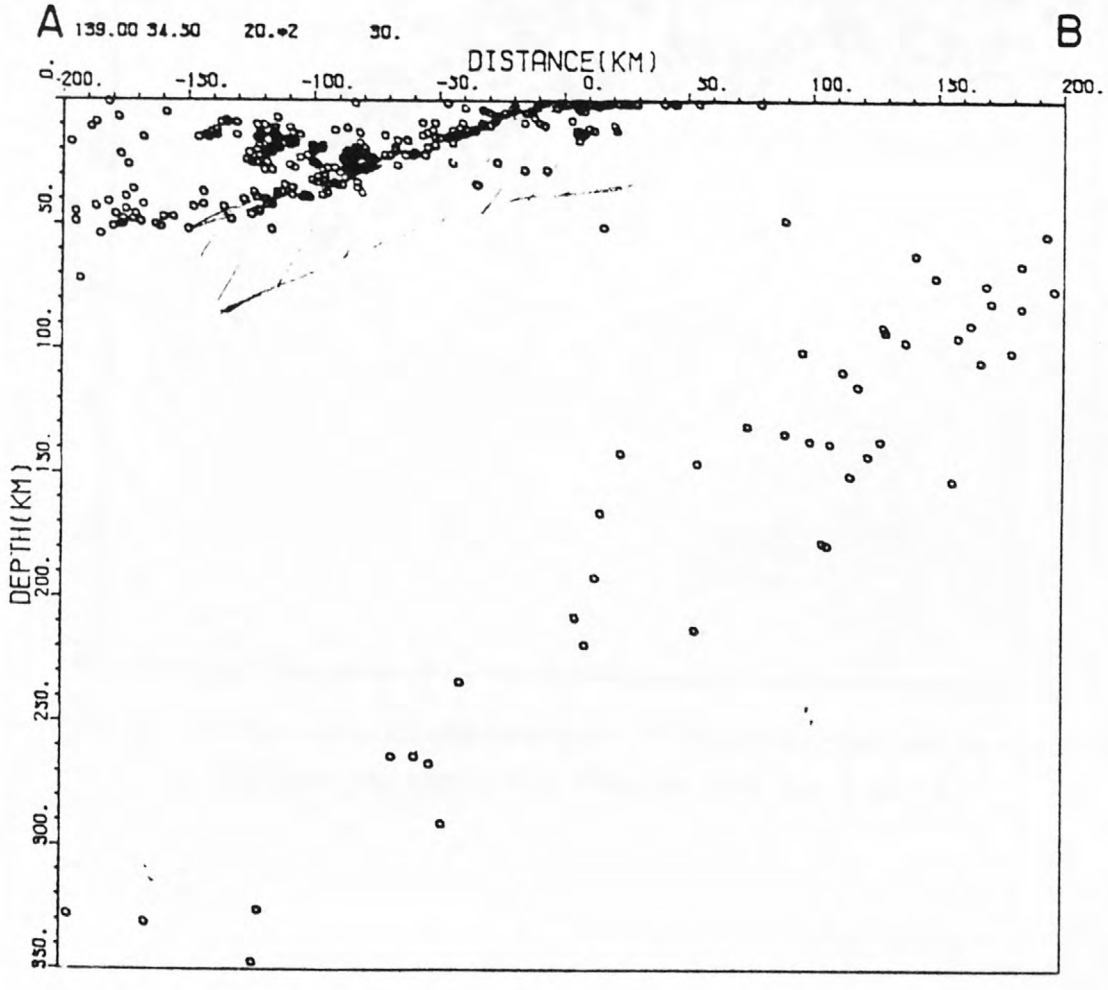

Fig. 5. Vertical distribution of microearthquakes located in the rectangular region A-B in Fig. 4.

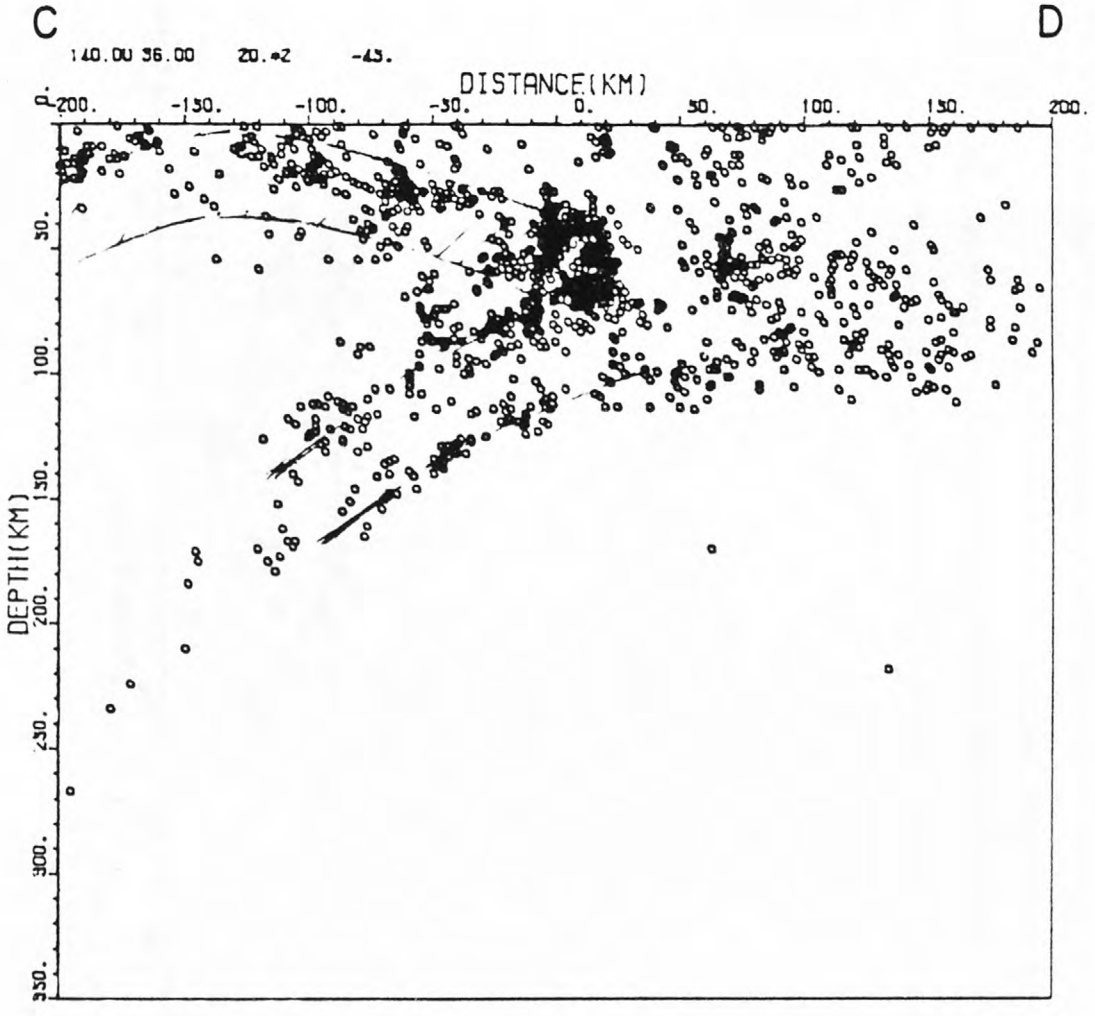

Fig. 6. Vertical distribution of microearthquakes located in the rectangular region C-D in Fig. 4.

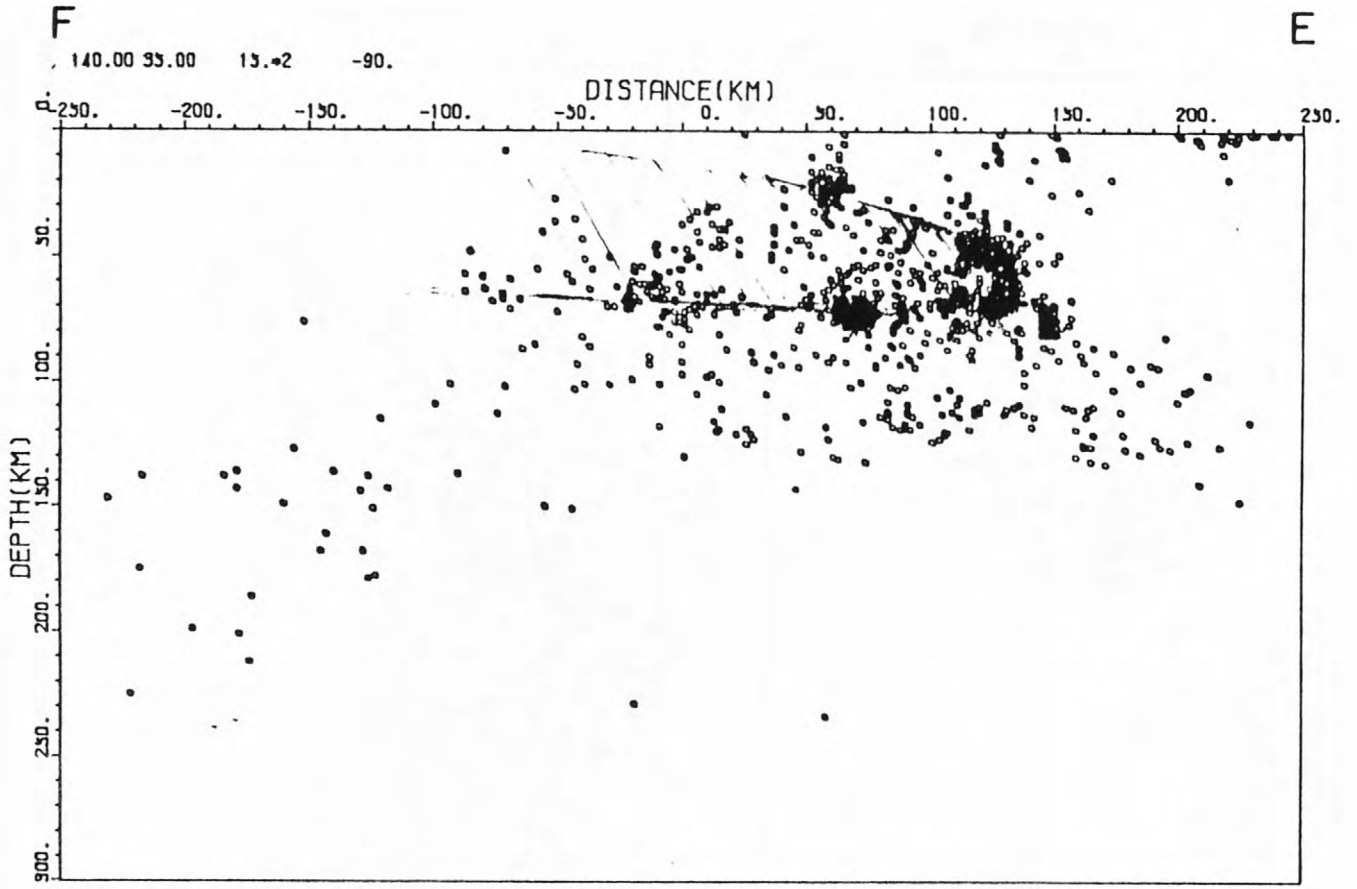

Fig. 7. Vertical distribution of microearthquakes located in the rectangular region E-F in Fig. 4.

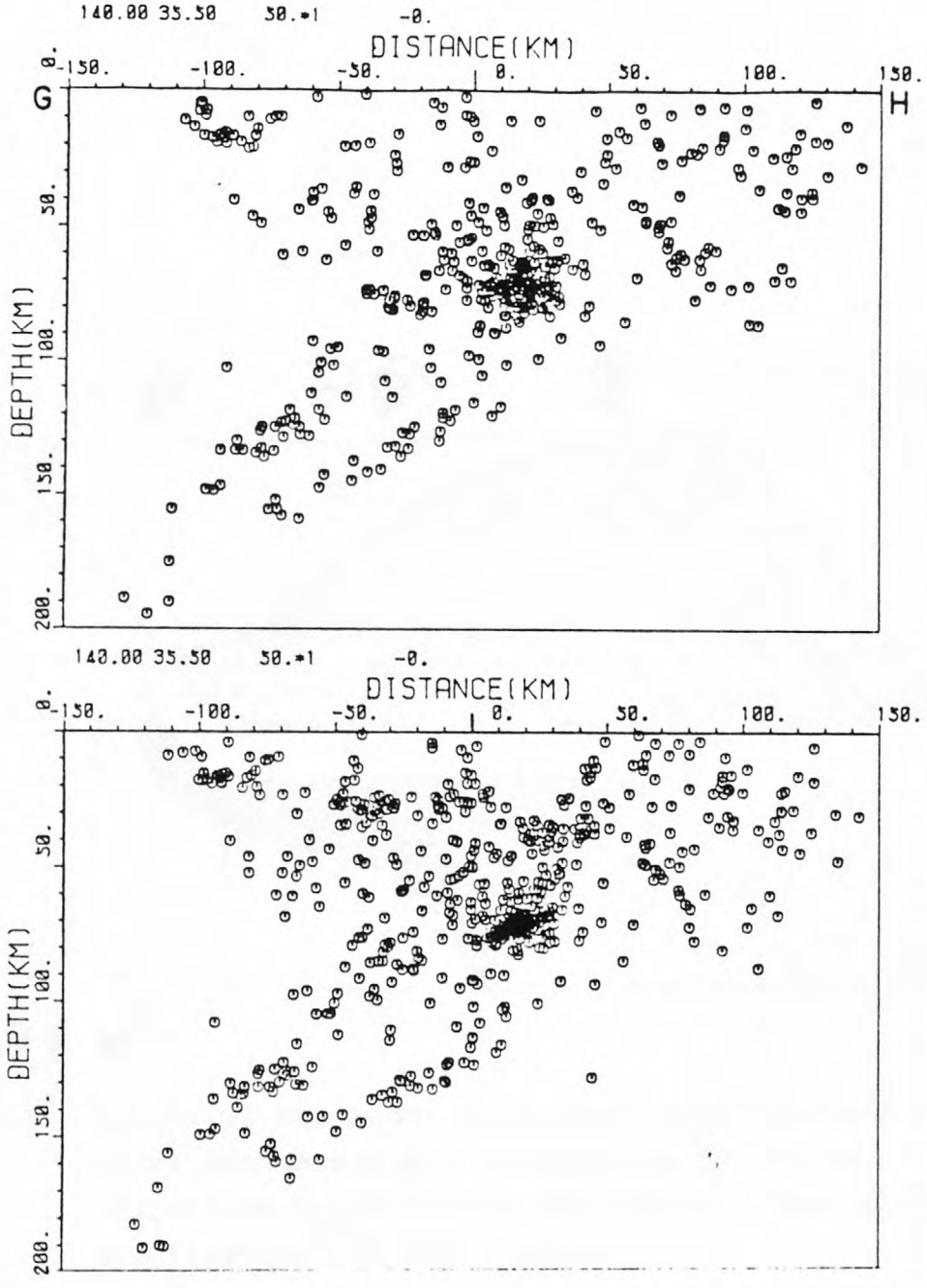

Fig. 8. Vertical distribution of microearthquakes located in the rectangular region G-H in Fig. 4. Hypocenters in the upper figure are particularly located, excluding the deep borehole measurements. Those in the lower figure are done, including the deep borehole measurements.

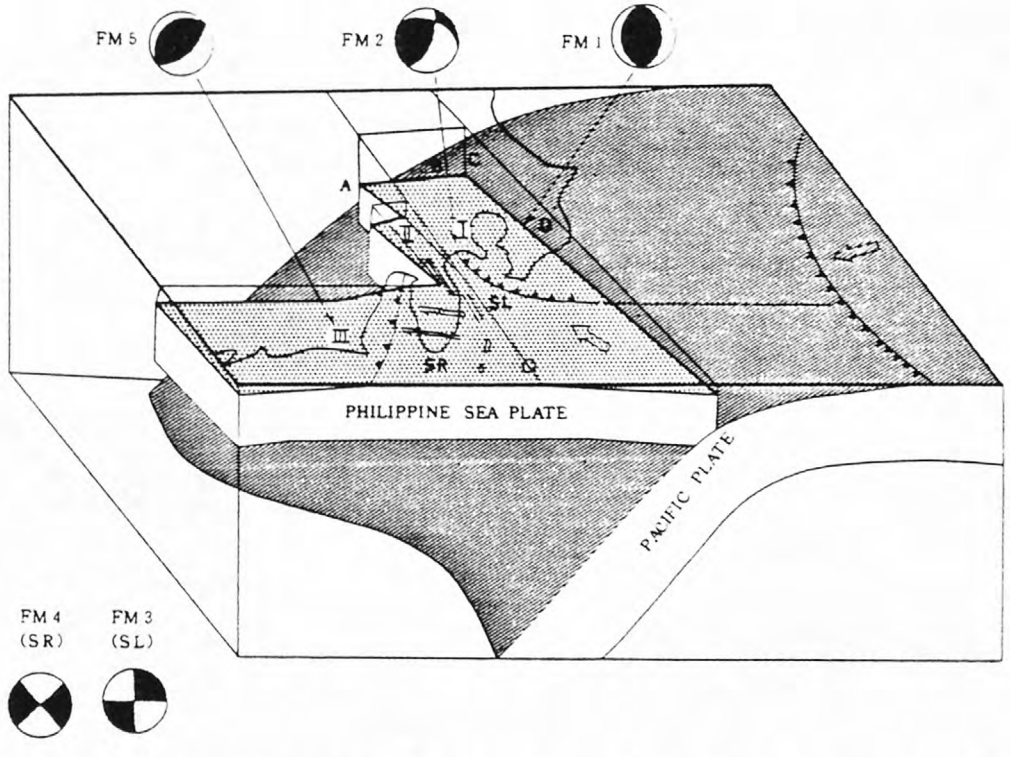

Fig. 9. Schema of the model consistent with the tectonics. Focal mechanisms are represented by the equal area projection on the lower hemisphere. Open areas are compressional at the source.

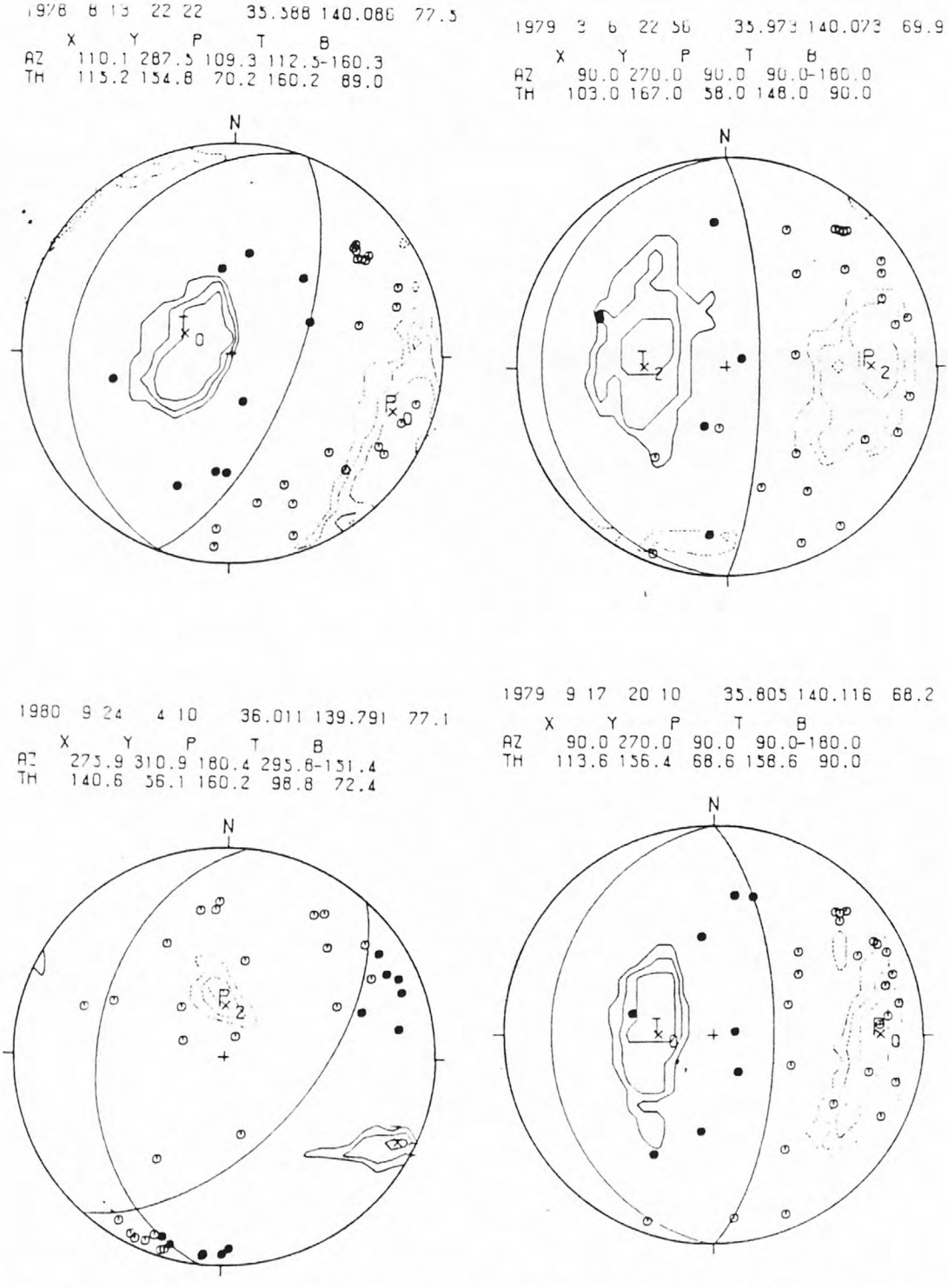

Fig. 10. Four examples of the focal mechanism of the earthquake with depths 60-90 km occurring at the location 140°E and 35.6°-36.0°N.

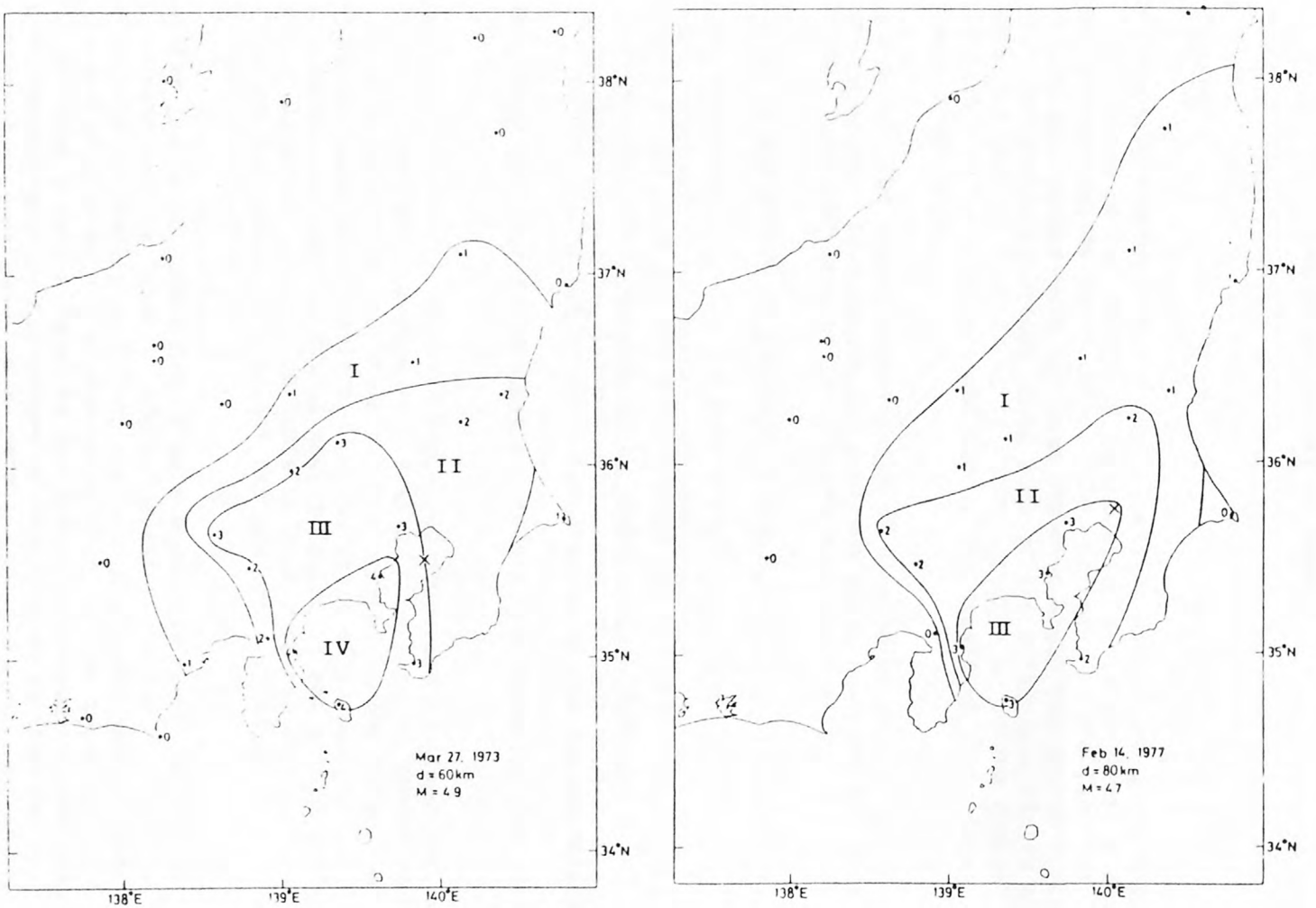

Fig. 11. Anomalous distribution of seismic intensities(Nakanishi and Horie, 1980).

ACTIVE FAULTS IN JAPAN: PRESENT STATE OF STUDIES AND PROBLEMS

Toshihiro Kakimi, Yoshihiro Kinugasa and Koji Ono
Geological Survey of Japan

1. Introduction

It is generally accepted that a geologically known offset along any active fault in Japan is the result of accumulation of intermittent and sudden slips accompanied by earthquakes. This is based on the fact that significant aseismic creeps have not been observed along the active faults except for postquake creeps along some of the earthquake faults as will be mentioned later. Therefore, in Japan, studies on active faults have been regarded to be important and useful for providing basic data for earthquake prediction.

In this paper, the recent achievements of studies on active faults in Japan are reported. Some topics and problems which have emerged after the time of the last UJNR meeting in 1979 are also dealt with.

II. Distribution and Degree of Activity of the Active Faults in Japan

In 1980, the Research Group for Active Faults in Japan (RGAFJ), which consists of about 40 researchers in geomorphology, geology, and geophysics affiliated with various universities and research institutes, published a book entitled Active Faults in Japan: Sheet Maps and Inventories in Japanese (RGAFJ, 1980a). This book consists mainly of sheet maps of active faults and detailed inventories of the mapped faults.

The following is a brief introduction of this book based on the RGAFJ (1980b):

The maps are drawn originally on the 1:200,000 scale for land faults and 1:200,000 or 1:500,000 for submarine faults. One hundred twenty-three sheets which cover the whole country are fully printed in the book. For submarine faults, seven sheets selected on the basis of scientific interest are shown. A compiled map of active faults in and around the main islands of Japan on 1:2,000,000 scale is also prepared as an appendix. The results shown on the last map are represented in a simplified fashion in Figure 1.

The active faults on land shown in each sheet are represented by lines of different symbols based on their "certainty of the existence". These were selected primarily by interpretation of air photographs and thus these symbols refer mainly to the reliability of the topographic reference. Earthquake faults found in the historical documents are also shown by a different symbol. Epicenters of destructive earthquakes during the historical ages from 679 to 1978 are shown in the same sheets.

Each sheet is followed by such information as general explanation, notes, previous literature, detailed maps, figures and photographs in the respective region, and by a table of data on the active faults shown in the sheet. An example of the tables is shown in Table 1. In the fifth column of this table, the degree of fault activity, which is another basic criterion for classifying the active faults, is shown for each fault. The degree of activity is expressed as classes A, B, and C based on an average slip rate: A for 10-1m/1000 yr, B for 1-0.1m/1000 yr, and C for 0.1-0.01m/1000 yr.

Active faults beneath the sea were selected from the records of airgun seismic reflection survey carried out by the Hydrographic Department of the Maritime Safety Agency. Since the age of submarine topography or seabottom deposits is generally difficult to determine, the classification based on the degree of fault activity usually cannot be applied to the submarine faults. Instead of this, submarine faults are divided into two classes of major and minor faults by the magnitude of vertical displacement of faulting, which in practice is based on the relative height of fault scarp. A major fault expressed as a thick line in the map has a relative height of 200m or more, and a minor one expressed as a thin line has a relative height less than 200m. The reason of choice of 200m fault scarp is that a fault with vertical displacement of 200m or more during the Quaternary is equivalent to the class B or class A fault on land.

In conclusion, it can be said that the present work of the RGAFJ (1980a) marks the final step in the "age of discovery" of active faults in Japan. Also, it is noted that this is the first answer to the demand for a nationwide set of active fault distribution maps of uniform quality and in large scale. It is expected that these maps will provide important basic data for earthquake prediction.

III. Regional Characteristics of Active Faults in Japan

The work of the RGARJ (1980a) described above also enabled us to examine the regional characteristics of active faults in Japan more precisely. A map showing the active fault provinces (Fig. 2) has been made on the basis of strikes, types and density of distribution of their faults, and the direction of the maximum horizontal shortening (MHS) deduced from fault strike and types of faulting. The charcteristics of active faults in the respective provinces are summarized in Table 2. Some of the active fault provinces and their boundaries closely correspond to the tectonic provinces and tectonic lines. For example, the Median Tectonic Line in southwest Japan and the Morioka-Shirakawa Line (nearly equivalent to the volcanic front line of northeast Japan) of northeastern Honshu are both coincident with the boundary line of these provinces. The Pacific sides (outer zones) of these lines have extremely low density of active faults as compared to the other sides (inner zones). The Itoigawa-Shizuoka Tectonic Line, the western boundary of the Fossa Magma Belt, also coincides with the boundary of active fault

provinces and divides Japan into the northeastern and southwestern regions not only in geology but also with respect to active faults. Both the northeastern and southwestern regions are markedly different from each other in the type of the active faults; the former characterized by reverse faults while the latter is characterized by dominantly strike-slip faults.

In general, faults are longer in length and higher in activity in the provinces with a high distribution density. Similarly, in the provinces with low distribution density, faults are shorter in length and are lower in activity. On the other hand, in the volcanic region, faults are shorter in length, although the density and activity are relatively high. This is consistent with the phenomenon that larger earthquakes are rather rare in volcanic regions, even though many earthquakes of smaller magnitude have occurred. These imply that the regional nature of active faults is affected by that of the rock materials in which the faulting occurs as well as of the tectonic stress.

The regionality in active faults corresponds closely to the regional nature of recent shallow earthquakes and historic destructive earthquakes in such respects as the density distribution, fault mechanism, largest magnitude, etc. Therefore, the map of the active fault provinces (Fig. 2) can be used for practical purposes such as the elevation of the regionality in the earthquake risk as a seismotectonic province map.

IV. Recent Progress of Detecting Methods for Active Faults Beneath the Alluvial Plains

It is difficult to detect active faults covered by thick sediments beneath alluvial plains by the interpretation of aerial photographs alone.

Therefore the development of land profiles similar to the marine seismic reflection equipment is a matter of urgency to those engaged in active fault survey. In this respect, development of new exploration equipment is underway. Of this equipment, the shallow seismic reflection method is most promising for obtaining details of lateral facies variations and structural discontinuity of beds. Recent routine seismic surveys are using frequency range of roughly 10 to 50 Hz, which corresponds to resolution of 20 to 40 m in a typical geological environment. Much higher resolution is needed for our present purpose.

Since 1975, intensive research and development for a shallow seismic reflection method have been made in Geological Survey of Japan (GSJ). The latest results of field experiments (Fig. 3) show that detection of marker horizon up to one second two-way time with resolution of less than 5 m is quite possible even in a noisy urban area. The increased temporal and spatial sampling rate, as well as the introduction of the Mini-Sosie system in conjunction with high frequency geophones, is responsible for the improvement in data quality.

Another promosing approach is a family of electromagnetic techniques; particularly, versatility of the VLF method has proved to be of great value as a reconnaissance tool. Although it has been developed originally for mining application, resistivity distribution along buried fractured zones can clearly be delineated by hand-carrying equipment with high operational efficiency (Fig. 4).

Geochemical techniques are also expected to be useful for detecting buried faults covered by soft sediments. The track-etch method, a conventional tool obtaining relative radon concentration in soil gas, has been successfully applied by the GSJ for the mapping and detection of active faults at about 20 sites crossing the faults including earthquake faults. Although the peak of α-track number appeared usually just above the fault line, sometimes it shifted slightly from the line toward the hanging-wall side. Therefore, relative position between the peak and the fault trace on the ground surface indicates the inclination of fault plane. The number of α-tracks counted on some earthquake faults was much larger, and the pattern of the peak was sometimes remarkably sharper than those on the faults without historic movement.

Other geochemical techniques using soil gases as CO_2, H_2, He Hg, etc. have also been applied by universities and the GSJ. Some attempts have succeeded in detecting active faults. For example, Wakita et al. (1980) found that the hydrogen concentration in soil gas was remarkably high just above the Yamasaki fault as compared with that apart from the fault.

Despite the rapid progress in techniques, it seems that no one method can be a panacea at present. Integrated application of various techniques is practical for the detection of buried active faults.

V. Geodetic Measurements of Active Fault Displacements

Geodetic measurements to monitor the displacement of the active faults are conducted by various institutes and by various methods. The triangulation/trilateration survey net of the Geographical Survey Institute (GSI) covers the whole country. Recently the GSI studied the regional crustal strain comparing modern survey results with the second order triangulation survey results obtained in the early 20th century. This study revealed many areas of high crustal strain, which are considered to be caused by co-seismic deformation, landslide, ground subsidence and other causes.

Distance measurements across active faults using EDM have been conducted mainly by universities and the GSI. However, almost all measurements are not corrected for the meteorological effects along the light pass but corrected only for the temperature at the endpoint. Early this year, the GSI measured the temperature along the light pass experimentally using a helicopter.

The precise triangulation survey to monitor the active fault movements are carried out by the GSJ. The distance between survey points of the nets are mostly 200-300 meters, not greater than 1 km. The nets of this dimension meet the purpose to detect the fault movement precisely, and the triangulation survey is much better than the EDM survey of a single wave without meteorological measurements along the light pass for the refractive index corretion.

At the Kitatake survey net, which will be mentioned later, the survey result by the Mekometer ME3000 reads up to 2-3" of angle closing errors, even with the drift of the frequency of the instrument checked and corrected during the survey. On the other hand, the closing errors of the triangulation survey remains less than 1" in most cases at the same net.

The following is the result of the triangulation survey of eleven years at the Kitatake fault which runs across the Miura peninsula and is classified as an active fault of the 'A' class (long-term slip rate being greater than 1m/10,000 yr).

The horizontal displacement vectors of each point are shown in Figure 5. Figure 6 shows side length changes and its strain. No identifiable movement of the fault has been detected. At this survey net, precise leveling and angle measurement were done simultaneously. The result of the leveling has been analyzed with the same method as the 'dry tilt' and shown in Figure 7. The tilts in six directions fit a sinusoidal curve excellently. The fact means that no vertical slip of the fault has occurred during the survey period but this net has tilted as a single block.

Large values of dilatation and the maximum shear strain of this quadrangle are noteworthy. The dilatation amounting to 65 microstrain has been accumulated during eleven years. The average strain rate of dilatation, 6 microstrain/year, is significantly greater than the rate of the regional crustal strain commonly detected at the large survey net. The cumulative maximum shear strain, the average value of four triangles, is 28 microstrain. The computed average rate of it, 2.6 microstrain/year, is also remarkably large. These large values are possibly due to the anomalous physical property of the faulted zone. If it is true, a denser network would be desirable to realize the strain state on and around a fault and to monitor an active fault movement.

The after-slip of an earthquake fault is measured at small quadrilaterals using well calibrated measuring tape. The interesting result we have detected is that the after-slip of the Irozaki fault, dislocated by the Izu-hanto-oki Earthquake of 1974, stopped since the Izu-Oshima-kinkai Earthquake of 1978 (Fig. 8). The earthquake faults accompanied by the Izu-Oshima-kinkai Earthquake itself shows no after-slip movement.

VI. Trenching of the Active Faults

To study detailed dislocation history, especially to define the recurrence interval of fault movements, trenching has been done at some major faults. The Shikano fault, which moved at the Tottori Earthquake of 1943 was excavated (Ando et al., 1980). The prehistoric faulting, dated between 4000 BP and 8000 BP, was observed at one of the trenches. The trench at the Yamasaki fault, a major strike-slip fault in western Japan, disclosed the fault displacement between 480 BP and 1710 BP. It is considered that this displacement corresponds to the tremor of 868 AD in historical records (Okada, et al., 1980).

The GSJ has excavated the Tanna fault (Yamazaki, et al., 1981). This is a left-lateral fault with very large displacement and the contribution of the Kita-Izu Earthquake of 1930 to the movement was 1.5 m with very small vertical slip. The trench is in 'T' shape and the main trench is 20 m long. Depth and width are 3 m and 6 m, respectively. The sheared zone of about 20 cm in width have been clearly observed at the bottom of the trench. The pebbles of the overlying gravel bed have been rotated and reoriented vertically at an upward extension of the sheared zone. Farther up, the sand layer and humic soil layer have been dislocated 20 - 30 cm vertically by faulting.

The ^{14}C ages of the charcoal from this humic soil are dated as 2040 BP and 2460 BP. This displacement does not continue to the overlying layers in which a layer of pumice fall is contained. The pumice is correlated to well known 'Kawago-daira Pumice' from the Amagi volcano which erupted at 2900 BP. A part of the discrepancy between the age of charcoal and the age of pumice can be explained as the result of the contamination of modern carbon to the charcoal. It is concluded from the detailed geologic studies that the time interval between the deposition of the charcoal and the fall of the pumice was short, and the event prior to the earthquake of 1930 is estimated at about 3000 BP.

The minor surface break with westside drop is considered to be the result of the earthquake of 1930.

The long-term slip rate of the Tanna fault is inferred as 2m/1000 yr. On the other hand, the calculated slip rate between two recent events is 1.5m/3000 yr. One possible interpretation for the difference between these two slip rates is that the long-term slip rate determined geologically is that of the system as a whole, and slip has been occurring not only at a single strand but also being shared by subsidiary faults.

A trench provides us with many, but not all, important evidences to understand the fault movement. Many studies such as more detailed geologic survey, drilling, geophysical survey and trenching are required for better understanding of the history and mechanism of faulting.

References

Ando,M., Tsukuda,T. and Okada,M. (1980) Trenches across the 1943 trace of the Shikano Fault in Tottori. Rept. Coordinating Committee for Earthquake Prediction. vol.23, p.160-165.

Okada,M., Ando,M. and Tsukuda,M. (1980) Trenches across the Yamasaki Fault in Hyogo Prefecture. Rept. Coordinating Committee for Earthquake Prediction. vol.24, p.190-194.

The Research Group for Active Faults of Japan (RGAFJ) (1980a) Active faults in Japan--- sheet maps and inventories. University of Tokyo Press, Tokyo, 363p. (in Japanese)

——— (RGAFJ) (1980b) Active faults in and around Japan, the distribution and the degree of activity. Jour. Natural Disaster Sci., vol.2, no.2, p.61-99.

Wakita,H., Nakamura,Y., Kita,I., Fujii,N. and Notsu,K. (1980) Hydrogen release : new indicator of fault activity. Science, vol.20, p. 188-190.

Yamazaki,H., Kakimi,T., Tsukuda,E. and Awata,Y. (1981) Trench survey of the Ukihashi-chuo Fault, Tanna Fault System. Program and abstracts, Seism. Soc. of Japan, 1981, no.1, p.118.

(Interpreter: H. Yamazaki, K. Nishida and A. Okada)

Fault No.	Name of fault	Sheet No.	Certainty	Activity	Length (km)	Strike	Dip	Fault trace features	Fault reference	Age 10^4yr	Fault displacement vert. (m)	Fault displacement horiz. (m)	Average slip rate (m/10^3yr)	Reference
1+	Ina F.	1	I	B	16	NNE		flexure scarp*	river terrace (MK surface)*	2.7*	W(4)*		0.2	*2), 3)
—	—	—	—	—	—	—	—	—	—	—	—	—	—	—
7	Tagiri F.[2]		I	B	30	NS	W*				W		0.7	*2)
a	[near Miyata]	2	I	B				flexure scarp[2]	MK' surface[2]	2.1[2]	W(9.5)[2]		0.4[2]	
b	[near Komagane]	2	I	B				flexure scarp[2]	MK' surface[2]	2.1[2]	W(6)		0.3[2]	
	[near Tagiri]	2	I	B				scarplet[2]	MD surface[2]	1.5[2]	W(7)[2]		0.5[2]	
	[near Katagiri]	3	I	B				flexure scarp[2]	OZ surface[2]	8[2]	W(15)[2]		0.2[2]	
c	[near Kitawari]	2	I	B				flexure scarp[2]	MK surface[2]	2.1[2]	W(4)[2]		0.15[2]	
d	[near Takao]	2	I	B				flexure scarp[2]	MD surface[2]	1.5[2]	W(9)[2]		0.5[2]	
e	[near Ichida]	3	I	B				bulge	OZ surface	8[2]	W(80)		1	
—	—	—	—	—	—	—	—	—	—	—	—	—	—	—
24	Atera F. System*	10	I	A	80	NW		discontinuity of height	Atera Mts. Mino-Hida Hills.		NE(600-1200)			*20), 21)
								offset*	Kiso R.			L(5000)		*17)
								offset*	Tsukechi R.			L(7000)		*17)
a	Atera F.*	10	I	A	35	NW								*16), 17, 19)
	[near Sakashita]	7	I					scarplet*	river terrace II[17]		NE(0.3)[17]			*17), 22), 25)
												L(17)[17]		
	[near Sakashita]	7	I					scarplet*	river terrace III[17]		NE(1.75)[17]	L(17)[17]		
	[near Sakashita]	7	I					scarplet*	river terrace IV[17]		NE(2.45)			
												L(17.5)[17]		
	[near Sakashita]	7	I					scarplet*	river terrace V[17]		NE(3.4)			
										0.5-1.5[17]		L(14)[17]	1-3[17]	
	[near Sakashita]	7	I					scarplet*	river terrace VI[17]		NE(10)	L(50)[17]		
	[near Sakashita]	7	I					scarplet*	river terrace VII[17]		NE(10)	L(90)[17]		

(to continue overleaf)

Table 1 An example of data table on the mapped faults on land (RGAFJ,1980-b). Data cited in this table correspond to some of the faults mapped in the "Iida" sheet.

Province	Sub-province	Density of faults	Length of major faults	Activity of major faults	Types of faults	Note
I. Main part of Hokkaido	a. inner belt of main Hokkaido	low	short	C	reverse?	
	b. outer belt of main Hokkaido	low	medium	B	reverse	
II. Inner belt of NE Japan	a. continental slopes of inner belt of NE Japan	high	long	A?	reverse	sea-bottom
	b. inland of inner belt of NE Japan	medium	short	B	reverse	volcanic region
III. Outer belt of NE Japan		very low	medium	B	reverse-strike-slip?	
IV. Continental slopes off the Pacific coast of NE Japan	a. off the south coast of Hokkaido	high	long	A?	reverse-strike-slip?	sea-bottom
	b. off Sanriku-Joban-Kashima	high	long	A?	reverse	sea-bottom
	c. around Sagami Trough	high	long	A	reverse-strike-slip	mainly sea-bottom
V. Northern tip of Izu-Ogasawara arc	a. around the Kanto Mountains	medium	short	B	reverse-strike-slip	
	b. around Izu Peninsula	high	short	B	strike-slip	volcanic region
BF. Western Fossa Magna belt		high	short	A	strike-slip·reverse	
VI. Eastern part of inner belt of SW Japan	a. around Noto Peninsula	low	short	B.C	reverse	land & sea-bottom
	b. around Oki Trough	medium	medium	B?	reverse?	sea-bottom
	c. Chubu Mountains	high	long	A	strike-slip-reverse	
	BT. Tsuruga Bay-Ise Bay Line belt	high	medium	A.B	strike-slip-reverse	
	d. Kinki triangle	high	medium	B.A	strike-slip-reverse	
	e. northwestern part of Kinki district	medium	medium	B	strike-slip-reverse	
VII. Western part of inner belt of SW Japan	a. Chugoku-Setouchi-northern Kyushu	low	short	B.C	strike-slip-reverse	
	b. volcanic field of central Kyushu	high	short	B	normal	volcanic region
BM. Median Tectonic Line belt		high	long	A	strike-slip	
VIII. Outer belt of SW Japan		very low	short	B.C	reverse-strike-slip	
IX. Continental slopes off the Pacific coast of SW Japan		high	long	AA	reverse-strike-slip	sea-bottom
X. Northern part of Okinawa Trough		medium	long	B?		sea-bottom
Nansei Islands		high-low	short	B.C	normal	land only
Izu-Ogasawara Islands		low?	short	C	reverse?	land only

Table 2 Characteristics of active fault provinces of Japan (RGAFJ,1980-a).

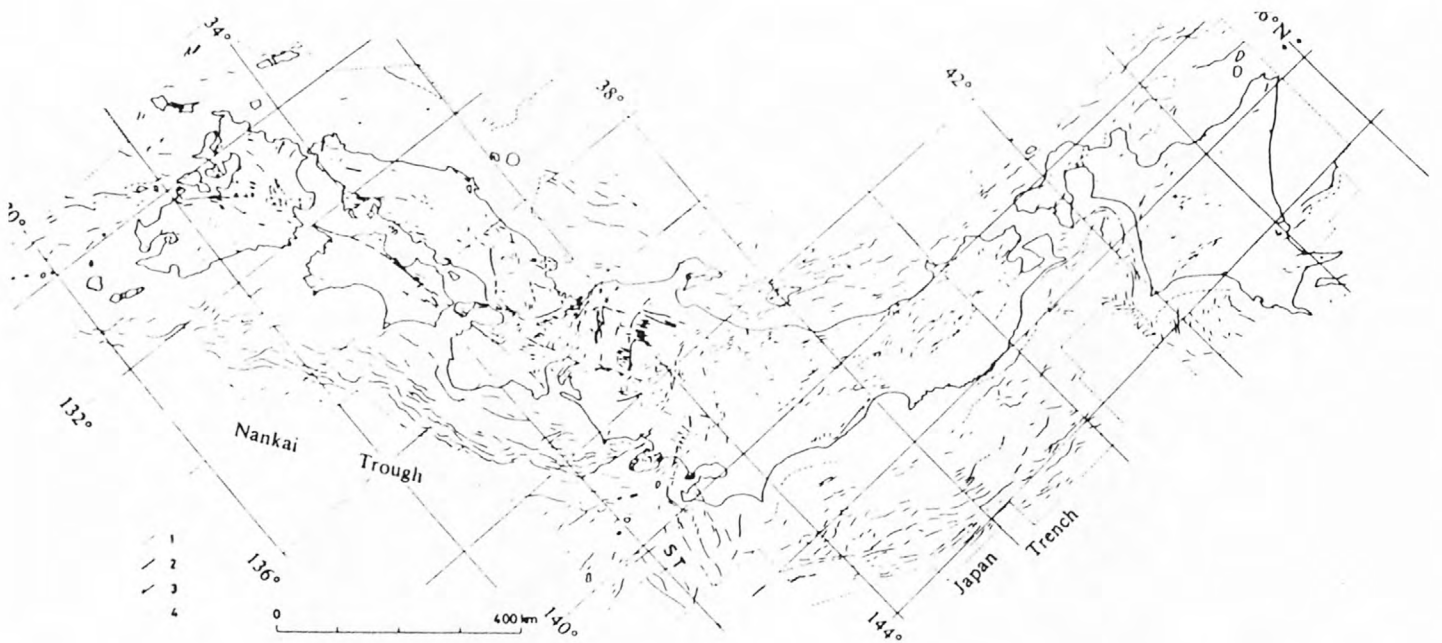

Fig.1 Main active faults in Japan (RGAFJ,1980-b).
1: dip-slip fault on land and beneath the sea, 2: fault having right-lateral slip component, 3: fault having left-lateral slip component, 4: monocline beneath the sea, ST: Sagami Trough.

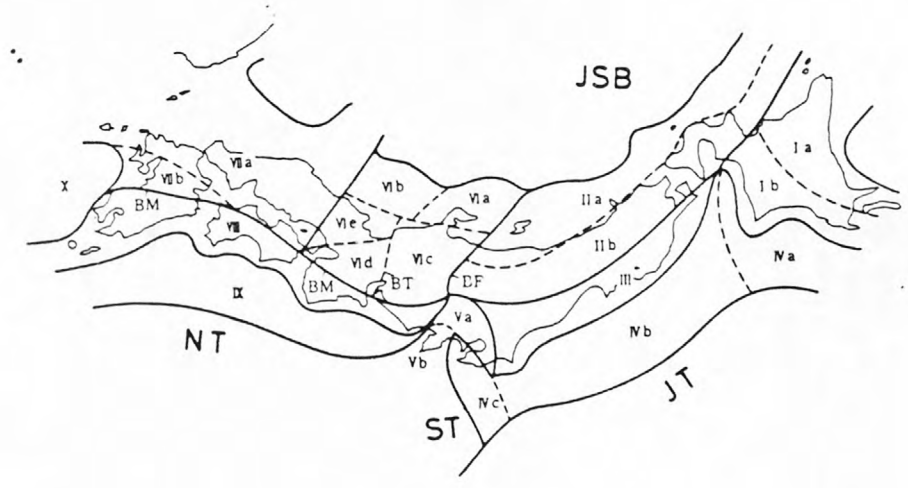

Fig.2 Active fault provinces of Japan (Originally by RGAFJ,1980-a).
JT: Japan Trench, ST: Sagami Trough, NT: Nankai Trough, JSB: Japan Sea Basin.
See Table 2 for the characteristics of respective province.

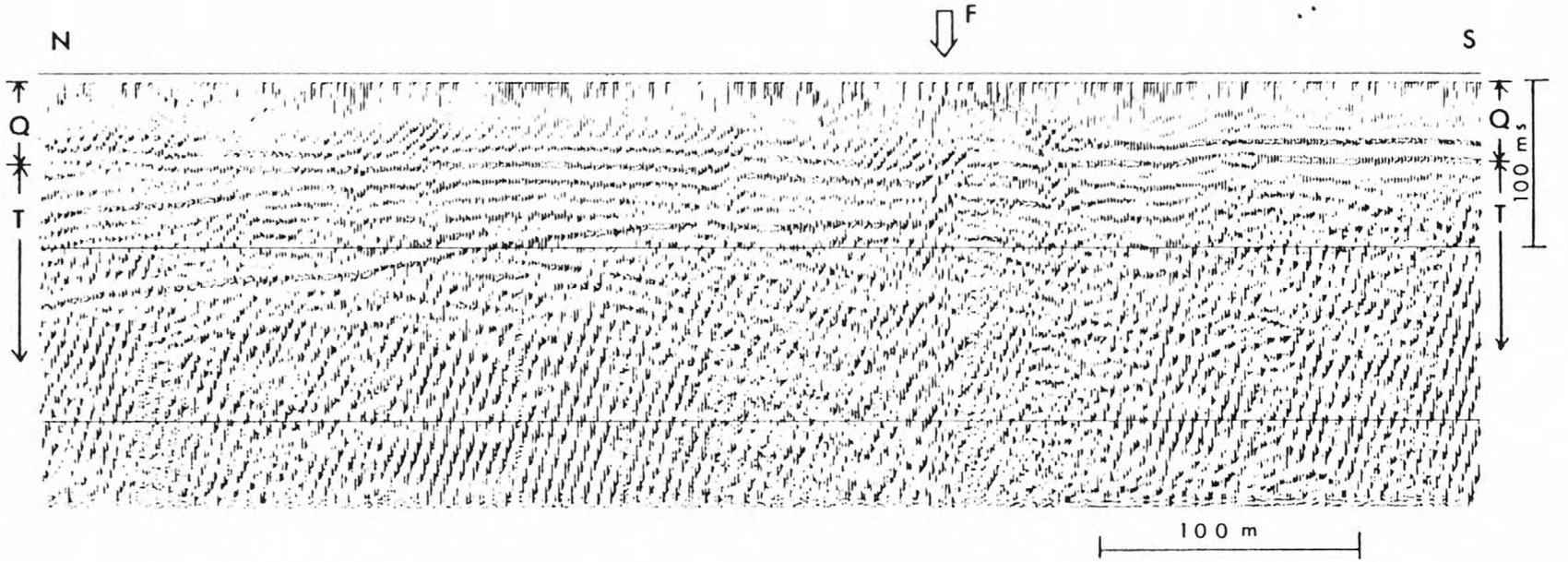

Fig.3 Seismic reflection profile across the Kushibiki Fault,Saitama Pref., showing notherly dipping reflectors at about 100ms lines and clear-cut discontinuity between the Neogene strata (T) and overlying Quaternaly beds (Q). Pop and geophone spacing 2.5m, 600% CDP stacking with sampling interval 0.25ms..
T: Kushibiki Fault with 3m scarplet observed at this point.

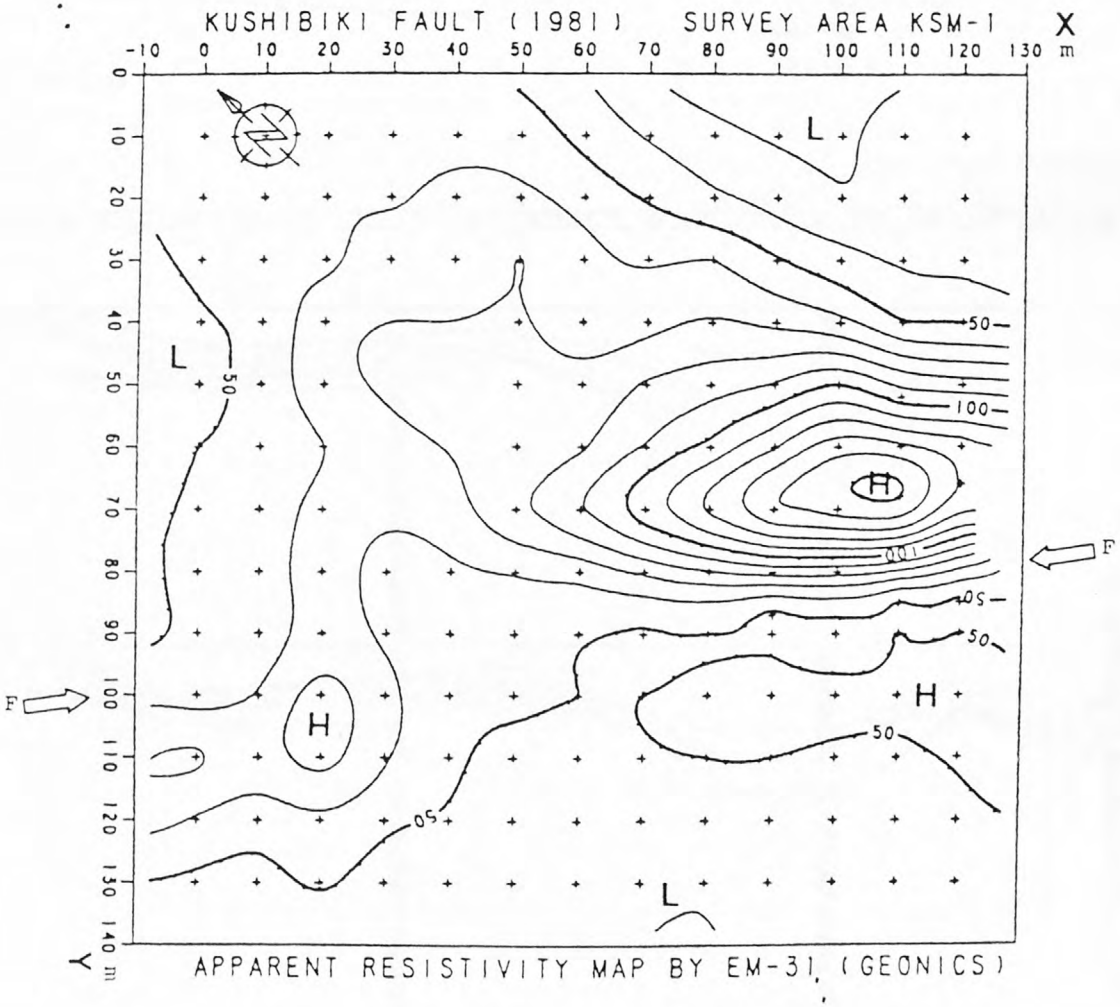

Fig.4 An examle of VLF-EM(EM-31) apparent resistivity map around the Kushibiki Fault, Saitama Pref.. Contour interval is 10 ohm-m. + indicates a survey point. F-F: surface trace of the Kushibiki Fault.

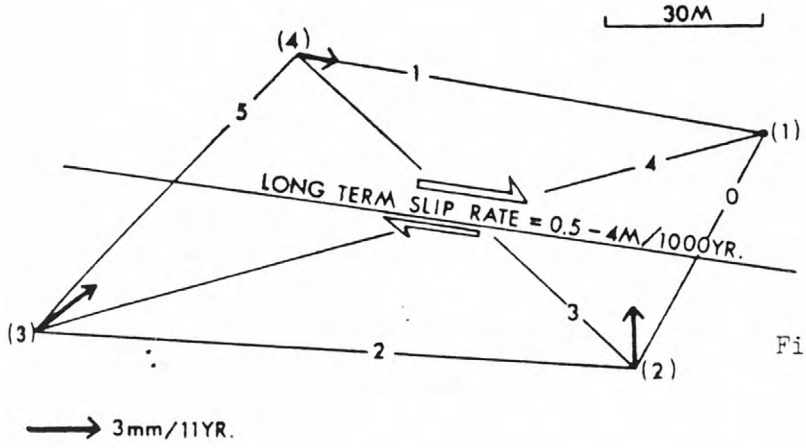

Fig.5 Configuration of the Kitatake survey net and the displacement vectors.
Location of point (1) and direction of (1)-(4) are fixed.

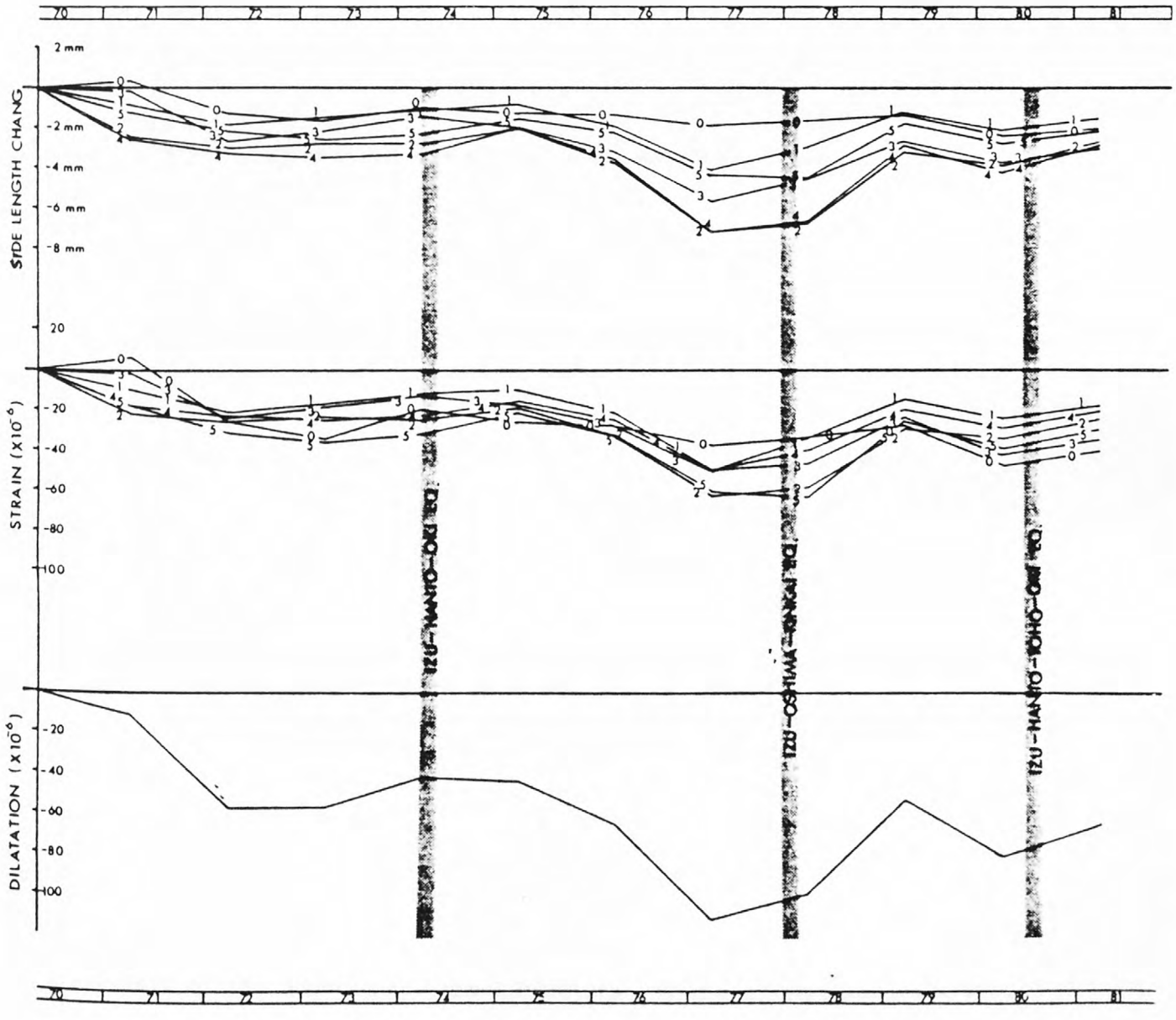

Fig.6 Result of the geodetic survey at the Kitatake fault.
Numbers on lines are line numbers same as shown in fig.5.

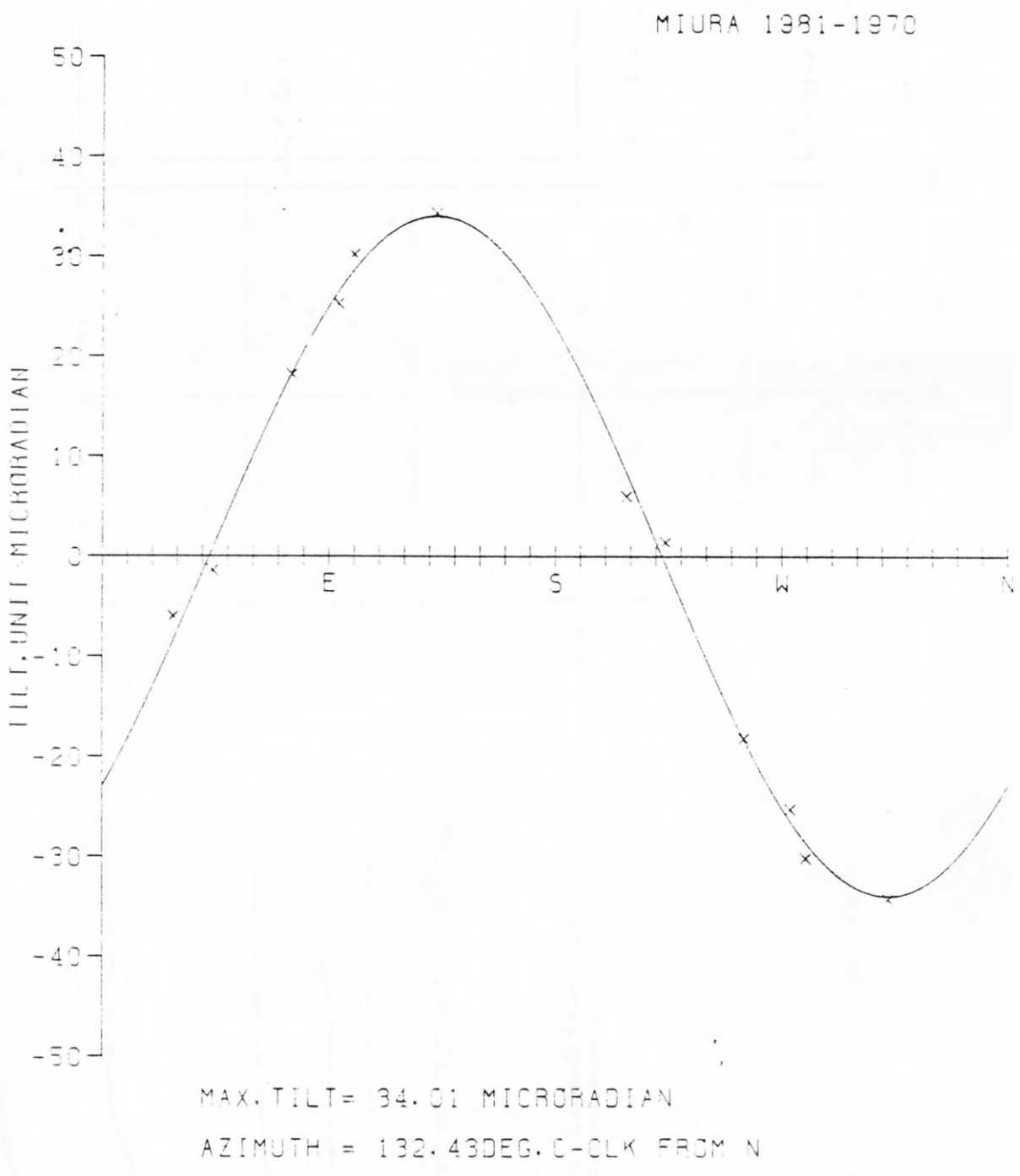

Fig.7 Tilt of the survey net (six directions and their reverses are plotted).

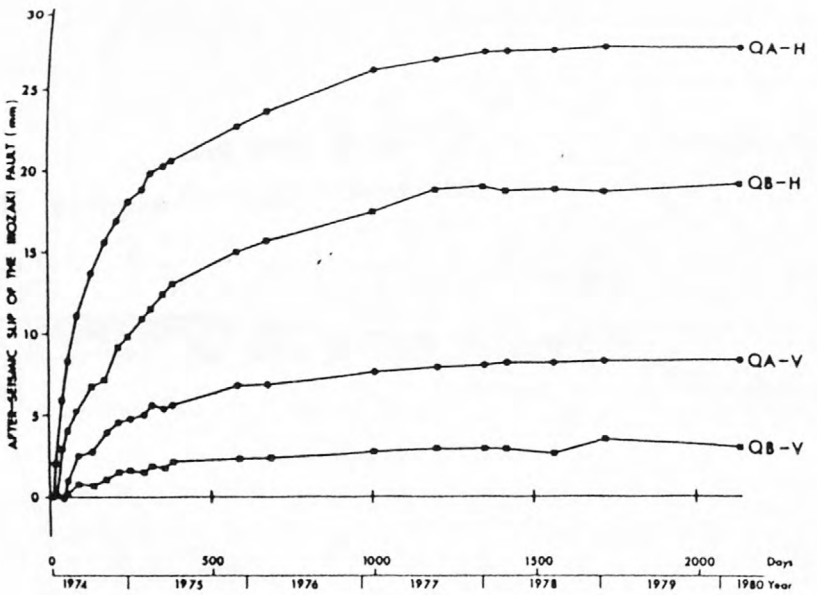

Fig 8a After-seismic slip of the fault. Right-lateral and north-side down are positive. QA and QB are quadrilateral A and B. H and V are horizontal and vertical slip.

Fig.8 After-seismic slip of the Irozaki fault.

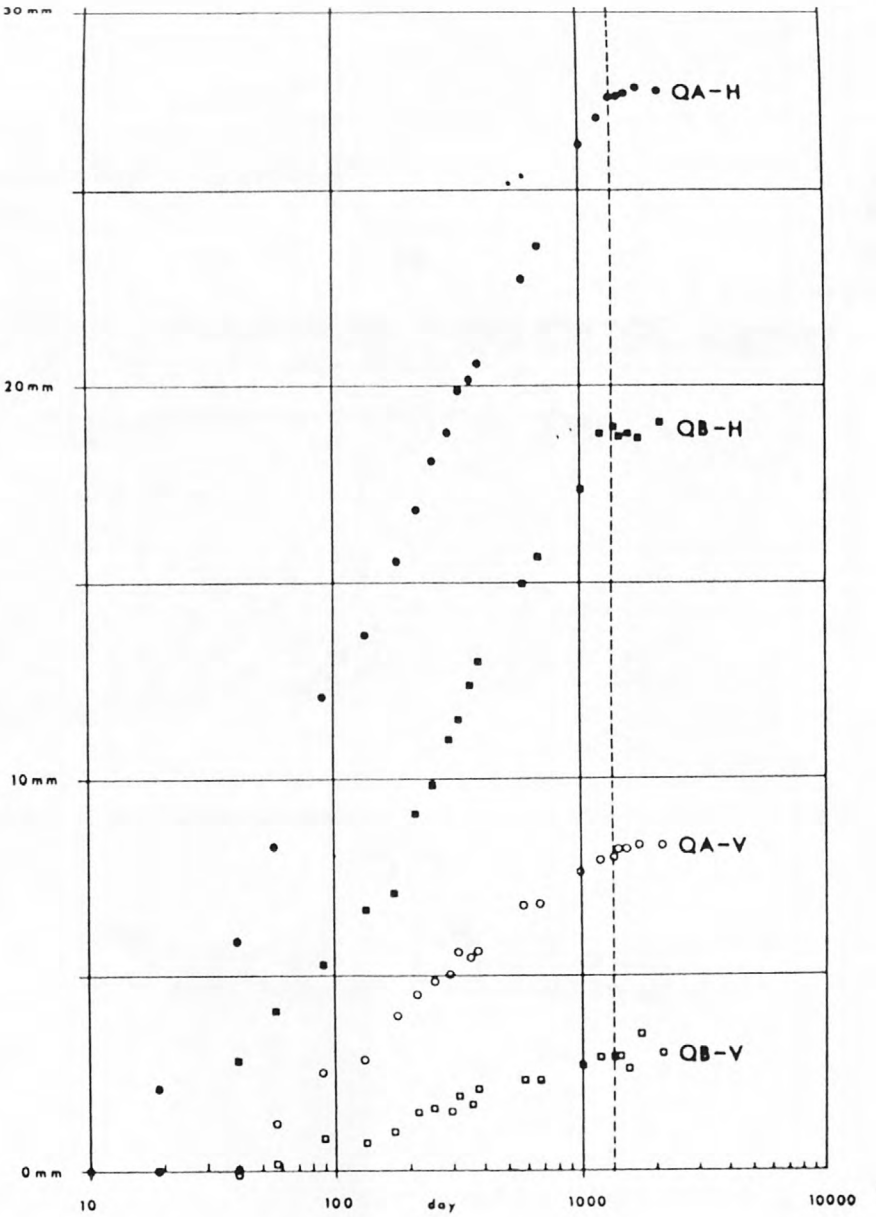

Fig. 8b Same as figure a in logalithmic expression. Vertical broken line shows the time of the Izu-Oshima-Kinkai earthquake of May 14th, 1978.

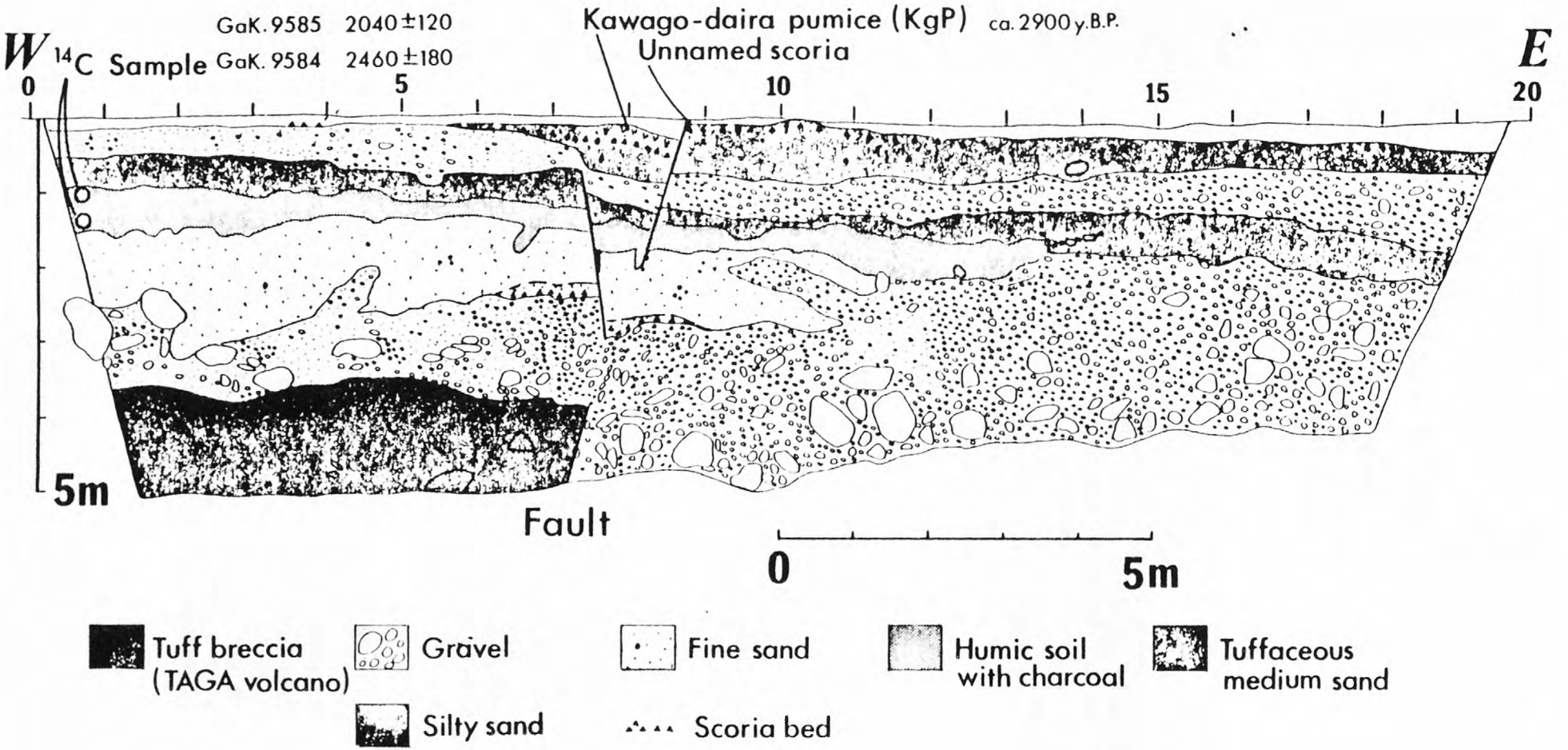

Fig.9 Log of the trench across the Tanna fault.

FAULT INTERACTION NEAR HOLLISTER, CALIFORNIA

Gerald M. Mavko
U. S. Geological Survey
Menlo Park, California

Abstract

A numerical model is used to study fault stress and slip near Hollister, California. The geometrically complex system of interacting faults, including the San Andreas, Calaveras, Sargent, and Busch faults, is approximated with a two-dimensional distribution of short planar fault segments in an elastic medium. The steady stress and slip rate are simulated by specifying frictional strength and stepping the remote stress ahead in time. The resulting computed fault stress is roughly proportional to the observed spatial concentration of small earthquakes, suggesting that the distinction between segments characterized by earthquakes and those with active creep results, in part, from geometry. A nonsteady simulation is made by introducing, in addition, stress drops for individual moderate earthquakes. A close fit of observed creep with calculated slip on the Calaveras and San Andreas faults suggests that many changes in creep rate (averaged over several months) are caused by local moderate earthquakes. In particular, a three-year creep lag preceding the August 6, 1979, Coyote Lake earthquake on the Calaveras fault seems to have been a direct result of the November 28, 1974, Thanksgiving Day earthquake on the Busch fault. Computed lags in slip rate preceding some other moderate earthquakes in the area are also due to earlier earthquakes. Although the response of the upper 1 km of the fault zone may cause individual creep events and introduce delays, the long term rate appears to reflect deep slip.

Introduction

The relation between observed surface fault slip and earthquakes has been unclear. Coseismic surface faulting is sometimes observed with shallow tectonic earthquakes, for example the 1906 San Francisco earthquake. But often ruptures from moderate earthquakes do not break the surface. Relatively little coseismic surface slip was observed for the 1966 Parkfield, California, earthquake (M=5.6) even though aseismic surface slip was observed both before (Allen and Smith, 1966) and after (Scholz et al., 1969) the earthquake.

In central California surface fault creep seems to be influenced by fault slip immediately below in the depth range of seismicity (4-12 km). Creepmeters often record small abrupt movements at the times of or shortly after nearby moderate earthquakes (Tocher, 1960; Bufe and Nason, 1973; Burford et al., 1973). Others show either an increased or decreased creep rate before or after earthquakes (King et al., 1977; Burford et al., 1973; Nason, 1973; Burford, 1976). Some correlations between creep and earthquakes may not be apparent, particularly when the earthquake is on a

different fault than the creepmeter. The correlation can be further obscured by delays introduced by the shallow fault zone material.

In this paper, I present a theoretical model for fault slip on the San Andreas, Calaveras, Sargent, and Busch faults near Hollister, California. In the first section I describe the model and the numerical method for solving for fault slip. Next, I describe a simulation of steady fault slip and stress accumulation representing an average over 10 years or more. Computed fault stress is determined, in part, by fault geometry. Furthermore, the computed stress and energy dissipation on the faults appear to be correlated with the observed spatial density of small earthquakes. Finally, episodic slip is superimposed onto the steady model by introducing stress drops for all earthquakes greater than local magnitude 4.0. In spite of its simplicity, the model, which is based on frictional sliding in the brittle seismic depth range, reproduces many of the temporal features of observed surface slip, including changes in creep rate, transient fault locking, and coseismic steps.

The Model

Sections of the San Andreas, Calaveras, and Sargent faults (Brown, 1970) are shown in Figure 1a. The location of the Busch fault was inferred from the main shock focal mechanism and aftershock locations of the November 28, 1974, earthquake (M_L= 5.1) (Savage et al., 1976). An obvious feature of the map is the geometric complexity of the faults over a wide range of length scales. There are four major faults at four quite different orientations; each of these consists of many individual segments with offsets and changes in strike. In modeling the stress and slip on these faults I have assumed that the trace geometry is representative of the fault below the surface, at least down to the lower depth of brittle seismicity (12 km). In support of this Bakun and others (1980), for example, have found good correlation between trace geometry and epicenter locations, directivity, and aftershock clustering.

The faults are modeled as cuts in an otherwise homogeneous linear elastic body of infinite extent. The models are two-dimensional in map view, and the calculations assume plane strain deformation. (Alternatively, the model can be interpreted as plane stress deformation of a thin elastic plate with through-going cuts.) Homogeneous stresses are applied at infinity; a stress-slip boundary relation is specified on the faults; and the resulting fault slip is found numerically.

Important limitations of the model are that the crust is not purely elastic nor homogeneous, and faults are not two-dimensional. Inelastic deformation (as evidenced by compression ridges, sag ponds, and permanently deformed rocks) and secondary fracturing relieve stresses, eventually, at discontinuities in the fault (Segall and Pollard, 1980). Although en echelon offsets are sites of inhibited slip, over some sufficiently long time scale the displacement across the fault zone is everywhere essentially uniform. In contrast, fault discontinuities in a two-dimensional elastic

model form permanent and unrealistic barriers to fault slip. Delaney and Pollard (1980) have found that sets of echelon dike segments sometimes deform as a single long segment due to inelastic deformation at closely spaced segment ends or due to coalescence into one segment just below the surface. Separate fault segments may coalesce below the surface although the depth and geometry are unknown (Segall and Pollard, 1980).

In constructing the two-dimensional models I have assumed that the spatial and temporal patterns of crustal deformation and fault interaction, on scales longer than a few kilometers and several months, are governed primarily by fault slip at the depths of observed seismicity (4-12 km). Aseismic slip above (i.e., surface creep) and below is assumed to follow passively. Furthermore I have assumed that the slip in the seismic depth range is best modeled by joining the separate segments within each of the four major faults to form crooked, though continuous cuts.

The vertical lithostatic pressure gradient and spatial variations of crustal stiffness are ignored for computational economy and also to model only the first order effects that result from fault geometry. Irwin and Barnes (1975) argue that the spatial patterns of fault creep and seismicity in this region are correlated with, if not controlled by, spatial variations of rock type. They suggest that variations of pore pressure and composition in the fault zone might cause variations in fault zone sliding behavior. Such variations could be included in the homogeneous elastic fault model in the form of boundary conditions on the fault surfaces, but have not been included for this paper.

The elastic boundary value problem is solved using the displacement discontinuity method, which is described in detail by Crouch (1976). The method uses Green's functions relating tractions and displacements along the prescribed cuts in the infinite body. The continously varying slip on each fault is approximated (for numerical purposes) by dividing the fault into many short planar segments, each having uniform slip. The various segments can have arbitrary length and orientation, and can be intersecting or not. By choosing the segments to be sufficiently short, geometric complications, such as steps and bends, are approximated to desired accuracy at the expense of longer computation time. Because each segment has uniform slip, it is identical to a pair of elastic edge dislocations, sharing a common slip (glide) plane and having equal and opposite Burger's vectors.

The advantage of this method is that only the faults have to be discretized. The Green's functions are exact elastic solutions everywhere in the body for a given fault slip. Finite difference and finite element procedures, on the other hand, require that the entire elastic body be discretized, both on and off the fault, with the elastic field equations approximated everywhere by a system of algebraic equations. Furthermore, constructing the solution from the known analytic solutions (Green's functions) saves computation time because the two-dimensional problem is reduced to a one-dimensional one.

The numerical problem is solved as follows. At any point in the body, in particular at the center of the jth segment, the shear stress in the plane of the fault τ_j is the sum of the remotely applied shear stress τ_j^A resolved in the plane of the jth segment plus the stress perturbations resulting from slip u_i on each of the N segments; i.e., the stress due to each pair of dislocations. Because the material is linear elastic the stress due to each segment is simply proportional to the slip on that segment. That is,

$$\tau_j = \tau_j^A + \sum_{i=1}^{N} A_{ji}^t u_i \qquad (1)$$

where A_{ji}^t are constant coefficients, that depend on the elastic moduli, the segment lengths and orientations, and the distance between the ith and jth segments. Similarly, the normal stress on the jth segment σ_j is the sum of the resolved normal component of applied stress σ_j^A plus the perturbations resulting from slip on each segment

$$\sigma_j = \sigma_j^A + \sum_{i=1}^{N} A_{ji}^n u_i \qquad (2)$$

where A_{ji}^n are a second set of coefficients depending on the elastic moduli, the segment lengths and orientations, and the distances between the ith and jth segments. The stress fields associated with elastic dislocations, from which A_{ji}^n and A_{ji}^n can be derived, are well known (Weertman and Weertman, 1964). Crouch (1976) has derived A_{ji}^t and A_{ji}^n for arbitrary segment size and orientation.

We specify the fault strength on each segment as an arbitrary function of slip or normal stress. For example, in this paper the fault strength is chosen to be proportional to normal stress on the fault. That is, for segments that are slipping

$$\left|\tau_j\right| = -f_j \sigma_j, \quad \text{if} \quad \sigma_j < 0$$

$$\tau_j = 0, \qquad \text{if} \quad \sigma_j \geq 0 \qquad (3)$$

This is mathematically like simple friction (static = dynamic) with a coefficient of friction f_j that may be different on each segment. A more sophisticated model might include a strain hardening and softening fault strength in order to predict instability. This is also where one could include the effects of pore pressure and fault zone composition on the sliding behavior.

For a given set of applied stresses the equations (1), (2), and (3) are solved numerically. A computer program, published by Crouch (1976), computes the influence coefficients A_{ji} and solves the linear equations (1) and (2) numerically. The program has been modified for the present study to include the nonlinearity introduced with the frictional boundary conditions (3).

Steady Simulation

The first model simulation approximates the average distributions of fault slip and stress accumulation in the Hollister area appropriate to the last 10 years or so. The model, shown in Figure 1b, consists of 9 straight cuts chosen to approximate some of the larger changes in fault strike. The model trace is smoother than the mapped geometry in Figure 1a to emphasize the large scale interactions. In the numerical calculations these cuts are further divided into a total of 53 segments (53 pairs of dislocations) of approximately equal length ($\sim$2.3 km), each having uniform slip. The portion of the Sargent fault and the northern limit of the San Andreas fault modeled in Figure 1b correspond to faults with significant seismicity in the last 10 years. The locked portion of the San Andreas fault, which slipped in 1906, is left out of the model. (No attempt was made to determine whether or not the locking is a geometric effect.) The northern end of the Calaveras fault and the southern end of the San Andreas fault were terminated arbitrarily to save computation time, though both faults are active beyond the limits chosen for the model. Uniform confining pressure and shear stress are applied remotely with the direction of maximum shear stress far from the faults oriented parallel to the local strike of the plate boundary (325°) given by Minster and Jordan (1978). The remote shear stress is stepped ahead uniformly in time resulting in steady rates of slip and of stress accumulation. Simple friction (static = dynamic) is assumed on the faults, so that no episodic behavior (viz., individual earthquakes) is modeled.

The results are shown in Figure 2. In the center of the figure is a seismicity map for the 10 years 1970-1979 showing earthquakes with magnitude greater than 2. At the top of the figure computed slip rate and shear stress along the Calaveras fault are plotted at the same scale as the map directly below. At the bottom of the figure, stress and slip rate along the San Andreas and Sargent faults are shown.

Slip rate is computed by successively increasing the remote shear stress and finding the difference in the static fault displacement between any two successive time steps. At very low shear stress some of the segments slip, and some remain frictionally locked, depending on the segment orientation. As the shear stress is increased, more of the segments slip causing non-steady, generally increasing, slip rates. Finally, when all segments are slipping, further steady increases in stress give the steady slip rates plotted in Figure 2.

The computed slip rate is proportional to the applied stress loading rate. The proportionality, however, is model dependent. For faults of finite extent in an infinite body, as modeled here, the slip rate is also roughly proportional to the fault length. Including more of the active portions of the San Andreas and Calaveras faults increases the computed slip rate. For the model in Figure 1b, an applied shear stress loading rate of 0.3 bar/year scales to a computed maximum slip rate of 20 mm/year on the Calaveras fault (for shear modulus $\mu = 6 \times 10^5$ bar). An additional caution is that terminating the northern extent of the Calaveras fault and the southern extent of the San Andreas fault causes the modeled slip rate to be artificially low near those ends.

The slip rates in Figure 2 were computed for the two friction coefficients, f=0 (no friction) and f=0.6. The slip rate is similar in the two cases except that increased friction decreases slip on the San Andreas fault and increases it on the Calaveras fault. This results from the orientations and the assumed dependence of fault strength on compressive stress. The normal to the San Andreas fault is oriented more toward the greatest compressive principal stress; the Calaveras, toward the least compressive. The slip rate is also influenced by fault interaction. The computed slip rate distribution from north to south along the San Andreas shows a pronounced dip just north of the junction with the Calaveras fault and a large increase to the south. A simple-minded explanation is that to the north the right lateral slip needed to accommodate the relative plate motion is distributed across both faults, while to the south only the San Andreas slips.

The computed shear stress on each fault segment is a function of the remotely applied normal and shear stresses, the fault strike, and the fault slip distribution everywhere in the system. Although the slip rate is steady everywhere, the stress is not. The shear stresses shown in Figure 2 are for two successive time steps, two years apart, for the case f=0.6. The difference between the two is the shear stress accumulation rate, which is proportional to the remote stress loading rate. The trend with time is to increase the stress maxima and to decrease stress minima. Consequently, the various plotted features become exaggerated with time. For example, the peak-to-peak difference in computed shear stress between points A and B grows by $\sim$0.4 bar/year ($\sim$40 bars in 100 years).

The zero shear stress level in Figure 2 is ambiguous and depends on the assumed value of confining pressure (applied normal stress) and the absolute level of remotely applied shear stress. In general the stress on the San Andreas fault is computed to be larger than on the Calaveras. This is again due to the orientation. The shear stress is proportional to the compressive stress, and the average normal compressive stress is larger on the San Andreas. Note the relatively low stress on the San Andreas just north of the junction with the Calaveras and the high stress just to the south. This large scale variation results from right lateral slip on the Calaveras which tends to compress and lock the San Andreas fault south of the junction and to unlock it to the north.

On the Calaveras fault note the large fluctuations in stress due to the large bend, plus the locking and unlocking influence of left lateral slip on the Busch fault. Smaller scale variations in computed stress occur every time a step or bend is modeled. In fact, a limitation of the model is that uncertainties in fault geometry have a large effect on the estimated stress.

Finally, note the apparent correlation between the spatial density of small earthquakes and computed stress. On the San Andreas fault the seismicity is high south of the junction with the Calaveras where the computed stress is high. This is the region of the 1972 Bear Valley and Stone Canyon earthquakes. North of the junction, where the computed stress is low, the seismicity is low. The model suggests that this is a relatively unlocked region that accumulates stress slowly. Farther north where the computed stress increases, so does the seismicity. One might expect that the seismicity should instead be correlated with the frictional energy dissipation rate, which is the product of the fault shear stress times the slip rate. This appears to be at least qualitatively true in Figure 2. Alternatively, if no assumptions are made about the fault constitutive law it still appears that seismicity is correlated with the modeled normal stress on the fault.

Nonsteady Simulation: 1969-1979

A nonsteady simulation of fault slip during the years 1969-1979 is made by superimposing moderate earthquake stress drops onto a steady simulation. The model, shown in Figure 1c, was constructed by drawing a continuous trace through each of the faults in Figure 1a and dividing these into 55 straight segments. The model is similar to that used for the steady simulation (Figure 1b) but more closely approximates the actual trace geometry.

The calculation is similar to the steady simulation. The 11-year period (1969-1979) is divided into 30 unequal time steps. Simple friction is assumed on the faults; the boundary shear stress is stepped uniformly in time; and the static fault slip and stress are computed at each time step.

The only nonsteady input to the model is the abrupt stress drop, actually a drop in coefficient of friction, specified for each moderate earthquake (local magnitude ≥ 4.0) shown in Figure 1c. Each stress drop is imposed on the single model segment closest to the earthquake epicenter and at the time step closest to the actual time of the earthquake. To save computation time events occuring within several months of each other are clustered into a single time step. Events used in the simulation are listed in Table 1. In detail, each earthquake is modeled in two steps. First, the remote boundary stress is advanced through time, and the static fault slip is found everywhere until just before the prescribed stress drop. Then keeping the remote stress fixed, the friction is decreased on the one model segment closest to the epicenter, and the static slip is

recomputed everywhere in the system. The change in frictional strength on just one of the 55 segments, with no change in the remote stress, leads to a readjustment of slip throughout most of the fault system. This readjustment, the difference between the static solutions before and after the stress drop, is interpreted as the sum of the coseismic slip plus the aftershocks, creep, and all preseismic and postseismic adjustments. There is no viscous or time dependent element in the model to spread these effects out in time. Consequently, the mainshock seismic moment is only a fraction of the total computed readjustment of the fault system.

Creep Solution. A model solution was developed by adjusting (by trial and error) the remote shear stress loading rate, the starting coefficient of friction, and the earthquake stress drops until a single simulation gave reasonable agreement to creep records at the five sites shown in Figure 1c and listed in Table 2. The model stress drops were adjusted arbitrarily to improve the fit, regardless of published earthquake moment. A comparison of observed and calculated slip is shown in Figure 3. Time in years is shown on the horizontal axis. The location in time and the magnitude of the modeled earthquakes are shown by the vertical lines along the time axis.

A friction coefficient $f = 0.40$ was used for the model solution in Figure 3. (In principle, 55 different coefficients on the 55 segments can be adjusted separately, but for simplicity they were kept uniform throughout the model.) Smaller coefficients give too large a slip rate on the San Andreas fault relative to the Calaveras, and vice versa for larger coefficients. A different coefficient, however, might be more appropriate for a different fault geometry or different orientation of the remote principal stresses.

The calculated slip and the creep data to which the model was fit are now discussed at each creepmeter. Many of the steps and long term changes in creep rate are reproduced by the model. Most individual creep events are not.

SHR1 The computed slip history at the site of creepmeter SHR1 resembles the observed creep record, but the comparison is more obvious if the computed slip is shifted (delayed) by 9 months (Figure 3a). Such a delay might be expected if the surface slip lags behind the slip at seismic depths because of near surface fault gouge or soil conditions. The record begins in 1971. On a gross scale both the observed (dots) and computed (solid) curves are concave upward until mid-1972, followed by a concave downward until mid-1974, a moderate slope during most of 1975, and a flat record after 1975. Looking closer, a few shorter term features seem to match. A slight increase in rate in early 1972 (point A') is correlated with an increase in computed rate beginning at point A. No event is modeled at A; instead, the change is a transient from earthquakes 1, 2, and 3 (Table 1) at Hollister in late 1969 and early 1970. A lower observed rate between B' and D' is correlated with a slight computed decrease starting at B resulting from the Bear Valley earthquake (event 4) and

another computed decrease at C from earthquakes 5-8 at San Juan Bautista, Cienega Road, and Stone Canyon. An observed step at D' correlates with a computed step at D from event 11 on the northern Calaveras. A moderate rate starting at E' matches that between E and F. The creep is stopped at F by the sequence of events 13-15 on the Busch fault beginning in November 1974. The observed and computed records are essentially flat for more than 3 years between F'-H' and F-H with a recovery in creep at H and H' in 1978. The flat or locked record appears to be initiated by the November, 1974, earthquake. A distant event is modeled G, with an increase in stress but no increase in creep rate. The resumption of creep at H marks the point at which the boundary stress has increased to recover from the disturbance created by the November, 1974, earthquake. The lag in creep is discussed more in a later section.

WRT1 The point by point correlation between observed and computed records at WRT1 is not as striking as at SHR1, but a comparison can be made with the computed record, again delayed by 9 months (Figure 3a). Overall, the average creep rate is higher before 1975 (point F') than after 1975 on both the observed and computed records. The change is roughly correlated with the earthquake sequence on the Busch fault beginning in November, 1974, the same sequence that locked the fault at SHR1. In detail, an increase in rate at A' compares with one at A. A step at B' correlates with one at B. A step and decrease in rate at C' match one at C. Finally a step at D' correlates with a computed step followed by a rapid increase at D. The earthquakes associated with the steps and rate changes at A-F are the same as already discussed for SHR1.

XSJ2 The most striking features of creep at XSJ2 (Figure 3b) are the change from a moderate rate before mid-1972 (point C') to a rapid rate lasting until 1975 and then a return to a moderate rate. The very rapid increase beginning in 1972 correlates with computed steps at B, C, D and E which are directly attributable to events 4-10 (Table 1) along much of the San Andreas fault. Smaller computed steps near F are caused by the Busch fault sequence.

HRS3, CWC3 The two creep meters HRS3 and CWC3, only 3 km apart, are modeled by the same model segment. Again, the most striking feature of the observed and computed records (Figure 3b) is the change from a relatively low rate before 1972 to a fast rate lasting to 1975, then a return to a low rate. A very slight decrease at A' is caused by earthquakes 1 and 2 at Hollister. The rapid creep between B' and E' is correlated with the computed steps at B, C, D and E which are directly attributable to events 4-10 all along the San Andreas fault.

Fault Slip before the Coyote Lake Earthquake

Burford (1976) has pointed out that many moderate earthquakes on the active portion of the San Andreas fault are preceded by precursory periods of anomalously low creep rates. There is some evidence that the rate recovers again shortly before some earthquakes. Similarly, Raleigh et al.

(1979) have noted that the three-year lag in creep at SHR1 on the Calaveras fault might be a precursor to the August 6, 1979, Coyote Lake earthquake. Because the model simulation discussed earlier reproduces the SHR1 creep lag quite well, we can use the model to study the locking process.

The computed stress at SHR1 is plotted with the creep records in Figure 3a. Before the November, 1974, earthquake the computed shear stress equals the frictional stress at SHR1. This is just the boundary condition, equation (3), for any segment that is slipping. At the time of the earthquake the left lateral slip on the Busch fault increases both the normal stress (i.e., the friction) and the applied shear stress. The increase in friction is greater, so the patch becomes locked. The model predicts that slip resumes again in 1978 (point H) when the shear stress has increased enough to meet the friction. The length of the locked period depends on the slip of the Busch fault earthquakes. Larger slip causes a greater increase in friction at SHR1, which takes longer to recover.

The computed slip, averaged over 30 km of the Calaveras fault (8 model segments between points A-A' in Figure 1c), is compared with the geodetically determined average slip (N. King et al., 1980) for the same region in Figure 4. The observed geodetic slip follows a nearly linear trend (slightly concave upward) beginning in mid-1971 until late 1974. A decrease in rate occurs in early 1975, followed by a gradual increase in slip rate for about 4 1/2 years. The apparent large change in geodetic slip rate in 1978, one year before the earthquake, may not be real (W. Prescott, pers. com.) because it is defined by only the single 1978 value. The computed record shows some of the same features. (Note, however, that the computed rate, which was matched to creep, is generally 50-60% of the geodetic rate, suggesting that creepmeters capture only that fraction of the total block offset across the Calaveras fault.) The Busch fault earthquakes lock or decrease the slip rate on much of the Calaveras beginning in November 1974. The locking gradually recovers on more and more segments, causing the average slip to be concave upward.

In summary, a period of decreased fault slip rate beginning in 1975 at creepmeter SHR1 and a questionable one in 1978 detected by geodolite measurements, preceded the 1979 Coyote Lake earthquake. There is no proof that these are precursors to the earthquake, but they do fit the pattern of precursory creep lags suggested by Burford (1976) for earthquakes on the San Andreas fault. The model results suggest that the creep lag beginning in 1975 was directly caused by the 1974-1975 earthquakes on the Busch fault. While only simple friction is included in the model, it appears that a rate-dependent (or aging) fault law, which causes strength to increase with decreased slip rate (Dieterich, 1979) would enhance the locking and possibly lead to instability. Even without such a law, it seems likely that the Coyote Lake earthquake was not an entirely random or spontaneous event, but rather a direct result of conditions set up by the November 1974 earthquake.

Computer Slip Before Other Earthquakes

The pattern of creep lags in an epicentral region caused by prior earthquakes is evident for several other events in the simulation. Computed slip histories at the epicenters of modeled events 5-9, 12-15, 17, and 18 are plotted in Figure 5. Creepmeters are not available at many of these sites, so it is important to remember that these are only model results. The slip at events 1-3 is not plotted because the events occur too early in the simulation for their preseismic slip to be examined. Events 4, 10, 11, and 16 are not plotted because they lie close to the model edges and may be influenced by events just outside the model that are not included. The star on each computed curve marks the time of the earthquake occuring at that model segment.

The fault at the site of the January, 1974, earthquake on the Sargent fault (event 12) is locked beginning in late 1969 (point A), by the 1969-1970 events at Hollister. In this case locking occurs because the frictional stress is increased by the events, while the shear stress is relaxed. The creep rate begins to recover in late 1970 (point B), but decreases again in late 1973 (point C), apparently due to earthquake 11 in 1973 on the Calaveras fault.

The computed slip before events 6-8, near San Juan Bautista (plotted for two adjacent model segments), becomes locked beginning in late 1969-early 1970 (point D) due to events 1-3 near Hollister. The locking occurs because the shear stress is slightly relaxed by the earthquakes, while the friction stays essentially the same. The computed creep rate begins to increase in late 1970 and is nearly up to the 1969 rate when the earthquakes 6-8 occur in late 1972. Events 5 and 9 farther south on the San Andreas are preceded by very slight (perhaps insignificant) decreases in computed creep rate (points E and F). Again the creep rate is recovered up to the 1969 rate during the year before the earthquakes.

The computed slip at the epicenter of the August 6, 1979, earthquake on the Calaveras fault (event 18) shows a slight decrease in slip rate at points G and H. Event 11 occurred $\sim$11 km to the northwest at point J. A very slight decrease in slip rate occurs at point K resulting from the Busch fault earthquakes, but the locking is not nearly as prounounced as that measured at the SHR1 creepmeter 20 km to the southeast.

The computed creep on the Busch fault (events 13-15) is stopped in late 1969-early 1970 (point L) by the Hollister earthquakes. In this case readjustments following the Hollister events decrease both the frictional stress and shear stress on the Busch fault, but the shear stress decreases faster, causing the locking. Creep on the Busch fault begins again in late 1970 but stops again in early 1974 (point M) following the January, 1974, earthquake on the Sargent fault.

To summarize, the model predicts periods of lower than average slip rate preceding some of the moderate earthquakes in the simulation. The

computed low slip rates are caused by earthquakes elsewhere in the simulation. Whether or not these low rates are premonitory or part of the failure process cannot be determined, however, since the model cannot predict instability.

Discussion and Conclusions

A theoretical model has been presented for fault slip and stress on interacting faults near Hollister, California. The results of a steady simulation suggest that the observed density of earthquakes is correlated with the long term calculated normal stress on the fault, or if simple friction is assumed, with shear stress. Alternatively, the seismicity may be correlated with the computed energy dissipation rate on the fault: actively creeping sections with low levels of seismicity might be those with low computed energy dissipation; sections with higher seismicity, including frequent moderate earthquakes, might be those with higher computed energy dissipation. Thus, the distinction between actively creeping faults with minor seismicity and faults with larger earthquakes might be due to geometry.

A nonsteady simulation of slip during 1969-1979 is made by superimposing stress drops from moderate earthquakes onto an otherwise steady model. The simulation is matched to creep data by adjusting the remote stress loading rate, coefficient of friction, and the earthquake stress drops. The simulation reproduces many long term features of observed slip including coseismic steps, changes in creep rate, and transient fault locking; individual creep events are not predicted. The close agreement leads to several conclusions:

(1) Trends in surface creep seem to mimic the slip expected in the depth range of brittle seismicity, although the response of the shallow fault zone material may introduce a delay.

(2) The slip model adjusted to match fault creep at 5 sites resembles changes in long-term geodetic slip rate averaged over 30 km of the Calaveras fault. The geodetic slip is nearly a factor of 2 larger, however, suggesting that only a fraction of the fault zone is sampled by creepmeters on the Calaveras fault.

(3) The modeled slip rate at most points is influenced by most of the larger earthquakes lying within several 10's of kilometers, even when those earthquakes are on other faults. That is, the various faults seem to interact.

(4) It has been suggested (Burford, 1976) that many moderate earthquakes along the San Andreas fault in central California are preceded by periods of anomalously low creep rate. The model results predict a decrease in slip rate before some earthquakes, and in each case, these are the direct result of an earthquake somewhere else in the fault system. In particular the model reproduces quite well the decrease in slip rate before the 1979 Coyote Lake earthquake and indicates that the decrease was a direct result of the 1974 sequence of earthquakes on the Busch fault.

REFERENCES

Allen, C. R. and Smith, S. W., 1966, Parkfield earthquakes of June 27-29, Monterey and San Luis Obisbo Counties, California. Pre-earthquake and post-earthquake surficial displacements: Seismological Society of America Bulletin, v. 56, p. 966-967.

Bakun, W. H., Stewart, R. M., Bufe, C. G., and Marks, S. M., 1980, Implication of seismicity for failure of a section of the San Andreas fault: Seismological Society of America Bulletin, v. 70, p. 185-202.

Brown, R. D., 1970, Faults that are historically active or that show evidence of geologically young surface displacement, San Francisco Bay Region. A progress report: Oct. 1970: U.S. Geological Survey Miscellaneous Field Studies Map MF-3.

Bufe, C. G. and Nason, R. D., 1973, Creep, strain, and seismicity in the vicinity of Stone Canyon Observatory, Earthquake Research in NOAA, 1971-1972: National Oceanic and Atmospheric Administration Technical Report ERL256-ESL28.

Burford, R. O., Allen, S. S., Lamson, R. J., and Goodreau, D. D., 1973, Accelerated fault creep along the central San Andreas fault after moderate earthquakes during 1971-1973, in Proceedings of the Conference on Tectonic Problems of the San Andreas Fault System, Proceedings: Stanford University Publications, Geological Science 13, p. 268-274.

Burford, R. O., 1976, Fluctuations in rates of fault creep associated with moderate earthquakes along the central San Andreas fault: EOS, American Geophysical Union Transactions, v. 57, p. 1012.

Crouch, S. L., 1976, Solution of plane elasticity problems by the displacement discontinuity method: International Journal for Numerical Methods in Engineering, v. 10, p. 301-343.

Delaney, P. T., and Pollard, D. D., 1981, Deformation of host rocks and flow of magma during growth of minette dikes and breccia-bearing intrusions near Ship Rock, New Mexico: U.S. Geological Survey Professional Paper (in press).

Dieterich, J. H., 1979, Modeling of rock friction. 1. Experimental results and constitutive equations: Journal of Geophysical Research, v. 84, p. 2116-2168.

Irwin, W. P., and Barnes, 1975, Effect of geologic structure and metamorphic fluids on behavior of the San Andreas fault system in central and northern California: Geology, p. 713-716.

King, C.-Y., Nason, R. D., and Burford, R. O., 1977, Coseismic steps recorded on creep meters along the San Andreas fault: Journal ofGeophysical Research, v. 82, p. 1655-1661.

King, N. E., Savage, J. C., Lisowski, M., and Prescott, W. H., 1981, Preseismic and coseismic deformation associated with the Coyote Lake, California, earthquake: Journal of Geophysical Research, v. 86, B2, p. 892-898.

Minster, J. B., and Jordan, T. H., 1978, Present day plate motions: Journal of Geophysical Research, v. 83, B11, p. 5331-5354.

Nason, R. D., 1973, Fault creep and earthquakes on the San Andreas fault in Conference on tectonic problems of the San Andreas fault system, Proceedings: Stanford University Publications, Geological Science 13, p. 275-285.

Raleigh, B., Stuart, W., and Harsh, P., 1979, Creep on the Calaveras fault near Coyote Lake (abs.): EOS, American Geophysical Union Transactions, v. 60, no. 46, p. 890.

Savage, J. C., Spieth, M. A., and Prescott, W. H., 1976, Preseismic and coseismic deformation associated with the Hollister, California, earthquake of November 28, 1974: Journal of Geophysical Research, v. 81, p. 3567-3574.

Scholz, C. H., Wyss, M., and Smith, S. W., 1969, Seismic and aseismic slip on the San Andreas fault: Journal of Geophysical Research, v. 74, p. 2049-2069.

Segall, P., and Pollard, D. D., 1981, Mechanics of discontinuous faults: Journal of Geophysical Research (in press).

Weertman, J., and Weertman, J., 1964, Elementary disloction theory: New York, MacMillan Co., 213 p.

Table 1. Earthquakes included in the nonsteady simulation.

	Date (yr.mo.day)	Time (GMT)	Lat.	Long	Depth (km)	Mag.*
1	691027	1059	36 47.48	121 22.65	10.9	4.5
2	691115	2058	36 46.24	121 21.78	11.3	4.1
3	700331	0702	36 52.06	121 24.47	11.3	4.5
4	720224	1556	36 34.69	121 12.54	7.5	5.0
5	720904	1804	36 37.48	121 16.46	5.7	4.6
6	720923	1507	36 47.58	121 31.57	6.8	4.1
7	721003	0630	36 48.15	121 31.73	5.0	4.8
8	721003	1110	36 48.82	121 32.71	5.1	4.0
9	730115	0943	36 40.32	121 20.02	6.3	4.1
10	730622	0129	36 33.79	121 12.29	9.6	4.2
11	731003	1007	37 12.26	121 35.12	4.7	4.6
12	740110	1122	36 57.08	121 35.71	7.7	4.3
13	741128	2301	36 54.96	121 28.68	5.8	5.1
14	741231	2022	36 55.96	121 28.01	8.7	4.3
15	750303	1134	36 56.03	121 28.25	7.8	4.2
16	771215	1115	36 35.00	121 13.50	10.0	4.2
17	790802	2143	36 48.34	121 32.64	5.0	4.0
18	790806	1705	37 6.59	121 30.68	6.8	5.9

*Events 1-16 have local magnitudes; events 17 and 18 have coda magnitudes.

Table 2. Creepmeters compared with the nonsteady results.

	Latitude	Longitude
CWC	36 45.0'	121 23.1'
HRS	36 46.3'	121 25.3'
SHR	36 56.6'	121 26.7'
WRT	36 52.2'	121 24.8'
XSJ	36 50.2'	121 31.2'

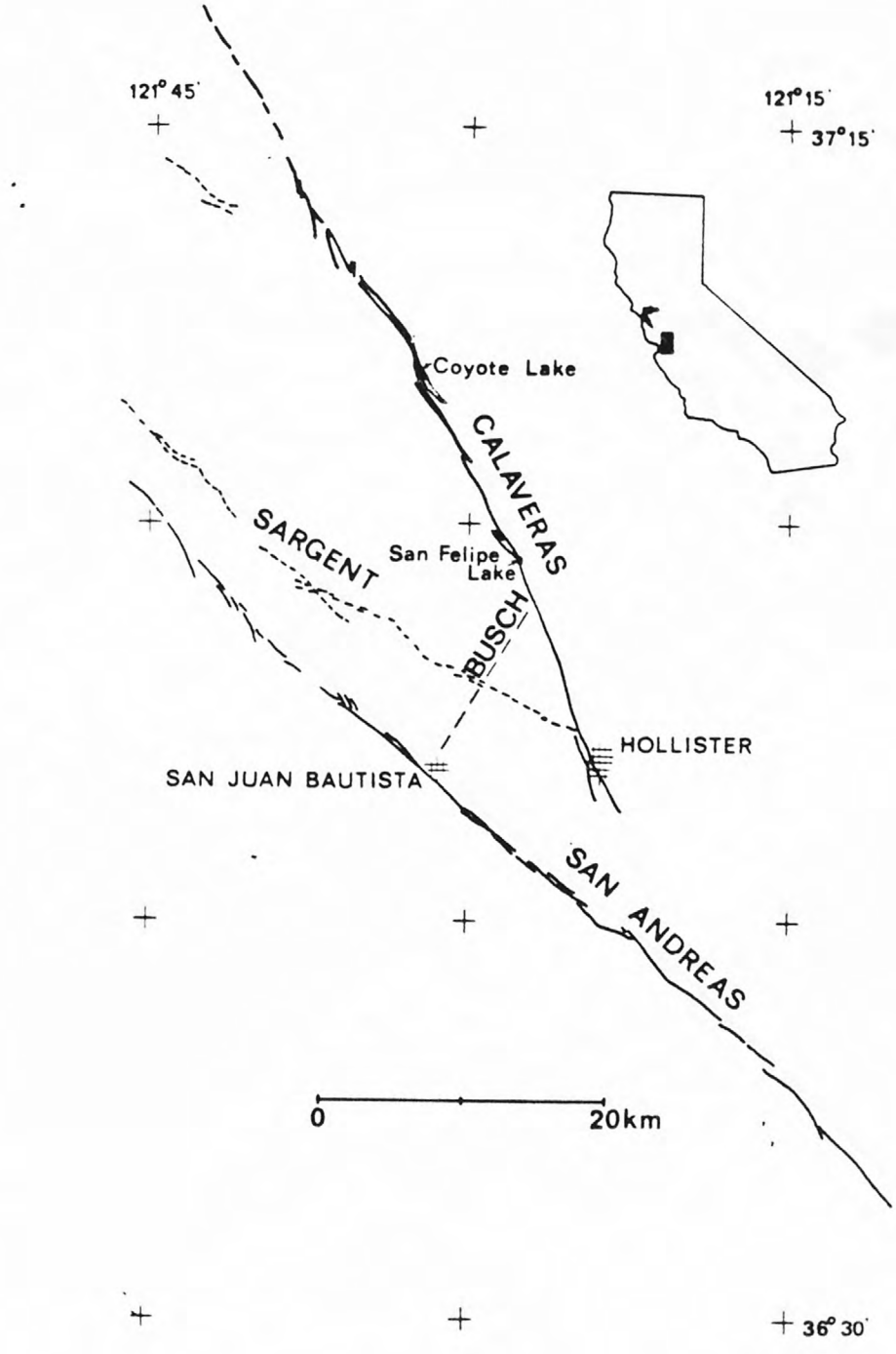

Figure 1(a): Portions of the San Andreas, Calaveras, Sargent, and Busch faults near Hollister, California (from a map by Brown [1970]).

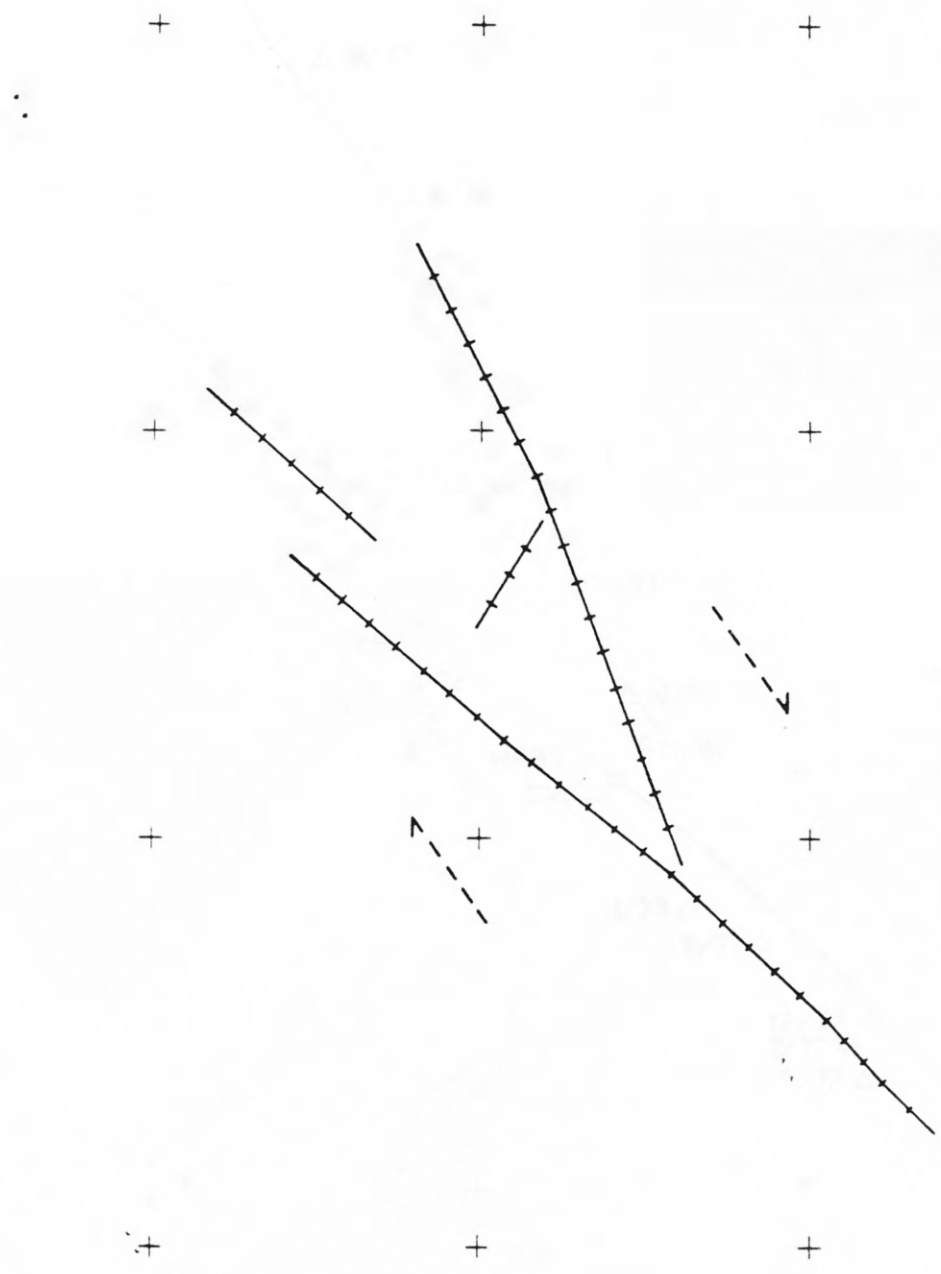

Figure 1(b): Model of the faults in Figure 1(a) for the steady simulation. Tic marks show the 53 individual segments. Dashed arrows show the orientation of the maximum remote shear stress.

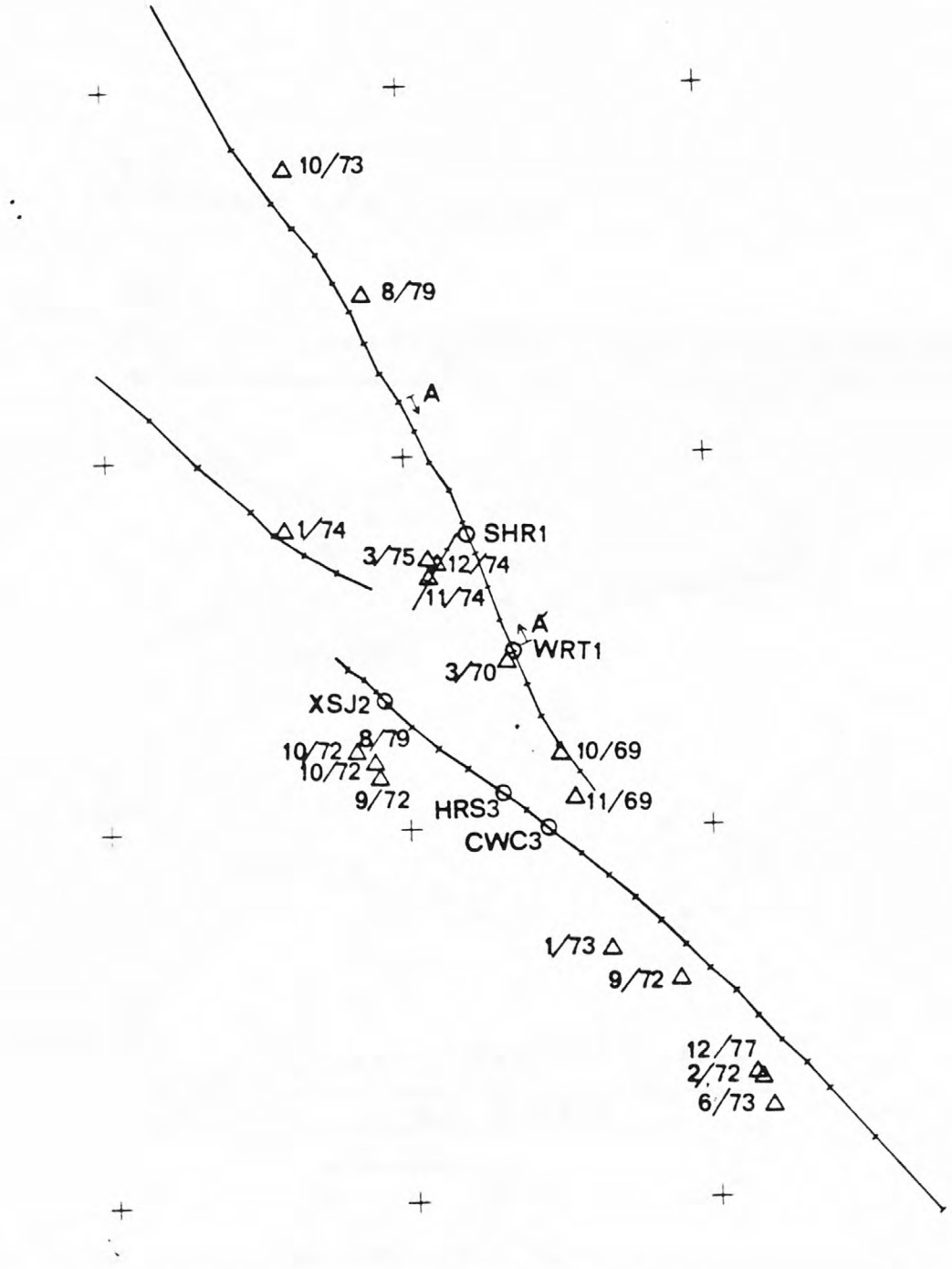

Figure 1(c): Model of the faults in Figure 1(a) for the nonsteady simulation. Triangles with dates show epicenters for earthquakes with magnitude greater than 4. Open circles are creepmeters. Letters A-A' mark the section of the Calaveras fault described in Figure 4.

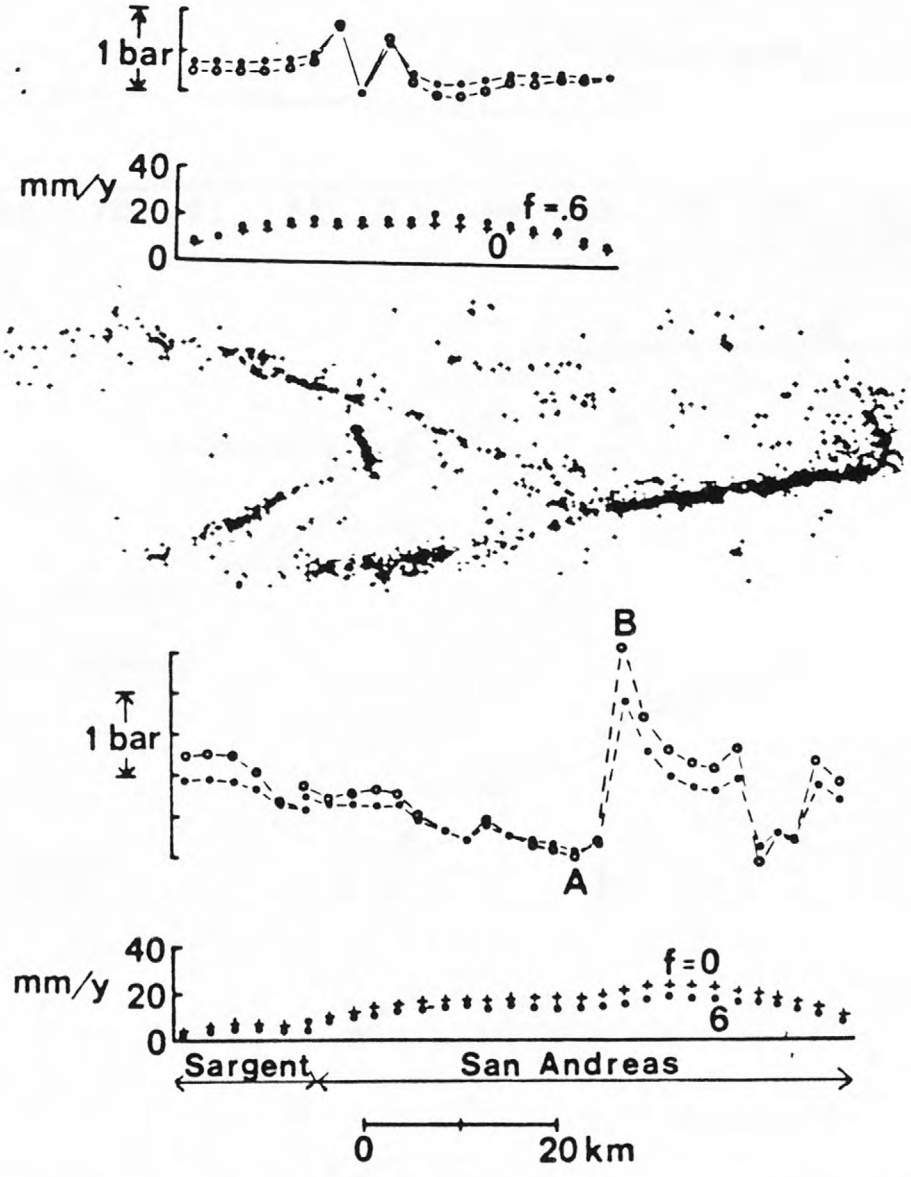

Figure 2: Results of the steady simulation. Map in the center shows epicenters for earthquakes larger than magnitude 2 during 1970-1979. At the top, computed fault shear stress and slip rate are plotted as a function of position along the Calaveras fault. Plots and map have the same distance scale. At the bottom, shear stress and slip rate are plotted for the Sargent and San Andreas faults. Stress plots compare two time steps in a simulation with coefficient of friction f=0.6: closed circles first, compared with open circles two years later. Slip rates are shown for two different simulations with coefficients of friction f=0 and f=0.6.

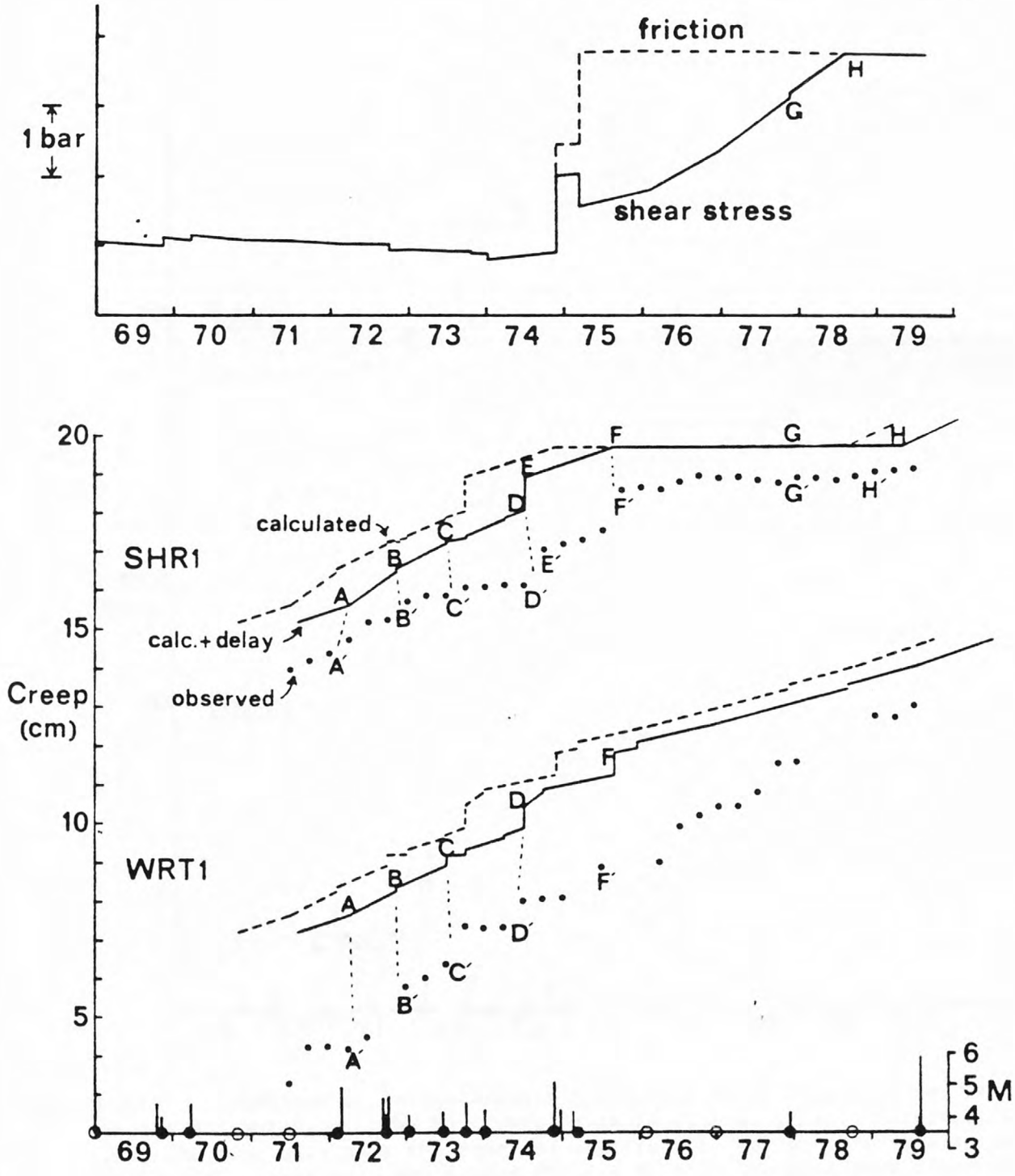

Figure 3(a): Comparison of observed fault creep with fault slip computed from the nonsteady simulation. The horizontal axis is time in years. Vertical lines along the time axis show the time and magnitude of earthquakes used in the simulation. Large open and closed circles on the time axis show times of computational time steps; the closed circles represent time steps with specified stress drops. (a) Observed and computed fault creep at creepmeters SHR1 and WRT1 on the Calaveras fault. Dotted curve is observed creep. Dashed curve is computed slip. Solid curve shows the computed slip delayed 9 months. In addition, computed fault shear stress (solid curve) and frictional stress (dashed curve) at SHR1 are shown at the top.

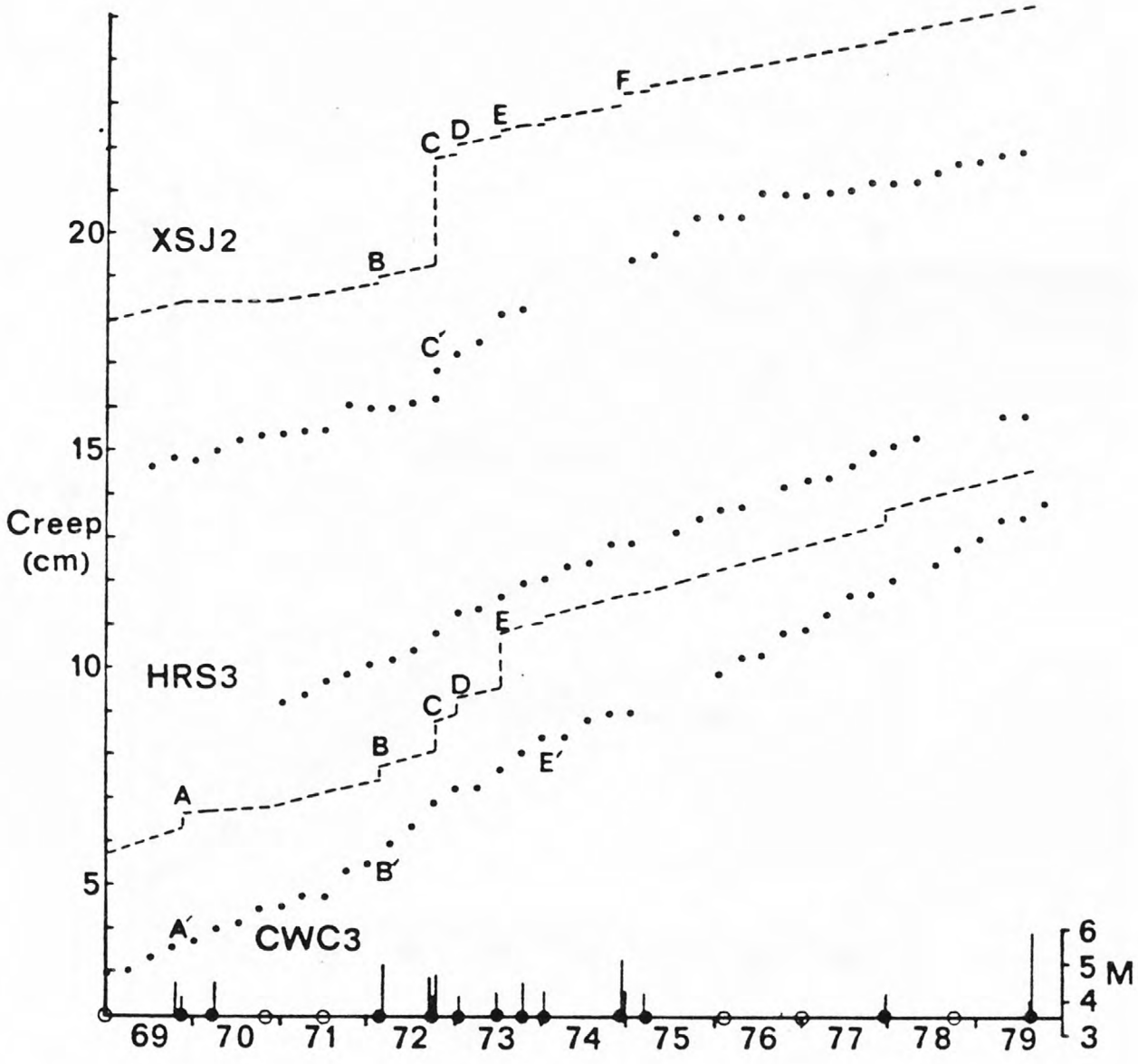

Figure 3(b): Comparison of observed fault creep with fault slip computed from the nonsteady simulation. The horizontal axis is time in years. Vertical lines along the time axis show the time and magnitude of earthquakes used in the simulation. Large open and closed circles on the time axis show times of computational time steps; the closed circles represent time steps with specified stress drops.
(b) Observed (small dots) and computed (dashed curves) slip at creepmeters XSJ2, HRS3, and CWC3 on the San Andreas fault.

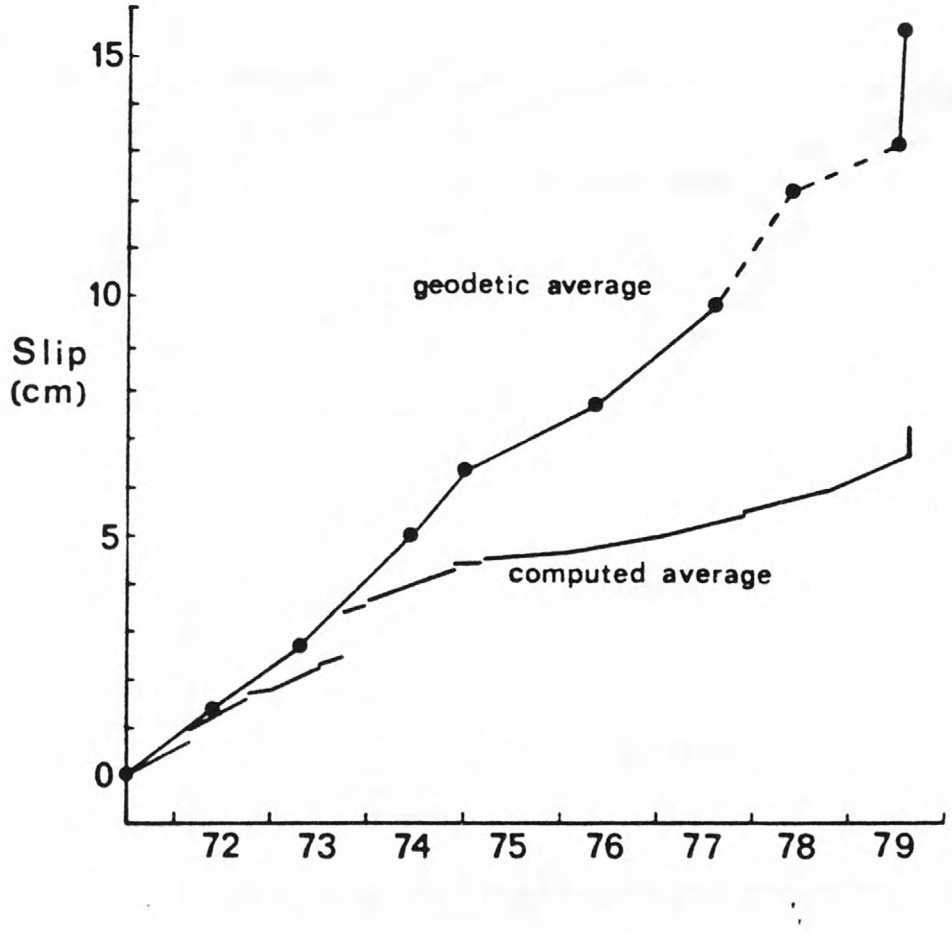

Figure 4: Comparison of geodetically determined slip (N. King et al., 1980) and computed slip on Calaveras fault. Large dots show the times of geodetic surveys.

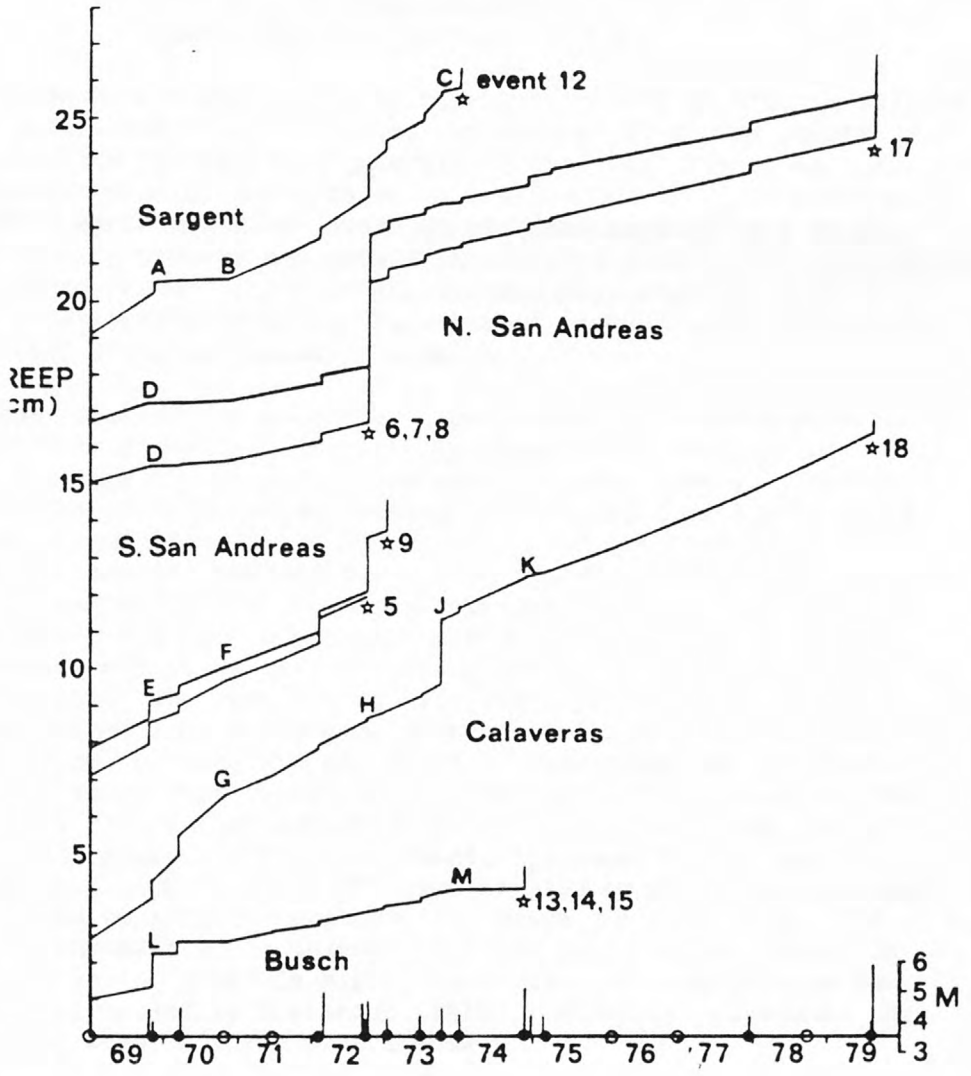

Figure 5: Modeled fault slip prior to several moderate earthquakes computed at the epicenters of those earthquakes. The top curve shows the computed slip near the epicenter of event 12 (Table 1) on the Sargent fault. The second and third curves show the slip on two adjacent model segments near the epicenters of events 6-8 near San Juan Bautista. The fourth curve shows slip near the epicenter of event 9, and so on. The star on each curve shows the time of the earthquake occurring at that site. Letters A-M mark features referred to in the text.

FAULT INSTABILITY MODELS WITH PRECURSORY SLIP

James H. Dieterich
U.S. Geological Survey
Menlo Park, California, U.S.A.

Although earthquake fault slip in many ways resembles brittle failure of initially intact materials, detailed representation of the mechanical properties of faults suitable for generalized analysis introduces constitutive features not usually encountered in brittle failure. In particular, because repeated earthquakes can occur on the same segment of a fault, some type of healing process not usually associated with brittle phenomena must take place to restore the strength between slip events. This paper summarizes a constitutive model for faults that is based upon experiments with artificially prepared faults in rocks.

Experiments demonstrate competing time-, velocity-, and displacement-dependence of fault strength. Strength is observed to increase with the logarithm of the time that the fault is nominally stationary. Initiation of sliding results in displacement weakening and stabilization of fault strength at a residual level that is a function of slip velocity. Observations of transient and residual velocity-dependent effects indicate a competition between a direct velocity-dependent process that operates continuously during slip and a process inversely dependence on velocity that becomes fully effective only following a finite displacement, d_r, at a specific velocity. The residual velocity-dependent effect results in strength changes that are of the same or opposite sign of the velocity change depending on the relative magnitude of the competing processes. Experiments with gouge show variations in the magnitude and sign of the residual velocity effect that appear to be correlated with the rate of comminution of the gouge. The displacement, d_r, required to reach a residual strength following the initiation of slip or following a change of velocity scales by surface roughness and gouge particle size. The parameter d_r is insensitive to thickness of the gouge layer indicating that deformation in the gouge is highly localized. A constitutive law of the general type proposed by Dieterich (1979) adequately represents the range of behavior seen in these experiments.

A simple deterministic spring-slider model that employs this constitutive law reproduces, in detail, the range of effects observed in laboratory experiments and for natural fault slip, including constant velocity fault creep, fault creep events, and unstable fault slip. Accelerating premonitory slip precedes all unstable slip events. Simulations with a plane strain model and laboratory experiments show that inhomogeneity of shear stress along the fault relative to fault strength increases the magnitude of premonitory fault creep displacement.

Reference

Dieterich, J. H., 1979, Modelling of rock friction, Pt. 2. Simulation of preseismic slip: Journal of Geophysical Research, v. 84, no. B5, p. 2169-2175.

HYPOCENTER DISTRIBUTION OF ACOUSTIC EMISSION UNDER UNIAXIAL COMPRESSION TEST

Kinichiro Kusunose, Osamu Nishizawa, and Koji Ono
Geological Survey of Japan

Rocks under high compressional stress emit elastic waves of high frequency from microfractures. It is called AE (acoustic emission). The earthquake phenomenon is understood as a sudden faulting of rocks in the earth's crust and upper mantle. Therefore, if we can obtain the precise scaling law between AE and the earthquakes, we will understand natural earthquakes better and can apply the experimental results to improve the reliability of the earthquake prediction techniques. With this in mind, we are performing the 'experimental seismology' at the Geological Survey of Japan. We began with the study of the distribution of AE hypocenters and their focal mechanisms.

Uniaxial compression tests were performed on dry cylindrical granite and andesite specimens (100 mm in length and 50 mm in diameter). Nine piezoelectrical transducers of compressional mode with resonant frequency of 2 MHz were stuck on the specimen to detect AE. Amplified wave trains were recorded by a data recorder. Axial and radial elastic wave velocities were detected by the same transducers that detect AE. AE hypocenters were determined from P-wave arrivals time with correction of velocity anisotropy.

The following results became clear from our experiment:

(1). The hypocenter distribution of AE can be used to determine the fault plane location and orientation. As shown in Figure 1, both the location and the direction of the clusters of the hypocenter agree with those of the fault planes.

(2) It is concluded that, in rock specimens, AE are not radiated from the tensile-type but from the shear-type cracking. The fault plane solution of the quadrant type have been obtained from the P-wave initial motion directions.

(3). Just before a large AE is radiated, a seismic gap is observed in some cases. The large AE itself is followed by an aftershock sequence. We expect that this time-space relationship of AE, similar to that of natural large earthquakes, provides us a clue for explaining the mechanism of the seismic gap formation.

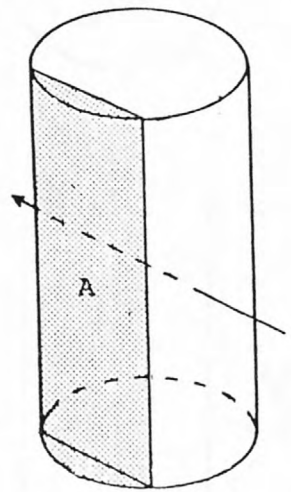

(a)

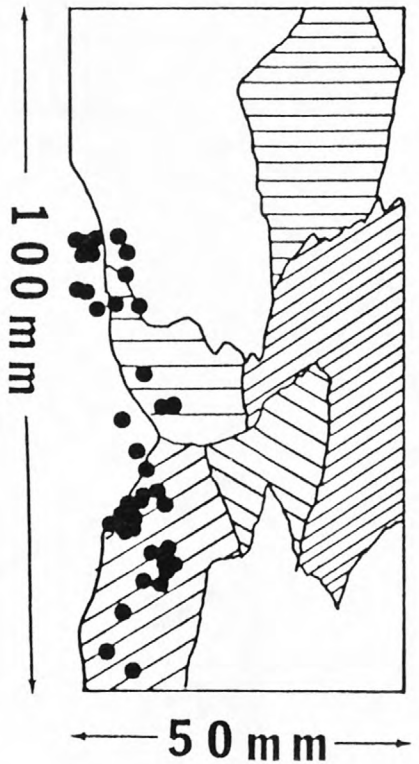

(b)

Fig. 1. Observed faults and AE hypocenters. To avoid complication, hypocenters located within volume A in figure (a) are plotted in figure (b).

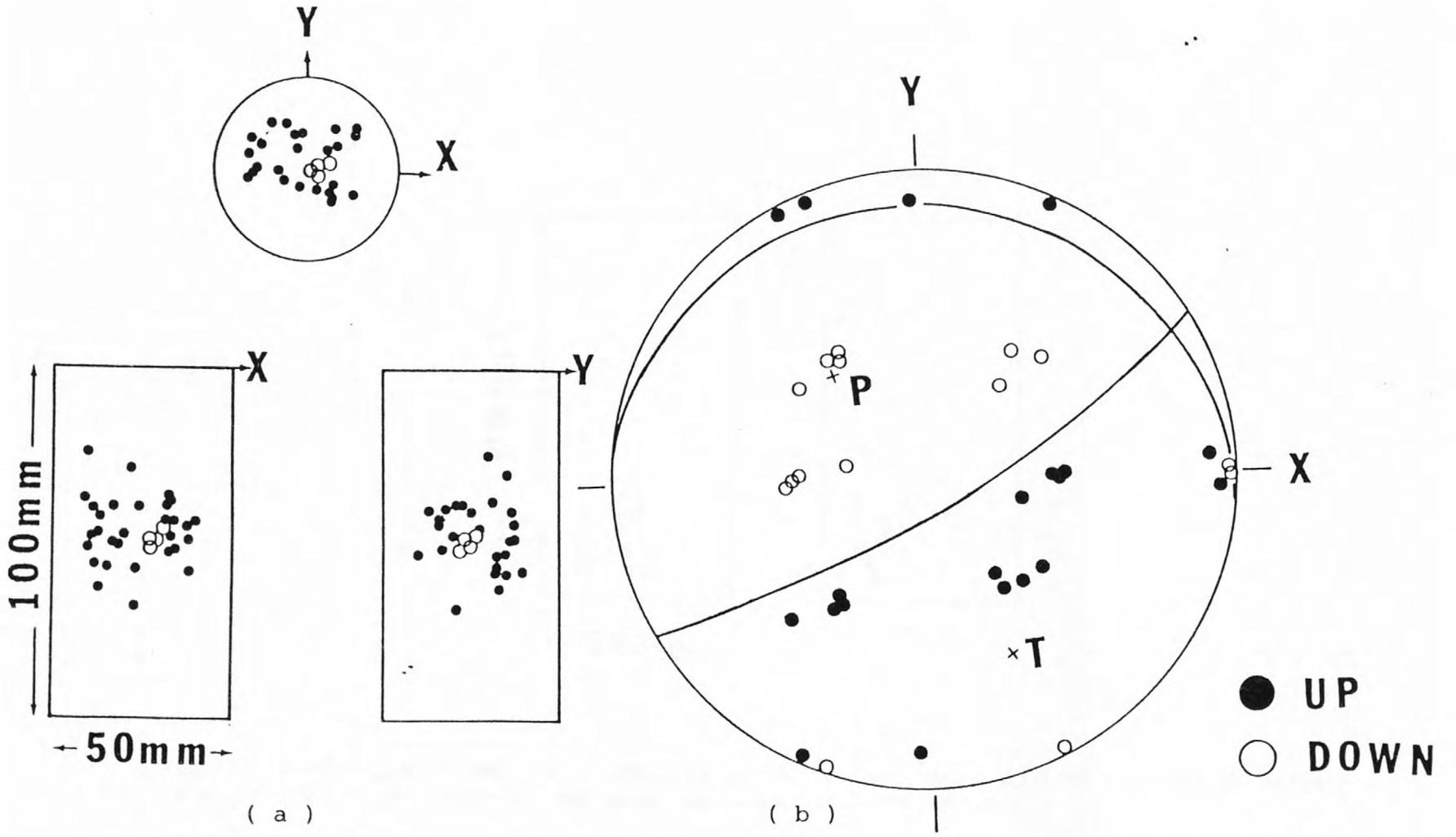

Fig. 2. Focal mechanism solution of AE. The solution (upper hemisphere equal area projection) was obtained by superposition of P-wave initial motion direction of AE shown by open circles in figure (a).

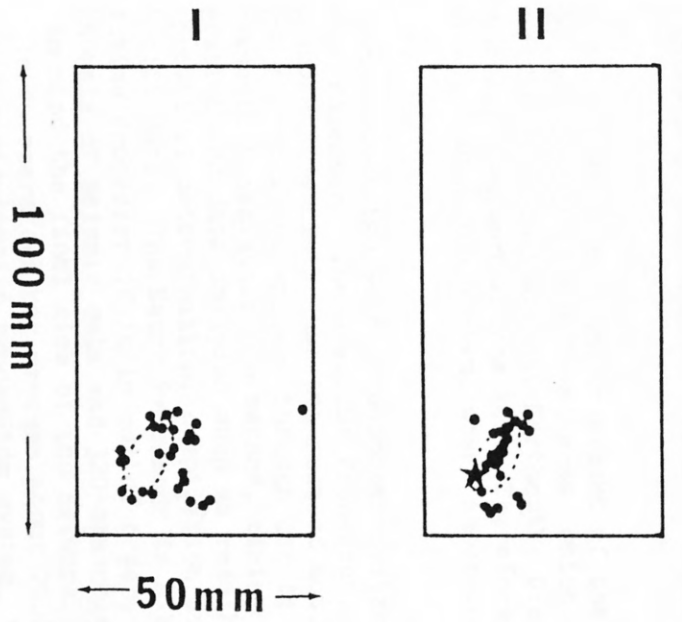

Fig. 3. Seismic gap of AE. I. Before large AE. Dashed line encircles the area of seismic gap. II: Large AE and its aftershocks. The star indicates the large AE.

DATA PROCESSING OF THE KANTO-TOKAI OBSERVATIONAL NETWORK FOR MICROEARTHQUAKES AND GROUND TILT

S. Matsumura, K. Hamada, Y. Katsuyama, M. Ishida, and T. Ohkubo
National Research Center for Disaster Prevention

Abstract

A data processing system by electronic computers has been developed in order to process the seismic and crustal tilt data from the Kanto-Tokai Observational Network of the National Research Center for Disaster Prevention (NRCDP).

The observation by the NRCDP network is a part of the continuous monitoring of crustal activities in the Tokai area, which is assigned as the Area under Intensified Measures against Earthquake Disaster based on the Large Scale Earthquake Countermeasures Act. Therefore, the processing system is a prediction-oriented system, where short-term prediction is stressed.

The system is composed of two sets of computer system: a Realtime Processor and a Batch Processor. The Realtime Processor, which is an automatic operation around the clock, has the role of monitoring crustal activities and filing the data transmitted through the telemetry system. The Batch Processor adopts a semiautomatic method, taking into consideration human interpretation for data analyses such as reading of seismic wave parameters, hypocentral determination, compilation and displaying of seismic and crustal tilt data. The Batch Processor is also a relief machine for the Realtime Processor if it is out of order. This system is designed for 198 channels of seismic data and 320 channels of crustal tilt data, bearing in mind the final size of the network, which will be completed in 1984. Three operators can process about 2000 earthquakes per month by using this semiautomatic processing system; that is sufficient capability for the present network in progress in the Kanto-Tokai area.

The data processing system has made possible on-line monitoring of crustal activities to some extent, and is unique as a prediction-oriented system.

I. Introduction

A program to construct a telemetry network for observation of microearthquakes and crustal tilt in the Kanto-Tokai area has been carried out by the National Research Center for Disaster Prevention (NRCDP). By the end of fiscal year 1980, the number of observational stations had reached 40, including three deep borehole observatories at Iwatsuki, Shimohsa, and Fuchu (see Fig. 1). All the data are telemetered to the NRCDP through telephone lines and recorded by both analog recorders and a computer system (cf. Ohtake, et al., 1979).

The Tokai area is assigned as the Area under Intensified Measures against Earthquake Disaster based on the Large Scale Earthquake Countermeasures Act. The observational network of the NRCDP is part of a continuous monitoring system of crustal activities operated by government organizations and universities, and is expected to detect any precursor of a large earthquake. Therefore, the data processing system adopted by the NRCDP is a short-term prediction-oriented system.

To make short-term prediction effective, continuous monitoring of the crustal activities is essential. By using a computer on line with the telemetry system, automatic monitoring of frequency of earthquake occurrence and crustal tilt change at each station is now possible; current information, and alarms when any abnormal change is detected, can be obtained at any time.

Moreover, this computer system responds to the demands of processing large amounts of data. The main routines of the current data processing are:

(1) to count and display frequencies of earthquake occurrence detected at each station,
(2) to compute hypocenters of earthquakes observed,
(3) to plot hypocentral maps regularly every ten days and every month, and
(4) to display crustal tilt change at each station.

At the present stage, most of the data processing is carried out by a few members of the staff. However, the volume of data to be processed is increasing and likely to overflow the capacity of processing as the construction of the network proceeds. Table 1 summarizes the number of seismograms manually processed from multichannel pen-records in 1980. The total number of seismograms visually read and the number of earthquakes detected were about 60,000 and 10,000, respectively; one-third of the detected earthquakes were located as shown in Figure 2. By the end of 1984, when the network is completed, the number of observation stations will be more than 60, and the number of seismograms to be processed will come to about 200,000 per year, which will require at least 16 persons to process the data if the processing method is not improved.

The data processing system is composed of two sets of computer systems for NRCDP exclusive use. It has been under development since 1978, and will be in routine-base operation in the latter half of 1981. The hardware and software which constitute the system are described below.

II. General Flow of Processing and Composition of Hardware

The general flow of the data processing is shown in Figure 3. The routine is divided into two parts: realtime processing and batch processing, which are carried out by using the Realtime Processor (RP) and the Batch Processor (BP), respectively.

The roles of the RP are (1) to monitor crustal activity on an on-line basis and give warnings automatically when any abnormal change occurs, and (2) to file the data from seismographs and tiltmeters into both magnetic tapes (MT) and disks (DK). The MT is used by the BP. The DK is used for monitoring by the graphic display device (GD). The RP is in automatic operation around the clock.

The main function of the BP is to process efficiently the data which have been filed by the RP, as well as (1) to read seismic wave parameters by semiautomatic method followed by computing hypocenters and to display hypocentral maps, (2) to display daily and hourly frequencies of earthquake occurrence, and (3) to compile and display crustal tilt change. Besides these routine works, the BP has two other roles. One is to back up the RP if it is out of order; the other is to answer requests for emergency data processing whenever abnormal crustal activity takes place. In such an emergency case, a special observational team is organized and offers hot information to the Assessment Committee for the Area under Intensified Measures against Earthquake Disaster in the Japan Meteorological Agency. Details of these operations are explained in sections III and IV.

The hardware compositions of the RP and the BP are shown in Figure 4. Both the systems are composed of a HITAC-20 as the Central Processor Unit (CPU) and peripheral equipment manufactured by the Hitachi Corporation. Representative values of processing ability are listed in Table 2 for both the RP and the BP. High-speed data transmission between GD and MEM of the BP makes a special feature of the semiautomatic method. That makes it possible to draw a picture about twenty times as fast as usual.

III. Realtime Processing

The data flow chart of realtime processing is shown in Figure 5. The RP is on line with the telemetry system (telemeters and JJY standard clock), and digital data from seismographs and tiltmeters are transmitted into the computer through the interface device (IF), where the data are preliminarily rearranged in one-second data packs of 8400 W every second. The data are allotted ten blocks; nine blocks for seismic data (22 channels for each block) corresponding to the nine regional blocks (see Figure 1), and one block for crustal tilt data (320 channels). Data for each block are independently recorded on magnetic tapes and disks. This blocking of the data is done in order not to record useless signals.

1) Crustal tilt data. Crustal tilt data are transmitted to the computer every one second, and one sample per minute as a rule is recorded in a disk file, which has space to store the data for eight days. The data in the disk file are transferred to magnetic tapes every week in order to keep continuously recording. When a triggering condition is satisfied, the data sampled every second are recorded in another disk file with a space of 24 minutes. The triggering condition is when

differences in the crustal tilts between two successive data exceed predetermined threshold levels at multiple stations. By this method, long-period 'seismograms' by tiltmeters are obtained.

2) Seismic data. Seismic data sampled at 80 Hz are not continuously recorded, but extracted data are recorded on a magnetic tape and a disk with a delay time of 30 seconds, only when a triggering condition is satisfied. The magnetic tape is used in the secondary processing by the BP and the disk is used for monitoring by the graphic display device.

The triggering condition is as follows: Calculations by digital filtering and integration are carried out for each item of channel data. When these values exceed predetermined threshold values for three successive seconds at two or more channels of a station, it is judged that a seismic wave has been detected at the station; that is called a station-onset. Then a message about the detection time, the station code, and the wave duration is typewritten on the data typewriter as shown in Figure 6. Recording of the data on a magnetic tape and a disk is carried out when the station-onsets are triggered for three or more different stations within a time interval of 30 seconds, which covers differences in arrival times of P waves among the stations. Such a triggering condition is designed to avoid noise and to catch all seismic signals. Four 2400-ft magnetic tape handlers are used in turn to file the seismic data. One cycle of recording covers about ten days' data under conditions of ordinary seismicity and the present number of observational stations.

3) Frequency of earthquake occurrence. Frequency of earthquake occurrence is automatically counted for each station assuming that one station-onset signal corresponds to one earthquake. Hourly frequency is regularly tabulated on the data typewriter at midnight every day, and can be typed out every hour when requested. Those data, once stored in a disk file of the RP, are transferred to a large disk file of the BP every month.

4) Warning against abnormal change of crustal activity. When an abnormal change of crustal activity is found by the RP, an alarm signal is generated by the digital output device (DO2 and DO3 in Fig. 4: relays), and a warning message is typewritten. For seismic data, the relay is switched on when the hourly frequency of earthquake occurrence exceeds a predetermined number for two successive hours. In the case of crustal tilt, the current value is always compared with that of 24.5 hours before, and the relay is switched on when the difference exceeds a predetermined threshold value for five successive minutes. The interval of 24.5 hours was found most effective for rejecting the influence of the earth tide. Each bit of DO2 (64 bits) and DO3 (32 bits) in Figure 5 is assigned to an earthquake and crustal tilt observation station, so that the location of the abnormal state can be immediately identified.

5) Monitoring messages. Detection of earthquake, warning, etc. are indicated by monitoring messages on the data typewriter as shown in Figure 6. The messages are as follows:

GOVR indicates that the value of crustal tilt exceeds the recording range.

GMOV indicates that difference of crustal tilt between two successive minutes exceeds a predetermined threshold value.

GABN. warns that an abnormal change of crustal tilt has been found by the procedure explained in 4).

EABN also warns that an abnormal number of earthquakes has been counted by the procedure explained in 4).

ETRG indicates a station-onset.

6) Support programs. Besides the realtime processing program, various kinds of support programs such as displaying program, labeling program, constant-setting program, etc., have been prepared and can be operated at the back of the realtime processing program. The data stored in the disk can be displayed on the graphic display device at any scale requested by the displaying program, examples of which are shown in Figure 7.

IV. Batch Processing

The flow chart of the batch processing is shown in Figure 8. It includes 1) data analysis of seismic waves, 2) displaying of frequency of earthquake occurrence, and 3) displaying of crustal tilt change.

1) Data analysis of seismic waves. This process is composed of three steps. The first step is to store the seismic data temporarily in a disk file. At the same time an information table is produced which includes the earthquake number, station codes, station-onset times determined by the RP, maximum amplitudes and wave durations. Wave parameters to be read in the routine work are arrival times of P and S waves, polarity of P initial phase, maximum amplitude and wave duration, the latter two of which are automatically determined in the first step. The first step takes about 30 minutes for seismic data recorded in one volume of 2400-ft magnetic tape. The second step is to read the other wave parameters by using the graphic display devices. Figure 9 is an example of a displayed picture in which 15 traces of five stations are shown. It takes about 8 seconds to display the whole picture on the graphic display with high-speed data transmission. Short vertical bars in this picture indicate the positions of P arrival times automatically read by the computer, as explained in the Appendix. When the automatic reading is not correct, an interpreter can correct it by pointing the exact position with a cross cursor. The picture can be enlarged or reduced when necessary. The arrival times of S waves and polarities of the P initial phases are read by the interpreter. After reading of wave parameters, hypocentral determination is carried out by using the P travel-time table by Ichikawa and Mochizuki (1971) whenever the earthquake

is detected by five or more stations. Earthquake magnitude is computed from the maximum amplitude based on Watanabe's (1971) formula and from the total duration time of seismic waves. Results of the processing are typewritten, and the interpreter can repeat the same procedure if any wrong result is found. For the second step, reading wave parameters is done by 1-3 interpreters using three sets of a graphic display device and a data typewriter, where the interpreters can work independently of each other. The third step is to file the data resulting from the second step in a disk file and to make a list and hypocentral maps from the file, an example of which is shown in Figure 10.

Such a semiautomatic method as used in this processing is considered to be practical and the best way in the present situation, although various techniques of automatic processing for seismic data have been developed. Regarding P arrival times, automatic reading presents satisfactory results. Table 3 shows the result of automatic reading of P arrival times by our method. Sharpness of P initial phases and accuracy of automatic reading are classified into 4 and 5 ranks in columns and rows of the table. The part above the stepped line in the table is judged to show good results, the ratio of which is 63 percent. However, there is a weakness of automatic reading: it cannot judge whether it has shown a good result or not. If hypocentral determination is carried out without any selection from the results of automatic reading, the overall results are not good. Figure 11 is an example showing hypocenters located only by automatic reading for the same data as Figure 10. The ratio of good location, where deviations of epicenters from those of Figure 10 are within 10 km, is only 21 percent.

The above semiautomatic system is expected to be capable of processing 2000 earthquakes per month, which is considered to be enough to process all the data of earthquakes observed when the Kanto-Tokai network is completed.

2) Displaying of frequency of earthquake occurrence. Frequency data of earthquake occurrence recorded by the RP are moved to a disk file of the BP, which has space to store one year's data. At any time, these data can be tabulated by the line printer and displayed on the graphic display device as shown in Figure 12. In the figure, the data counted by an interpreter from analog records are shown together for reference. Both the results are in good agreement.

3) Displaying of crustal tilt change. Crustal tilt data recorded on magnetic tapes are compiled and stored in a disk file of the BP, which has space for one year's data. In this process, the data are sampled every hour, and if wrong data such as spike noises are found, they are omitted from the file and the gap is filled up with the data from within five successive minutes. By using the hourly data stored in the disk, tilt changes are displayed on the graphic display device at various kinds of scale prepared. In order to avoid an entangled picture, parallel shift in the vertical direction is possible by arbitrary amounts for each trace. An example is shown in Figure 13.

V. Conclusion

The ideal data processing system by computer should be full automatic processing. However, experience has shown that it is not yet practical, though various techniques for automatic processing have been developed. Our system is composed of two sets of computers, the RP and the BP. The former is for automatic processing and the latter is for semiautomatic processing. Fundamentally automatic monitoring of crustal activities is taken charge of by the RP, and secondary analysis to produce a detailed data base is taken charge of by the BP.

The data processing system by computers is expected to play an important role in the whole prediction system, especially in short-term prediction. However, automatic processing in the present operation is so elemental that it is necessary to improve the monitoring functions for practical use for earthquake prediction. Our further study will include development of automatic monitoring of other parameters such as "b" value, and full automatic location of earthquakes. Moreover, various kinds of monitoring in realtime will be realized in future processing systems. Then these computer systems will play an essential role in practical earthquake prediction.

Acknowledgements

We are grateful to Mr. Y. Sugimoto, Mr. K. Nishikawa, and Mr. H. Mori for making the computer programs. We wish to thank Mr. H. Sato for his valuable comments on the system design.

Appendix

The method for automatic reading of P arrival time is as follows: as explained in Figure 14, an iteration technique is used. A data zone of 6.4 seconds including the station-onset time detected by the RP is extracted and divided into eight parts, each of which has 64 samples of the data. A value of $Z_i^{(1)}$ representing a mean level of the signal in the i-th part, is calculated by low-cut digital filtering and integration for each part. Then a new zone is sought, which is put between the 1-th and the m-th part of the original zone, where a ratio $Z_i^{(1)}/Z_0^{(1)}$ ($Z_0^{(1)}$ is a noise level estimated from the minimum value among $Z_i^{(1)}$) crosses threshold levels $A_L^{(1)}$ and $A_R^{(1)}$ for the first time. The new zone is divided into eight parts again and the same procedure is repeated, and so on. At the final stage, only eight samples of the data are left and the center of the zone is concluded as the position of the P arrival time.

References

Furuzawa,T.,1974, Some Problems of Seismic Data Processing, Bull.Disas. Prev.Res.Inst.,Kyoto Univ.,24,Part 3,No.222,127-145.

Ichikawa;M.and E.Mochizuki,1971, Travel Time Tables for Local Earthquakes In and Near Japan, Papers in Meteorology and Geophysics,22,229-290 (in Japanese).

Katsuyama,Y. and I.Watanabe,1975, Automatic Detection Method for Micro-earthquakes (II), Rep.NRCDP,12,27-51 (in Japanese).

Kuroiso,A. and H.Watanabe,1977, On the Telemetered Array System for Micro-earthquake Observation at Abuyama Seismological Observatory, ZISIN 2, 30,91-106 (in Japanese).

Matsumura,S. and K.Hamada,1976, Determination of P Wave Onset Times by a Digital Computer, ZISIN 2,29,383-394 (in Japanese).

Ohtake,M., H.Takahashi and K.Hamada,1979, The NRCDP Network for Micro-earthquake and Ground Tilt Observation Covering the Kanto-Tokai Area, Processings of 1st Joint U.J.N.R. Panel on Earthquake Prediction Technology,142-168.

Stevenson,P.R.,1976, Microearthquakes at Flathead Lake, Montana: A Study Using Automatic Earthquake Processing, Bull.Seism.Soc.Amer.,66,61-80.

Stewart,S.W.,1977, Real-Time Detection and Location of Local Seismic Events in Central California, Bull.Seism.Soc.Amer.,67,433-452.

Watanabe,H.,1971, Determination of Earthquake Magnitude at Regional Distance in and near Japan, ZISIN 2,24,189-200 (in Japanese).

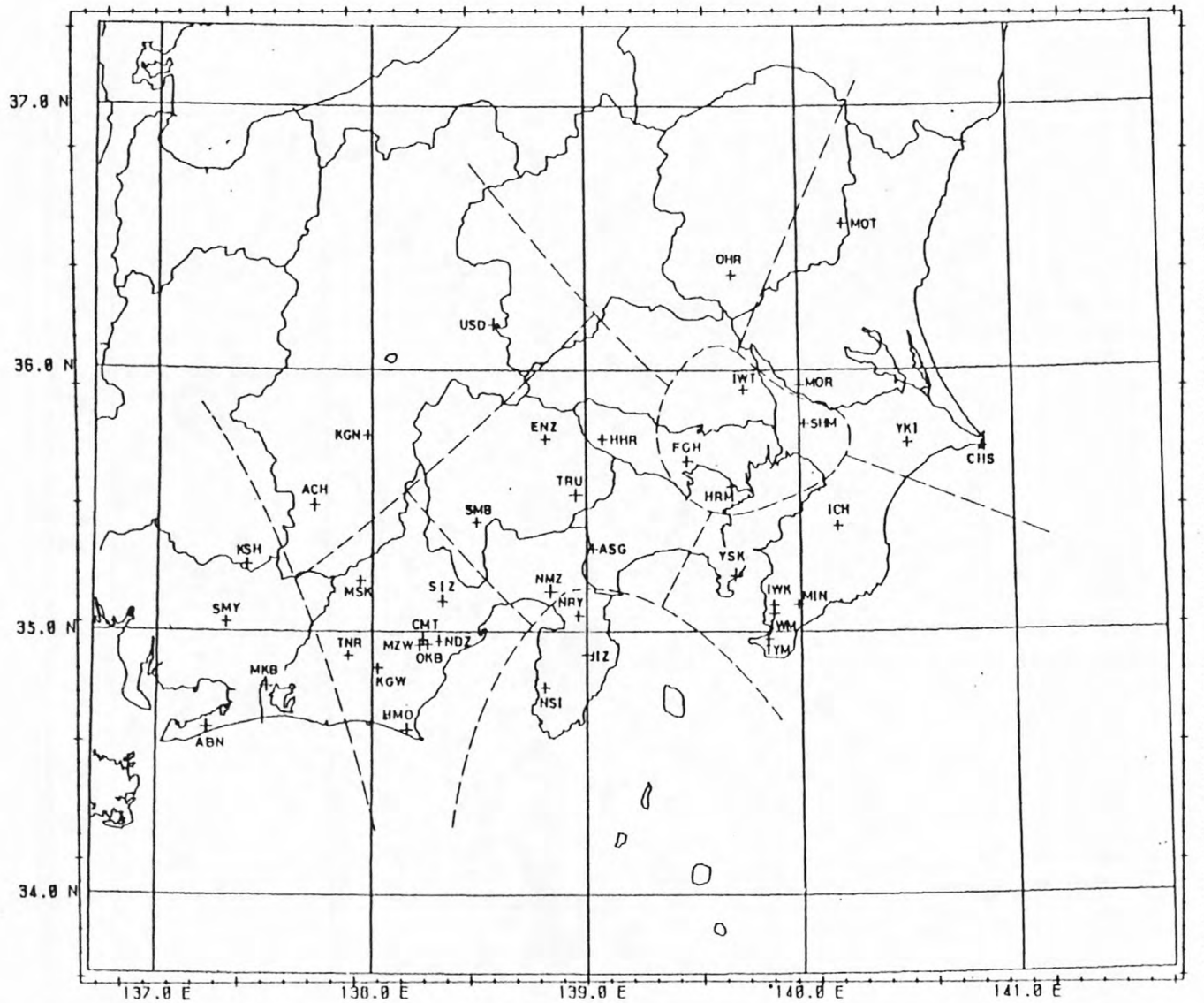

S: SEISMOMETER
T: TILTMETER

S	ABN	AKABANE
S	ACH	ACHI
S,T	ASG	MINAMIASHIGARA
S,T	CHS	CHOSHI
T	CMT	CHIKAMATA
S,T	ENZ	ENZAN
S,T	FCH	FUCHU
S	HHR	HINOHARA
S	HMO	HAMAOKA
S	HRM	KAWASAKI
S	ICH	ICHIHARA
S,T	IWK	IWAI-KITA
T	IWM	IWAI-MINAMI
S,T	IWT	IWATSUKI
S,T	JIZ	NAKAIZU
S	KGN	KOMAGANE
S	KGW	KAKEGAWA
S	KSH	KUSHIHARA
S	MIN	MINEOKA
S,T	MKB	MIKKABI
S	MOR	MORIYA
S	MOT	MOTEGI
T	MZW	MATOZAWA
T	NDZ	NODAZAWA
S	MSK	MISAKUBO
S	NMZ	NUMAZU
S,T	NRY	NIRAYAMA
S	NSI	NISHIIZU
S	OHR	OHIRA
S,T	OKB	OKABE
S,T	SHM	SHIMOHSA
S,T	SIZ	SHIZUOKA
S	SMB	SHIMOBE
S	SMY	SHIMOYAMA
S	TNR	TENRYU
S	TRU	TSURU
S	TYM	TATEYAMA
S	USD	USUDA
S	YKI	YOKAICHIBA
S	YSK	YOKOSUKA

Fig.1 Location of the observational stations at the present stage. Broken lines divide the observational area into nine blocks. Seismic data in each block are treated as a processing unit by the computer.

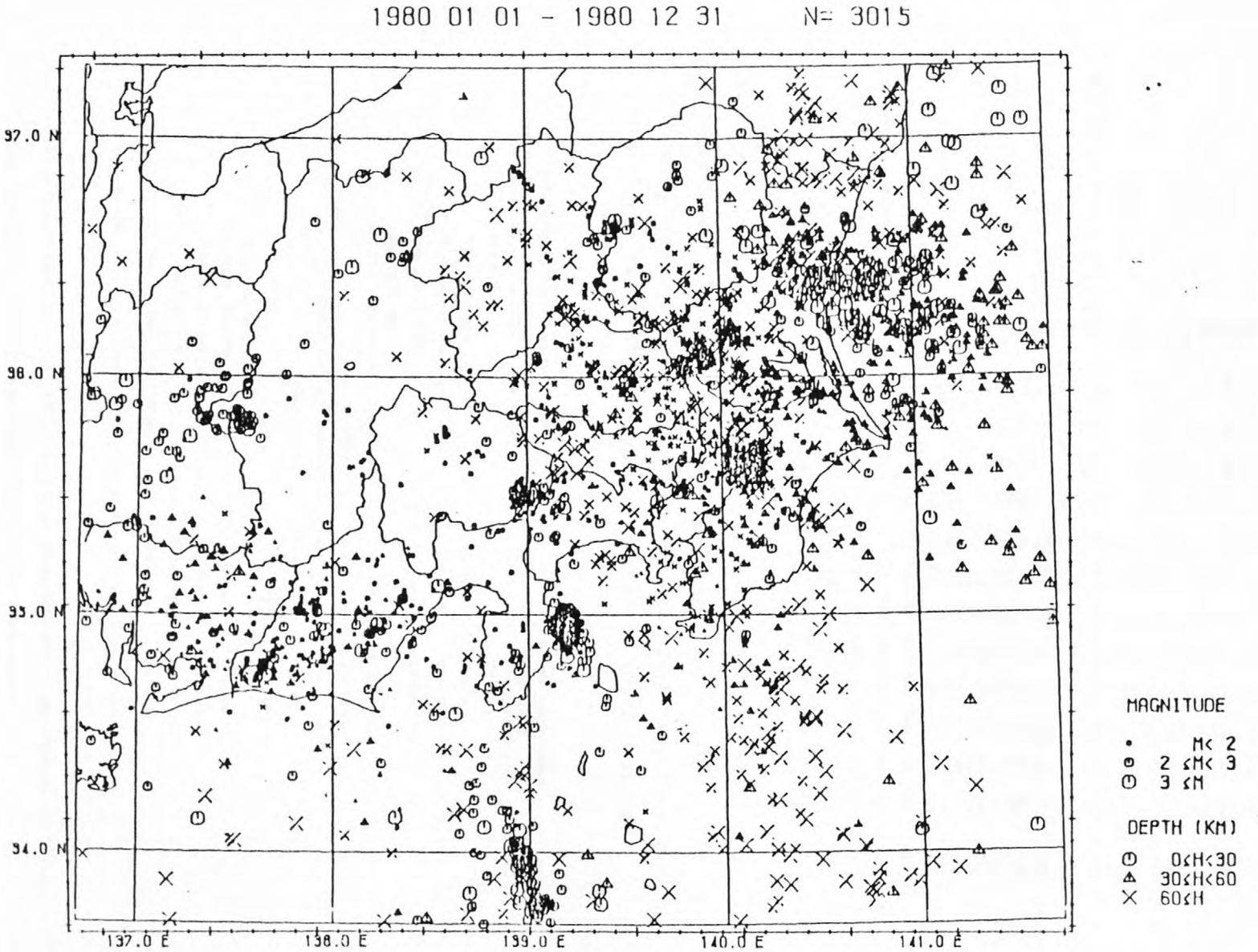

Fig.2 Seismicity map of the Kanto-Tokai area for 1980.

1980	JAN	FEB	MAR	APR	MAY	JUN	JUL	AUG	SEP	OCT	NOV	DEC	TOTAL
Number of Seismic Signals Detected													
ASG	111	125	149	131	104	243	154	201	258	170	138	136	1920
CHS					119	254	186	125	123	121	132	151	1211
EN2	105	109	226	292	200	352	303	211	371	318	279	299	3065
HHR					7	234	418	340	550	441	458	453	2901
HRM	24	32	55	54	41	166	102	32	70	68	49	53	746
ICH	74	76	74	100	89	218	168	100	145	119	112	113	1388
IWK	82	93	109	117	102	244	183	116	167	131	123	125	1592
IWT	464	420	467	468	372	524	449	367	498	391	382	452	5254
JIZ	114	140	158	159	116	250	162	220	362	182	147	161	2171
KGN					26	300	263	186	388	257	243	232	1895
KGW					122	281	259	146	291	202	184	177	1662
KSH					192	319	236	155	372	271	255	245	2045
MIN	77	90	107	117	93	248	191	126	171	144	138	136	1638
MOR	61	52	64	62	57	117	72	47	79	70	69	57	807
MOT					452	589	523	465	555	484	432	516	4016
MSK	117	121	113	194	84	321	256	195	385	270	232	241	2529
NRY					64	219	146	214	318	172	139	90	1362
NSI	112	119	135	141	99	229	157	207	341	180	139	153	2012
OHR	533	487	496	484	430	585	492	398	555	457	442	501	5860
OKB	135	120	150	160	144	291	263	151	312	223	191	185	2325
SHM	436	400	425	483	440	573	519	423	469	210	52	459	4889
SMS	107	115	137	145	126	276	257	150	295	186	168	165	2127
SMY					191	147	188	178	365	274	253	230	1826
TNR	129	115	143	148	123	285	248	154	303	216	183	181	2228
TYM	67	78	105	103	89	224	173	105	150	120	111	119	1444
YKI	60	64	125	122	120	257	183	139	189	179	135	155	1728
Total(A)	2808	2756	3238	3480	4002	7746	6551	5151	8082	5856	5186	5785	60641
Number of Earthquakes Detected (B)	659	618	692	843	737	996	861	802	1178	879	860	940	10065
Number of Hypocenters Determined(C)	116	97	145	165	229	395	394	324	540	360	283	366	3414
A/B	4.3	4.5	4.7	4.1	5.4	7.8	7.6	6.4	6.9	6.7	6.0	6.2	6.0
C/B (%)	17.6	15.7	21.0	19.6	31.1	39.7	45.8	40.4	45.8	41.0	32.9	38.9	33.9

Table 1 Lists of number of seismograms(A), earthquakes(B) and hypocenters(C) observed by the NRCDP network in 1980. A/B is mean number of stations where one earthquake was detected. C/B is the ratio of earthquakes located to those detected.

	REALTIME PROCESSOR	BATCH PROCESSOR
Memory Size	64 KW	256 KW
Fixed Word Length	16 bits	16 bits
Floating-point Word Length	32/64 bits	32/64 bits
Memory Cycle Time	650 nsec	650 nsec
Processing Speed		
Fixed-point Arithmetic Summation	2.16 μsec	2.40-3.84 μsec
" Multiplication	6.48-9.82 μsec	6.72-12.52 μsec
Floating-point Arithmetic Summation	8.16-13.92 μsec	8.88-16.56 μsec
" Multiplication	14.40-15.84 μsec	15.12-18.48 μsec
Gibson Mix	3.23 μsec	4.86 μsec
Data Transmission Speed		
between MT & MEM	20 KW/sec	20 KW/sec
between DK & MEM	156 KW/sec	156 KW/sec
between GD & MEM	9600 bits/sec	307 Kbits/sec
Maximum Speed through DMA Bus	1.2 MW/sec	0.7 MW/sec

Table 2 Comparison of memory size and processing speed between the Realtime Processor and the Batch Processor.

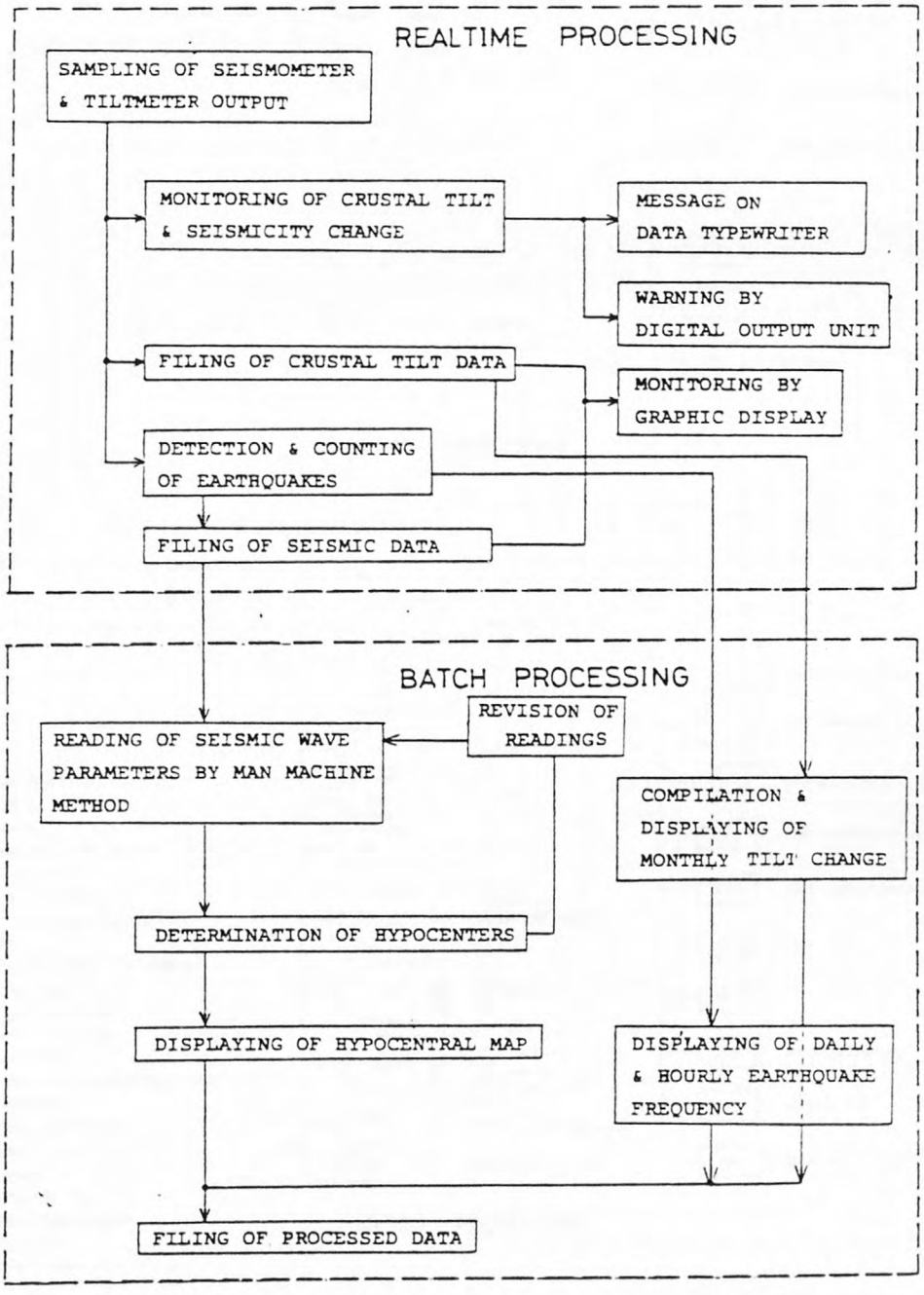

Fig.3 General flow chart of data processing by two sets of computer systems.

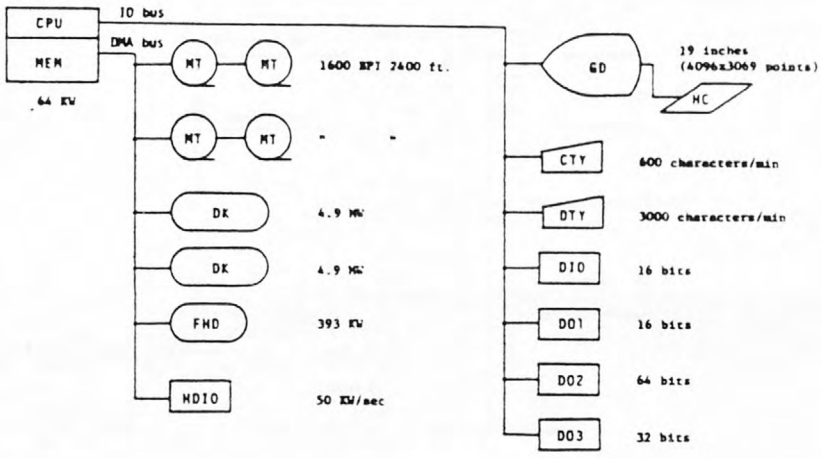

REALTIME PROCESSOR

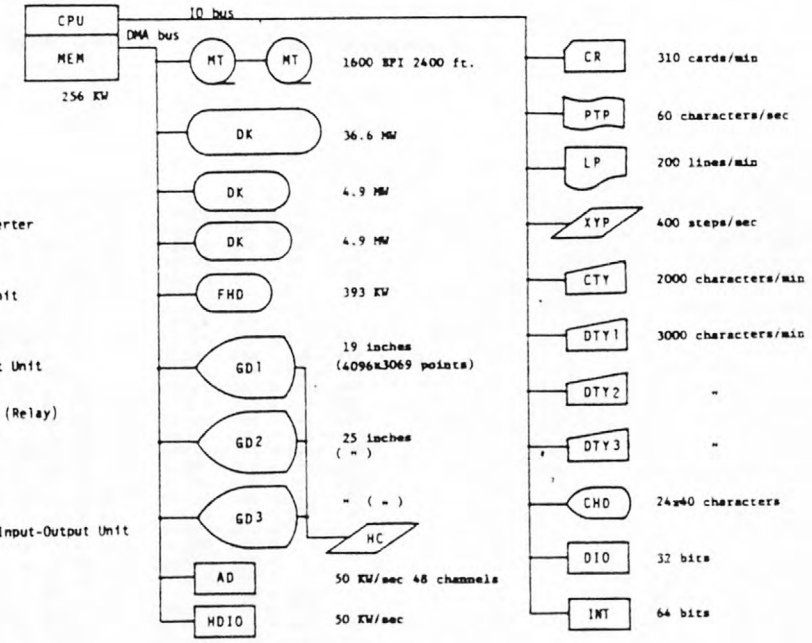

AD : Analog-Digital Converter
CHD : Character Display
CLK : Clock
CPU : Central Processor Unit
CR : Card Reader
CTY : Console Typewriter
DIO : Digital Input-Output Unit
DK : Disk
DO : Digital Output Unit (Relay)
DTY : Data Typewriter
FHD : Fixed Head Disk
GD : Graphic Display
HC : Hard Copy
HDIO: High Speed Digital Input-Output Unit
IF : Interface
INT : Interruption Unit
LP : Line Printer
MEM : Memory
MT : Magnetic Tape
PTP : Paper Tape Puncher
TM : Telemeter
XYP : X-Y Plotter

BATCH PROCESSOR

Fig.4 Compositions of the computer systems.

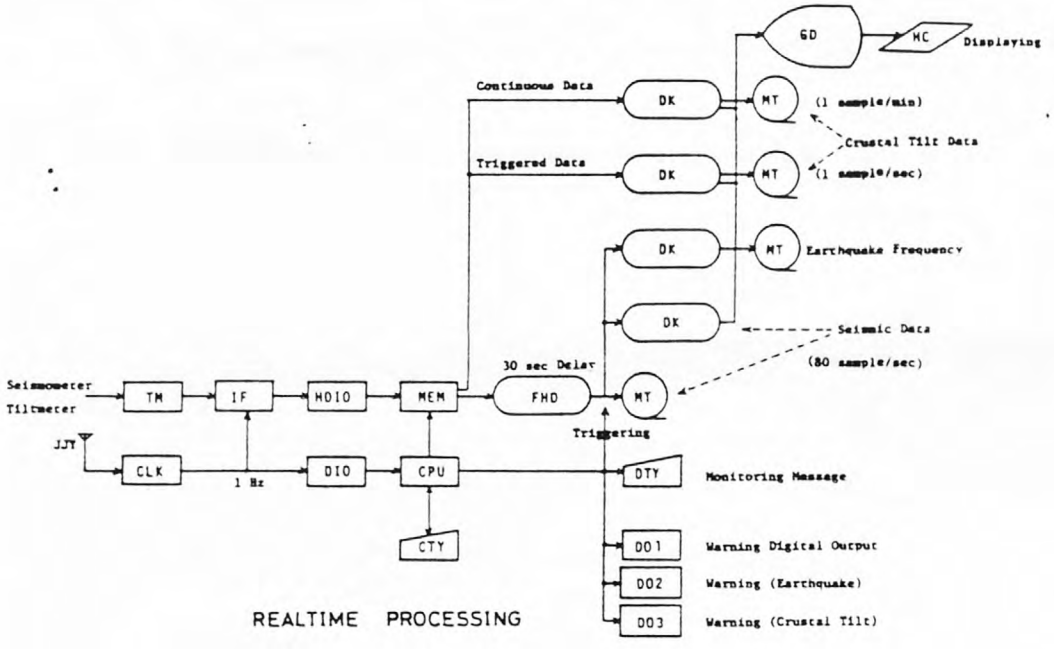

Fig.5 Flow chart of the realtime processing.

```
***ETRG  81 01/16 21:42 55.   CN0311  MOT N FPT   78
***ETRG  81 01/16 21:44 55.   CN0201  OHR U FPT   70
***ETRG  81 01/16 21:44 54.   CN0107  SHM U FPT   73
***ETRG  81 01/16 21:45 05.   CN0610  HHR U FPT   68
***ETRG  81 01/16 21:44 55.   CN0103  IWT Y FPT   92
***ETRG  81 01/16 21:44 48.   CN0310  MOT U FPT  134
***ETRG  81 01/16 22:09 23.   CN0504  NSI U FPT    8
 --GABN  81 01/16 22:18       CN1017  JIZ N A8L+1702
 --GABN  81 01/16 22:18       CN1018  JIZ E A8L+1279
 --GABN  81 01/16 22:18       CN1033  MZW N A8L- 790
 --GABN  81 01/16 22:18       CN1034  MZW E A8L+9999
 --GABN  81 01/16 22:18       CN1041  CMT N A8L+  88
 --GABN  81 01/16 22:18       CN1042  CMT E A8L- 444
 --GABN  81 01/16 22:18       CN1049  MOZ N A8L+ 502
 --GABN  81 01/16 22:18       CN1050  MOZ E A8L+1523
 --GABN  81 01/16 22:18       CN1058  OKB E A8L+ 848
 --GABN  81 01/16 22:18       CN1066  IWT Y A8L+ 398
 --GABN  81 01/16 22:20       CN1057  OKB N A8L+  28
 --GABN  81 01/16 22:20       CN1065  IWT X A8L+ 352
***ETRG  81 01/16 22:20 30.   CN0504  NSI U FPT   22
***ETRG  81 01/16 22:20 45.   CN0501  JIZ U FPT   10
 --GMOV  81 01/16 22:45       CN1057  OKB N
 --GMOV  81 01/16 22:45       CN1065  IWT X
 --GOVR  81 01/16 22:45       CN1057  OKB N
 --GOVR  81 01/16 22:45       CN1065  IWT X
 --GABN  81 01/16 22:53       CN1057  OKB N A8L+  28
***ETRG  81 01/16 23:13 06.   CN0310  MOT U FPT   14
 --GABN  81 01/16 23:29       CN1057  OKB N A8L+  25
 --GABN  81 01/16 23:29       CN1065  IWT X A8L+ 353
   DAILY NUMBER OF EARTHQUAKES  81/01/16
      0  1  2  3  4  5  6  7  8  9 10 11 12 13 14 15 16 17 18 19 20 21 22 23
IWT   0  0  0  0  0  0  0  0  0  0  0  0  0  1  1  1  0  1  1  0  4  2  0  0  11
SHM   2  0  1  1  0  0  1  0  0  1  0  0  0  0  1  0  1  0  0  0  2  1  0  0  11
      0  0  0  0  0  0  0  0  0  0  0  0  0  0  0  0  0  0  0  0  0  0  0  0   0
HRM   0  0  0  0  0  0  0  0  0  0  0  0  1  0  0  0  0  0  0  0  0  0  0  0   1
      0  0  0  0  0  0  0  0  0  0  0  0  0  0  0  0  0  0  0  0  0  0  0  0   0
OHR   0  0  0  0  0  0  0  0  0  0  0  0  4  5  0  1  0  1  2  1  0  3  1  0  0  18
      0  0  0  0  0  0  0  0  0  0  0  0  0  0  0  0  0  0  0  0  0  0  0  0   0
      0  0  0  0  0  0  0  0  0  0  0  0  0  0  0  0  0  0  0  0  0  0  0  0   0
```

Fig.6 Output list from the data typewriter of the Realtime Processor.

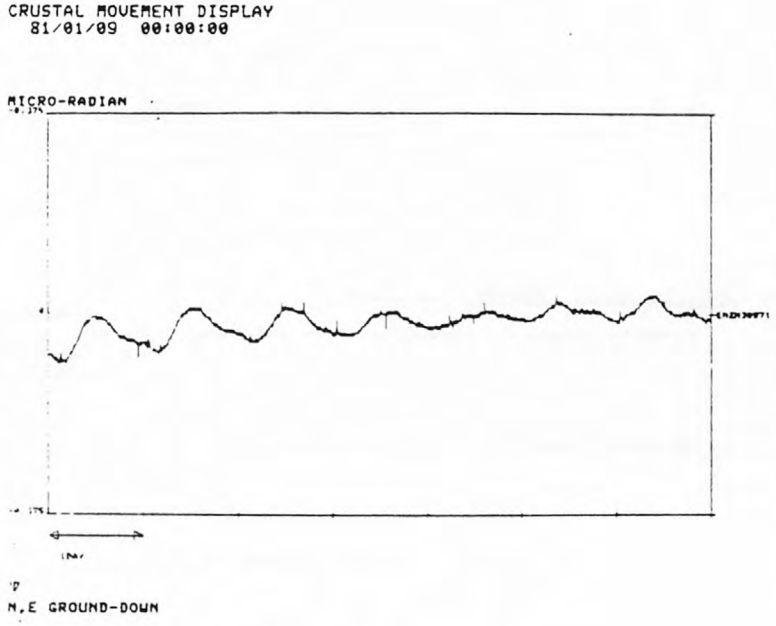

(a) Crustal tilt change.

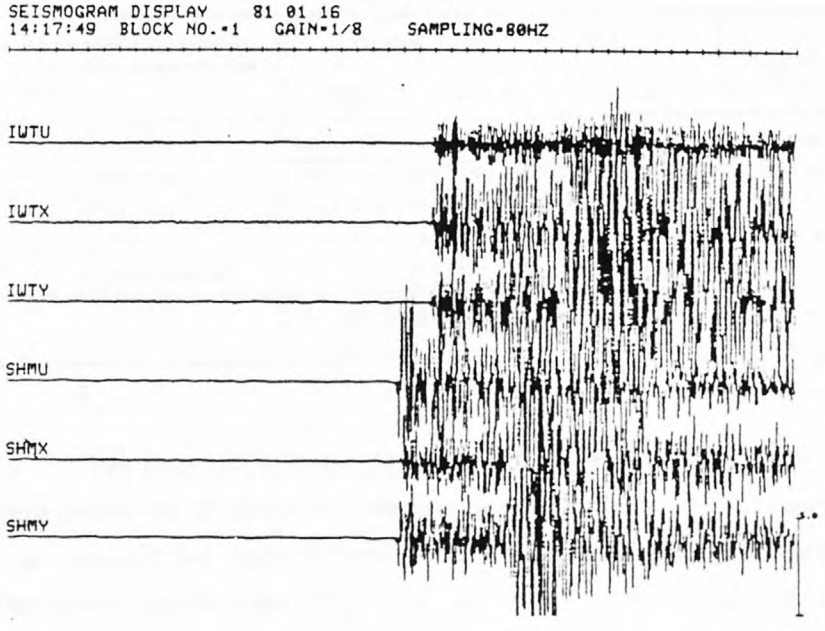

(b) Seismic waves.

Fig.7 Examples of graphic displaying.

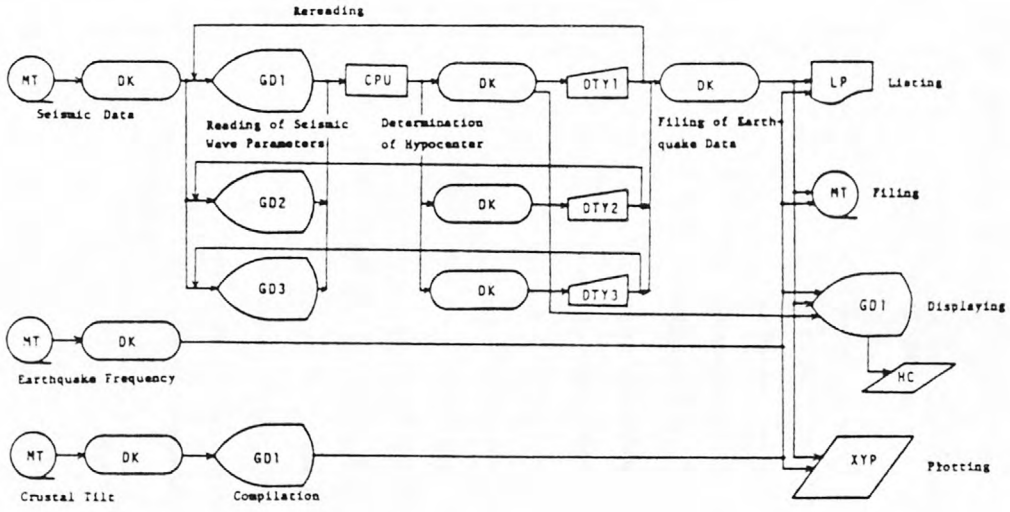

FIg.8 Flow chart of the batch processing.

Time Correction for Automatic Reading by an Interpreter (sec)	Sharpness of P Initial Phase (sec)				
	A (0.0-0.1)	B (0.1-0.3)	C (0.3-1.0)	D (1.0-)	
A (0.0-0.1)	260 (31.1)	86 (10.3)	22 (2.6)	3 (0.4)	371 (44.3)
B (0.1-0.3)	36 (4.3)	83 (9.9)	27 (3.2)	0 (0.0)	146 (17.4)
C (0.3-1.0)	27 (3.2)	68 (8.1)	48 (5.7)	0 (0.0)	143 (17.1)
D (1.0-)	0 (0.0)	9 (1.1)	35 (4.2)	0 (0.0)	44 (5.3)
E (wrong detection)	22 (2.6)	60 (7.2)	47 (5.6)	4 (0.5)	133 (15.9)
	345 (41.2)	306 (36.6)	179 (21.4)	7 (0.8)	837 (100.0) Number (%)

Table 3 Results of automatic reading of P arrival times. Sharpness of P initial phases and accuracy of automatic reading are classified into 4 and 5 ranks in columns and rows of the table, The part above the stepped line (63 %) is judged to show good results of automatic reading.

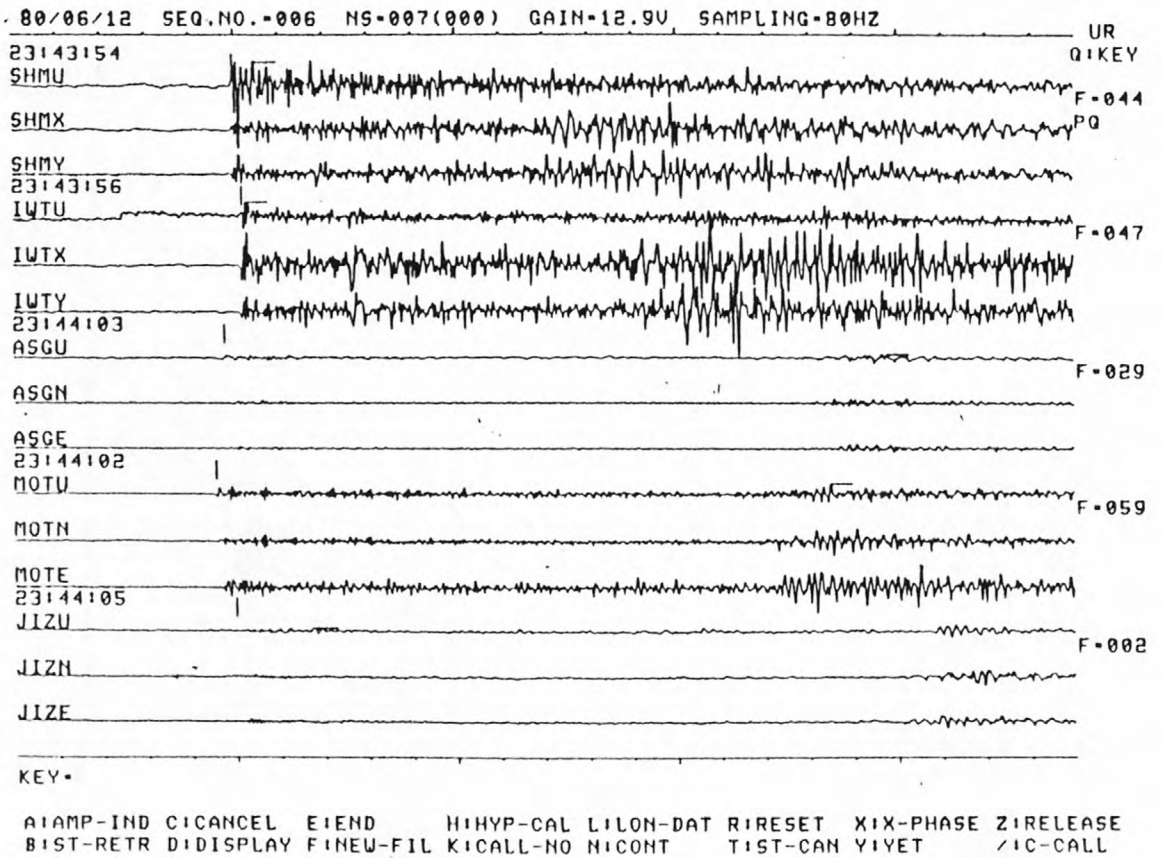

Fig.9 Standard picture for reading of wave parameters by semi-automatic method. Short vertical bars indicate positions of P arrival times determined by automatic reading. Short horizontal bars indicate maximum amplitudes of seismic waves in Up-Down component.

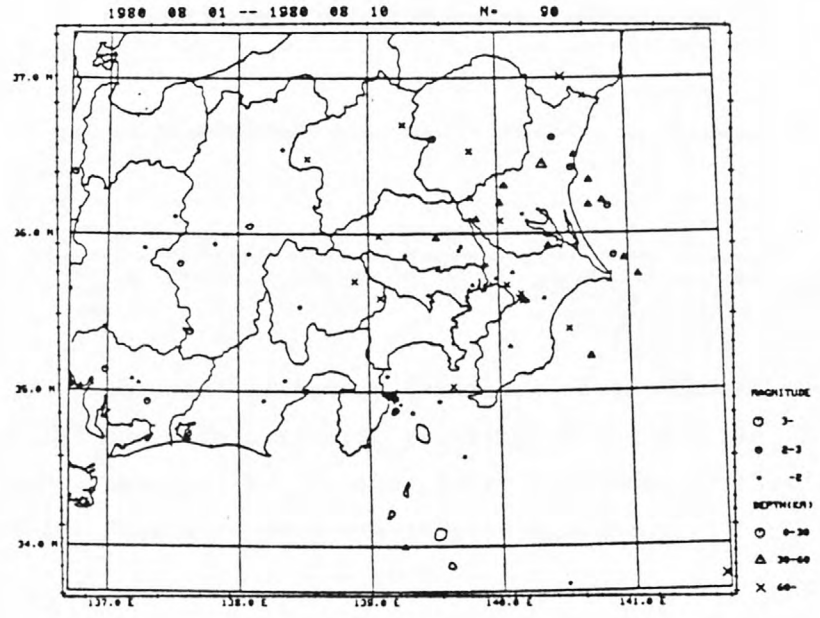

Fig.10 Hypocentral map determined by semi-automatic method.

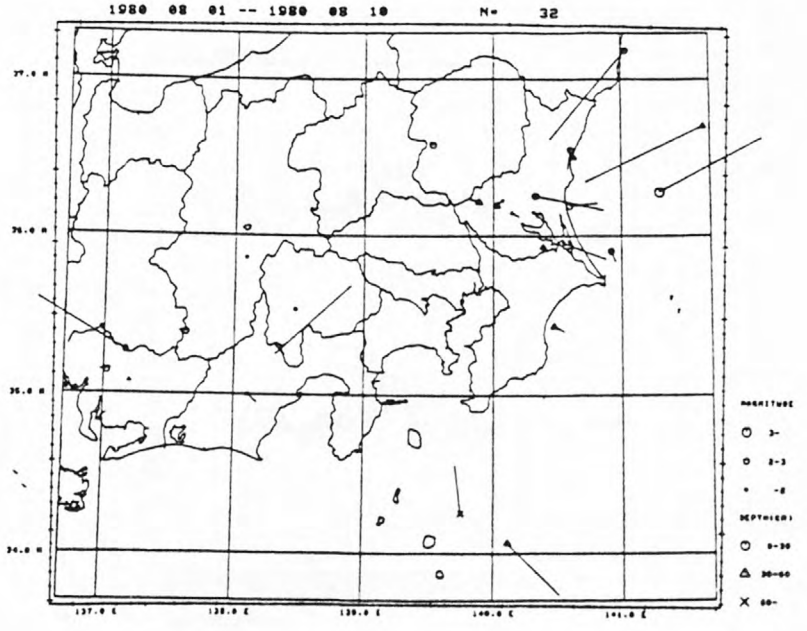

Fig.11 Hypocentral map determined by automatic reading.
Deviations of epicenters from those determined by semi-automatic method are shown by lines.

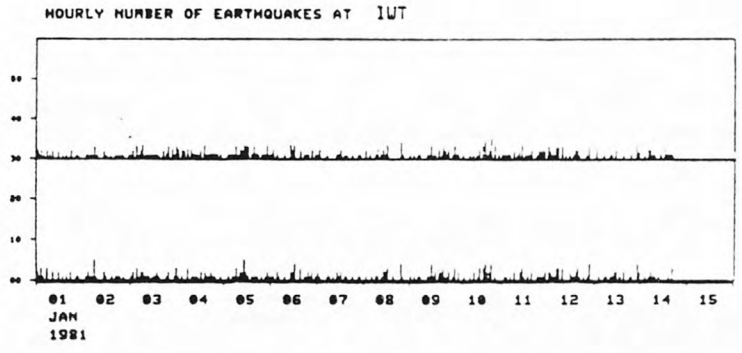

Fig.12 Displaying of hourly frequency of earthquake occurrence at IWT based on automatic counting by the Realtime Processor. Counts measured by an interpreter are shown in the middle step of the figure. Both are in good agreement.

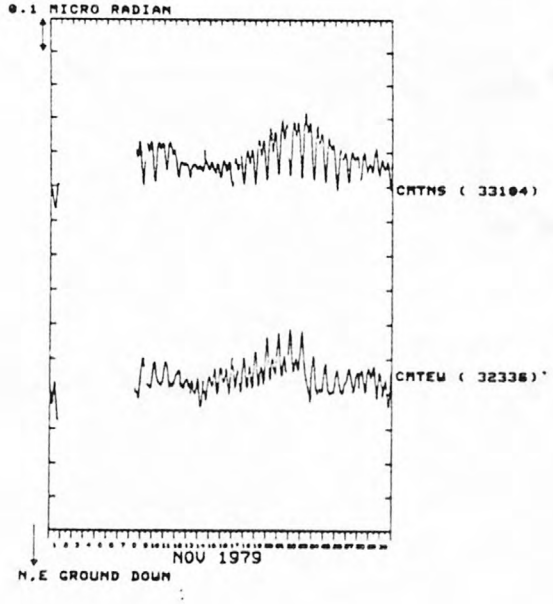

Fig.13 Displaying of crustal tilt change observed at CMT.

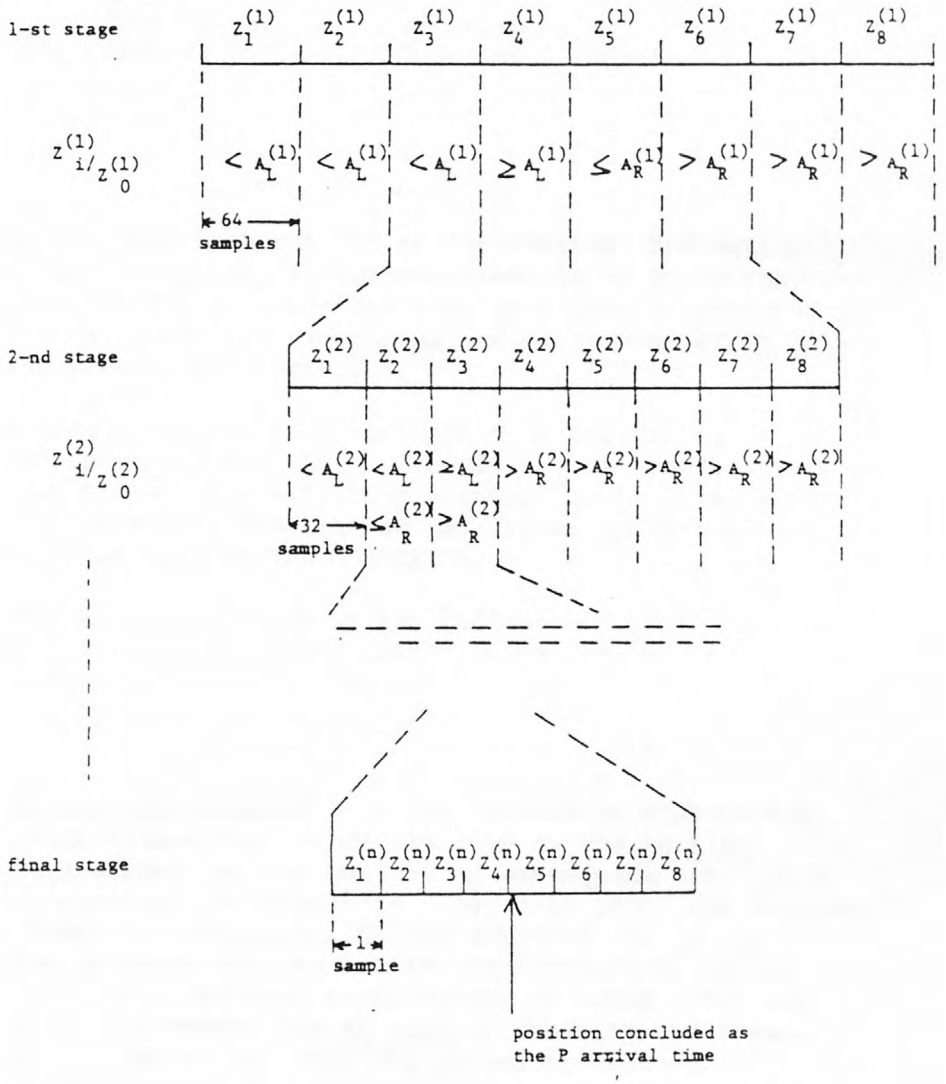

Fig.14 Procedure of automatic reading of P arrival time.

IN SITU MEASUREMENTS OF CRUSTAL STRESS IN KANTO-TOKAI REGION

Hitoshi Koide*, Hiroaki Tsukahara**, Koji Ono*

*Geological Survey of Japan
**National Research Center for Disaster Prevention,

Abstract

Since 1978, the National Research Center for Disaster Prevention of Japan has conducted several in situ stress measurements by hydrofracturing, and the Geological Survey of Japan has also made some attempts of in situ stress measurements by shallow overcoring and monitoring of in situ stress changes in the Kanto-Tokai region.

The state of stress in the Kanto-Tokai region is controlled by interactive motion of three plates: the Asian plate, the Pacific plate and the Philippine Sea plate. The collision between the Philippine Sea plate and the Asian plate causes high horizontal stress concentration of north-south compression in the Tanzawa Mountains.

Stress change which was monitored in the Tanzawa Mountains is related to the interaction of the plates which causes frequent earthquakes in the Kanto-Tokai region (Fig. 4).

Introduction

Although many stress measurements were carried out in engineering practices of underground excavations since the 1960's, the in situ measurements of crustal stress for the purpose of earthquake prediction research had not been realized until 1978 in Japan. In 1978, the National Research Center for Disaster Prevention (NRCDP) measured the in situ stresses by the hydraulic fracturing method in the Kanto-Tokai region (Tsukahara et al., 1978a,b). The Geological Survey of Japan (GSJ) and the Kyoto University, too, measured the in situ stresses by the stress relief method in 1978, in the Kanto-Tokai region and in western Japan, respectively (Koide, 1980; Tanaka and Saito, 1980).

Hydrofracturing

Since 1978, the National Research Center for Disaster Prevention has made a series of in situ measurements using the hydraulic fracturing technique in five boreholes of 450 m deep (Fig. 1, Fig. 2). The host rocks of the stress measurements are Neogene tuffaceous sandstone at Nishiizu (Tsukahara et al., 1980). Neogene siltstone at Futtsu (Ikeda et al., in preparation), Neogene mudstone at Yokosuka (Tsukahara et al., in preparation), Cretaceous mudstone at Choshi (Tsukahara et al., in press) and Cretaceous sandstone at Nakaminato (Ikeda et al., in preparation).

Some of the boreholes have been used for microearthquake observation after hydrofracturing with seismometers which were installed at the bottom of boreholes. They are included in the Kanto-Tokai seismic observation network of NRCDP.

Acoustic emissions (AE) associated with the hydraulic fracturing were observed by hydrophones placed in the fracturing well. A close relationship between the numbers of AE's and the water pressure injected was found (Ikeda et al., 1978).

The state of stress in this district is considered to be controlled by the interactive motion of the three plates: the Pacific plate, the Philippine Sea plate and the Asian plate.

The orientations of the maximum in situ stresses at Nisiizu and Yokosuka are both expected to be north-south because of the northward motion of the Philippine Sea plate relative to the Asian plate. The directions of the stresses observed are consistent with this expectation as shown in Figure 1, and also consistent with the directions derived from active fault analyses, cinder cone alignments, dike trends, and focal mechanism solutions in and around this area.

The stress state at Nakaminato and Choshi is possibly controlled by the westward motion of the Pacific plate against the Asian plate. The orientation of the stresses observed at Nakaminato is probably influenced by the inclination of the formation (strike; N 60°W, dip; 40°N) at the site. We could not detect the azimuth of a new crack in the Choshi well. The stress direction observed at Futtsu can be explained in terms of the interaction among the westward-moving Pacific plate, the northward-moving Philippine Sea plate, and the Asian plate.

The most important aspect of these measurements is prevalence of compressive stresses relative to overburden pressures. However, the difference in stress gradient suggests that the vertical stress may become the intermediate stress at Nishiizu and Nakaminato below a critical depth. Transitions could occur at the depths of about 550 m (Nishiizu) and 500 m (Nakaminato). In the case of Nishiizu, this state of stress is consistent with the strike-slip type of focal mechanism solutions and active faults in the vicinity.

Overcoring

The Geological Survey of Japan measured the in situ stress at the Tanzawa Mountains in the Kanto-Tokai region by an overcoring of shallow vertical boreholes from the earth's surface (Koide et al., in preparation). At Tanzawa, the in situ stress state of the maximum horizontal stress of 11.7 MPa and the minimum horizontal stress of 3.2 MPa was measured in 1978 at the depth of 5.73 m by a deformation cell (Suzuki and Ishijima, 1970) which contains three cantilevers that push with a negligible load against the interior to the borehole. The azimuth of the maximum horizontal stress was N 7°E-S 7°W.

In 1979, another type of overcoring technique, in which a five-component deformation cell (Hayashi et al., 1979) was cement-bonded to the interior of the borehole, was applied in the vicinity of the 1978 measurement site at Tanzawa. The in situ stress state measured in 1979 was the maximum horizontal stress of 7.5 MPa and the minimum horizontal stress of 2.6 MPa at the depth of 14.89 m. The azimuth of maximum horizontal stress was N 9°E-S 9°W. These stress values are about two-thirds of the 1979 values but the sense of stress state is similar between both measurements.

The sites of stress measurements at Tanzawa are located at about the center of Tanzawa quartz diorite intrusive body which forms the core of recent rapid domal uplift. The measured high horizontal stress may be partly due to the rapid uplift of the Tanzawa Mountains. However, the active fault system and frequent earthquake activity strongly suggest the presence of high horizontal compressive tectonic stress of approximately north-south trend due to the collision of the Philippine Sea plate with the Asian plate (Fig. 3).

Tentative results of shallow overcoring in 1981 suggest a very low stress level at Shimoda in the Izu Peninsula, although high stresses were detected at Nishiizu by hydrofracturing method (Fig. 3). This contrast is related to the left-lateral shear of the Izu deformation belt of NNE-SSW trend.

Monitoring of Stress Change

The in situ stress change has been monitored by a borehole inclusion stress meter which was inserted at the point in the borehole of the 1979 stress measurement at Tanzawa (Koide et al., in preparation). Four strain meters of strain gauge base were embedded with cement mortar in the borehole. A significant change in stress orientation (Fig. 4) was recorded during and before an earthquake swarm which occurred about 60 km to the south of the stress-monitoring site on June and July of 1980 including the maximum event of M 6.7 on June 29. Since then, the azimuth of maximum compression became near to the direction of the absolute maximum horizontal stress. The horizontal shearing stress apparently increased about 0.1 MPa from October 1980 to March 1981 (Fig. 4).

Conclusion

Several attempts of in situ measurement of stress by hydrofracturing method and by overcoring have been made in the Kanto-Tokai region, Japan. The state of stress in this region is controlled by the interactive motion of the three plates: the Philippine Sea plate, the Asian plate and the Pacific plate. The collision between the Philippine Sea plate and the Asian plate causes high horizontal compressive stress concentration of north-south trend in the Tanzawa Mountains.

Stress increase which was monitored in the Tanzawa mountains is related to the active plate interaction which causes frequent earthquakes in the Kanto-Tokai region.

The in situ measurement of absolute stress state and stress change is one of the promising methods for earthquake prediction. Detection and observation of stress concentration areas are essential to earthquake prediction.

References

Hayashi, M., T. Kanagawa, S. Hibino, M. Motozima and Y. Kitahara: Detection of anisotropic geo-stresses trying by acoustic emission and non-linear rock mechanics on large excavating caverns, Proc. 4th I.S.R.M. Congress, Montreux, 1979.

Ikeda, R., H. Tsukahara, H. Sataki and H. Takahashi: Observation of acoustic emissions during the hydrofracturing of the base rocks, Zishin, 31, 435-444, 1978 (in Japanese with English abstract).

Ikeda, R., H. Satake and H. Takahashi, in preparation.

Koide, H., Problems on in situ stress measurements for earthquake prediction, The Earth Monthly, 2, 578-585, 1980 (in Japanese).

Koide, H., K. Hoshino, K. Kusunose and K. Inami, in preparation.

Suzuki, K. and Y. Ishijima: Rock stress measurements at rockburst danger area, Proc. 2nd I.S.R.M. Congress, Beograd, 1970.

Tanaka, Y. and T. Saito: In situ measurements of crustal stress by stress relief method, The Earth Monthly, 2, 630-647, 1980 (in Japanese).

Tsukahara, H., R. Ikeda, H. Satake, M. Ohtake and H. Takahashi: Hydrofracturing stress measurements at Okabe Town, Shizuoka Prefecture, Zishin, 31, 415-433, 1978a (in Japanese with English abstract).

Tsukahara, H., R. Ikeda, H. Satake, M. Ohtake and H. Takahashi: In situ stress measurements by hydrofracturing in Japan, International Symp. Earthquake Prediction, UNESCO, Paris, 1978b.

Tsukahara, H., R. Ikeda, H. Satake and H. Takahashi: Stress measurements by hydrofracturing at Nishiizu Town, Shizuoka Prefecture, Zishin, 33, 317-327, 1980 (in Japanese with English abstract).

Tsukahara, H., R. Ikeda, H. Satake, and H. Takahashi: Stress measurements by hydrofracturing at Choshi City, Chiba Prefecture, Zishin, (in press) (in Japanese with English abstract).

Tsukahara, H., R. Ikeda and H. Takahashi, in preparation.

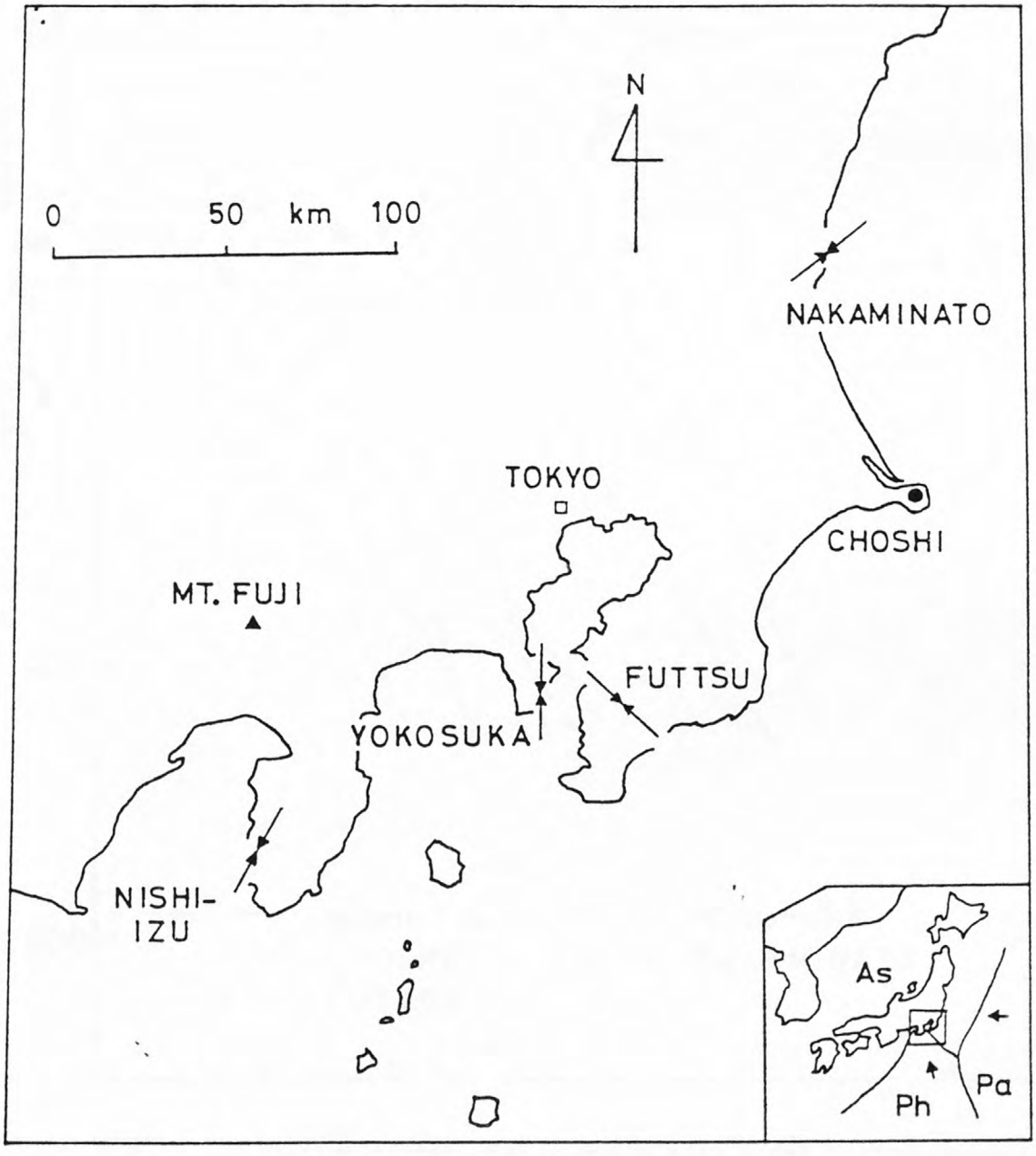

Fig. 1. Maximum horizontal stress direction measured by hydro-fracturing method in the Kanto-Tokai region. As: the Asian plate, Pa: the Pacific plate, Ph: the Philippine Sea plate.

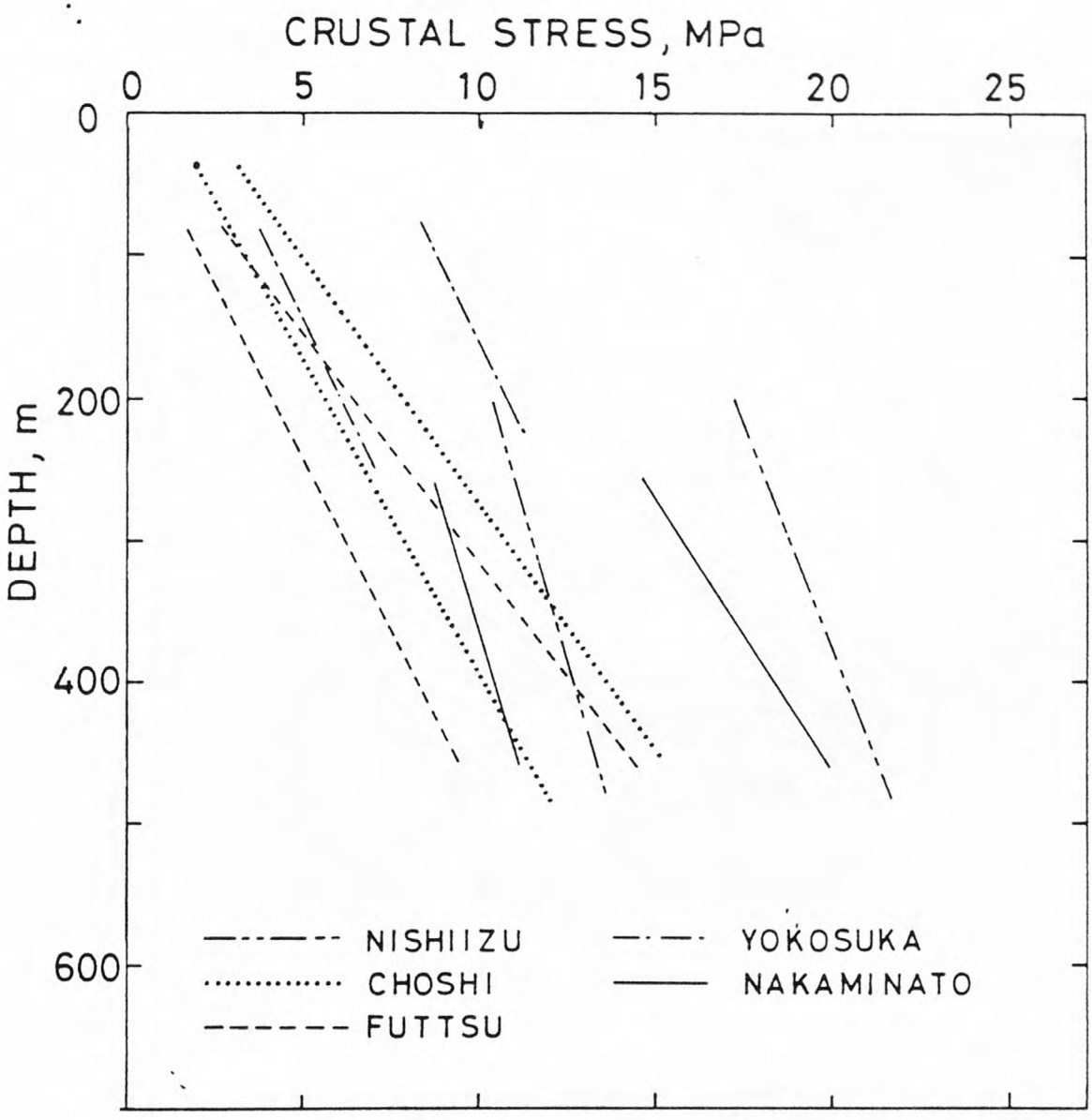

Fig. 2. Variation of measured stresses with depth in the Kanto-Tokai region (Tsukahara et al., in preparation; Ikeda et al., in preparation).

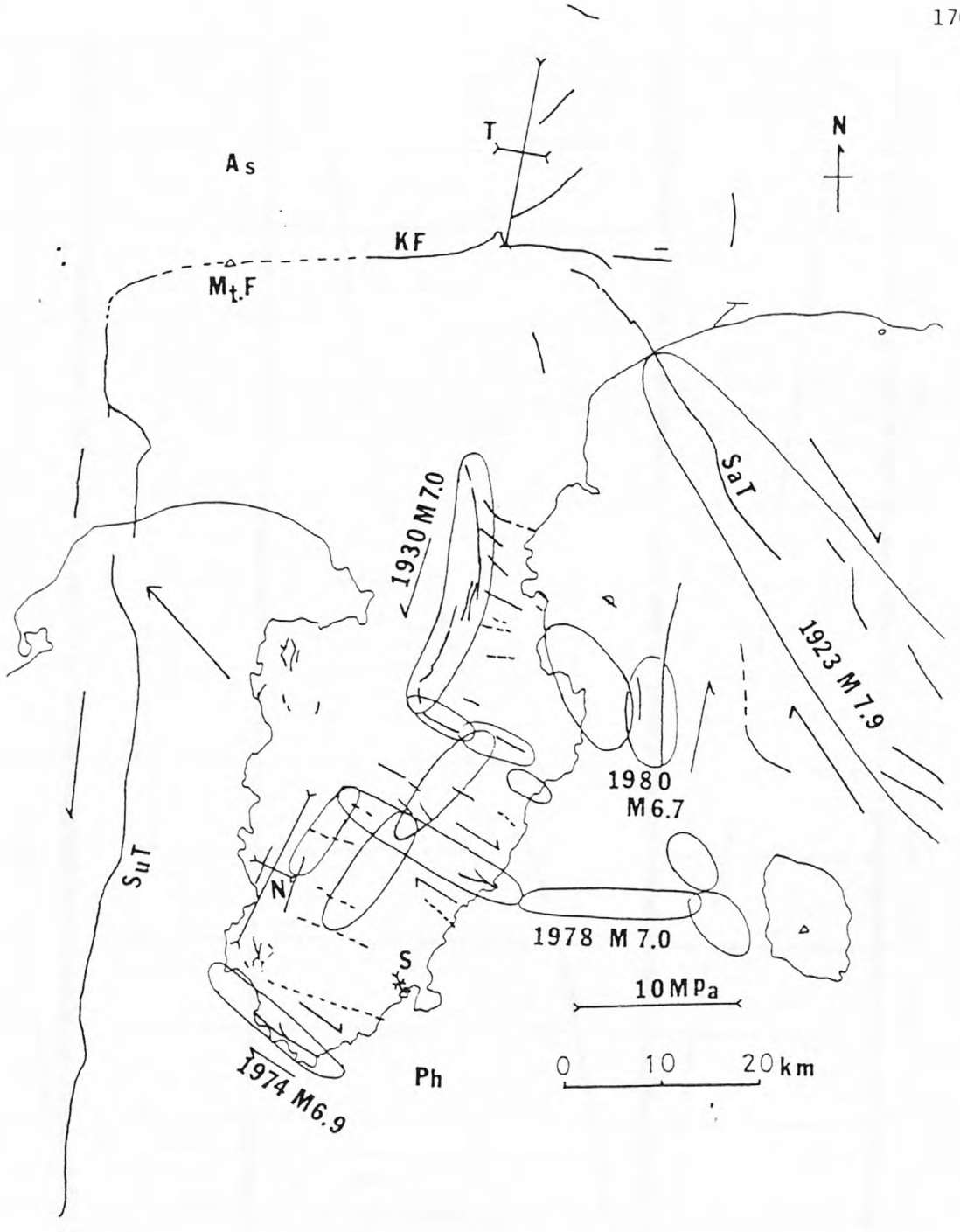

Fig. 3. Horizontal stresses measured by shallow overcoring. T: Horizontal stress at Tanzawa (overcoring), S: horizontal stress at Shimoda (overcoring, tentative result), N: horizontal stress at Nishiizu in excess of lithostatic stress (hydrofracturing, after Tsukahara, et al., 1980). Solid lines: active faults, broken lines: possible active faults, As: the Asian plate, Ph: the Philippine Sea plate, KF: the Kannawa thrust fault, SaT: the Sagami trough, SuT: the Suruga trough. Recent fractured zones by large earthquakes and earthquake swarms are shown. Arrows indicate direction of horizontal displacement.

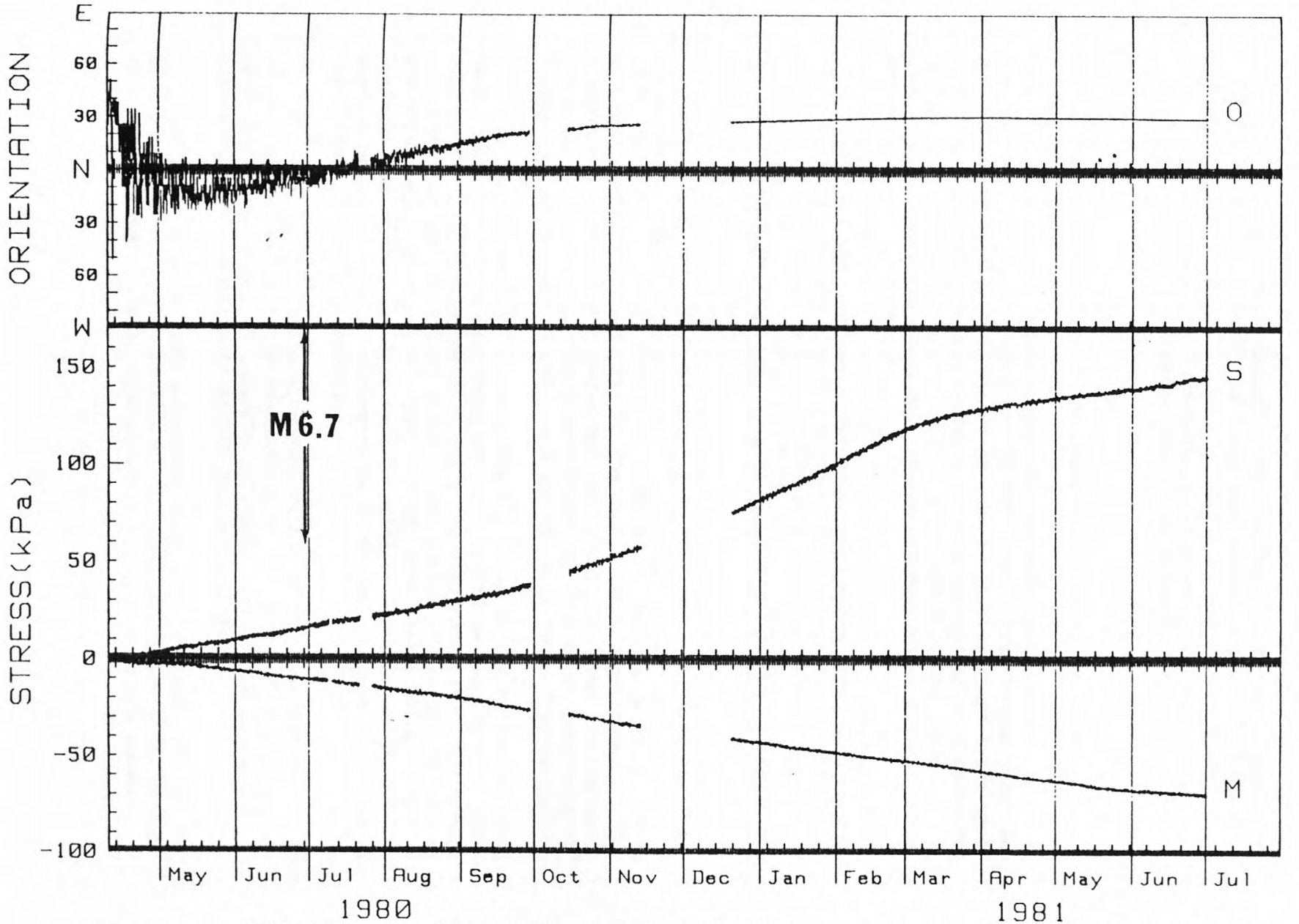

Fig. 4. STRESS CHANGE(TANZAWA). S: maximum horizontal shear stress change N: mean horizontal stress change, O: direction of maximum horizontal compression. Measured depth is 14.89 m. Host rock is quartz diorite.

DEEP BOREHOLE MEASUREMENTS OF THE CRUSTAL ACTIVITIES AROUND TOKYO --INTRODUCTION OF THE THREE DEEP BOREHOLE OBSERVATORIES--

K. Hamada, H. Takahashi, M. Takahashi, and H. Suzuki
National Research Center for Disaster Prevention

Abstract

For a long time, high-sensitivity observations of earthquakes and the movement of the earth's crust in the capital area around Tokyo could not easily be carried out because of high-level background noise generated by active industry and concentrated transportation. In addition, the Tokyo region is covered by thick, soft layers of the Quaternary and Tertiary, and there is subsidence of the ground, caused by the pumping of ground water and natural gas.

However, there has been progress in earthquake prediction, and the Science and Technology Agency's National Research Center for Disaster Prevention (NRCDP) has introduced the deep borehole observation of the earth's crustal activities in the Tokyo area. This observation forms part of the Japanese national program of prediction, and has been planned to overcome the surface noise.

After ten years of development and improvement starting in 1970, three deep borehole observatories for microearthquakes and ground tilt were completed in 1980. The first observatory, with a depth of 3500 m was completed at Iwatsuki City at the end of 1972. Continuous observation of microearthquakes and ground tilt has been carried out since 1973. The second observatory Shimohsa, 2300 m was completed at Shonan Town at the end of 1977, and the third in Fuchu City in 1980.

The sensor capsule, which is rigidly fixed at the bottom of the hole, contains a three-component set of velocity seismometers, a three-component set of accelerometers, and a two-component set of thermometers. Amplitudes of the background noise at the bottom of the deep boreholes are very small, as expected: for 1-25 Hz, less than 5 μkine at the Iwatsuki observatory and less than 10 μkine at Shimohsa and Fuchu. The surface noise at all the observatories is several hundred times that at the bottom of the deep boreholes.

High-sensitivity tripartite observation of microearthquakes by means of deep boreholes, with the cooperation of the surrounding stations, provides a huge amount of accurate information about the space-time distribution of seismic activity in the capital area.

New force-balance type tiltmeters have been developed for the bottom of a borehole, and are so sensitive that they can record tidal change with a double amplitude of approximately 1/100th of an arc second.

A remaining problem is long-term drift over several months. The tilt measurements are expected to detect short-term precursors to an impending earthquake.

All observational data are telemetered through telephone lines to the NRCDP in Tsukuba Science City, Ibaraki Prefecture, where observational data from other seismometers and tiltmeters covering the south Kanto and Tokai area are collected and continuous monitoring of crustal activities is carried out besides ordinary data processing.

Table 1. Summary of performance of the three deep borehole observatories.

STATION	IWATSUKI	SHIMOHSA	FUCHU
CODE	IWT	SHM	FCH
LOCATION	35°55'33"N	35°47'36"N	35°39'2"N
	139°44'17"E	140°1'26"E	139°28'25"E
ALTITUDE	-3502m	-2277m	-2707m
TEMPERATURE	85.6°C	61.0°C	82.0°C
VELOCITY SEISMOMETER			
SENSITIVITY	X;1.71V/kine	X;1.89V/kine	X;1.77V/kine
	Y;1.65 "	Y;1.97 "	Y;1.73 "
	Z;1.70 "	Z;1.43 "	Z;0.97 "
FREQUENCY	X;0.98Hz	X;1.00Hz	X;1.03Hz
	Y;1.00 "	Y;1.00 "	Y;1.03 "
	Z;1.01 "	Z;0.98 "	Z;1.05 "
DAMPING	X,Y,Z;0.65	X,Y,Z;0.62	X,Y,Z;0.62
ACCELEROMETER			
SENSITIVITY	X,Y,Z;16.1V/G	X,Y,Z;16.1V/G	X,Y,Z;1.17V/G
FREQUENCY	X,Y,Z;50Hz	X,Y,Z;50Hz	X,Y,Z;100Hz
TILTMETER			
SENSITIVITY	X,Y;100mV/sec	X,Y;100mV/sec	X,Y;100mV/sec
THERMOMETER			
SENSITIVITY	A,B;0.2V/°C	A,B;0.2V/°C	A,B;0.2V/°C
OVERALL RECORDABLE RANGE OF OBSERVATION			
VELOCITY	2μ-10mkine,1-25Hz maximun magnification at 10Hz; 1,000,000	5μ-70mkine,1-25Hz max. mag.,10Hz 570,000	7μ-16mkine,1-25Hz max. mag.,10Hz 630,000
ACCELERATION	5m-30gal,0-30Hz	5m-30gal,0-30Hz	0.1-850gal,0-30Hz
TILT	0.01-5" re-adjustable within $\pm$3°	0.01-5" re-adjustable within $\pm$3°	0.01-5" re-adjustable within $\pm$3°
TEMPERATURE	80-90°C	56-68°C	76-86°C

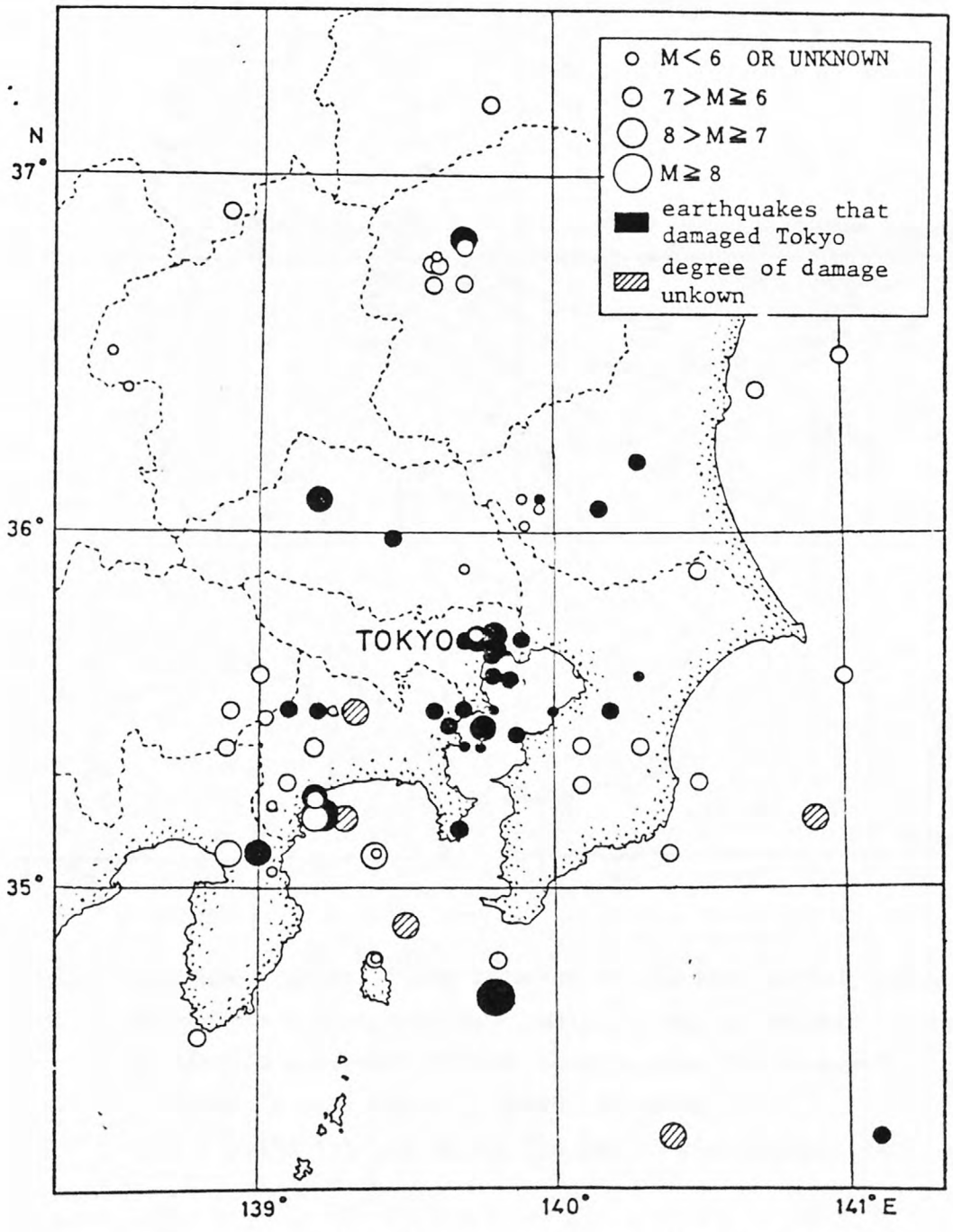

Fig. 1. Epicentral distribution of earthquakes that damaged Tokyo during the period 799-1975(after Usami, 1977).

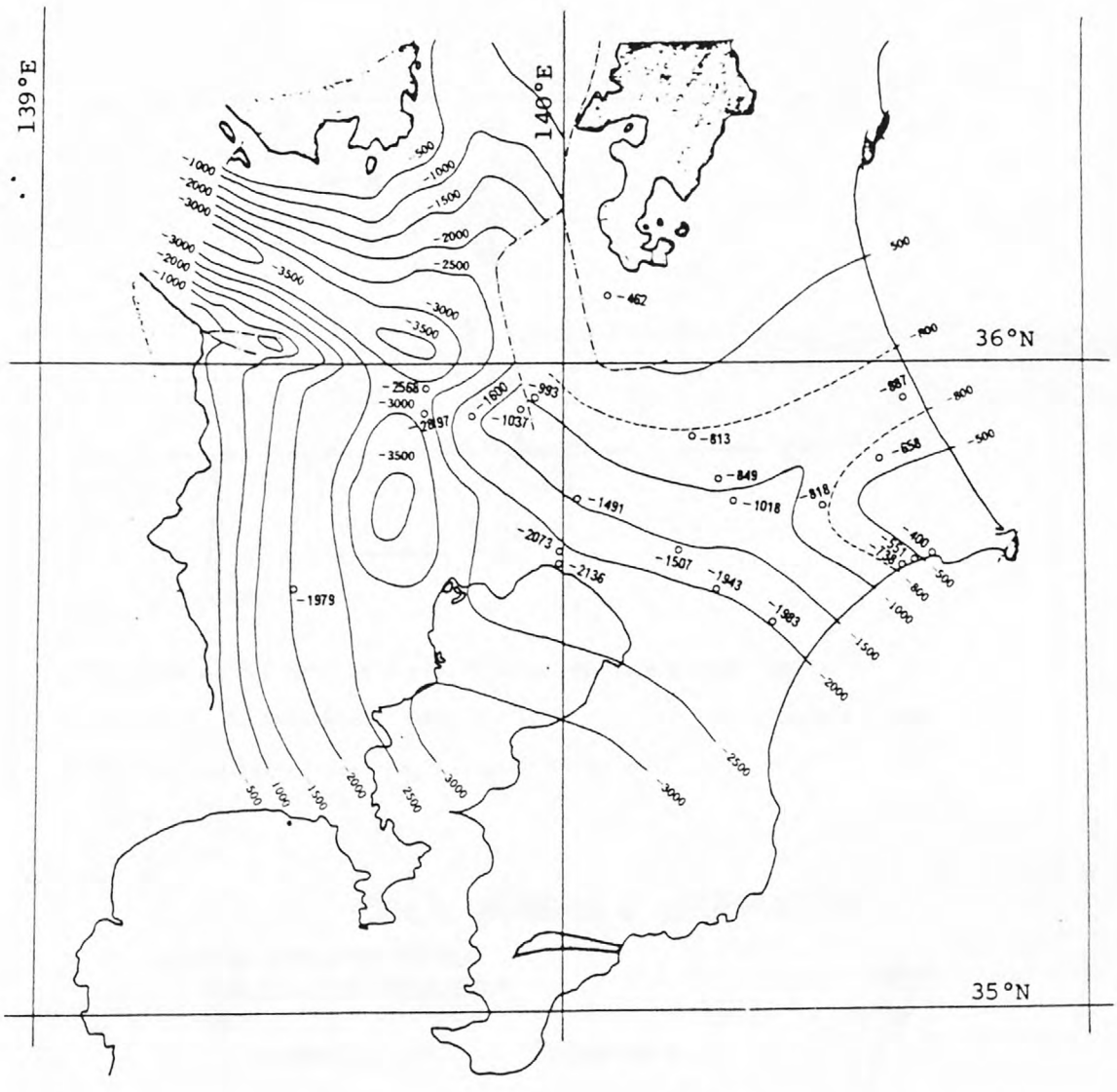

Fig. 2. Estimated contour lines in meter of the Pre-Tertialy basement. Depths are outline estimated mainly based on seismic prospecting.

O :Locations of test borings that reached the basement, where numerals show basement depths in meter.

-·-·-:Faults that accompany the gap in the basement depth.

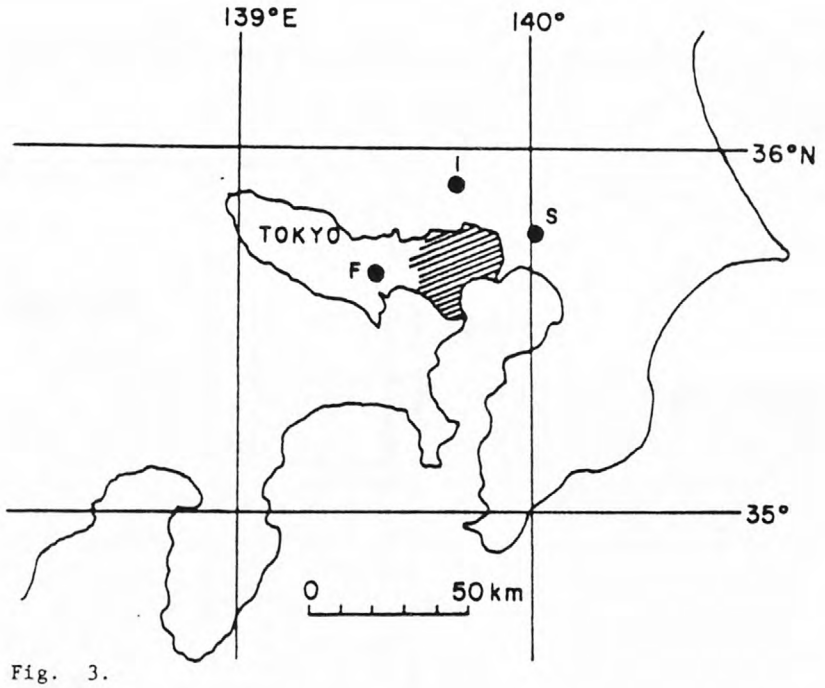

Fig. 3.

Localities of the deep borehole observatory in and near Tokyo. I, Iwatsuki; S, Shimohsa; F, Fuchu. Oblique lines show most populated area, central part of Tokyo.

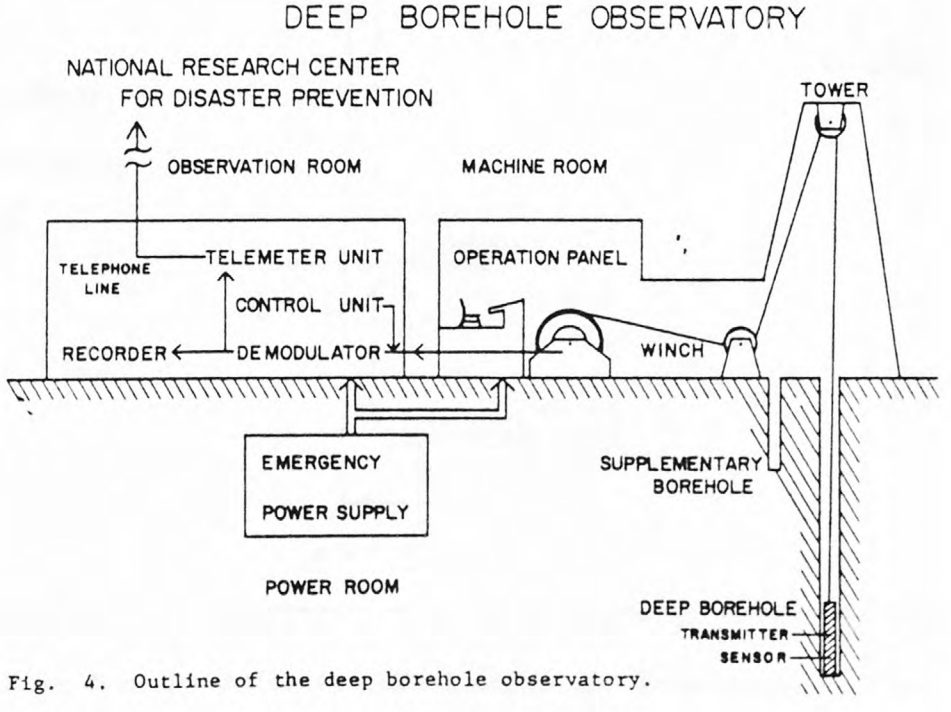

Fig. 4. Outline of the deep borehole observatory.

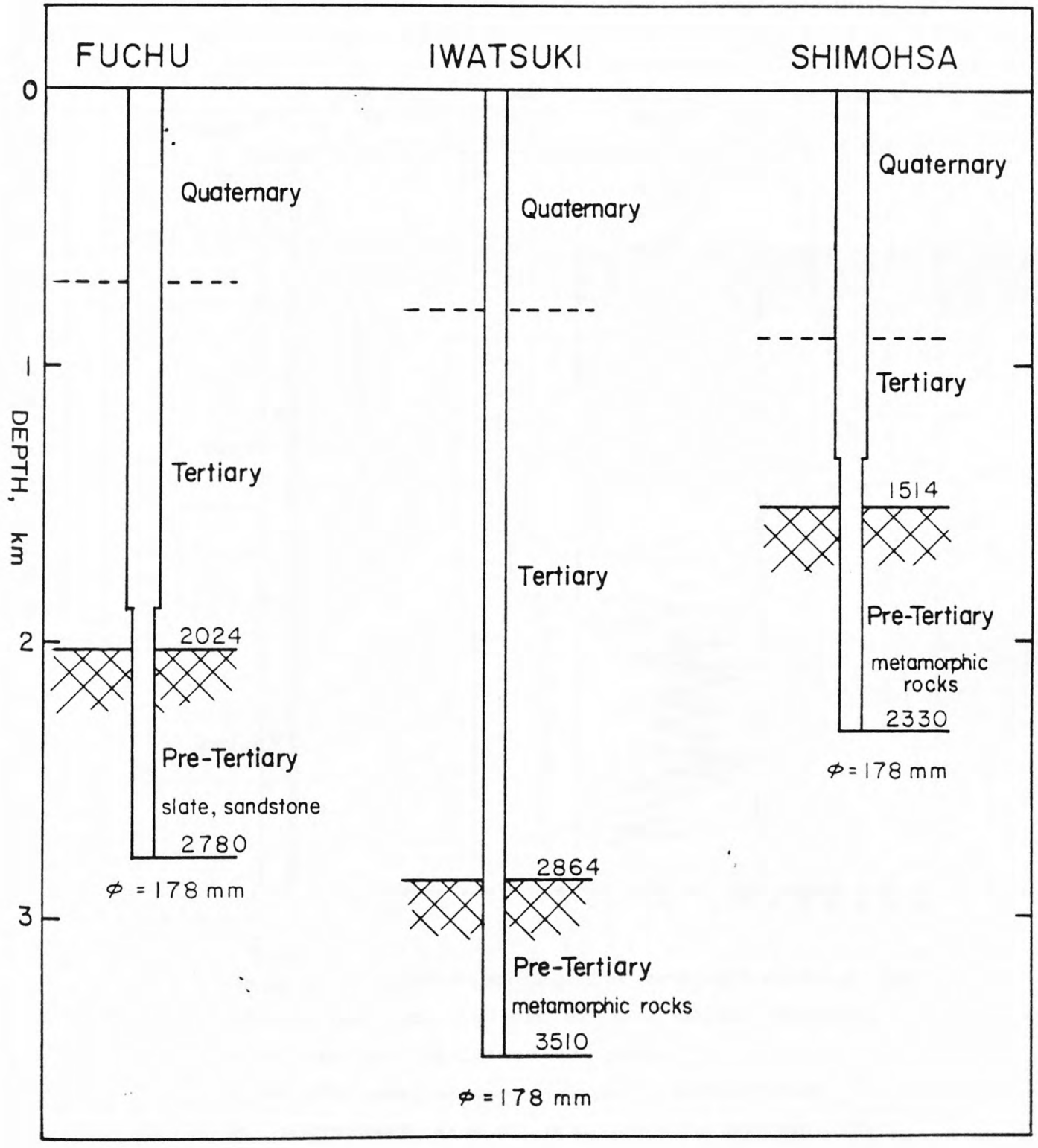

Fig. 5. The three deep boreholes for observation and surrounding geology. Numerals are depth in meter.

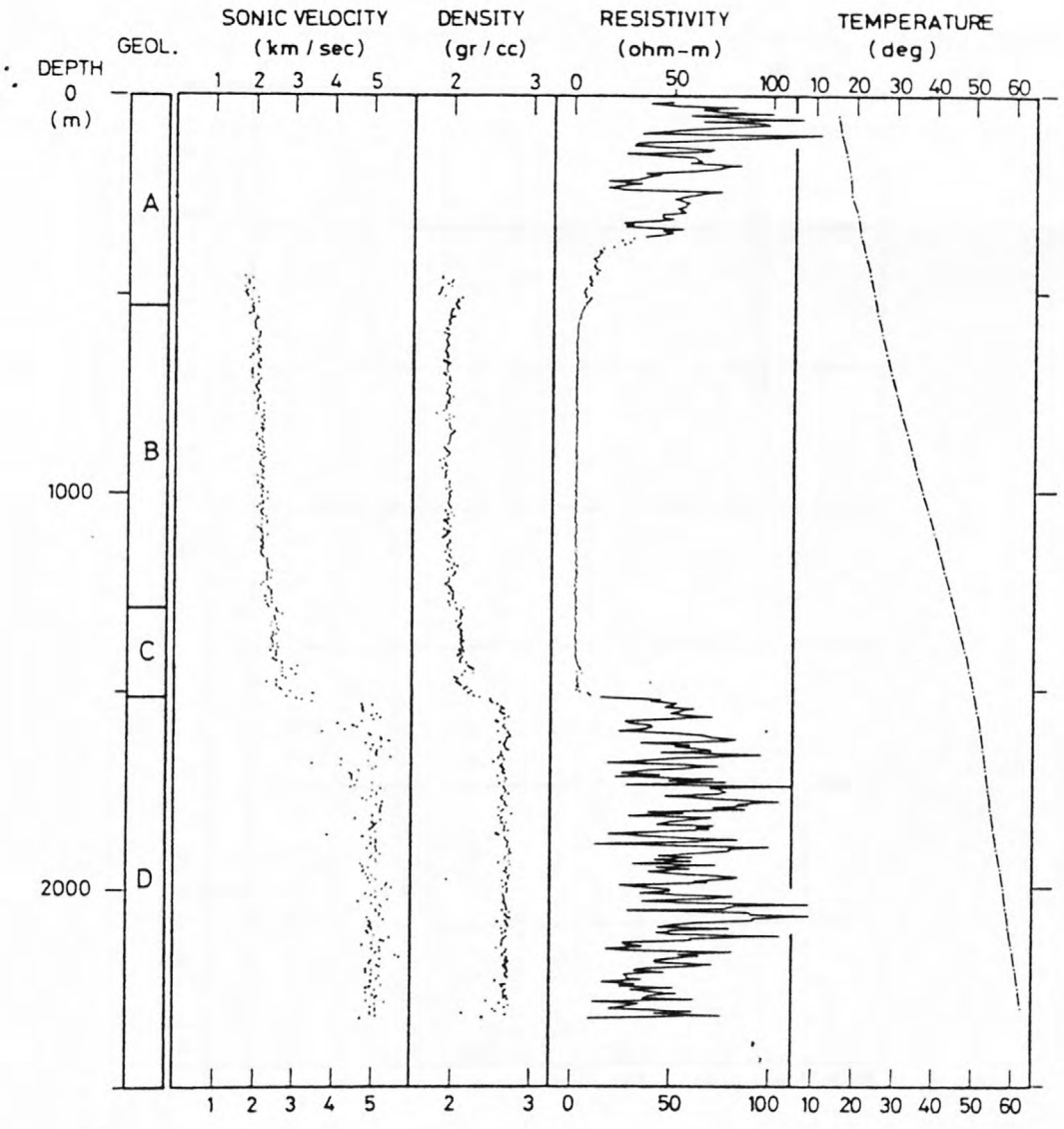

Fig. 6.

Geological and geophysical surroundings at the Shimohsa observatory site.

A; 0-531m depth, sand, sandy silt, and gravel, Holocene-Pleistocene.

B; 531-1289m depth, silt, Pleistocene-Pliocene.

C; 1289-1514m depth, siltstone, sandstone, and breccia, Miocene.

D; 1514-2330m depth, metamorphic rocks, crystalline shist and phyllite, pre-Tertiary.

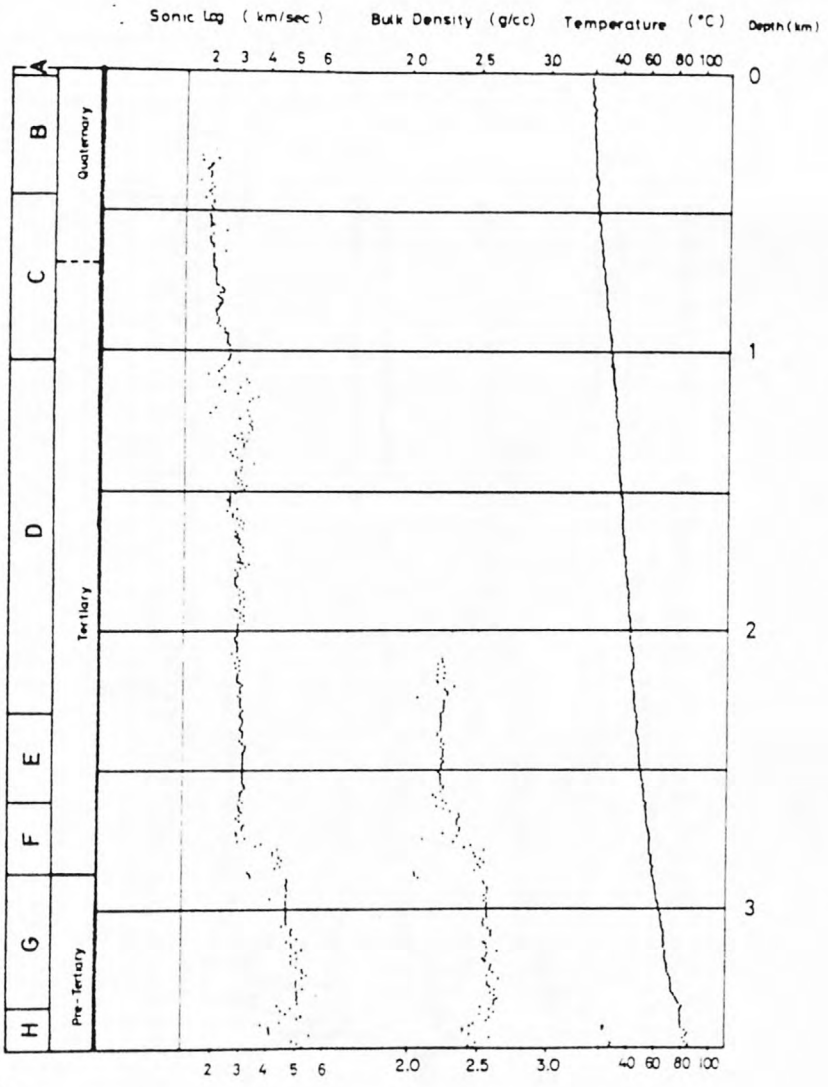

Fig. 7.
Geology, sonic velocity, density, and temperature at the Iwatsuki observatory site. A (0–20 m depth) sand and mud, Holocene. B (20–447 m) gravel, silt, sand, and mud, Pleistocene. C (447–1039 m) sand, silt, and gravel, Plio-Pleistocene. D (1039–2291 m) tuff, sandstone, and conglomerate, Miocene. E (2291–2610 m) sandstone, Miocene. F (2610–2864 m) mudstone, and conglomerate (quartz porphyry), Miocene. G (2864–3346 m) quartz porphyry rarely intervened by tuff, pre-Miocene. H (3346–3510 m) metamorphic rocks, pre-Tertiary

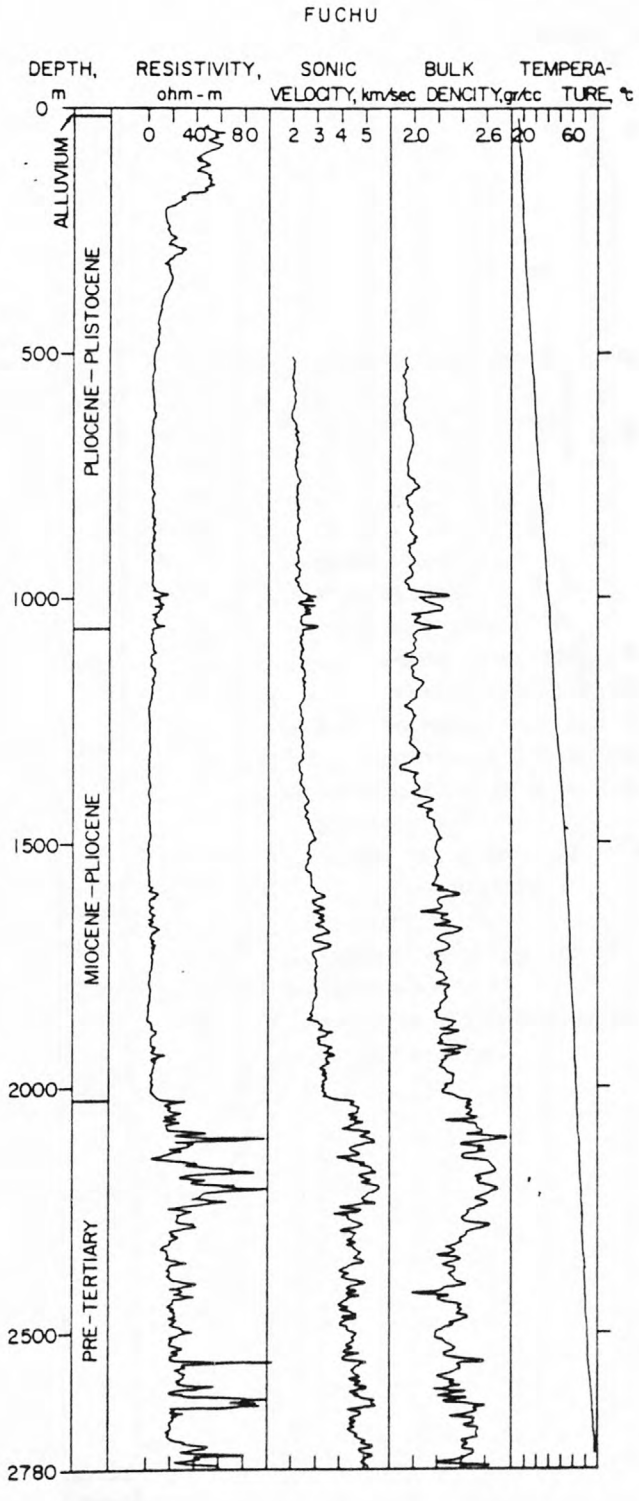

Fig. 8. Geological and geophysical surroundings at the Fuchu observatory.

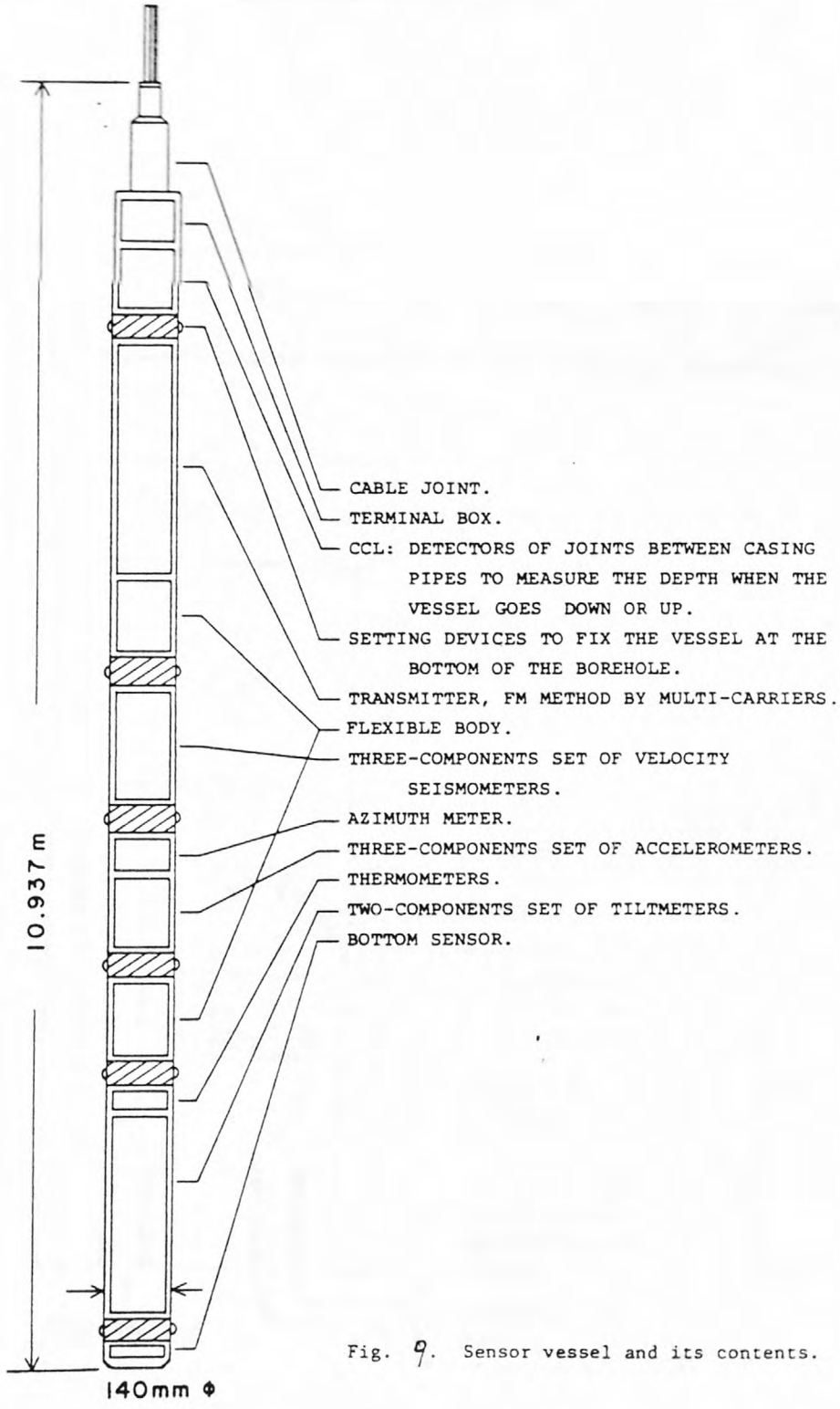

Fig. 9. Sensor vessel and its contents.

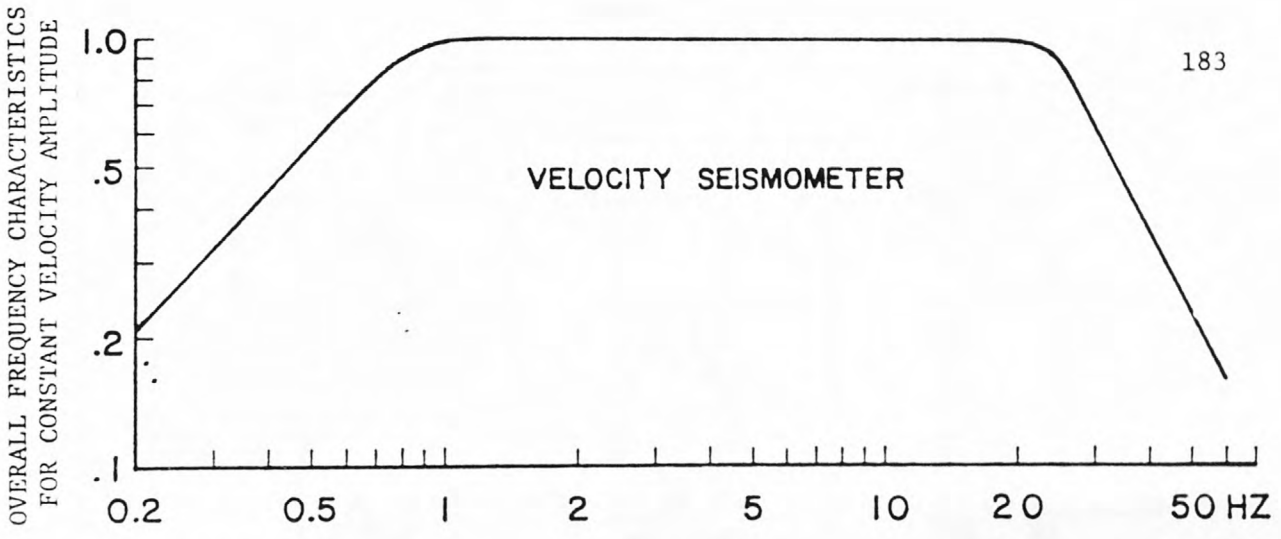

Fig. 10. Overall frequency characteristics of the velocity seismometer.

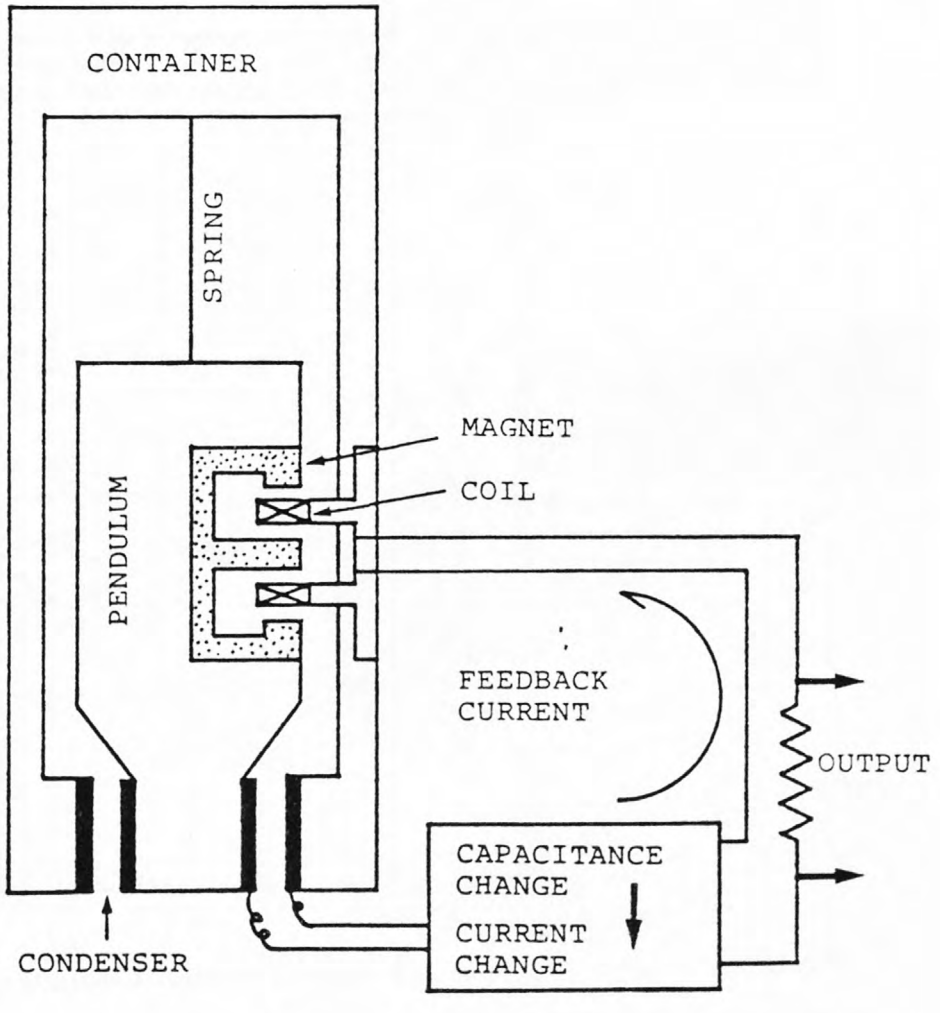

Fig. 11. Schematic structure of the borehole type tiltmeter.

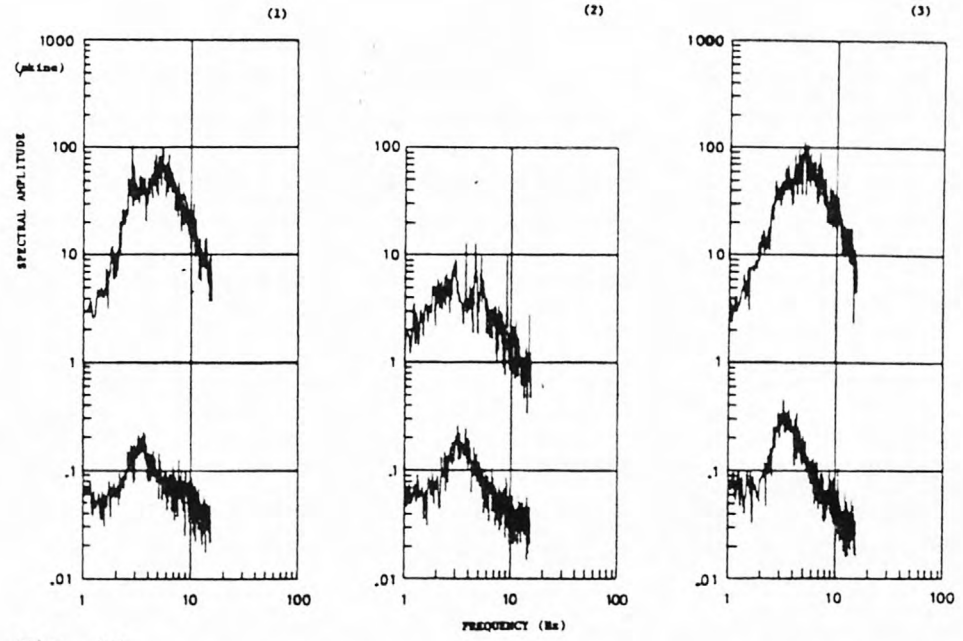

Fig. 12.
Background noises in spectral amplitude at the bottom of the hole and at the surface. Below: at the bottom of the hole. Above: at the surface. 1) Vertical, night-time, the case of heavy cars passing by the observatory; 2) vertical, night-time, the case of no heavy cars passing by the observatory; 3) vertical, daytime, the case of heavy cars passing by the observatory

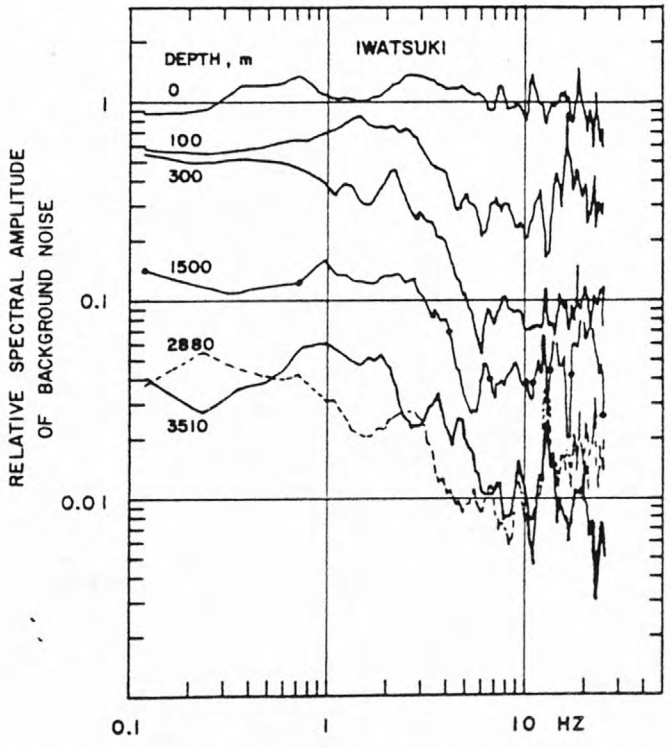

Fig. 13. Reduction of background noise with respect to depth at the Iwatsuki observatory. Vertical components of velocity seismometers. Relative spectral amplitudes were caliculated, being divided by spectral amplitudes of noise simultaneously observed at the surface. after Yamamoto et al.(1976).